

**DEVELOPMENT AND APPLICATION OF SPECTROSCOPY
TECHNIQUES FOR MONITORING HYDRATE AND CORROSION
RISKS**

by

Reza Khodaparast Haghi

Submitted for the degree of Doctor of Philosophy

Heriot-Watt University

School of Energy, Geoscience, Infrastructure and Society

Institute of Petroleum Engineering

January 2017

The copyright in this thesis is owned by the author. Any quotation from the thesis or use of any of the information contained in it must acknowledge this thesis as the source of the quotation or information.

ABSTRACT

Pipelines are used to transport hydrocarbons from production wells to different locations for various purposes (e.g. processing, refinery, power generation, etc.) and CO₂-rich fluids from the emission sources for disposal in suitable geological storage sites. The presence of water in such hydrocarbon and/or CO₂ transport pipelines may result in corrosion, ice and/or gas hydrate formation and even pipeline blockage, so the fluid system should meet certain dehydration and/or inhibition requirements. This work describes the development and application of different spectroscopic (UV-VIS and NIR) methods for identifying and controlling flow assurance issues relating to gas hydrate and corrosion.

For hydrates, a Fourier Transform Near-Infrared (FTNIR) spectroscopy method using chemometric models was developed to measure the concentration of main hydrocarbon gases (Methane through butanes) under in-situ pressure (up to 13.8 MPa). This approach was then used for detecting initial signs of hydrate formation based on reduction in the concentration of some preferential components in the gas phase.

Furthermore, injection of hydrate inhibitors based on the calculated/measured hydrate phase boundary, water cut, pressure and temperature conditions, and the amount of inhibitor lost to non-aqueous phases is a commonly used method for avoiding gas hydrates problems. Thus, it is crucial to monitor salt and inhibitor concentration in the fluids along the pipeline and/or downstream in order to optimise the injection rate. To address this requirement, a novel method was developed by combining UV and NIR spectra to predict the concentration of salt and hydrate inhibitors (THIs and KHIs) simultaneously in aqueous solutions.

In the case of corrosion, the potential of visible spectroscopic technique was investigated for determining the pH in CO₂/ CO₂-rich mixtures saturated water, and CO₂/ CO₂-rich mixtures saturated NaCl solutions at pressures up to 15 MPa and temperature ranges from 293.15 to 323.15 K. Furthermore, we described and evaluated a model that uses a robust thermodynamic basis for describing the solubility of gases in the aqueous phase and Pitzer's theory for determining the activity coefficients of the ionic species involved. The model was tested in concentrated NaCl solutions under CO₂ pressure at realistic industrial operating temperatures.

The developed spectroscopic techniques were experimentally evaluated at lab conditions. Results show that these techniques can be applied to detect initial signs of hydrate formation, to optimise hydrate inhibitor injection rate, and to measure the pH of CO₂ saturated H₂O/brine systems in the downhole/wellbore/pipeline region.

DEDICATION

Dedicated to my parents, Iraj and Aban and my sister, Parastou

ACADEMIC REGISTRY

Research Thesis Submission



Name:	REZA KHODAPARAST HAGHI		
School:	School of Energy, Geoscience, Infrastructure and Society		
Version: <i>(i.e. First, Resubmission, Final)</i>	Final	Degree Sought:	PhD in Petroleum Engineering

Declaration

In accordance with the appropriate regulations I hereby submit my thesis and I declare that:

- 1) the thesis embodies the results of my own work and has been composed by myself
- 2) where appropriate, I have made acknowledgement of the work of others and have made reference to work carried out in collaboration with other persons
- 3) the thesis is the correct version of the thesis for submission and is the same version as any electronic versions submitted*.
- 4) my thesis for the award referred to, deposited in the Heriot-Watt University Library, should be made available for loan or photocopying and be available via the Institutional Repository, subject to such conditions as the Librarian may require
- 5) I understand that as a student of the University I am required to abide by the Regulations of the University and to conform to its discipline.
- 6) I confirm that the thesis has been verified against plagiarism via an approved plagiarism detection application e.g. Turnitin.

* Please note that it is the responsibility of the candidate to ensure that the correct version of the thesis is submitted.

Signature of Candidate:		Date:	
-------------------------	--	-------	--

Submission

Submitted By <i>(name in capitals)</i> :	
Signature of Individual Submitting:	
Date Submitted:	

For Completion in the Student Service Centre (SSC)

Received in the SSC by <i>(name in capitals)</i> :			
1.1 Method of Submission <i>(Handed in to SSC; posted through internal/external mail):</i>			
1.2 E-thesis Submitted (mandatory for final theses)			
Signature:		Date:	

ACKNOWLEDGMENTS

This thesis is submitted in partial fulfilment of the requirements for the PhD degree at Heriot-Watt University. This work has been conducted at the Institute of Petroleum Engineering (IPE) from February 2013 to January 2017 under the supervision of Professor Bahman Tohidi, Dr. Jinhai Yang and Dr. Antonin Chapoy.

Foremost, I would like to express my gratitude to Professor Bahman Tohidi for providing me the opportunity to work in the Hydrates, Flow Assurance & Phase Equilibria Group and also for his outstanding supervision, guidance and support throughout my thesis. I also would like to express my sincere gratitude to my second supervisor Dr. Jinhai Yang for the continuous support of my PhD study and research, for his patience, motivation, enthusiasm, and immense knowledge. His guidance helped me in all the time of research and writing of this thesis. Also in this regard, I also would like to thank Dr. Antonin Chapoy for his sincere guidance and help during the last year of my PhD and for giving me the opportunity to work in his group. My profound thanks are also extended to Dr. Rod Burgess and Alastair Reid for their support in my experimental works and also for their valuable suggestions with all my questions.

I am also grateful to all my friends and colleagues at Heriot-Watt University who made my stay in Edinburgh very pleasant and memorable.

Many appreciations go to the PhD external examiner Professor Bertrand Chazallon and PhD internal examiner Dr. Morteza Haghighat Sefat for reviewing thoroughly my thesis and providing me many helpful corrections for improving my thesis.

The project has been financed by grants by a Joint Industrial Project (JIP) “Hydrate Monitoring and Early Warning System” and “Phase Behaviour and Thermophysical Properties of Acid Gases and CCS Fluid Systems” conducted at the Institute of Petroleum Engineering, Heriot-Watt University. The JIP is supported by Total, Statoil, National Grid, BP, Linde Group, Petronas and Galp Energia which is gratefully acknowledged.

Lastly, I am very thankful to my parents for their love, moral support and patience during my absence.

TABLE OF CONTENTS

ABSTRACT	ii
DEDICATION	iv
ACKNOWLEDGMENTS	v
TABLE OF CONTENTS	vii
LIST OF TABLES	xi
LIST OF FIGURES	xiv
LIST of publications	xxi
List of important symbols	xxii
Chapter 1: INTRODUCTION	1
1.1 Gas Hydrates	1
1.1.1 Gas hydrate stability zone (HSZ)	3
1.1.2 Gas hydrate control and prevention	4
1.1.3 Initial hydrate formation detection techniques	6
1.1.4 Monitoring hydrate inhibition techniques	8
1.2 pH of CO ₂ Acidified Aqueous Systems	10
1.3 Thesis Outline	11
Chapter 2: DEVELOPMENT OF AN FTNIR SPECTROSCOPY METHOD FOR MONITORING COMPOSITIONAL CHANGES IN HYDROCARBON GASES UNDER IN-SITU PRESSURE ...	14
2.1 Introduction	14
2.2 Conventional Method for Analysing the Composition of Fuel Gas	17
2.3 Spectroscopy Methods	17
2.3.1 Infrared spectroscopy	17
2.3.2 Raman spectroscopy	20
2.3.3 NIR vs. Raman	21
2.4 NIR Spectral Data Modelling	23
2.4.1 Principal component analysis (PCA)	23
2.4.2 Partial least squares (PLS)	24
2.4.3 Artificial neural network (ANN)	28
2.5 Preprocessing Methods	29
2.5.1 Normalisation	30
2.5.2 Derivatives	30
2.5.3 Multiplicative scatter correction (MSC)	31
2.5.4 Standard normal variate (SNV)	32
2.5.5 Orthogonal signal correction (OSC)	33
2.5.6 Mean-centring	35
2.6 Model Evaluation	35
2.6.1 Limit of detection (LoD)	36
2.7 Experimental Methodology	37
2.7.1 Experimental equipment	37

2.7.2	Experimental procedure	39
2.7.3	Experimental material	40
2.8	Result and Discussions	42
2.8.1	Influence of temperature, pressure and path-length on FTNIR spectrum of hydrocarbons mixtures	42
2.8.1.1	Influence of temperature	42
2.8.1.2	Influence of pressure	42
2.8.2	Selection of optimum path-length	43
2.8.3	Spectral range selection and construction of the calibration models	45
2.8.4	PLS results	48
2.8.5	ANN Results	62
2.8.6	PLS vs. ANN	70
2.8.7	Comparison of the gas compositions measured by GC and the FTNIR method	72
2.8.8	Temperature and pressure sensitivity analysis for a specific PLS regression model	79
2.9	Graphical User Interface (GUI) for FTNIR Prototype	85
2.10	Conclusions	87
Chapter 3: DETECTION OF INITIAL SIGNS OF HYDRATE FORMATION BY FTNIR SPECTROSCOPY TECHNIQUE		89
3.1	Introduction	89
3.2	Methods to Detect Early Signs of Gas Hydrate Formation	91
3.2.1	FTNIR	91
3.2.2	GasPT	92
3.2.3	V-V _{tc} technique	93
3.3	Detection of Early Signs of Gas Hydrate Formation Using FTNIR Technique	94
3.3.1	Apparatus	94
3.3.2	Experimental procedure	96
3.3.3	Hydrate calculation	97
3.3.4	Materials	98
3.3.5	Results and discussions	98
1.1.1.1	Test 1: Natural gas + deionised water	99
1.1.1.2	Test 2: Natural gas + deionised Water + 5 mass% NaCl	104
1.1.1.3	Test 3: Natural gas + deionised water + 5 mass% NaCl + 10 mass% MEG	109
1.1.1.4	Test 4: Natural gas + deionised water + 5 mass% NaCl + 15 mass% Methanol	113
1.1.1.5	Test 5: Natural gas + deionised water + 5 mass% NaCl + 2.5 mass% Luvicap	117
1.1.1.6	Test 6: Natural gas + deionised water + 5 mass% NaCl + 10 mass% Methanol + gas condensate	122
1.1.1.7	Test 7: Natural gas + deionised water + salt (low water to gas ratio)	126
3.4	Integration of the FTNIR Spectroscopy and GasPT Techniques	131
3.4.1	Apparatus	131
3.4.2	Experimental procedure	132
3.4.3	Results and discussion	132
3.4.4	NIR vs. GasPT	134
3.5	Integration of NIR Spectroscopy Technique with V-V _{tc} Technique	135
3.5.1	Apparatus	135
3.5.2	Experimental procedure	135
3.5.3	Results and discussions	137
3.6	Field Test Results of Monitoring Hydrates Formation by Gas Composition Changes during Gas/Condensate Production with AA-LDHI	137
3.6.1	Presentation of MEILLON field	138
1.1.1.8	LANOT4 well production data	139
1.1.1.9	Gas composition analyser installed on-site	139

3.6.2	Results and discussions	139
3.7	Conclusions	144
Chapter 4: INTEGRATED FTNIR AND UV SPECTROSCOPY TECHNIQUE FOR DETERMINATION OF BOTH THIs AND KHIs		146
4.1	Introduction	146
4.2	Spectroscopy Technique	148
4.2.1	Partial Least Squares Model	150
4.3	Experimental Methodology	151
4.3.1	Experimental equipment	151
4.3.2	Experimental procedure	152
4.3.3	Experimental material	152
4.4	Result and Discussions	152
4.4.1	MEG Systems with NaCl	153
4.4.2	Methanol systems with NaCl	158
4.4.3	MEG-PVCap systems with NaCl	160
4.5	Evaluation of the Spectroscopic Techniques	164
4.6	Conclusions	168
Chapter 5: SPECTROSCOPIC AND ELECTROMETRIC pH MEASUREMENTS AND pH MODELLING		169
5.1	Introduction	169
5.2	Theory of Spectrophotometric for pH Measurement	173
5.2.1	Experimental	176
5.2.1.1	Materials	176
5.2.1.2	Apparatus	176
5.2.1.3	Experimental Procedure	177
5.3	Electrometric Technique for pH Measurements	179
5.3.1	Experimental	181
5.3.1.1	Apparatus	181
5.3.1.2	Experimental Procedure	183
5.4	Modelling Approach	183
5.5	Results and Discussions	185
5.5.1	Spectroscopic Technique – (The dissociation constant of BPB, molar absorptivity coefficients of BPB)	185
5.5.2	Equilibrium pH of CO ₂ in Contact with Water and Brine	187
5.6	Modelling Results	194
5.6.1	Equilibrium pH of multicomponent mixtures in contact with water and brine	203
5.7	Conclusions	208
Chapter 6: CONCLUSIONS AND RECOMMENDATIONS OF FUTURE WORK		211
6.1	Conclusions	211
6.1.1	Initial Hydrate Formation Detection Techniques	211
6.1.2	Hydrate Inhibition Monitoring Techniques	213
6.1.3	pH of CO ₂ saturated water and CO ₂ saturated brines: Experimental measurements and modelling	214

6.2	Recommendations of Future Work	215
REFERENCES.....		217

LIST OF TABLES

Table 2.1. Purity and source of samples used in this study.	41
Table 2.2. Calibration samples used for the construction of the PLS models, mol%.....	41
Table 2.3. Comparison of RMSECV and latent variables of different pre-processing methods at a pressure of 6.89 MPa and temperature of 293.15 K.	51
Table 2.4. Results of the PLS model to estimate the concentration of methane (mol%) in synthetic gas mixtures at different temperatures and pressures (spectral region: 1670 – 1800 nm).	60
Table 2.5. Results of the PLS model to estimate the concentration of ethane in synthetic gas mixtures at different temperatures and pressures (spectral region: 1670 – 1800 nm).	60
Table 2.6. Results of the PLS model to estimate the concentration of propane in synthetic gas mixtures at different temperatures and pressures (spectral region: 1670 – 1800 nm).	60
Table 2.7. Results of the PLS model to estimate the concentration of i-butane in synthetic gas mixtures at different temperatures and pressures (spectral region: 1670 – 1800 nm).	61
Table 2.8. Results of the PLS model to estimate the concentration of n-butane in synthetic gas mixtures at different temperatures and pressures (spectral region: 1670 – 1800 nm).	61
Table 2.9 Calculated LoD for developed PLS models for each component (mol%).....	61
Table 2.10. Results of the ANN model to estimate the concentration of methane in synthetic gas mixtures at different temperatures and pressures (spectral region: 1670 – 1800 nm).	68
Table 2.11. Results of the ANN model to estimate the concentration of ethane in synthetic gas mixtures at different temperatures and pressures (spectral region: 1670 – 1800 nm).	68
Table 2.12. Results of the ANN model to estimate the concentration of propane in synthetic gas mixtures at different temperatures and pressures (spectral region: 1670 – 1800 nm).	68
Table 2.13. Results of the ANN model to estimate the concentration of i-butane in synthetic gas mixtures at different temperatures and pressures (spectral region: 1670 – 1800 nm).	69
Table 2.14. Results of the ANN model to estimate the concentration of n-butane in synthetic gas mixtures at different temperatures and pressures (spectral region: 1670 – 1800 nm).	69
Table 2.15. Comparison of the NIR results using developed PLS models at 293.15K and various pressures with GC for natural gas sample 1, average of three measurements, in mol%.	74
Table 2.16. Comparison of the NIR results using developed ANN models at 293.15 K and various pressures with GC for natural gas sample 1, average of three measurements, in mol%.	74
Table 2.17. Comparison of the NIR results using developed PLS models at 293.15 K and various pressures with GC for natural gas sample 2, average of three measurements, in mol%.	75
Table 2.18. Comparison of the NIR results using developed ANN models at 293.15K and various pressures with GC for natural gas sample 2, average of three measurements.	75
Table 2.19. Summary of FTNIR analyser testing.	79
Table 3.1. The composition of the natural gas used.	98
Table 3.2. Evolution of C ₁ /C ₃ ratio in vapour phase in the presence of NGA and deionised water.	103
Table 3.3. Evolution of C ₁ /C ₂ ratio in vapour phase in the presence of NGA and deionised water.	103
Table 3.4. Evolution of C ₁ /C ₃ ratio in the vapour phase in the presence of natural gas and deionised water and 5 mass% NaCl.	107

Table 3.5. Evolution of C_1/C_2 ratio in the vapour phase in the presence of natural gas and deionised water and 5 mass% NaCl.	107
Table 3.6. Comparison of NIR results with GC for methane, average of three measurements, mol%	108
Table 3.7. Comparison of NIR results with GC for ethane, average of three measurements, mol%	108
Table 3.8. Comparison of NIR results with GC for propane, average of three measurements, mol%	108
Table 3.9. Evolution of C_1/C_3 ratio in the vapour phase in the presence of natural gas, deionised water, salt and MEG.	112
Table 3.10. Evolution of C_1/C_2 ratio in the vapour phase in the presence of natural gas, deionised water, salt and MEG.	112
Table 3.11. Comparison of NIR results with GC for propane, mol%.	113
Table 3.12. Evolution of C_1/C_3 ratio in the vapour phase in the presence of natural gas, deionised water, salt and methanol.	116
Table 3.13. Evolution of C_1/C_2 ratio in the vapour phase in the presence of natural gas, deionised water, salt and methanol.	116
Table 3.14. Evolution of C_1/C_3 ratio in vapour phase in the presence of natural gas, deionised water and Luvicap.....	120
Table 3.15. Evolution of C_1/C_2 ratio in vapour phase in the presence of natural gas, deionised water and Luvicap.....	121
Table 3.16. Comparison of NIR results with gas chromatograph for propane and ethane, mol%.	122
Table 3.17. Evolution of C_1/C_3 ratio in vapour phase in the presence of natural gas, deionised water, salt, methanol and gas condensate.	125
Table 3.18. Evolution of C_1/C_2 ratio in vapour phase in the presence of natural gas, deionised water, salt, methanol and gas condensate.	126
Table 3.19. Evolution of C_1/C_3 ratio in vapour phase in the presence of natural gas, deionised water and salt.	130
Table 3.20. Evolution of C_1/C_2 ratio in vapour phase in the presence of natural gas, deionised water and salt.	130
Table 3.21. Changes in gas composition due to hydrate formation, C_1/C_3 ratio.	131
Table 3.22. Composition of the natural gas.....	132
Table 3.23. Test results of compositional change techniques (NIR prototype, GasPT and GC) system (C_1/C_3 ratio in vapour phase).....	134
Table 3.24. Test results of the integrated NIR-V- V_{tc} system.	137
Table 3.25. Composition of the natural gas.....	139
Table 4.1. Range of concentrations for the three calibration series.....	152
Table 4.2. Summary of results for calibration and prediction sets for MEG and NaCl in the water samples using NIR spectra and PLS.	156
Table 4.3. Calculated LoD for developed PLS models by using a Savitzky–Golay derivative pre-treatment with 5-point moving window in 1400-1850 nm wavelength range.....	157
Table 4.4. Calculated RMSECV and RMSEP in mass% and latent variables for developed PLS models by using a Savitzky–Golay derivative pre-treatment with a second-order polynomial and a 5-point moving window.....	159

Table 4.5. Calculated LoD for developed PLS models by using a Savitzky–Golay derivative pre-treatment with 5-point moving window in 1400-1800 nm wavelength range.....	160
Table 4.6. Calculated RMSECV and RMSEP in mass% and latent variables for developed PLS models by using a Savitzky–Golay derivative pre-treatment with a second-order polynomial with 5-point moving windows.	164
Table 4.7. Calculated LoD for developed PLS models by using a Savitzky–Golay derivative pre-treatment with 5-point moving window in 1400-1850 nm wavelength range.....	164
Table 4.8. Composition of the natural gas.....	165
Table 4.9. Test results of the NIR method.....	167
Table 5.1. Measured pK_a , e_1 , e_2 and e_3 of BPB at atmospheric pressure and different temperatures and ionic strengths.	186
Table 5.2. Measured and predicted pH values (electrometric technique) in the CO ₂ -H ₂ O system.	187
Table 5.3. Measured and predicted pH values (spectroscopic technique) in the CO ₂ -H ₂ O system.....	188
Table 5.4. Measured and predicted pH value (spectroscopic technique) for different CO ₂ saturated brine systems.....	193
Table 5.5. Summary of the calculated %AAD value between the pH measured and predicted values in various fluid systems.....	195
Table 5.6. Ternary gas composition.	203
Table 5.7. Measured and predicted pH values for ternary gas composition (Aqueous fraction = 0.921).	204
Table 5.8. Measured and predicted pH values for ternary gas mixture (Aqueous fraction = 0.942).	206
Table 5.9. Multicomponent gas composition.	207
Table 5.10. Measured and predicted pH values for ternary gas composition for (Aqueous fraction = 0.912).	208

LIST OF FIGURES

Figure 1.1. Hydrate crystal structures [4].	2
Figure 1.2. Hydrate risk and free zone.	3
Figure 1.3. Predicted hydrate phase boundaries for a typical natural gas for different fluid systems.	4
Figure 1.4. Hydrate safety margin determined by the developed hydrate inhibition monitoring techniques could be used as traffic lights to help the operators have a better control of hydrate inhibition.	10
Figure 2.1. The electromagnetic spectrum.	18
Figure 2.2. Schematic representation showing that light of initial intensity, I_0 passing through an absorbing in the sample cell with a specific pathlength, l , will emerge with a final intensity, I .	19
Figure 2.3. Major analytical bands and relative peak positions for prominent near-infrared [53].	20
Figure 2.4. FTNIR Spectra of the pure hydrocarbons at atmospheric pressure and room temperature that captured by the FTNIR spectrometer.	20
Figure 2.5. Spectra of deionised water with optical path length of 1.4 cm.	22
Figure 2.6. Model structure of PLS [56].	25
Figure 2.7. The structure of developed multi-layer feed forward ANN for calculating the hydrocarbons concentration.	28
Figure 2.8. An example of Savitzky-Golay method. (a) Original spectrum before applying the Savitzky-Golay pretreatment method. (b) After applying the Savitzky-Golay pretreatment method using different smoothing points.	31
Figure 2.9. The original spectrum versus the reference spectrum. b_0 and b_{ref} represent the intercept and slope of the fitted line.	32
Figure 2.10. Pictures of the FTNIR spectroscopy test setup.	38
Figure 2.11. Schematic diagram of the FTNIR setup, 1: Cooling / Heating bath, 2: NIR light source, 3: Fibre optic, 4: Collimating lens, 5: Sapphire windows, 6: High-pressure cell, 7: Spectrometer, 8: Pressure transducer, 9: Temperature probe, 10: Vacuum pump.	39
Figure 2.12. FTNIR Spectra of one synthetic gas mixture at 6.89 MPa and three different temperatures.	42
Figure 2.13. FTNIR Spectra of one synthetic gas mixture at 293.15 K and four different pressures.	43
Figure 2.14. FTNIR Spectra of 30 synthetic gas mixtures with different methane, ethane, propane, i-butane and n-butane contents at various pressures in the range of 3.44 - 13.78 MPa and various temperatures in the range of 278.15 – 313.15 K (The range shaded (1670 – 1800 nm) used for developing of the regression models).	45
Figure 2.15. Weighted regression plot, showing important variables in modelling.	46
Figure 2.16. A flowchart showing the sequence of steps that followed to develop the final PLS models.	48
Figure 2.17. Comparison of RMSECV with respect to the number of latent variables for developed PLS model – SG1 + OSC pre-treatment, at a temperature of 293.15 K and various pressures (3.44 (a), 6.89 (b), 10.34 (c), and 13.78 (d) MPa).	52
Figure 2.18. Comparison of RMSEP of different pre-processing methods for PLS developed models at a pressure of 6.89 MPa and temperature of 293.15 K.	53
Figure 2.19. NIR spectra after SG1 pre-treatment for all the calibration samples.	54
Figure 2.20. NIR spectra after SG1 + OSC treatment for methane, ethane, propane, i-butane and n-butane at pressure of 6.89 MPa and temperature of 293.15 K.	55

Figure 2.21. PLS regression plot of predicted versus actual concentration of methane (a), ethane (b), propane (c), i-butane (d) and n-butane (e) in synthetic gas mixtures (independent samples) at temperature of 278.15 K and various pressures.	57
Figure 2.22. PLS regression plot of predicted versus actual concentration of methane (a), ethane (b), propane (c), i-butane (d) and n-butane (e) in synthetic gas mixtures (independent samples) at temperature of 293.15 K and various pressures.	58
Figure 2.23. PLS regression plot of predicted versus actual concentration of methane (a), ethane (b), propane (c), i-butane (d) and n-butane (e) in synthetic gas mixtures (independent samples) at temperature of 313.15 K and various pressures.	59
Figure 2.24. Schematic of the developed ANN models for all the hydrocarbon components at various pressures and temperatures.....	64
Figure 2.25. ANN regression plot of predicted versus actual concentration of methane (a), ethane (b), propane (c), i-butane (d) and n-butane (e) in synthetic gas mixtures (independent samples) at temperature of 278.15 K and various pressures.	65
Figure 2.26. ANN regression plot of predicted versus actual concentration of methane (a), ethane (b), propane (c), i-butane (d) and n-butane (e) in synthetic gas mixtures (independent samples) at temperature of 293.15 K and various pressures.	66
Figure 2.27. ANN regression plot of predicted versus actual concentration of methane (a), ethane (b), propane (c), i-butane (d) and n-butane (e) in synthetic gas mixtures (independent samples) at temperature of 313.15 K and various pressures	67
Figure 2.28. The comparison of developed PLS and ANN models at various pressures and temperature of 278.15 K.....	70
Figure 2.29. The comparison of developed PLS and ANN models at various pressures and temperature of 293.15 K.....	71
Figure 2.30. The comparison of developed PLS and ANN models at various pressures and temperature of 313.15 K.....	71
Figure 2.31. FTNIR spectra of pure carbon dioxide methane and nitrogen at a pressure of 3.44 MPa and room temperature from FTNIR spectrometer.....	73
Figure 2.32. Absolute residual (Difference between GC and FTNIR measured values) distribution for methane.	76
Figure 2.33. Absolute residual (Difference between GC and FTNIR measured values) distribution for ethane.	77
Figure 2.34. Absolute residual (Difference between GC and FTNIR measured values) distribution for propane.....	77
Figure 2.35. Absolute residual (Difference between GC and FTNIR measured values) distribution for i-butane.	78
Figure 2.36. Absolute residual (Difference between GC and FTNIR measured values) distribution for n-butane.	78
Figure 2.37. Effect of pressure variation on the FTNIR predicted values (mol%) for methane on the 293.15 K.....	80
Figure 2.38. Effect of pressure variation on the FTNIR predicted values (mol%) for ethane on the 293.15 K.....	80

Figure 2.39. Effect of pressure variation on the FTNIR predicted values (mol%) for propane on the 293.15 K.....	81
Figure 2.40. Effect of pressure variation on the FTNIR predicted values (mol%) for i-butane on the 293.15 K.....	81
Figure 2.41. Effect of pressure variation on the FTNIR predicted values (mol%) for n-butane on the 293.15 K.....	82
Figure 2.42. Effect of temperature variation on the FTNIR predicted values (mol%) for methane at a pressure of 6.89 MPa.....	83
Figure 2.43. Effect of temperature variation on the FTNIR predicted values (mol%) for ethane at a pressure of 6.89 MPa.....	83
Figure 2.44. Effect of temperature variation on the FTNIR predicted values (mol%) for propane at a pressure of 6.89 MPa.....	84
Figure 2.45. Effect of temperature variation on the FTNIR predicted values (mol%) for i-butane at a pressure of 6.89 MPa.....	84
Figure 2.46. Effect of temperature variation on the FTNIR predicted values (mol%) for n-butane at a pressure of 6.89 MPa.....	85
Figure 2.47. Main window of the FT-NIR analyser.....	86
Figure 2.48. The Data Dashboard application for controlling and monitoring the compositional change in the gas sample.....	87
Figure 3.1. Schematic of GasPT.....	92
Figure 3.2. Flowchart of the V-V _{tc} technique.....	93
Figure 3.3. Picture of the developed V-V _{tc} prototype.....	94
Figure 3.4. Schematic illustration of high pressure rig.....	95
Figure 3.5. Schematic diagram of the experimental setup.....	95
Figure 3.6. Temperature-pressure profile and sampling points for the system with NG-A and deionised water.....	100
Figure 3.7. Compositional monitoring of C ₁ /C ₃ ratio in the gas phase using GC and FTNIR at 3.44 MPa and 293.15 K. Connection trend between points are only for visual clarification.....	101
Figure 3.8. Compositional monitoring of C ₁ /C ₂ ratio in the gas phase using GC and FTNIR at 3.44 MPa and 293.15 K. Connection trend between points are only for visual clarification.....	101
Figure 3.9. Compositional monitoring of C ₁ /C ₃ ratio in the gas phase using GC and FTNIR at 6.89 MPa and 293.15 K. Connection trend between points are only for visual clarification.....	102
Figure 3.10. Compositional monitoring of C ₁ /C ₂ ratio in the gas phase using GC and FTNIR at 6.89 MPa and 293.15 K. Connection trend between points are only for visual clarification.....	102
Figure 3.11. Temperature-pressure profile and sampling points for the system with NG-A, deionised water and salt.....	105
Figure 3.12. Compositional monitoring of C ₁ /C ₃ ratio in the gas phase using GC and FTNIR at 6.89 MPa and 293.15 K. Connection trend between points are only for visual clarification.....	106
Figure 3.13. Compositional monitoring of C ₁ /C ₂ ratio in the gas phase using GC and FTNIR at 6.89 MPa and 293.15 K. Connection trend between points are only for visual clarification.....	106
Figure 3.14. Temperature-pressure profile and sampling points for the system with NGB, deionised water, MEG and salt.....	109

Figure 3.15. Compositional monitoring of C_1/C_3 ratio in the gas phase using GC and FTNIR at 6.89 MPa and 313.15 K. Connection trend between points are only for visual clarification.....	110
Figure 3.16. Compositional monitoring of C_1/C_2 ratio in the gas phase using GC and FTNIR at 6.89 MPa and 313.15 K. Connection trend between points are only for visual clarification.....	110
Figure 3.17. Compositional monitoring of C_1/C_3 ratio in the gas phase using GC and FTNIR at 10.34 MPa and 313.15 K. Connection trend between points are only for visual clarification.....	111
Figure 3.18. Compositional monitoring of C_1/C_2 ratio in the gas phase using GC and FTNIR at 10.34 MPa and 313.15 K. Connection trend between points are only for visual clarification.....	111
Figure 3.19. Temperature-pressure profile and sampling points for the system with NGB, deionised water, methanol and salt.....	114
Figure 3.20. Compositional monitoring of C_1/C_3 ratio in the gas phase using GC and FTNIR at 6.89 MPa and 313.15 K. Connection trend between points are only for visual clarification.....	114
Figure 3.21. Compositional monitoring of C_1/C_2 ratio in the gas phase using GC and FTNIR at 6.89 MPa and 313.15 K. Connection trend between points are only for visual clarification.....	115
Figure 3.22. Compositional monitoring of C_1/C_3 ratio in the gas phase using GC and FTNIR at 10.34 MPa and 313.15 K. Connection trend between points are only for visual clarification.....	115
Figure 3.23. Compositional monitoring of C_1/C_2 ratio in the gas phase using GC and FTNIR at 10.34 MPa and 313.15 K. Connection trend between points are only for visual clarification.....	116
Figure 3.24. Temperature-pressure profile and sampling points for the system with NG-B, deionised water, Luvicap and salt.	118
Figure 3.25. Compositional monitoring of C_1/C_3 ratio in the gas phase using GC and FTNIR at 10.34 MPa and 313.15 K. Connection trend between points are only for visual clarification.....	118
Figure 3.26. Compositional monitoring of C_1/C_2 ratio in the gas phase using GC and FTNIR at 10.34 MPa and 313.15 K. Connection trend between points are only for visual clarification.....	119
Figure 3.27. Compositional monitoring of C_1/C_3 ratio in the gas phase using GC and FTNIR at 13.78 MPa and 313.15 K. Connection trend between points are only for visual clarification.....	119
Figure 3.28. Compositional monitoring of C_1/C_2 ratio in the gas phase using GC and FTNIR at 13.78 MPa and 313.15 K. Connection trend between points are only for visual clarification.....	120
Figure 3.29. Temperature-pressure profile and sampling points for the system with NGB, deionised water, methanol, gas condensate and salt.....	123
Figure 3.30. Compositional monitoring of C_1/C_3 ratio in the gas phase using GC and FTNIR at 6.89 MPa and 293.15 K. Connection trend between points are only for visual clarification.....	123
Figure 3.31. Compositional monitoring of C_1/C_2 ratio in the gas phase using GC and FTNIR at 6.89 MPa and 293.15 K. Connection trend between points are only for visual clarification.....	124
Figure 3.32. Compositional monitoring of C_1/C_3 ratio in the gas phase using GC and FTNIR at 10.34 MPa and 293.15 K. Connection trend between points are only for visual clarification.....	124
Figure 3.33. Compositional monitoring of C_1/C_2 ratio in the gas phase using GC and FTNIR at 10.34 MPa and 293.15 K. Connection trend between points are only for visual clarification.....	125
Figure 3.34. Temperature-pressure profile and sampling points for the system with NGB, deionised water and salt.	127
Figure 3.35. Compositional monitoring of C_1/C_3 ratio in the gas phase using GC and FTNIR at 6.89 MPa and 293.15 K. Connection trend between points are only for visual clarification.....	127

Figure 3.36. Compositional monitoring of C_1/C_2 ratio in the gas phase using GC and FTNIR at 6.89 MPa and 293.15 K. Connection trend between points are only for visual clarification.....	128
Figure 3.37. Compositional monitoring of C_1/C_3 ratio in the gas phase using GC and FTNIR at 10.34 MPa and 293.15 K. Connection trend between points are only for visual clarification.....	128
Figure 3.38. Compositional monitoring of C_1/C_2 ratio in the gas phase using GC and FTNIR at 10.34 MPa and 293.15 K. Connection trend between points are only for visual clarification.....	129
Figure 3.39. Temperature and pressure profiles and test points in the test of the integrated water content (re-calibrated HMT360)-compositional change (NIR prototype, GasPT and GC) system.	132
Figure 3.40. Temperature and pressure profiles and test points in testing of the integrated water content (HMT360)-compositional change system (GasPT).....	133
Figure 3.41. Schematic of the experimental setup for testing the integrated NIR spectroscopy and V-V _{tc} system.....	135
Figure 3.42. Temperature and pressure profiles and test points in the test of the integrated NIR spectroscopy technique and the V-V _{tc} technique.	136
Figure 3.43. Schematic diagram of the separator unit.	139
Figure 3.44. Predicted hydrate phase boundaries for the structure I and II hydrates for LANOT4 well. The red line represents hydrate phase boundary sII, and the green line represents hydrate phase boundary sI.	140
Figure 3.45. Hydrate subcooling temperature. White region: system is outside hydrate stability zone, red region: system is inside hydrate sII and outside hydrate sI stability zone and blue region: system is inside hydrate sI and sII stability zone.....	141
Figure 3.46. Gas compositional changes due to hydrate formation indicated by the GC analysed C_1/C_3 (a) and C_1/iC_4 (b) ratios.	143
Figure 4.1. FTNIR Spectra of the pure water, methanol and MEG in a cuvette with a pathlength of 1 mm at atmospheric pressure and 293.15 K that captured by the FTNIR spectrometer.	149
Figure 4.2. UV spectra of solutions with various PVCap concentrations captured by the UV-Vis-NIR spectrometer.	150
Figure 4.3. Schematic diagram of the spectroscopy setup, 1: Cooling / heating bath, 2: FT-NIR source, 3: UV-Vis-NIR source, 4: Fibre optic, 5: Cuvette, 6: Cuvette holder with a metallic jacket, 7: NIR detector and 8: UV-Vis detector.	151
Figure 4.4. NIR Spectra of 35 water samples with different MEG and salt concentrations without applying any pre-processing method in the wavelength range from 900 to 2500 nm.	153
Figure 4.5. NIR Spectra of 35 water samples with different MEG and salt concentrations after applying the Savitzky-Golay pre-treatment in the wavelength range from 1400 to 1850 nm.....	154
Figure 4.6. PLS regression plot of predicted versus actual concentration of MEG at different wavelength ranges.	155
Figure 4.7. PLS regression plot of predicted versus actual concentration of NaCl at different wavelength ranges.	155
Figure 4.8. The comparison of root mean square of prediction (RMSEP) for MEG and NaCl at various wavelength ranges.	157
Figure 4.9. PLS regression plot of predicted versus actual concentration of methanol at different wavelength ranges.	158

Figure 4.10. PLS regression plot of predicted versus actual concentration of NaCl at different wavelength ranges.	159
Figure 4.11. The comparison of root mean square of prediction (RMSEP) for MEG and NaCl at various wavelength ranges.	160
Figure 4.12. PLS regression plot of predicted versus actual concentration of MEG.	162
Figure 4.13. PLS regression plot of predicted versus actual concentration of MEG.	162
Figure 4.14. PLS regression plot of predicted versus actual concentration of PVCap.	163
Figure 4.15. Schematic of the experimental setup.	165
Figure 4.16. Temperature-pressure profile and sampling points for the system with natural gas, deionised water, MEG and NaCl.	166
Figure 5.1. The absorbance spectrum of BPB solutions at pH of 7 (Base form) and pH of 1.5 (Acid form) using the UV-Visible spectrometer (1.4 cm path length).	176
Figure 5.2. Schematic diagram of the spectroscopy setup for pH measurements, 1: Cooling / Heating bath, 2: Deuterium and tungsten light sources, 3: Fibre optic, 4: Sapphire windows, 5: High pressure cell, 6: Spectrometer, 7: Pressure transducer, 8: Temperature probe and V: Valve.	177
Figure 5.3. Spectra of BPB solutions with different pH values at a pressure of 0.1 MPa, the temperature of 298.15 K and zero ionic strength.	178
Figure 5.4. Picture of glass and reference electrode.	180
Figure 5.5. Schematic diagram of the glass and reference electrode.	181
Figure 5.6. Picture of the autoclave for pH measurements.	182
Figure 5.7. Schematic diagram of the high pressure setup for pH measurements using the glass electrode, 1: pH probe 2: Temperature probe, 3: Magnetic stirrer, 4: Pressure transducer and V: Valve.	182
Figure 5.8. pH of CO ₂ saturated solutions as a function of pressure in the CO ₂ -H ₂ O system. Filled symbols represent experimental data measured in this work using electrometric technique and empty symbols represent the literature data measured using the electrometric technique.	189
Figure 5.9. pH of CO ₂ saturated solutions as a function of pressure in the CO ₂ -H ₂ O system. Filled symbols represent experimental data measured in this work using the spectroscopic technique and empty symbols represent the literature data measured using the spectroscopic technique.	190
Figure 5.10. pH of CO ₂ saturated solutions as a function of pressure in the CO ₂ -H ₂ O-NaCl system. Filled symbols represent experimental data measured in this work using the spectroscopic technique ($m = 1 \text{ mol.kg}^{-1}$). Empty symbols represent the data measured using the electrometric technique by Schaef <i>et al.</i> [111], ($m = 1.01 \text{ mol.kg}^{-1}$).	191
Figure 5.11. pH of CO ₂ saturated solutions as a function of pressure in the CO ₂ -H ₂ O-NaCl system. Filled symbols represent experimental data measured in this work using the spectroscopic and empty symbols represent the data measured using the spectroscopic technique by Shao <i>et al.</i> [118]. ($m = 3 \text{ mol.kg}^{-1}$). .	192
Figure 5.12. Effect of variation in ionic strength on the pH value of the CO ₂ saturated solutions as a function of pressure.	194
Figure 5.13. Experimental and predicted pH values in the CO ₂ -H ₂ O system. Empty symbols represent the experimental data obtained using the electrometric technique and filled symbol represent the experimental data obtained using the spectroscopic technique. Solid lines represents the prediction from the model.	196
Figure 5.14. pH of CO ₂ saturated solutions as a function of pressure in the CO ₂ -H ₂ O system. Symbols represent experimental data from the literature (electrometric technique).	197

Figure 5.15. pH of CO ₂ saturated solutions as a function of pressure in the CO ₂ -H ₂ O system. Empty symbols represent experimental data from the literature and solid lines represent the prediction from the model.	198
Figure 5.16. pH-pressure and x _{CO₂} -pressure diagrams of the CO ₂ -H ₂ O and CO ₂ -H ₂ O-NaCl systems at temperature of 323.15 K. Empty symbols represent experimental mole fraction data of CO ₂ in aqueous phase and filled symbols represent experimental pH data. Dashed and solid lines represent the pH and x _{CO₂} predictions at various ionic strengths from the model respectively.	199
Figure 5.17. pH of the CO ₂ -H ₂ O system as a function of $-\log_{10}(x_{\text{CO}_2})$ at temperature of 323.15 K.	200
Figure 5.18. Experimental (Spectroscopic technique) and predicted pH values in the CO ₂ -H ₂ O-NaCl systems with various ionic strengths (1 m (a), 2 m (b) and 3 m (c) NaCl).	201
Figure 5.19. pH of the CO ₂ -H ₂ O-NaCl systems as a function of $-\log_{10}(x_{\text{CO}_2})$ at a temperature of 323.15 K (spectroscopic technique).	202
Figure 5.20. Experimental and predicted pH values in the CH ₄ -CO ₂ -N ₂ -H ₂ O system. Filled symbol represent the experimental data that obtained using spectroscopic technique and Solid lines represent the prediction from the model using an aqueous fraction of 0.921.	204
Figure 5.21. Experimental and predicted pH values in the CH ₄ -CO ₂ -N ₂ -H ₂ O-NaCl system. Empty symbol represent the experimental data that obtained using spectroscopic technique. Solid lines represent the prediction from the model using an aqueous fraction of 0.921.	206
Figure 5.22. Experimental and predicted pH values in the multicomponent gas mixture system. Empty symbol represent the experimental data that obtained using spectroscopic technique. Solid lines represent the prediction from the model using an aqueous fraction of 0.921.	207

LIST OF PUBLICATIONS

Reza K. Haghi, Jinhai Yang, Bahman Tohidi “FTNIR spectroscopy methodology for monitoring compositional changes in hydrocarbon gases under in-situ pressure” (*Fuel*, *Under Review*).

Reza K. Haghi, Antonin Chapoy, Luís M. C. Peirera, Jinhai Yang , Bahman Tohidi “pH of CO₂ saturated water and CO₂ saturated brines: Experimental measurements and modelling” (*International Journal of Greenhouse Gas Control*, *Under Review*).

Glénat, P., J. M. Munoz, **R. Haghi**, B. Tohidi, S. Mazloun, and J. Yang. "Field Test results of monitoring Hydrates formation by gas composition changes during gas/condensate production with AA-LDHI." In The proceeding of the 8th International Conference on Gas Hydrates, Beijing, China. 2014.

PAPERS IN PREPARATION

Detection of initial signs of hydrate formation using FTNIR spectroscopy.

Determination of hydrate Inhibitor and salt concentrations by coupling UV and FTNIR spectroscopic techniques.

Utilisation of FTNIR spectroscopy technique for wax appearance temperature and characterization of wax inhibitors.

LIST OF IMPORTANT SYMBOLS

AAs	Anti-Agglomerants
ANN	Artificial neural network
C ₁	Methane
C ₂	Ethane
C ₃	Propane
CCS	Carbon capture and storage
CO ₂	Carbon dioxide
FT-NIR	Fourier transform near-infrared
GC	Gas chromatography
I ₀	Incident light
i-C ₄	Iso-butane
KHIs	Kinetic hydrate inhibitors
LDHIs	Low dosage hydrate inhibitors
LoD	Limit of detection
MEG	Ethylene glycol
MSC	Multiplicative scatter correction
N ₂	Nitrogen
NaCl	Sodium chloride
n-C ₄	Normal-butane
NG	Natural gas
OSC	Orthogonal signal correction
P	Pressure
PCA	Principal component analysis
PLS	Partial least square
PVCap	Poly-nvinylcaprolactam
SGD1	First Savitzky-Golay derivative
SGD2	Second Savitzky-Golay derivative
sI	Structure-I hydrate
sII	Structure-II hydrate
HSZ	Hydrate stability zone
GasPT	Gas properties transmitter
CPA EoS	Cubic-plus-association equation of state
M	Molarity
m	Molality
H ₂ O	Water
HPHT	High pressure and high temperature
BPB	Bromophenol blue
UV-Vis	Ultraviolet–visible

SNV	Standard normal variate
T	Temperature
THIs	Thermodynamic hydrate inhibitors
MIR	Middle-infrared
RMSECV	Root mean square error of cross validation
RMSEC	Root mean square error of calibration
RMSEP	Root mean square error of prediction
RPD	Relative prediction deviation
SNR	Signal-noise-ratio
LVs	Latent variables
SEP	Standard error of prediction
GUI	Graphical user interface
EOR	Enhanced oil recovery
H ₂ S	Hydrogen sulphide
AAD	Average absolute deviation
NIPALS	Nonlinear iterative partial least squares
SD	Standard deviation

CHAPTER 1: INTRODUCTION

In oil and gas industry, mitigation of problems that caused by flow assurance issues is of considerable importance. With the current low oil and gas prices, the oil and gas industry are looking for cost effective and novel technologies for tackling flow assurance problems as well as avoiding unnecessary expenditures. Formation of gas hydrates in subsea pipelines where unprocessed reservoir fluids are being transported at high pressures and low temperatures is one of the major flow assurance issues. Prevention of gas hydrate blockages in transport pipelines is one of the key challenges facing the oil and gas industry. Applying and selecting an appropriate monitoring and detection techniques could help to reduce the risk of hydrate plug formation.

Furthermore, pipelines are conventionally used to transport CO₂-rich mixtures from emission sources to deep geologic formations such as oil and gas reservoirs and deep saline aquifers for CO₂ storage as well as enhanced oil recovery (EOR). The nature of these fluids combined with compression and potentially long distance transportation could also cause some flow assurance issues. Hence, it is necessary to understand the interactions between CO₂ and brine solutions at downhole wellbore conditions (high pressure and temperature) properly in order to avoid the generation of scale and corrosion in pipelines as well as for safety concerns in the downhole/wellbore region.

This thesis provides a valuable account of the development and validation of different types of spectroscopy methods in petroleum engineering to push the limits of the technologies currently available for avoiding some of the major flow assurance issues. This chapter starts with an overview of gas hydrates and methods that are currently being used to avoid and detect the formation of gas hydrates. The following is a brief review of carbon capture and storage process and its contribution to emission reduction, and the rest of this chapter presents an overview of each chapter.

1.1 Gas Hydrates

Gas hydrates are solid crystalline compounds that form when guest molecules of a suitable size are embedded in lattices of water under conditions of low temperature and elevated pressure [1]. Each crystalline structure contains geometrically distinct water cages with different size cavities which normally house one guest molecule with diameters between 0.40 - 0.90 nm [2]. More commonly, the guest molecules are light alkanes (methane through butane), and other gases such as carbon dioxide (CO₂), nitrogen

(N₂) and hydrogen sulphide (H₂S). Three most common types of structure have been identified, sI, sII and sH [3]. The type of the structure directly relates to the size of the guest molecules and its thermodynamic stability. Small molecules such as methane and ethane prefer to form hydrate structure I, while relatively large and round molecules such as propane and i-butane tend to form hydrate structure II. Furthermore, hexagonal structure (sH) encases small molecules such as methane and large molecules such as cycloheptane. Regarding sI hydrates, the unit cell consists of 46 water molecules forming two small cavities formed by twelve pentagonal cages (5^{12}) and six medium-sized cavities with two hexagonal and twelve pentagonal faces ($5^{12}6^2$). The unit cell of structure II consists of 136 water molecules. The unit cell of sII has 16 small cages created by twelve pentagonal faces (5^{12}) and eight large cages with twelve pentagonal and four hexagonal faces ($5^{12}6^4$).

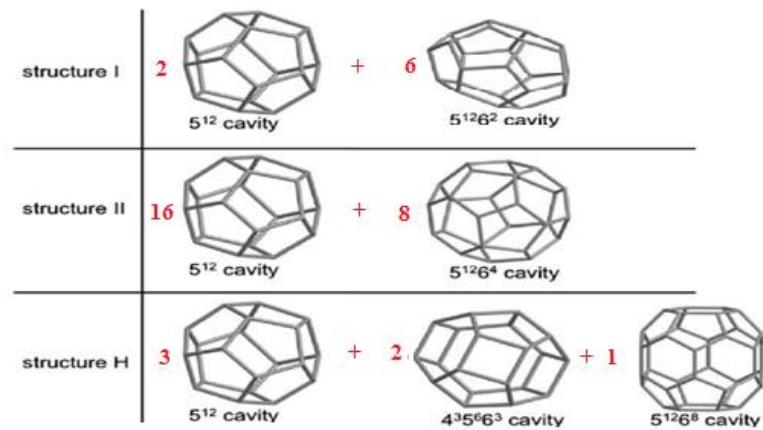


Figure 1.1. Hydrate crystal structures [4].

Ripmeester *et al.* [5] detect the structure H by employing NMR spectroscopy together with X-Ray and power diffraction. They found that the unit cell of type H structure consists of 34 water molecules. Three different types of cages were observed, two small and one very large. Overall the structure H hydrate is constructed of three small cavities with 12 pentagonal faces, two medium sized cavities with 3 square faces, 6 pentagonal faces, and 3 hexagonal faces and one very large cavity with 12 pentagonal faces and 8 hexagonal faces. The three common hydrate unit crystal structures are illustrated in Figure

1.1. A detailed description of the molecular structure has been given by Sloan *et al.* and Makogon [3, 6].

1.1.1 Gas hydrate stability zone (HSZ)

Formation of gas hydrates can occur while water and gas molecules exist under proper conditions of pressure and temperature. Hydrate stability zone (HSZ) is an area where pressure and temperature meet the requirements to form gas hydrates. The hydrate management philosophy is based on hydrate phase boundary prediction considering the operating system pressure and taking the corresponding temperature which forms the hydrate dissociation temperature. Pressure versus temperature gas hydrate curves can plot for sI and sII using thermodynamic modelling software. For this purpose, the composition of natural gas, the salt and hydrate inhibitor concentrations are fed into the thermodynamic model in which the region to the left of the predicted hydrate phase boundary is referred to as hydrate stability region showing the favourable region for hydrate formation (see Figure 1.2). While to the right of the hydrate line is the hydrate free region, at which there is no risk of hydrate formation.

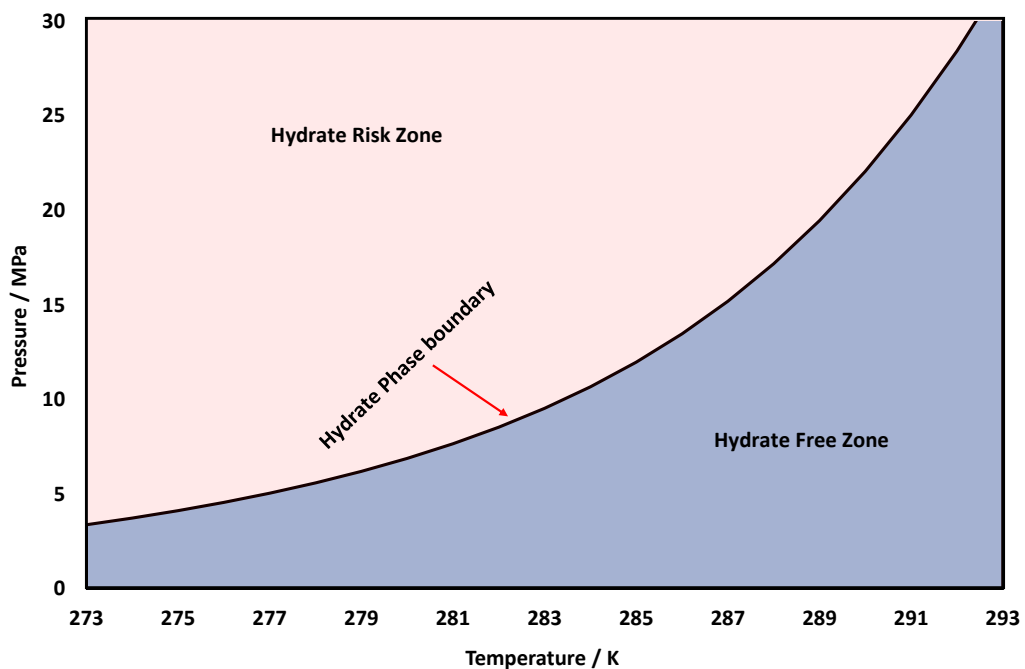


Figure 1.2. Hydrate risk and free zone.

In Figure 1.3, the hydrate sII phase boundary was predicted for systems with different inhibitors and salt concentrations, using HWHYD 2.1 software, which is developed by the Centre for Gas Hydrate Research at Heriot-Watt University [7]. It is obvious that addition of thermodynamic inhibitors such as salt, methanol and ethylene glycol (MEG)

to the aqueous phase moves the hydrate phase boundary to the left (higher pressures/lower temperatures). In another word, the hydrate phase boundary can be employed by the operator to estimate the risk of hydrate formation based on operating conditions.

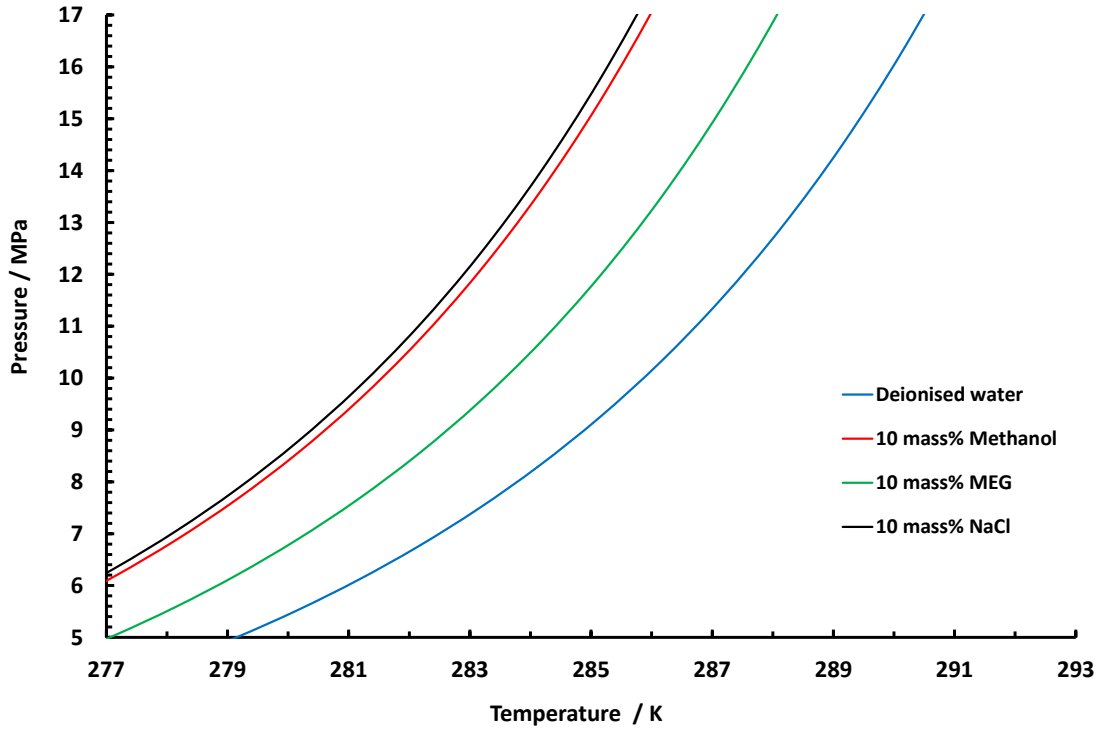


Figure 1.3. Predicted hydrate phase boundaries for a typical natural gas for different fluid systems.

1.1.2 Gas hydrate control and prevention

Generally, there are two main options to avoid the formation of gas hydrates. One option is to eliminate one of the elements (e.g. pressure, temperature and water content) that are required for hydrate formation. For example, insulating subsea pipelines helps to keep the operating system outside the hydrate stability zone. Furthermore, dropping the operating pressure and reducing water content are other alternatives methods for controlling gas hydrates. Due to the high cost of insulation, heating, and dehydration, these methods may not be feasible and economical [8].

Inhibitor injection is probably the most popular option for avoiding gas hydrate problems. Different types of hydrate inhibitors are used to prevent the formation of gas hydrates or hydrate plugs in hydrocarbons transport pipelines. Hydrates inhibitors are divided into two categories, i.e., thermodynamic hydrate inhibitors (THIs) and low dosage hydrate inhibitors (LDHIs). THIs such as methanol, ethanol and MEG hinder hydrate formation by shifting the hydrate phase boundary to lower temperatures and higher pressures by

decreasing the water activity. Thereby, the system can be operated in a safe region, outside the hydrate stability zone. To select the appropriate type of the THIs, several factors such as the possibility of regeneration required dosage, capital/operating cost, physical properties (such as viscosity, volatility and solubility in liquid hydrocarbon phase), gas dehydration capacity, corrosion inhibition effect and also safety and environmental issues need to be considered. As can be seen from Figure 1.3, methanol inhibits the hydrate formation more than MEG while the equivalent volume of both inhibitors is injected into the well. Nevertheless, Methanol has its own safety issues; it is a flammable, volatile and highly toxic liquid and also could lead to increase in the possibility of formation of corrosions in pipes and equipment [9]. Furthermore, due to its high volatility and solubility in liquid hydrocarbon phase, it cannot be recovered and reused. Unlike methanol, MEG is not flammable, and it is not miscible in hydrocarbons. Furthermore, it is not very volatile and can be easily recovered for further use. However, MEG has its own drawbacks as well. It is more expensive and viscous than methanol, which increases the pump requirement. Therefore, it is required to employ stronger pumps (increase the pressure of the pump) and larger diameter lines for MEG injection. Moreover, for recovery, there is a certain need for extra, costly and space consuming, onshore or offshore plants. Consequently, the formation of gas hydrates can be avoided by either MEG or methanol but the appropriate type of the THIs must be selected based on the well conditions.

THIs are commonly injected in high dosage (between 10-60 mass %), as a result, KHIs inhibitors are become more popular in the last decades as the typical concentrations of LDHIs is between 0.5-3.0 mass%. There are two types of LDHIs: the kinetic hydrate inhibitors (KHIs) and the anti-agglomerants (AAs). High molecular weight polymer components are the most commonly used KHIs (e.g. poly (N-vinyl caprolactam)). KHIs could prevent the hydrate nucleation within a certain degree of subcooling. The effectiveness of KHIs directly depends on how far the system is inside the hydrate stability zone and/or the residence time (the amount of time that the fluid spends in the system) [10].

In contrast, AAs are surface chemicals (e.g. alkyl aromatic sulfonates) which allow hydrate to form but prevent them from agglomerating together. Specifically, these type of inhibitors retain the hydrate particles small. Therefore, hydrate crystals can transport as slurry through the length of a pipeline [11, 12].

The amount of inhibitor injection rates is normally considered based on worst operating conditions (i.e., maximum pressure and minimum temperature) with a significant safety margin (e.g., 3–5 °C). Though the system pressure normally drops during the depletion of the reservoir, the injection rates are not normally changed. In fact, during the life of the reservoir, the amount of inhibitors required is going to change. To avoid the formation of gas hydrates large quantities of inhibitors are being used resulting in extra CAPEX (e.g. pumps, storage tanks) and OPEX (e.g. cost of inhibitor, disposal and damage to the environment) [13]. Therefore, there is significant interest in developing monitoring and warning systems that can monitor hydrate safety margin for optimising hydrate inhibitor injection rates and warn against any potential hydrate blockage [14].

1.1.3 Initial hydrate formation detection techniques

The initial signs of hydrate formation in the pipeline and also in onshore processes and platforms is very substantial as it can give adequate time to operators to avoid the formation of gas hydrates. There are several methods such as pigging return, variation in fluid rates and compositions at the separator, pressure drop increases, acoustic detection and gamma ray densitometer [15]. The advantages and disadvantages of these methods are described briefly in below:

- *Pigging return:*

Pigs are plastic balls or cylinders that are launched through the pipelines by pressure driven to sweep the debris from the pipeline into a trap pig located at the end of the pipe. The pig trap could provide valuable information about solid deposition in the pipeline. In terms of hydrate, hydrate particles could frequently be found in pig traps before hydrate blockages happen in the pipelines [16]. Pigging returns are carefully examined for evidence of hydrate particles. Hydrate masses are stable even at atmospheric pressure in a pig receiver discharge. The endothermic process of hydrate dissociation causes released water to form ice, which inhibits rapid dissociation. Although onshore pigging is commonly done to keep lines clear, it may be very expensive to provide offshore pigging either through a mobile pigging vessel over the well or from the wellhead without round trip pigging capability. Therefore, high costs limit the frequent examination of offshore pigging returns.

- *Changes in Fluid Rates of Composition at Separators*

Initial signs of formation of the gas hydrates could be detected by monitoring the rate of water production at the separator. Hydrate may be forming in the pipeline if the water

arrival at the separator reduces significantly. This has been stated by Corrigan *et al.* on the controlled experiment by British Petroleum for 13.7 miles gas line in the southern North Sea [17]. However, based on their results, this method is applicable while the water production is low. This technique will not be applicable as an early warning when water production is substantially higher or intermittent.

- *Pressure drop increase*

Hydrates formed in a pipeline could partly deposit on the internal surfaces of a pipeline (reducing the pipeline diameter) or dispersed in the fluid phases (increasing aqueous phase viscosity). In both cases, there would be an increase in the pressure drop across the pipeline. For a fixed pressure slug-catcher system, the increase in the pressure drop will result in an increase in the average pipeline pressure, pushing the system further inside hydrate phase boundary, forming more hydrates and increasing the risk of hydrate blockage. Pressure drop in a multiphase system is more complicated than a single phase system due to changes in the fluid flow patterns and liquid hold up, however, it should be possible to model/distinguish pressure drop changes due to multiphase flow with those associated with hydrate formation and build up (e.g., an increase in liquid hold up is normally associated with a reduction in gas flow rate). Furthermore, hydrates trap a significant amount of gas in their structures, hence their formation and in particular, dissociation could change the rate of gas production. Therefore, monitoring changes in gas production rate could help in detecting if hydrates are forming in the pipeline (a decrease in gas production).

- *Thermocamera:*

The infrared spectral transmission is used as an indicator of system temperature (Sloan, 2000). This method can only apply onshore or topside offshore. Temperature variations in the system can be monitored using the thermocamera, mainly at points where hydrates might form [18]. The main drawback of this method is that this thermocamera is very sensitive to pipe coating, variation in wall thickness and pipe roughness.

- *Acoustic detection:*

In terms of hydrate, this method is limited to onshore pipeline. This technique has been widely employed for sand monitoring by detecting sand impingement on the pipe [15].

- *Gamma ray densitometer:*

A gamma ray densitometer uses an emitter and sensor on opposite external of pipe walls. The transmission of the gamma ray to the sensor is a function of the density of the pipe contents. This technique is based on combined gamma ray densitometry with the temperature downstream of densitometry to indicate changes in conditions that could be hydrate present [19]. This combination is needed since the gamma ray alone will not be able to discriminate density of water and hydrate. Hydrates are indicated by a low temperature (owing to the Joule-Thomson effect) and an increase in density, whereas the water temperature is similar to that of gas. A high-density, low temperature mass in the pipeline is likely to be hydrates, whereas a high density slug without a temperature drop is probably water. This technique is a useful tool for onshore, but it could not be applied to subsea due to the limitation on temperature sensing requirement [16].

Initial hydrate formation does not cause blockage in pipelines. In fact, further hydrate formation can occur if initial hydrate formation is not detected and it could result in a build-up of hydrates and pipeline blockage [20]. Hydrates prefer large and round molecules in their structures. For example, the presence of large and round molecules such as propane and i-butane minimise the distance between the host molecule and the guest molecule and that increases the attraction force, resulting in the formation of gas hydrates. [21]. Therefore, monitoring the composition of the produced gas could be used for detecting early signs of hydrate formation, though the sensitivity of this technique is a function several factors, including the gas composition and stable hydrate structure. In this work, this opportunity was seized to examine the capability of this method using optical techniques. A new prototype was developed for detecting initial signs of hydrate formation using NIR spectroscopic technique based on a reduction in the concentration of some preferential components in the gas phase.

1.1.4 Monitoring hydrate inhibition techniques

Utilization of THIs may cause four possible inhibition degrees, depending on the dosage of a THI injected, Figure 1.4 illustrates insufficient dosage of the THI will cause the system under-inhibited and exposed to hydrate risk (red line), while high dosage will make the system over inhibited, resulting in high inhibition cost and severe impact on the environment (blue line). The green line shows that the system is inhibited with an optimal dosage of the THI, while the yellow line suggests that the system is slightly inhibited. In

Figure 1.4 it is presumed that the particular wellhead and the offshore or onshore platform conditions are outside the HSZ, which could be the case for a deep-water development.

Monitoring the concentration of hydrate inhibitors in the pipeline can help the operator to determine the hydrate safety margin accurately which would result in optimising inhibitor injection rate (i.e., ensuring adequate inhibition or avoiding over inhibition). In this thesis, a novel technique by coupling UV and NIR spectroscopic techniques have been introduced and developed for monitoring hydrate inhibition and initial hydrate formation detecting based on downstream sample analysis and online measurements. This method is more promising in compare with other available methods such as GC and densitometer. The presence of salts worsened the performance of the GC and could even damage the columns of the GC and densitometer is not capable of measuring the concentration of alcohols precisely while the concentration of salt is varying in the system. Both GC and densitometer are not able to predict the concentration of salt in the aqueous solutions. Based on the results of Chapter 4, the developed spectroscopy method is capable of predicting the concentration of NaCl and hydrate inhibitors accurately and can be used as a suitable method for monitoring hydrate safety margin with a high level of confidence.

It is believed that hydrate safety margin monitoring and hydrate early detection systems and, in particular, integration of the two techniques could massively improve the reliability of hydrate prevention strategies, reducing the costs associated with avoiding gas hydrates as well as improving their environmental impact. In fact, although hydrate inhibitors are used, there is a chance of formation of gas hydrates in hydrocarbon transport lines due to unforeseen issues such as water cut change (water-cut increases during the life of the reservoir) [22], equipment malfunction, and human errors. Therefore, further hydrate formation can be avoided in transport pipelines if the operator is warned timely.

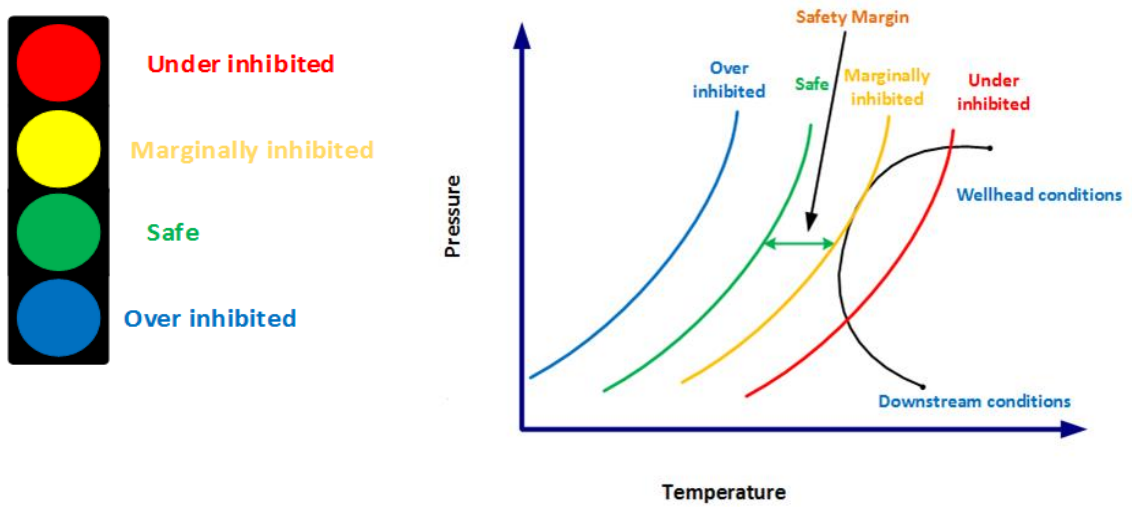


Figure 1.4. Hydrate safety margin determined by the developed hydrate inhibition monitoring techniques could be used as traffic lights to help the operators have a better control of hydrate inhibition.

1.2 pH of CO₂ Acidified Aqueous Systems

CO₂ emissions by the industrial sectors are one of the main causes of global warming, hence, in the last decades, developing methods for CO₂ reduction in the atmosphere has become an important topic. This issue has prompted researchers to identify methods to combat global warming. Carbon Capture and Storage (CCS) is currently one of the most widespread technologies aimed at alleviating the increase of CO₂ in the atmosphere.

The concept of pH and pH scales were introduced at the beginning of the last century, and since then they have been the most important parameters used to describe the acidity or basicity of aqueous solutions. Since determining of pH is essential for different applications such as marine, pharmaceutical and petroleum industries [23-25], it is important to measure the pH value with high accuracy. In the CCS contexts, the CO₂ injection will cause many chemical reactions as well as hydrodynamic and mechanical changes [26]. As the formation water in deep geological formations (i.e., deep saline aquifers) contains salts, measuring the pH with high accuracy in saline water is a prerequisite to characterise the properties of solutions. For instance, the pH level starts to drop in brine solutions due to CO₂ dissolution and formation of carbonic acid in the reservoir as a result of the CO₂ injection. This variation in pH value in water might cause corrosion of metallic materials in oil and gas wells and can also lead to mineral precipitation and scaling in pipelines transporting oil field waters [27, 28]. Moreover, low values of pH can have a substantial impact on the capture, storage and transportation of

CO₂ due to the changes in the porosity and permeability of the reservoir rock [29]. Hence, it is necessary to understand the interactions between CO₂ and brine at downhole wellbore conditions (high pressure and temperature) to prevent the formation of scales and corruptions in pipelines as well as for safety concerns in the downhole/wellbore region.

The spectroscopic method was employed to measure the pH of different fluid systems using a UV-Visible spectrometer, and a fully predictive model was developed to predict the changes in the pH due to the solubility of CO₂ in the aqueous phase at high pressure and high temperature conditions as well as the effect of NaCl. The pH model was developed by coupling the Cubic-Plus-Association Equation of State (CPA EoS) and the Pitzer equations.

1.3 Thesis Outline

The aim of this study was developing novel flow assurance techniques employing various spectroscopic methods for identifying and controlling flow assurance issues relating to gas hydrate and corrosion. This thesis consists of six chapters. The current chapter defines the basic subjects and principal of the work and introduces different hypothesis that investigated and developed in this work.

In Chapter 2, a new NIR setup was developed to monitor the changes in the composition of main hydrocarbons in the gas phase. The ability of the NIR spectroscopy method in association with chemometric methods to measure the composition of main hydrocarbon components in various gas samples were investigated. As mentioned earlier, the formation of gas hydrates could result in a reduction in the concentration of some preferential components in the gas phase. Therefore, monitoring the composition of the produced gas could be used for detecting early signs of hydrate formation. To monitor these changes, a prototype was developed with a simple end-user interface for real-time/remote monitoring the composition of methane, ethane, propane, i-butane and n-butane in the gas phase at pressures up to 13.78 MPa and temperatures up to 313.15 K using FT-NIR spectrometer. Chapter 2 deals with the experimental equipment and calibration models that were employed to develop this prototype. Partial least square (PLS) and artificial neural network (ANN) models were developed for determining the concentration of interested components in gas phase. A detailed description of experimental procedures and modelling are given in Chapter 2.

In Chapter 3, the feasibility of the NIR developed method was investigated for monitoring compositional change in gas phase for detecting early signs of hydrate formation and

hydrate history. The FT-NIR spectroscopy along with compositional change technique was tested for seven different fluid systems containing salt, methanol, MEG and KHI. The accuracy of NIR spectroscopy and compositional change technique with different calibration models were also investigated. For this purpose, hydrate was formed and dissociated in different runs in the high-pressure cell. Furthermore, in Chapter 3, the feasibility of monitoring gas phase compositional changes for detecting early signs of hydrate formation was evaluated for the first time in one gas field in France using a gas chromatography.

In Chapter 4, under “monitoring hydrate inhibition” category, a new optical method was developed by coupling UV and NIR spectrometers to measure the concentration of thermodynamic and low dosage hydrate inhibitors in water samples. This method is applicable for three different systems: a) MEG-NaCl, b) methanol-NaCl and c) PVCap-MEG-NaCl systems. Various spectral regions were selected to construct the PLS calibration models.

In Chapter 5, Spectroscopy and electrometric measurements were carried out to measure the pH in different fluid systems at pressures up to 6 MPa, three different temperatures (293.15, 323.15 and 353.15 K) and salinity from 0 to 3 mol.kg⁻¹ NaCl. A good understanding of the chemical reaction between CO₂ and the reservoir fluids is an important issue regarding the safety assessment of CO₂ pipelines. pH is the critical variable that describes the dissolution mechanisms. Extensive research studies were carried out to measure the pH of seawater in high salinity. Most of these experiments were performed at low temperatures and atmospheric pressure. To our knowledge, very limited experimental works were carried out to measure the pH for CO₂-H₂O and CO₂ acidified brine systems at high temperature and high pressure conditions. Hence, investigation of pH in the CO₂-brine solutions, particularly at high pressures and high salinities, can greatly improve our knowledge about the change of pH after injecting CO₂ into Deep Ocean or saline aquifers. One of the main objectives of this study was to major the pH of CO₂ acidified aqueous systems at reservoir conditions. These experimental data then can be used to examine the predictive capabilities of the available thermodynamic models

For this purpose, two experimental setups based on either electrical or spectroscopic methods were employed to measure the pH in CO₂-H₂O and CO₂-H₂O-NaCl systems. All the experimental results were compared with the gathered literature data within the range of the P–T conditions studied. Spectroscopy measurements were also carried out to

measure the pH of CO₂ rich mixtures and water at pressures up to 15 MPa and at temperatures up to 323.15K. Furthermore, we described and evaluated a model that uses a robust thermodynamic basis for describing the solubility of gases in the liquid phase and Pitzer's theory for determining the activity coefficients of the ionic species involved. This approach proved to be capable of describing the chemical equilibria of the ionic species in the liquid phase under HPHT conditions and in systems of interest.

In Chapter 6, the main conclusions of this thesis and recommendation for future work are summarised.

CHAPTER 2: DEVELOPMENT OF AN FTNIR SPECTROSCOPY METHOD FOR MONITORING COMPOSITIONAL CHANGES IN HYDROCARBON GASES UNDER IN-SITU PRESSURE

2.1 Introduction

Nowadays, natural gas is one of the most efficient and popular sources of energy in the world, and it plays an essential role in the manufacturing industry and transportation, commercial and residential sectors [30]. Methane is the main component of natural gases and is typically between 87 to 97 mol%, and ethane, propane, butanes and pentanes are others main hydrocarbon components in natural gases [31, 32]. Natural gas also contains non-hydrocarbon gases such as nitrogen and carbon dioxide [33]. Monitoring the hydrocarbon compositions of natural gas is important to evaluate the quality of gas, and for various application in oil and gas industry during hydrocarbon production, transportation and processing of natural gas. For instance, in oil and gas sector, it is important to monitor and characterise the composition of natural gas products precisely and continuously to ensure the quality of natural gas. Moreover, monitoring the composition of produce gas could provide an early indication of hydrate formation based on the reduction of some hydrocarbon components in the gas phase [20, 34-36]. Gas chromatography (GC) is by far one of the most promising methods for measuring the concentration of hydrocarbons in the natural gas.

Over the last decades, spectroscopic methods have become more and more favourable in the food, pharmaceutical, and petroleum industries [37-41]. The major advantages of these methods compared to other analytical methods are that they can be used for at-line and in-line measurement to determine the selected species of interest inside the sample with fast response and high accuracy [42]. Moreover, there is no need for carrier gas such as helium or nitrogen that are required by a GC, which further reduces the operational cost. In particular, vibrational spectroscopy methods such as near-infrared (NIR), middle-infrared (MIR) and Raman spectroscopy are well-suited for the determination of hydrocarbon species inside the natural gas [43, 44]. However, each method has its advantages and disadvantages [45].

A number of research projects have been carried out for the development and improvement of MIR and NIR and Raman spectroscopy techniques to monitor and determine the selected species of interest in the gas mixtures [45]. The applicability of near-infrared spectroscopy was investigated for analysis of n-alkanes in gaseous alkane mixtures with the aid of chemometric techniques by Boelens *et al.* [46]. Danta *et al.* [47] employed NIR spectroscopy to monitor the changes in the concentration of methane in natural gas for quality control where the pressure for calibration and test samples were fixed at 0.4 MPa at room temperature. They selected the spectral range from 9100 to 4800 cm^{-1} (1099 to 2083 nm) since it carries the relevant spectroscopic information to monitor the methane content in natural gas. A comparison was made between NIR and MIR spectroscopy to measure methane, ethane and propane contents in natural gases using various chemometric algorithms by Makhoukhi *et al.* [48]. They found that NIR spectroscopic method is more accurate than MIR to measure the methane, ethane, and propane contents in synthetic gas mixtures. In 2014, Rohwedder *et al.* [49] reported the use of a MicroNIR spectrometer to determine the concentration of methane, ethane, propane and butane in synthetic gas mixtures in atmospheric pressure. Partial least square (PLS) was employed to develop the calibration model to relate the spectrum of synthetic gas mixtures and its content of methane, ethane, propane and butane. The results reveal that the instrument can be employed as an optical hydrocarbon analyser with good accuracy and fast response. A novel heart-shaped substrate-integrated hollow waveguide (hiHWG) was integrated with a near infrared micro-spectrometer by Ribessi *et al.* to determine the concentration of main hydrocarbons in natural gas at atmospheric pressure [50]. In this work, first Savitzky-Golay pre-treatment method was applied to spectra to develop PLS models. The obtained results for all studied components by the developed instrument was in good agreement with those obtained by an acousto-optic tuneable filter (AOTF) NIR spectrometer.

Raman spectroscopy method is another suitable method to detect the concentration of natural gas components. One of the main advantages of Raman spectroscopy method compared to NIR is its capability to detect all relevant species in natural gas simultaneously. This is because homonuclear diatomic molecules like nitrogen, hydrogen and oxygen are not NIR active [51]. Details about Raman and NIR spectroscopy methods are explained later in this chapter. Due to the applicability of Raman spectroscopy to detect the composition of nitrogen and oxygen, as well as hydrocarbons, it has become increasingly interested by different research groups for characterising of natural gas. In

1980, the applicability of Raman spectroscopy to measure the composition of hydrocarbons and nitrogen at ambient temperature and at pressures up to 0.8 MPa was investigated by Diller *et al.* [52] Eichmann *et al.* developed a Raman sensor for real-time determination of the main species in natural gas at low pressures up to 1.5 MPa and at temperatures up to 473 K [43]. In this work, the effect of a change in pressure and temperature on the accuracy of measurements was investigated. They concluded that the variation of pressure does not affect any significant changes on the recorded Raman spectra and hence the error of the measurement is negligible while the pressure is varying. In contrast, noticeable errors were noticed while the temperature was varied from 298 K to 473 K.

Literature survey shows that there are limited NIR spectroscopy works reported for measuring the concentration of hydrocarbon compounds (methane through butanes) in natural gas at high pressures. For field applications where pipeline systems are operating at high pressures, there is a strong demand for a fast response, user-friendly, and cost-effective methods for composition analysis of hydrocarbon gases at in-situ pressures. Dong *et al.* [53] developed a downhole NIR analyser to predict the concentration of hydrocarbons in natural gases using chemometric methods under in-situ pressure up to 137.89 MPa and temperature up to 423.15 K. It should be mentioned that in their study propane, butanes and pentanes were grouped together in order to improve the accuracy of the gas analyser and these components cannot be measured separately in natural gases by the analyser.

In this work, the ability of Fourier Transform Near-Infrared (FTNIR) spectroscopy and chemometric methods was investigated to determine the major hydrocarbon components of natural gas at pressures from 3.44 to 13.78 MPa and temperatures from 278.15 to 313.15 K. Different pre-processing methods were applied to spectra prior to the construction of Partial Least Square (PLS) and Artificial Neural network (ANN) calibration models to investigate the model prediction capability. Moreover, we examined the influence of a change in pressure and temperature in the accuracy of one of the created PLS regression models that were calibrated at the known condition of temperature and pressure. Finally, a comparison was made between the hydrocarbons measured value by the FTNIR spectrometer and GC for some unknown natural gas samples to investigate the accuracy of the FTNIR method.

2.2 Conventional Method for Analysing the Composition of Fuel Gas

GC is the conventional method for natural gas analysis. GC involves a mobile phase and a stationary phase. The mobile phase consists of inert gases such as helium and nitrogen that typically called as a carrier gas. Carrier gases used to move the gas sample through the packed or capillary column, and the stationary phases is a liquid film (high boiling liquids) coated to the wall of the packed or capillary column. Once the sample is transported through the GC, the substances of gas mixture start to travel through the column and interact with the stationary phase. The time that is taken from the injection until the component hit the detector is called retention time. When the retention time was measured, the concentration of the components in the gas mixture can be calculated. GC is by far the most promising method for measuring the concentration of hydrocarbons in natural gases [43]. However, this approach has some certain drawbacks, e.g., the long measurement time. The time taken for the analysis of natural gas using GC is varied from 5 minutes to 30 minutes depending on the length and temperature of the columns. Longer column and lower temperature will increase the retention time (required time for a compound to pass through the column). Furthermore, GC analysis is pricey as a carrier gas, maintenance, and special skills are needed for programming, calibrating and running GCs. GC analysis just can be performed close to atmospheric pressure, and it is necessary to regulate the pressure of gas from high pressures to low pressures. This reduction in pressure can cause a change in the composition of the hydrocarbon mixtures as heavy hydrocarbons drop out from the gas phase into the liquid phase. Nowadays, it is necessary to measure the composition of interested components in natural gas for different purposes at the end-user location, and there is a great demand for a fast, accurate and user-friendly gas composition analyser.

2.3 Spectroscopy Methods

2.3.1 Infrared spectroscopy

The infrared region is based on the interaction of electromagnetic radiation with the compounds and is described by the energy transfer between the light and the matter, from 780 nm to 10^6 nm. The infrared region is split into three subsets, near-infrared (NIR), middle-infrared (MIR) and far-infrared (FIR). MIR and NIR are employed commercially in the context of natural gas analysis, where MIR takes the measurement wavelength between 2500 to 25000 nm, in which fundamental vibrational bands can be found. NIR covers the ranges between 780 to 2500 nm where represents the vibrational overtone and

combination bands that are derived by the fundamental vibrational that observed in the MIR region. NIR spectroscopy has found broader applications in the industrial process than MIR spectroscopy. One of the reasons is that transmitting materials for NIR are less expensive than MIR [54]. Also, due to high absorption of materials in MIR region and low amount of energy that produce by MIR sources, samples need to be analysed through a very efficient and tiny path length [55]. Furthermore, the presence of water droplets can results in inaccurate measurements because of strong absorption of water in the MIR region.

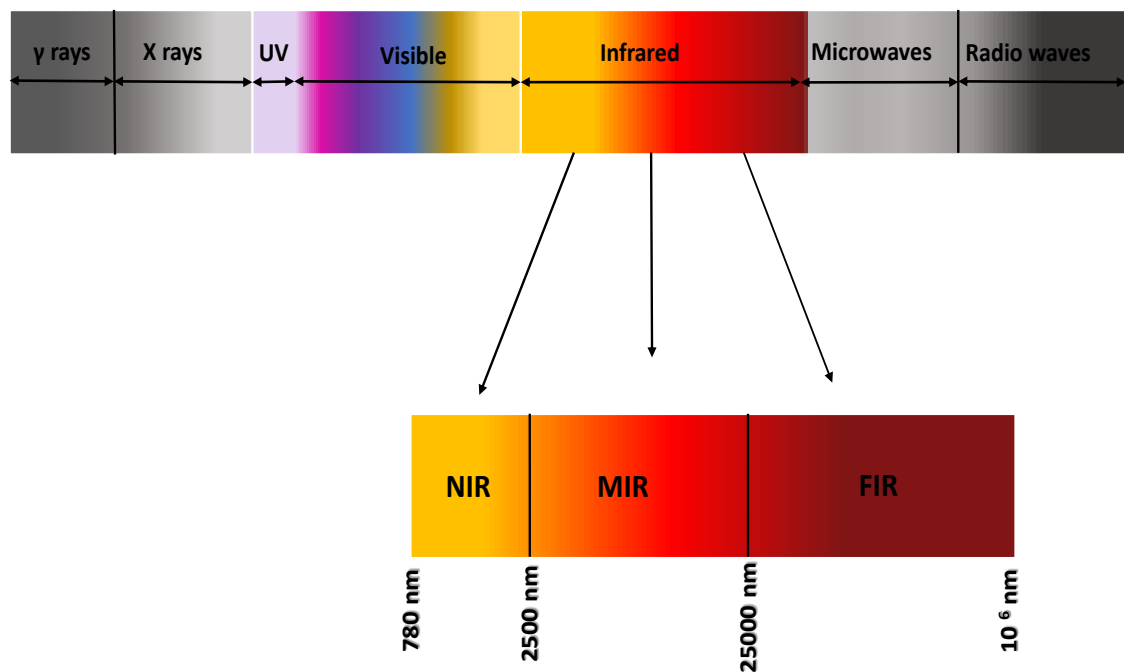


Figure 2.1. The electromagnetic spectrum.

The basic of NIR spectroscopy measurement is based on the Beer-Lambert's law given in Equation 2.1:

$$A = \log\left(\frac{I_0}{I}\right) = \xi lc \quad \text{Equation 2.1.}$$

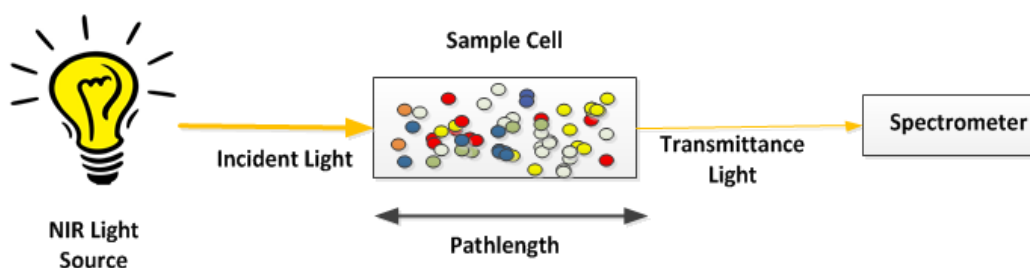


Figure 2.2. Schematic representation showing that light of initial intensity, I_0 passing through an absorbing in the sample cell with a specific pathlength, l , will emerge with a final intensity, I .

In which A represents the absorbance of the beam, I_0 is the intensity of incident light, I is the intensity of incident light after passing through the sample, ξ is the molar absorptivity, l is the sample path length (the length that light travels), and c is the sample concentration. Major absorption bands for hydrocarbons in the NIR region normally occur in the ranges 1100-1200 nm, 1350 to 1450 nm, 1600 to 1850 nm and 2200 to 2300 nm as illustrated in Figure 2.3. NIR absorption by hydrocarbons is caused by their carbon-hydrogen molecular bond. However, the NIR absorption of hydrocarbons depends on the structure of their molecules. Methane molecules contain four C-H bonds. Light hydrocarbons such as ethane and propane are dominated by the methyl group ($-\text{CH}_3$). Heavy hydrocarbons also usually have a large amount of methyl group with a small amount of methylene group ($-\text{CH}_2$). It is clear from Figure 2.4 absorption spectra of hydrocarbon components are different due to the difference in the structure of hydrocarbons molecule. It can be seen methane has a unique spectrum and the spectra of other hydrocarbons are very similar. The absorption bands of hydrocarbons overlap with each other in almost the entire region. Chemometric techniques such as PLS and ANN have become standard tools for quickly analysing complex samples from their spectral signatures.

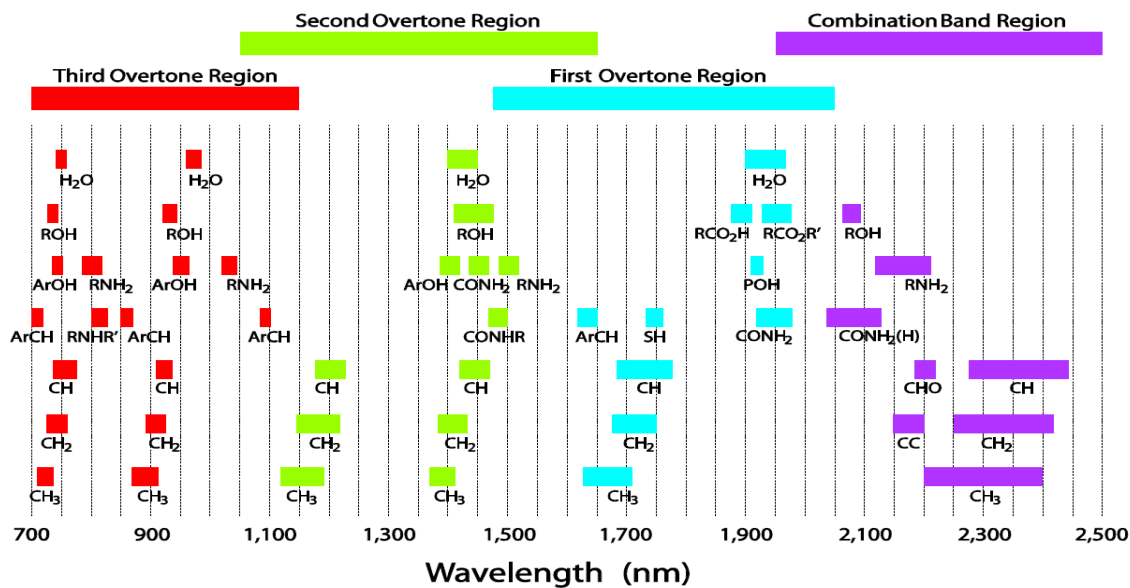


Figure 2.3. Major analytical bands and relative peak positions for prominent near-infrared [56].

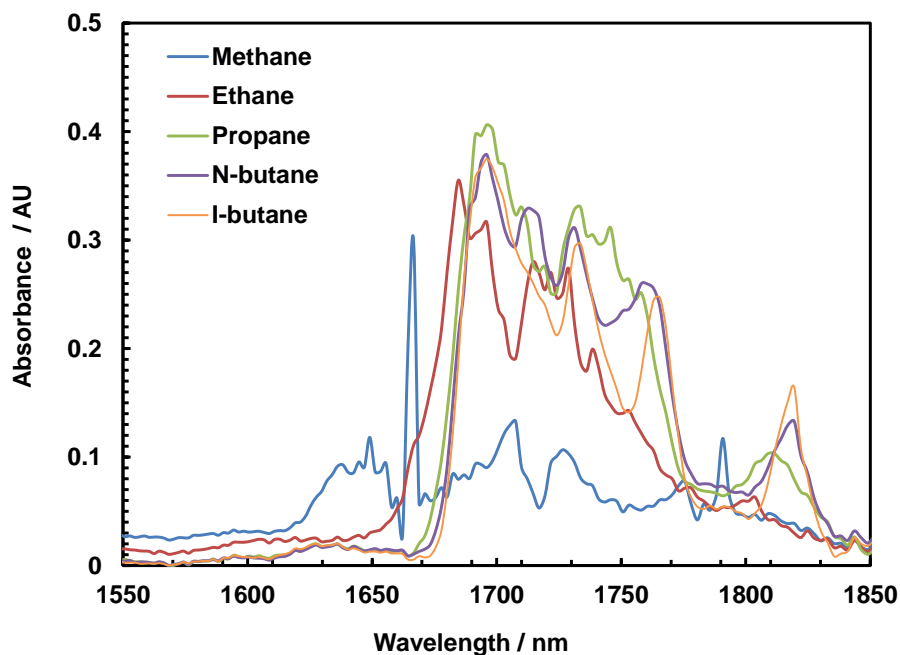


Figure 2.4. FTNIR Spectra of the pure hydrocarbons at atmospheric pressure and room temperature that captured by the FTNIR spectrometer.

2.3.2 Raman spectroscopy

Raman spectroscopy is not an absorption technique in contrast to infrared spectroscopy, indeed Raman spectroscopy is a light scattering technique that used to find out the information about the vibrational, rotational and other low-frequency transitions in

molecules. Simply, when the laser light (monochromatic light) incident through the sample, most of the light bounces off and the wavelength of the light remains unchanged, that is called elastic Rayleigh scattering and very small amount of the light are absorbed by the sample and re-emitted, that causes shift in wavelength, this shift is called inelastic Raman scattering. It should be noted that the laser beam can be in the UV, visible and NIR ranges. Raman-active molecules absorb a photon with frequency ν_0 and a part of the photon's energy transferred to ν_m . The frequency of the re-emitted light shifted-down (stokes frequency) and shifted-up (anti-stokes frequency). This shift in wavelength for each molecule is based on the structure of the molecule and can be used to extract the desired information for the material of interest and is also independent of the excitation frequency. The main drawback of this method is that only very low amount of the incident light produces Raman scattering. Hence, it is necessary to employ highly sensitive camera such as cooled CCD camera to detect the Raman scattered radiation from the output signal of the Raman spectrometer [57]. Furthermore, different types of filters (i.e., notch filters and edge filters) can also be employed to reduce the elastic Rayleigh scattering and drawing out a quantifiable Raman signal.

2.3.3 NIR vs. Raman

NIR and Raman spectroscopy methods are the most commonly used methods to monitor the concentration of hydrocarbons in natural gases. By comparison to conventional methods like GC, the main advantages of both spectroscopy methods are that they are rugged, portable and non-invasive, can be used for in-situ measurements and controlled remotely by the user through wireless. Moreover, there is no need for sample preparation and samples with different physical states can be used for NIR and Raman measurements. The simplicity, high precision and speed of the analysis are without any hesitation the most convincing assets of NIR and Raman spectroscopy methods in the context of natural gas. Though NIR is not as sensitive as MIR to water, is a method that can be employed to measure the water content in different products. Hence, the presence of few amount of water in the sample may affect the accuracy of developed chemometric models, whereas Raman is much less sensitive to water compared to NIR. A simple test was carried out to indicate the sensitivity of this method to water. For this purpose, the NIR cell was filled with deionised water. It was observed that the laser beam in the frequency range of interest is fully attenuated. It seems that at this condition molecules absorb almost the

whole the energy of the beam in the wavelength region of interest causing no energy received by the detector and light cannot travel the distance between source and detector.

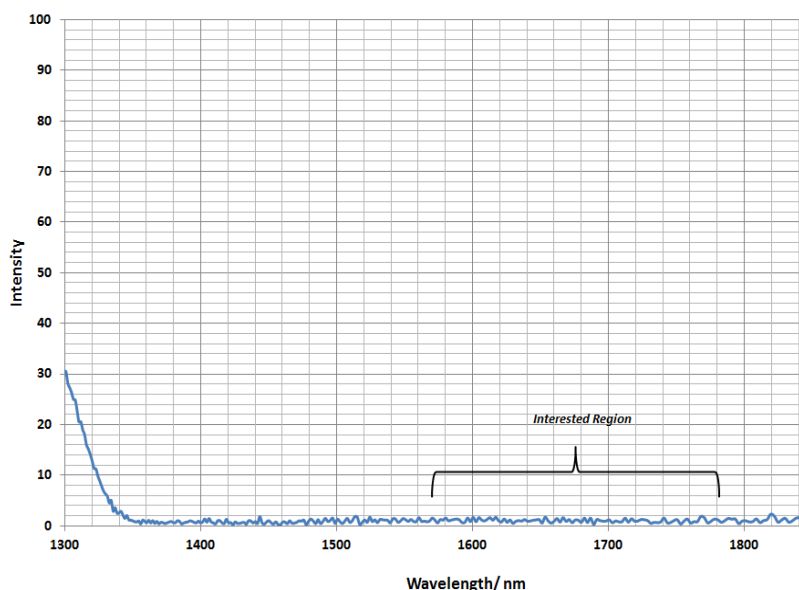


Figure 2.5. Spectra of deionised water with optical path length of 1.4 cm.

Furthermore, it is well known that NIR is not sensitive to inert gases such as nitrogen and oxygen. In contrast, Raman is a suitable method to measure the content of inert gases as well as hydrocarbons in gas phase which led to a great interest in the different context (i.e., natural gas and biogas measurements). Comparison of instrumentation cost of NIR and Raman sensors for hydrocarbons measurement indicates that the NIR sensors are less expensive than Raman sensors [58]. As mentioned earlier, the Raman scatter light is weak. Therefore, it is required to use the high power light source to compensate the low intensity of Raman scatters light which increases the total cost of this method significantly. The main purpose of this study is to develop a cost-effectively and online analyser to monitor the concentration of hydrocarbons in gas samples at high pressures to predict and detect the formation of gas hydrates based on compositional change techniques [34]. For better comparison, the advantages and disadvantages of available technologies for fuel composition monitoring are tabulated in Table 2.1.

In this study, NIR method was selected as an appropriate method for measuring the content of hydrocarbons in gas samples. This chapter, for the first time, presents the development of an NIR natural gas analyser for monitoring the changes in the concentration of main hydrocarbon components in the natural gas.

Table 2.1. Comparison between available techniques for natural gas composition monitoring.

Method	FTNIR	Raman	GC
Response time	Seconds	Seconds	5-15 minutes
Calibration	Permanent	Permanent	Recalibration requires
Accuracy	High accuracy	High accuracy	High accuracy
Maintenance Cost	Low	Low	High
Operating pressure	Wide range	Wide range	Atmospheric pressure
Carrier gas	No-carrier gases	No-carrier gases	Carrier gases require
Other limitations	-Sensitive to water -Nitrogen & oxygen are not NIR active	-high power laser sources requires	-Skilled operators requires

2.4 NIR Spectral Data Modelling

It is difficult to find the appropriate wavelength ranges that provide proper information about all the components that constitute the sample particularly while all these components have the very similar chemical structure (i.e., hydrocarbons and alcohols, see Figure 2.4). In the NIR region, each component typically absorbs NIR light at more than one wavelength region, and consequently, there is a possibility that absorbance at the given wavelength may have contributions from more than one species. Hence, it is necessary to use multivariate regression methods to determine the concentration of interested components in the unknown sample. A variety of chemometric methods such as PLS and ANN can be employed to extract the desired information from NIR recorded spectra. Generally, use of NIR spectroscopy is associated with partial least squares model (PLS) and principal component analysis (PCA) [59]. But, use of ANN as nonlinear models have been reported in the literature with some advantages in some cases compare to PLS models [37, 60]. The aim of this work is to assess the use of the NIR spectroscopy with multivariate calibration and artificial neural network models to predict the composition of main hydrocarbons in the natural gas.

2.4.1 Principal component analysis (PCA)

The first step to perform the Partial Least Square (PLS) regression is to run principal component Analysis (PCA) in the data matrix. The PCA goal is to extract the information from a data matrix (X) by explaining the variation in the data.

$$X = TP^T + E \quad \text{Equation 2.2.}$$

The data X are modelled as a product TP^T plus the residual (E), in which, T is the score vector, and P is the loading vector. Scores describe the sample patterns and show how much the samples are similar together. Loadings define the data structure in terms of variable contributions. Each principal component (PC) has one score vector and one loading vector. The first principal component has the maximum variance in the data and spans the maximum variability in the data (the most explained variance), the second PC is orthogonal to the first PC and explains the variation in the residual data that were not taken by the first PC and so on. Details about this method are described in section 2.4.2.

2.4.2 Partial least squares (PLS)

The partial least square algorithm is used to perform the calibration and the regression to determine the concentration of methane, ethane, propane, i-butane, and n-butane in natural gas. PLS is a multivariate analysis method which models the relation between the spectra data and the components concentration using latent variables. This can be done by using all the calibration spectra in the region of interest. These latent variables capture the maximum covariance between the reference data and the recorded spectrum. The equations of PLS model are derived as follows:

$$X = TP^T + E \quad \text{Equation 2.3.}$$

$$Y = UQ^T + F \quad \text{Equation 2.4.}$$

Where X is the spectral data (wavelength matrix), Y represents the content of hydrocarbons (methane through butanes) in synthetic gas mixtures. P and Q resemble the loadings matrix of the X and Y respectively. T and U are correspondingly the score matrices of X and Y . E and F are both the residual errors of the X and Y that represent the noise or irrelevant variable. In this method, the principal components of the dependent variable (X) are correlated to the principal components of the independent variable (Y). In other words, the aim of using a PLS regression model is to decompose both X and Y into two loadings and scores matrices and then find a regression model between the score matrices of X and Y with a maximum covariance.

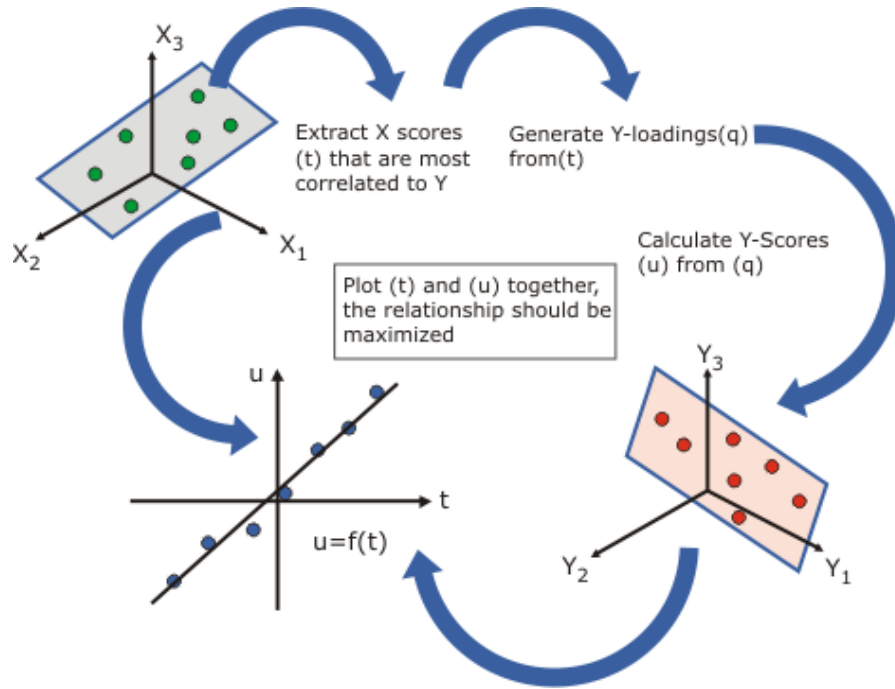


Figure 2.6. Model structure of PLS [61].

As mentioned above, the main idea is to decompose both X and Y by finding the principal components of X , and there are two iterative algorithms to find the principal components of the matrix, the singular value decomposition (SVD) and nonlinear iterative partial least square (NIPALS) [62, 63]. The SVD is related to well-known eigen-decomposition:

$$Z = U\Delta V^T$$

Equation 2.5.

In which U is the matrix of the normalised eigenvectors of ZZ^T and V is a matrix made of the normalised eigenvectors of Z^TZ (principal components), and Δ is a matrix made up of the eigenvalues of ZZ^T and Z^TZ . The idea behind the PLS method is to first decompose both X and Y and then generate a regression between independent and dependent variables and find the relation between scores T and U .

Another algorithm to calculate the principal components of a matrix is nonlinear iterative partial least squares (NIPALS). In this work, the NIPALS algorithm was employed to create the PLS models. In this method, firstly, the matrix X was mean-centred and scaled.

1. An initial value is created for t_1 (this value can be selected randomly or can be found from a column of matrix X). Hence, every column in X is taken and is used as an initial column for t_1 .

$$t_1 = x_i \quad \text{Equation 2.6.}$$

2. Project the matrix X onto t_1 to compute p_1 . (This procedure must be repeated for all the column of the matrix X until the p_1 is filled).

$$p_1 = \frac{t_1 X}{t_1 t_1^T} \quad \text{Equation 2.7.}$$

3. Rescale the vector p_1 to have magnitude 1.0:

$$p_1 = \frac{p_1}{|p_1|} \quad \text{Equation 2.8.}$$

4. Project the matrix X (each column of X) onto normalised vector p_1 to find corresponding score value (t_1).
5. Repeat step 1 to step 4 until the change in t_1 is small (1×10^{-6}).
6. After convergence, final t_1 and p_1 vectors are selected as first PCA component.
7. Subtract the PCA component (score and loading) from Matrix X.

$$X_r = X - t_1 p_1^T \quad \text{Equation 2.9.}$$

8. Use X_r as new X and repeat the above procedure to find the second PCA for the residuals.

The aim of PLS is to calculate both PCA components of both X and Y by taking information from each other into account. The prediction of Y can be found using following equations:

$$X = t_1 p_1^T + t_2 p_2^T + t_3 p_3^T + \dots + t_n p_n^T = TP^T + E \quad \text{Equation 2.10.}$$

$$Y = u_1 q_1^T + u_2 q_2^T + u_3 q_3^T + \dots + u_n q_n^T = UQ^T + F \quad \text{Equation 2.11.}$$

$$U = TB \quad \text{Equation 2.12.}$$

$$Y = TBQ^T + F \quad \text{Equation 2.13.}$$

Where B is a diagonal matrix that represents the regression coefficients between T and U and F is the residual value. This regression coefficient can be used for future content prediction of the component of interest. The major point of PLS is the construction of components by projecting X on the weights w. The first step is to find the first PCA (NIPALS algorithm is used) component by maximising covariance between Y and t_1 with the constraints that $w^T w = 1$:

$$t_1 = Xw_1 \quad \text{Equation 2.14.}$$

$$w_1 = \arg \max (Cov(Xw, Y)) \quad \text{Equation 2.15.}$$

$$w_1 = \frac{X^T Y}{\|X^T Y\|} \quad \text{Equation 2.16.}$$

$$p_1 = \frac{t_1 X}{t_1 t_1^T} \quad \text{Equation 2.17.}$$

$$q_1 = \frac{t_1 Y}{t_1 t_1^T} \quad \text{Equation 2.18.}$$

When the first PCA component is created, it is subtracted from both X and Y matrices and the procedure is repeated for the residuals until the optimum number of components is found.

$$X_r = X - t_1 p_1^T \quad \text{Equation 2.19.}$$

As an iterative process, PLS constructs other latent components by means of the residuals as new X_r and Y_r . Each PLS iteration signifies some information which could not describe by previous steps and consequently it is necessary to generate another latent component [64]. The number of components is the only parameter of PLS which can be fixed by the user or decided by a cross-validation scheme [65]. The scores T then was used to compute the regression coefficients according to the number of components.

2.4.3 Artificial neural network (ANN)

An Artificial neural network is a useful approach that is used in spectroscopy studies in order to correlate independent data (wavelength) that obtain by the spectrometer to dependent data which are the concentration of calibration sample [66] . The development of neural network model consists of few steps. The generation of data that required construct the ANN model, evaluation of the created ANN architecture by selecting the optimal number of neurons and testing the developed ANN model using independent data [67]. The artificial neural network consists of large numbers of computational units called neurons, connected to each other by means of direct weighted communication links as shown in Figure 2.7 [68]. The input layer of the network receives all the input data and introduces scaled data to the network. The data from the input neurons are propagated through the network via weights [67].

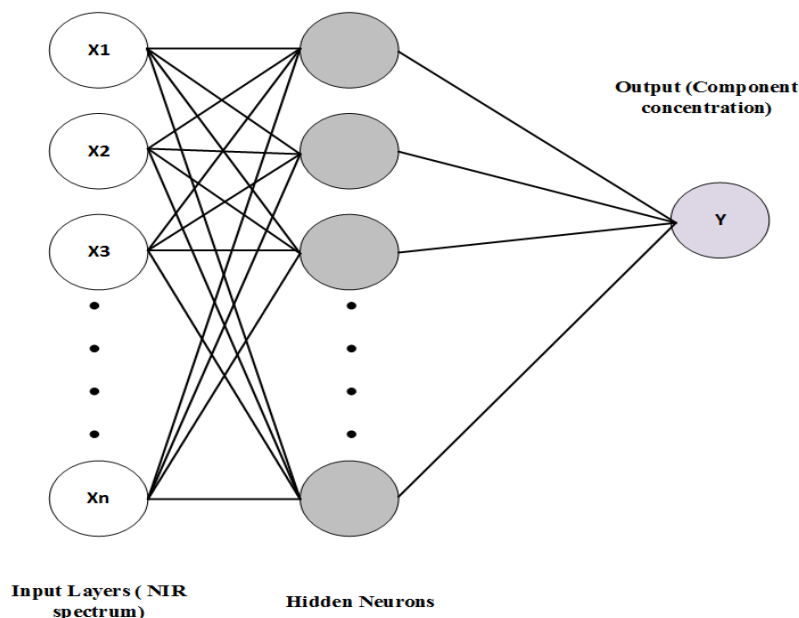


Figure 2.7. The structure of developed multi-layer feed forward ANN for calculating the hydrocarbons concentration.

The prediction efficiency of ANN is investigated in this study and is compared with the results that obtained by PLS. The ANN are applied by various researchers but has only recently applied in chemometric. In this work, a multilayer perceptron feed forward neural network was applied, with the Bayesian regularization algorithm. The structure of the network consists of one hidden layer where the number of neurons was set 5, for all the cases. In the algorithm, the number of training iteration was 200 and the activation function of all neurons at the hidden layer was hyperbolic tangent (tansig) and output layers was linear transfer functions (purelin). Choice of transfer function depends on the nature of data (linear or non-linear). In this study, the best results were obtained while the tansig-purelin pair was applied to ANN data. More details about ANN transfer functions can be found in the literature [69].

30 spectra were used as input to training data, 15 spectra data was used as testing data for developed ANN model. The optimal network which had minimum RMSEC values and maximum R^2 values between experimental and estimated data was nominated as the final model. Details about the algorithm are described. The MATLAB R2013b neural network toolbox had been used to develop the ANN models.

2.5 Preprocessing Methods

The main concept behind the pre-processing methods is to eliminate unwanted background data and reduce noise level before construction of the calibration models [54, 70]. Pre-processing or pre-treatment of spectral data are often employed to increase the signal resolution by reducing the noise and remove the baseline shift and slope changes in the spectra that provide the chemical information. Noise can be generated while recording the spectra data by the instrument. It should be mentioned that regions that absorb the NIR light weakly are much more significantly affected than those regions that generate strong absorptions. One of the important step to reduce the influence of noise levels in the spectrum is to record the spectrum in multiple averages to reduce the noise levels. Multiplicative scattering commonly noticed when the sample consists of particles with a different size and this difference in size of the particles is the main source of variation in the NIR spectra [71]. Hence, it is necessary to select the appropriate pre-processing techniques in order to eliminate and correct the effect of undesirable scatter on the spectrum. Terms that were used to select the best pre-processing methods are described in section 2.6.

2.5.1 Normalisation

Normalisation is one of the most commonly pre-processing methods that was applied to raw data (I_0 & I) before converting the data to absorbance. The FTNIR spectra are affected by intensity fluctuations which are due to fluctuation in generated light by NIR source. These fluctuations produce some shifts in the intensity of spectra that is not associated with a change in the concentration of species. Various normalisation methods are used to overcome to these variations. In this work, all the sample's spectra and background's spectra were normalised by dividing all variables for given sample to the maximum value that observed between all the variables.

2.5.2 Derivatives

The derivative is one of the most popular pre-processing methods to highlight the useful information of the spectra without greatly distorting the spectra. Calculation of the derivatives of the spectra is used to smooth the spectra, to overcome the overlap between peaks, and to remove baseline offset. The Savitzky-Golay method is the most commonly used method to solve this problem and smooth the spectra and calculate derivatives. Three parameters should be considered in the Savitzky-Golay method: the degree of derivative, the number of smoothing points (window size) and the polynomial order of the smoothing function. In this method, firstly a smoothing step apply to a specific segment of data by fitting a polynomial order and then derivatives are calculated from the smoothed spectra. The first derivative and the second derivative are most often used. The key part of this technique is to select the appropriate number of smoothing points. If the segment is too large, there is a possibility to remove some useful information from the spectra, and if the number of points that are used for smoothing is low, the result may be no better than before applying the Savitzky-Golay smoothing point, and the noisy features may remain in the spectra. One can also find an optimum number of smoothing point by checking model accuracy and robustness by selecting a different number of smoothing points. The first Savitzky-Golay derivatives with different smoothing points are given in Figure 2.8.

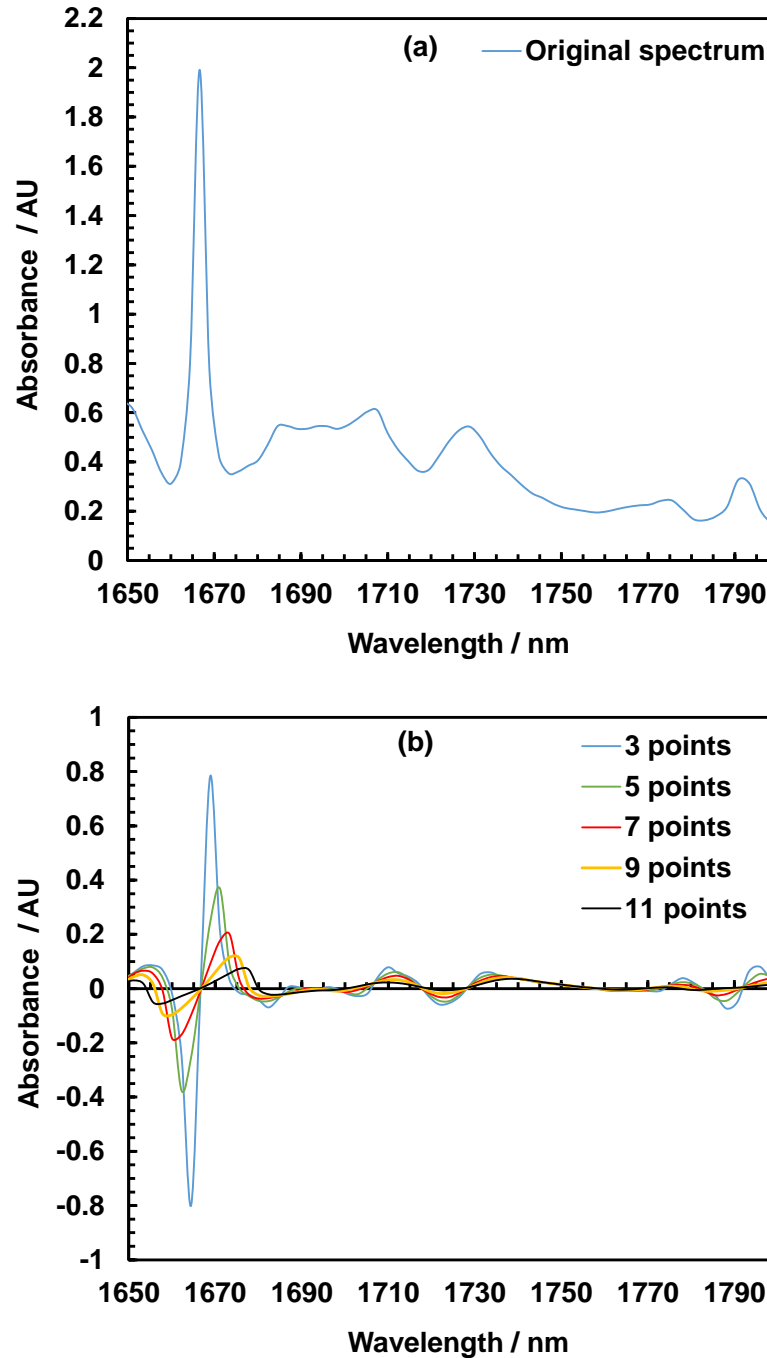


Figure 2.8. An example of Savitzky-Golay method. (a) Original spectrum before applying the Savitzky-Golay pretreatment method. (b) After applying the Savitzky-Golay pretreatment method using different smoothing points.

2.5.3 Multiplicative scatter correction (MSC)

Multiplicative scatter correction is a pre-processing method that used to remove the light scattering effects and multiplicative interferences that caused due to the difference in size and shape of particles that absorb the NIR light. The main idea behind this method is to correct the scatter level of all recorded spectra to a standard level which is the average

spectrum of all recorded spectra [72]. The MSC method assumes that all the recorded spectra have the same scatter source. MSC includes two steps:

One can estimate the MSC correction coefficients (b_0 , b_{ref}) by plotting original spectrum (x_{org}) against reference spectrum (x_{ref}) using following equation:

$$x_{org} = b_0 + b_{ref} \times x_{ref} \quad \text{Equation 2.20.}$$

Where x_{org} is the measured spectrum by the spectrometer (independent sample) and x_{ref} is the average of all recorded spectrum (calibration samples). The corrected spectrum can be calculated from the original spectrum minus the intercept divided by the slope.

$$x_{corr} = \frac{x_{org} - b_0}{b_{ref}} \quad \text{Equation 2.21.}$$

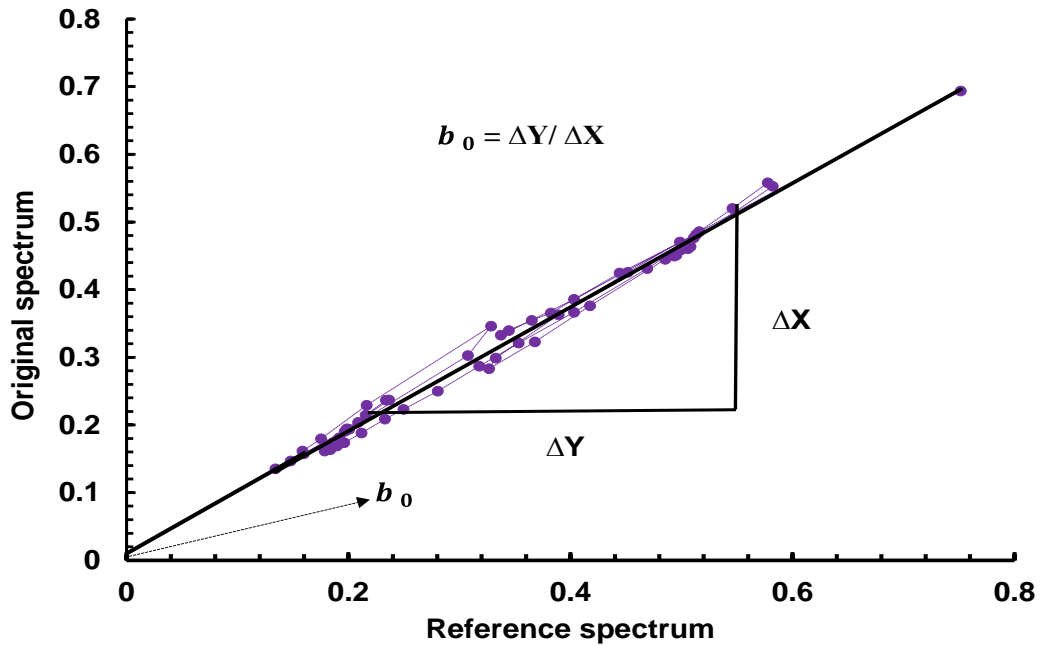


Figure 2.9. The original spectrum versus the reference spectrum. b_0 and b_{ref} represent the intercept and slope of the fitted line.

2.5.4 Standard normal variate (SNV)

Standard Normal Variate (SNV) is a simple scatter correction technique that uses the same type of equation as basic MSC equation.

$$x_{corr} = \frac{x_{org} - a_0}{a_{SD}} \quad \text{Equation 2.22.}$$

Where x_{org} is the sample spectrum, a_0 is the mean of the sample spectrum and a_{SD} is its standard deviation. Oppose of the MSC; SNV doesn't use any reference spectrum, and it is just applied to individual spectrum [73]. Actually, there is little difference between the dataset that treated by MSC and SNV pre-processing techniques [61]. The choice between SNV and MSC is a matter of taste. For a similar data set, it is better to apply MSC method to data set because MSC uses the mean spectrum.

2.5.5 Orthogonal signal correction (OSC)

Orthogonal signal correction (OSC) is a method that designed to eliminate the data that are unrelated to the dependent variables (X, components concentration) to reduce the data variance in the spectra [74]. This is done by removing independent variables that are mathematically orthogonal or as close orthogonal as possible to dependent variable [74]. For this purpose, the independent matrix needs to be decomposed into loading (t) and score (p) matrices. The mathematical procedure that is used for OSC correction is very similar to Nonlinear Iterative Partial Least Squares (NIPALS). Before starting the calculation, the X and Y matrices were centred and scaled. Below a brief review of the OSC algorithm is given:

$$t = Y(Y^T Y)^{-1} Y^T \quad \text{Equation 2.23.}$$

$$t_n = (1 - t)t \quad \text{Equation 2.24.}$$

Where t is the initial score vector which is obtained by calculating the first principal component of X and then it is required to orthogonalize t to t_{new} as follows:

$$t_{new} = (1 - Y(Y^T Y)^{-1} Y^T)t \quad \text{Equation 2.25.}$$

A new weight vector can be determined by:

$$w = \frac{x^T t_n}{t_n^T t_n} \quad \text{Equation 2.26.}$$

Then, a new t value can be determined using the weight vector:

$$t = Xw \quad \text{Equation 2.27.}$$

Equations (2.25) to (2.28) must repeat until the final t is a good describer of the part of X that is orthogonal to Y . The next step is to develop a PLS model with an optimum number of components that ensure t is described by the model as much as possible.

$$w_{final} = W (P^T W)^{-1} q \quad \text{Equation 2.28.}$$

Where W is the weight matrix of the model, P represents the loading matrix; q is the regression coefficient between t and the score matrix T .

The final score vector can be calculated as follows:

$$t_{final} = Xw_{final} \quad \text{Equation 2.29.}$$

And the loading vector is calculated by:

$$p_{final} = \frac{x^T t_{final}}{t_{final}^T t_{final}} \quad \text{Equation 2.30.}$$

Finally, the corrected spectrum can be reached using following equation:

$$X_{OSC} = X - t_{final} p_{final} \quad \text{Equation 2.31.}$$

2.5.6 Mean-centring

Mean-centring is a method that used to transform given spectra to comparable levels prior to construction of the calibration models. It is derived by subtracting the average spectrum of a dataset from each of the individual spectra. Before construction of PLS models, all the spectra were mean centred.

2.6 Model Evaluation

One of the important factors to develop an appropriate PLS using the FTNIR spectra of calibration data is selecting the optimum number of latent variable (LV). In this work, the leave-one-out cross-validation was employed to develop the PLS model. In this method, after removing of one sample from the calibration data set a developed PLS model is used for the remaining samples to predict the concentration of the removed sample. This procedure was repeated for all the calibration data set, and then the root mean square errors of cross-validation (RMSECV) was calculated:

$$RMSECV = \sqrt{\frac{\sum_{i=1}^n (y_{ci} - \hat{y}_{ci})^2}{n}} \quad \text{Equation 2.32.}$$

Where y_{ci} and \hat{y}_{ci} are the actual and predicted value of the sample that leave out from the validation set and n is the number of validation samples. Regarding created ANN models, RMSECV was derived to evaluate the performance of these developed models. After selecting the appropriate calibration model based on number of LVs and RMSECV, a series of raw data that were not part of the calibration data set used to determine the accuracy of both PLS and ANN developed models. Therefore, RMSEP was measured for the predicted concentration of each individual component using following equation:

$$RMSEP = \sqrt{\frac{\sum_{i=1}^n (y_{pi} - \hat{y}_{pi})^2}{n}} \quad \text{Equation 2.33.}$$

In which \hat{y}_{pi} is the predicted value by the developed PLS model and ANN model for independent samples and y_{pi} is the reference value of the independent samples.

The standard error of prediction (SEP) was calculated using Equation 2.34 to examine the significance of bias in each PLS model.

$$SEP = \sqrt{\frac{\sum_{i=1}^{i=n} (y_{pi} - \hat{y}_{pi} - bias)^2}{n-1}} \quad \text{Equation 2.34.}$$

The bias was calculated via Equation 2.35:

$$bias = \frac{\sum_{i=1}^{i=n} (y_{pi} - \hat{y}_{pi})}{n} \quad \text{Equation 2.35.}$$

Student's t statistic test was also carried out as described in ASTM E 1655 [75], to calculate the systematic errors:

$$t_{value} = \frac{|bias|\sqrt{n}}{SEP} \quad \text{Equation 2.36.}$$

Finally, relative prediction deviation (RPD) was calculated to investigate the predictive performance of the developed model. RPD is the ratio of the standard deviation of the all the prediction set (SD) to SEP.

$$RPD = \frac{SD}{SEP} \quad \text{Equation 2.37.}$$

The greater the RPD value, the higher ability of the PLS model to predict the concentration of species. An RPD value below 1.5 reveals that the calibration model is poor and cannot be used as a reliable model for further prediction [76].

The pre-processing methods including MSC, SNV, first and second Savitzky-Golay derivatives and OSC plus PLS analyses were all performed in Unscrambler® X10.3 (CAMO, Oslo, Norway).

2.6.1 Limit of detection (LoD)

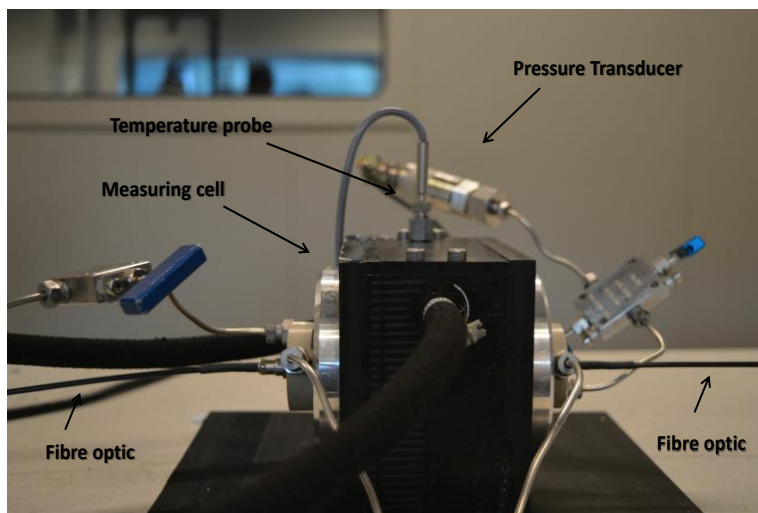
The limit of detection (LoD) is a term used to define the minimum concentration of an analyte that can be measured by an analytical procedure. The replicate spectra of 10 samples without any solute (pure nitrogen) and the spectra of 10 samples with the highest

value of solute were measured. Then, the final PLS regression models were employed to predict the concentration of each component at different pressure and temperature conditions. Then, the average standard deviation of the predicted values was calculated for each model and was multiplied by $10/3$ to roughly calculate the LoD [77].

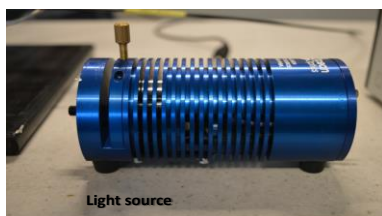
2.7 Experimental Methodology

2.7.1 Experimental equipment

Figure 2.10 and Figure 2.11 show a picture of the NIR test setup and the schematic of the experimental apparatus, respectively. An FTNIR spectrometer (Arcoptix) was used for spectra acquisition in the working range between 900 to 2600 nm and with a resolution of 2.5 nm. A 20-watt halogen light sources with attenuator (HL-2000-FHSA, Ocean Optics) was guided to the FTNIR spectrometer via a high-pressure cell containing the test sample through fibre optic cables. The sample cell used for the FTNIR measurements is made of titanium with an effective optical path length of 1.4 cm, the internal diameter of 5.0 cm (inner volume of about 28 cm³), and operating temperature from 273.15 to 323.15 K, and maximum operating pressure of 35 MPa. The high pressure cell was designed in-house and built by Proserv Ltd. Each end of the cell is equipped with a sapphire window (Diameter \approx 5 mm, Thickness \approx 10 mm) that allows the light pass through the sample. A lens holder was positioned at one end of the cell window to house the collimating lens. The collimating lens (74-UV, Ocean Optics) was employed to convert the divergent beam of the light source into a parallel beam to improve the signal intensity. The FTNIR spectrometer has USB connectivity for control and data acquisition. For measurements of test samples, an average of thirty spectra was recorded, and the spectrum measurement was repeated three times. The analysis for each measurement typically took about 90 seconds.



(a) FTNIR setup



(b) Light source



(c) FTNIR spectroscopy

Figure 2.10. Pictures of the FTNIR spectroscopy test setup.

The temperature of the cell was controlled using a jacket connected to a temperature-controlled bath that circulates coolants through the jacket. A high precision Platinum Resistance Temperature (PRT) probe was used to measure the temperature of the sample. A precision thermometer (Prema 3040) was employed to calibrate the temperature probe. The uncertainty of the calibrated PRT probe is estimated to be within ± 0.1 K. A piezo resistive silicon pressure transducer (Druck PDCR 4060) was used to measure the pressure inside the sample cell. The pressure transducer was regularly calibrated against a dead weight pressure balance. This calibration procedure ensures that the pressure measurement is accurate to ± 0.01 MPa. The pressure and temperature of the system were monitored and recorded every 30 seconds.

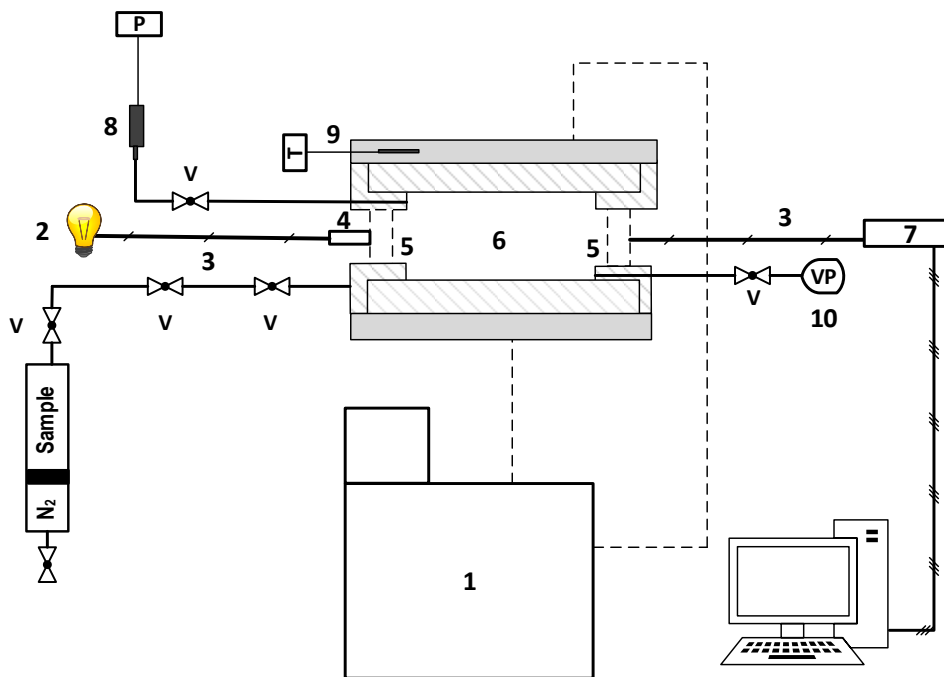


Figure 2.11. Schematic diagram of the FTNIR setup, 1: Cooling / Heating bath, 2: NIR light source, 3: Fibre optic, 4: Collimating lens, 5: Sapphire windows, 6: High-pressure cell, 7: Spectrometer, 8: Pressure transducer, 9: Temperature probe, 10: Vacuum pump.

2.7.2 Experimental procedure

Before starting the experiments, the high-pressure cell, sample cylinders, and the sapphire windows were cleaned thoroughly via n-heptane and then compressed air was passed inside the line, valve, and cell to dry the whole system. To ensure there is no leakage in the entire system, a pressure test was performed by injecting nitrogen into the cell, and the system was left for few hours. Once no leakage was observed in the system, a vacuum pump was used to remove air from the high-pressure cell as well as its whole loading lines. A spectrum of the empty cell (vacuumed) with an average of thirty scans was recorded as the reference spectrum before each measurement.

A typical spectrum of the gas mixture was measured at various pressures and temperatures following the below procedure. Firstly, the FTNIR cell was set at desired temperature, and then the cell was connected to a pressure cylinder containing the synthetic gas mixture and then filled with a gas mixture. A floating piston in the middle of the pressure cylinder was driven using pressurised nitrogen. Hence, the pressure of cell can be adjusted by injection/withdrawal of nitrogen behind the piston. The gas samples were injected slowly into the FTNIR cell to avoid damage to the sapphire windows. Once the desired equilibrium pressure had been reached the line was disconnected from the pressure cylinder, and the spectrum was recorded three times by the averaging of thirty scans to

reduce the noise level. The pressure of the cell was kept constant during FTNIR measurements. The averaged spectrum was then used for data pre-processing and developing the partial least squares (PLS) regression model. This procedure was repeated for all the samples at three different temperatures.

2.7.3 Experimental material

The specification and suppliers of the materials used in this study are listed in Table 2.2. Compositions of 30 calibration gas mixtures and 15 prediction gas mixtures were prepared in the laboratory with the percentage composition of methane varying between 80 and 100 mol%, ethane between 1 to 12 mol%, propane between 1 to 6 mol%, i- butane between 0.5 to 2 mol% and n-butane between 0.5 to 2 mol%. All the synthetic gas mixtures were prepared into the high-pressure vessel by combining pure components on a weight basis using a two digit electronic balance (Sartorius, Cubis MSA8201S-0CE-D0, accuracy ± 0.01 g). To prepare the gas mixtures, the component with the lowest vapor pressure was first introduced into a high pressure vessel (in this work, N-butane) and the exact weight of the injected pure component was measured using a two digit balance. Then the calculated amount of the second pure component with the lowest vapor pressure (I-butane) was then injected into another high pressure vessel with a floating piston. The exact amount of the second component was also measured using the balance. Two vessels were then connected through a very small line together. The floating piston in the middle of the pressure vessel was driven using pressurized nitrogen to transfer i-butane into the connected vessel, containing n-butane. It should be noted that a mixing ball was placed into the vessel to accelerate the process of mixing. After injecting all the pure components using the procedure explained in above into the vessel, the mole percent of the mixtures were calculated for each sample based on the amount of pure components that transferred into the vessel.

The concentration of the calibration mixtures was designed according to typical components concentration of natural gases (see Table 2.2) in order to cover all the ranges of interest. All the synthetic gas mixtures were then analysed using a gas chromatography (Varian model CP-3800) to validate their compositions. A small difference was observed between the experimental value and measured value by GC. Average of three measurements by GC was chosen as the true value for the calibration and prediction data set.

Table 2.2. Purity and source of samples used in this study.

Chemical name	Source	Mole fraction purity	Analysis method
Methane	BOC	0.999	GC
Ethane	BOC	0.995	GC
Propane	BOC	0.995	GC
i-butane	BOC	0.995	GC
n-butane	BOC	0.995	GC
Carbon dioxide	BOC	0.999	GC
Nitrogen	BOC	0.999	GC

Table 2.3. Calibration samples used for the construction of the PLS models, mol%.

No.	Methane	Ethane	Propane	I-butane	N-butane
1	79.89	12.04	5.51	2.01	0.55
2	80.02	11.03	6.01	0.97	1.97
3	80.0	10.54	6.41	1.07	1.98
4	80.11	9.11	8.12	1.15	1.51
5	84.05	11.06	4.03	0.45	0.41
6	84.01	10.02	5.01	0.49	0.47
7	84.0	9.02	4.52	0.41	2.05
8	84.03	7.05	6.01	1.99	0.92
9	84.05	11.95	3.31	0.38	0.31
10	87.05	8.01	2.01	1.41	1.52
11	86.50	5.40	4.89	1.11	2.10
12	87.05	6.94	4.03	1.53	0.45
13	87.11	7.92	2.53	0.84	1.60
14	87.06	10.91	1.35	0.35	0.33
15	87.05	5.28	5.45	1.10	1.12
16	90.11	5.91	3.05	0.41	0.52
17	90.05	5.40	2.45	0.89	1.21
18	90.01	7.98	1.01	0.43	0.57
19	90.02	7.02	1.95	0.46	0.55
20	93.07	5.09	1.08	0.28	0.48
21	93.04	4.05	0.98	0.89	1.04
22	92.98	4.44	1.45	0.61	0.52
23	93.01	3.01	2.01	1.01	0.96
24	93.0	6.48	0.52	0	0
25	93.01	5.90	0.49	0.29	0.31
26	96.12	2.12	1.11	0.35	0.30
27	96.0	3.05	0.95	0	0
28	98.05	1.45	0.50	0	0
29	99.38	0	0	0.29	0.33
30	99.05	0.43	0.52	0	0
31	100	0	0	0	0

2.8 Result and Discussions

2.8.1 Influence of temperature, pressure and path-length on FTNIR spectrum of hydrocarbons mixtures

2.8.1.1 Influence of temperature

In order to examine the influence of temperature on FTNIR spectra at constant pressure, the pressure of the synthetic gas mixture inside the cell was kept constant at 6.89 MPa, and the FTNIR spectra were recorded at three different temperatures (278.15 K, 293.15 K, and 313.15 K). As it is apparent in Figure 2.12, the absorbance spectrum of the gas mixture increase slightly with decreasing temperature at regions those hydrocarbons absorbs the FTNIR light. These changes with temperature designate that the FTNIR spectra of hydrocarbons mixtures are dependent on temperature. Because of the temperature dependence of the FTNIR spectra of gas mixtures, it is necessary to record the FTNIR spectrum at different temperatures within a certain range to expand the range of applicability of this method.

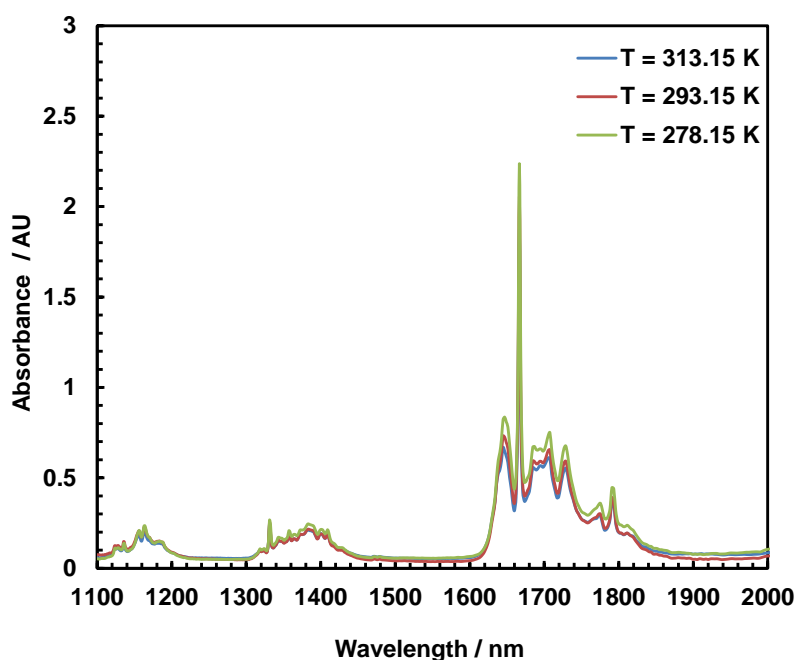


Figure 2.12. FTNIR Spectra of one synthetic gas mixture at 6.89 MPa and three different temperatures.

2.8.1.2 Influence of pressure

Spectra of one gas mixture at constant temperature and four different pressures are presented in Figure 2.13. It is evident that the absorbance spectrum of the gas mixture is highly dependent on pressure, and an increase in pressure leads to an increase in

absorbance spectrum at three different NIR regions that carry the relevant information for interested hydrocarbon species that compose the gas mixture. All this analysis confirms that the spectroscopic signals are temperature and pressure dependent and variation in pressure and temperature may affect the accuracy of chemometric models that is constructed in a single operational temperature and pressure. Thereby, individual PLS models were built at various temperatures and pressures to extend the application of this method since the temperature and pressure of gas mixtures may vary in natural gas pipelines. The operation range of pressure was chosen for the construction of the calibration model according to the path-length of the FTNIR cell.

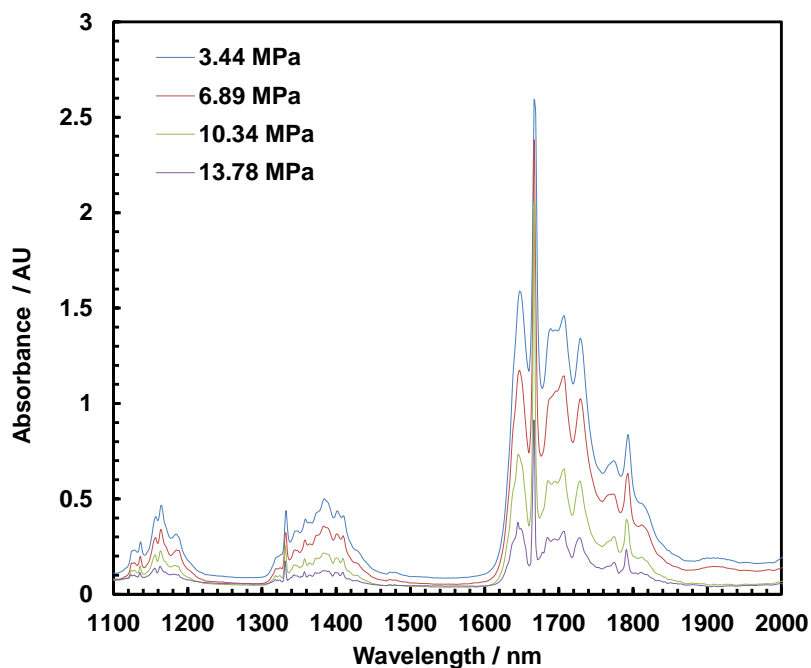


Figure 2.13. FTNIR Spectra of one synthetic gas mixture at 293.15 K and four different pressures.

2.8.2 Selection of optimum path-length

Path-length is the distance that the light travels through the gas samples, and this length can be carefully chosen in accordance with the amount of an absorber along the distance that light travels. Hence, selection of optimum optical path length is the first important step in the development of FTNIR spectroscopy method. By comparing the absorbance of spectra in the interested spectral region based on different optical path length the best indicators of optical path length were identified. Three different path lengths (28, 5 and 1.4 cm) were made. The preliminary measurements were performed using a 28 cm cell path length. The spectra were collected at three different pressures (0.1, 0.68 and 3.44

MPa). It was observed that the light beam in the frequency range of interest is fully attenuated at a pressure of 3.44 MPa. At this condition, molecules absorb almost the whole the energy of the beam in the wavelength region of interest causing no energy received by the detector. Hence, two new test cells with the shorter path length (5 and 1.4 cm) were built in order to perform the NIR measurements at pressures 0.68 MPa and higher. At first, the cell with the optical path of 5 cm was used for NIR measurements. Using this cell at a pressure higher than 10.34 MPa, the absorption peak was appeared to become flat because of the almost 100% absorption of the light by molecules. However, when a 1.4 cm path length cell was used, no flat peak was observed in all regions showing that all hydrocarbons present in the synthetic gas mixtures could be clearly detected using a cell with this path length. One criterion is to achieve sufficient signal-to-noise ratio in the interested spectra region. The signal-to-noise ratio (SNR) is used to determine the quality of measurements performed using the system. The accuracy, resolution and repeatability of a measurement are directly related to SNR. Very strong absorbance ($AU > 2$) increases the error of measurement because the sample absorbs most of the lights and only a small amount of light can be detected by the detector. On the other hand, very low absorbance provides not so much information about the evolution of the species concentration. Consequently, to decrease the error and uncertainty of the measurement and to achieve to a good signal to noise ratio, the operating pressure is chosen to be in a range between 3.44 MPa to 13.78 MPa where the absorbance unit varies from around 2 to 0.05 AU (Figure 2.14).

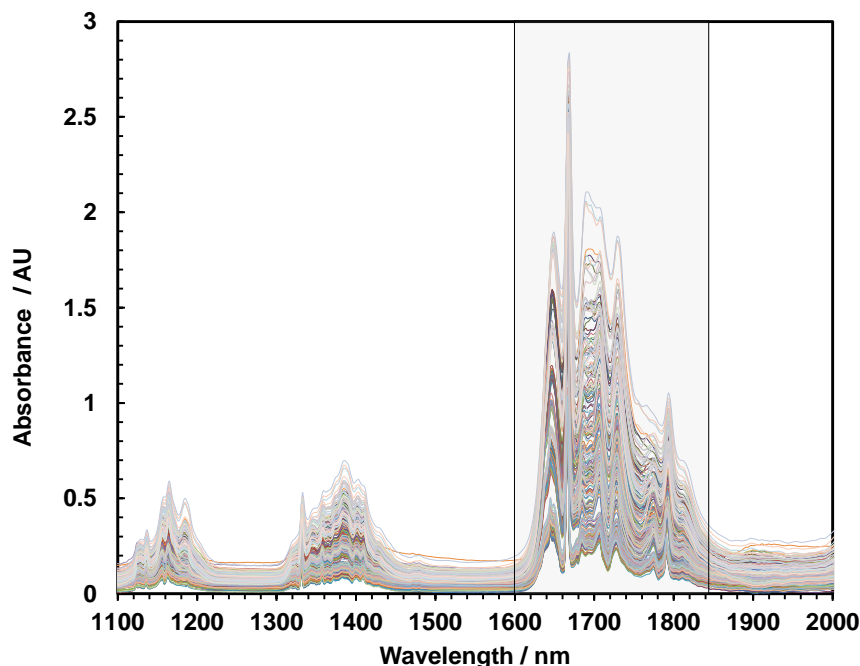


Figure 2.14. FTNIR Spectra of 30 synthetic gas mixtures with different methane, ethane, propane, i-butane and n-butane contents at various pressures in the range of 3.44 - 13.78 MPa and various temperatures in the range of 278.15 – 313.15 K (The range shaded (1670 – 1800 nm) used for developing of the regression models).

2.8.3 Spectral range selection and construction of the calibration models

Selection of the right wavelength region plays an important role to improve the performance of the calibration model. The idea behind the optimum wavelength selection is the identification of an appropriate subset that will provide lower error values for the validation and prediction data set. To arrive at the true wavelength region, the region with less RMSECV value and latent variable numbers should be selected as an optimal subset of wavelengths for a given data set.

In Figure 2.14, the FTNIR spectra of all thirty synthetic gas mixtures containing methane, ethane, propane, i-butane and n-butane that used for quantitative analysis are shown. After inspecting the whole NIR spectral region, the spectral range lower than 1100 nm and higher than 2100 nm were excluded from data set due to poor and extreme absorption of hydrocarbons in these areas, respectively. Major absorption bands for hydrocarbons in the NIR region typically occur in the ranges 1100-1200 nm, 1350 to 1450 nm, and 1600 to 1850 nm as illustrated in Figure 2.4. The absorption bands in the ranges from 1100 to 1200 nm are related to the second overtone of the hydrocarbons, whereas the absorption bands between 1350 to 1450 nm belongs to the first overtone of the combination modes of the hydrocarbons which are associated with CH bonding [32]. The main features of the spectra are the absorption in the range of 1600 to 1850 nm that is associated with the first

overtone stretching of the CH, CH₂ and CH₃ bands that are related to the methane, ethane, propane, i-butane and n-butane in the synthetic gas mixtures [32]. In this work, the region from 1670 to 1800 nm was selected for the quantitative analysis due to the intense absorption of hydrocarbons in this region by comparison with the second overtone region and the first combination band region of the CH, CH₂, and CH₃. The first overtone region provides better accuracy for the gas species with lower molar absorptivity due to high absorbance of hydrocarbon components in this region. Furthermore, lower RMSECV values and few numbers of latent variables were observed for all the individual components in this region for all the calibration pressures and temperatures. To find the optimum wavelength region for quantitative determination of interested hydrocarbon components, the NIR spectrum from 1600 to 1850 nm was split into several intervals. The results revealed that the restricted region between 1670 to 1800 nm provides lower RMSECV and RMSEP values compare to other regions.

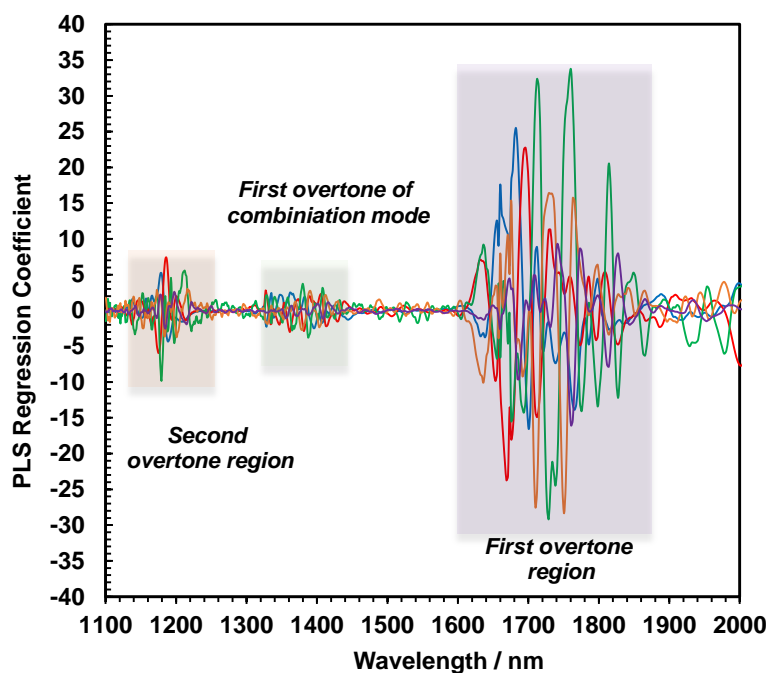


Figure 2.15. Weighted regression plot, showing important variables in modelling.

In order to select the appropriate spectral range for the generation of the calibration models, a PLS model pre-treated with first Savitzky-Golay derivative (SGD1) was developed for one of the given data set at a specific temperature and pressure condition ($T = 293.15$ K and $P = 6.89$ MPa). The plots of weighted regression coefficients for the developed PLS model in the NIR range between 1100 to 2000 nm were plotted for all the

components together in order to discover the regions that are mostly contributed in the generation of the calibration model (Figure 2.15). PLS regression coefficients whether positive or negative is an indication of the importance of the variable in modelling for the response [78]. It is apparent that the magnitude of the regression coefficients for all the components are negligible at the second overtone (1100-1200 nm) and the first overtone of the combination modes of hydrocarbons (1350 -1400 nm) and consequently these regions cannot provide valuable information for the construction of the calibration models. As can be seen, the first overtone region of hydrocarbons (1600 -1850 nm) is contributed most to the construction of the calibration model. Large deviations were associated with all the components with the PLS models developed using regions between 1100-1200 nm, 1350 to 1450 nm, and 1600 to 1850 which directed that the predictions of methane, ethane, propane, i-butane and n-butane cannot be trusted for models that developed across these regions. To find the optimum wavelength region for quantitative determination of interested hydrocarbon components, the NIR spectrum from 1600 to 1850 nm was split into several intervals. The results revealed that the restricted region between 1670 to 1800 nm provides lower RMSECV and RMSEP values compare to other regions. The procedure that followed to select the appropriate spectral range and pre-processing method is illustrated in Figure 2.16. A detailed description of developed PLS models is given later.

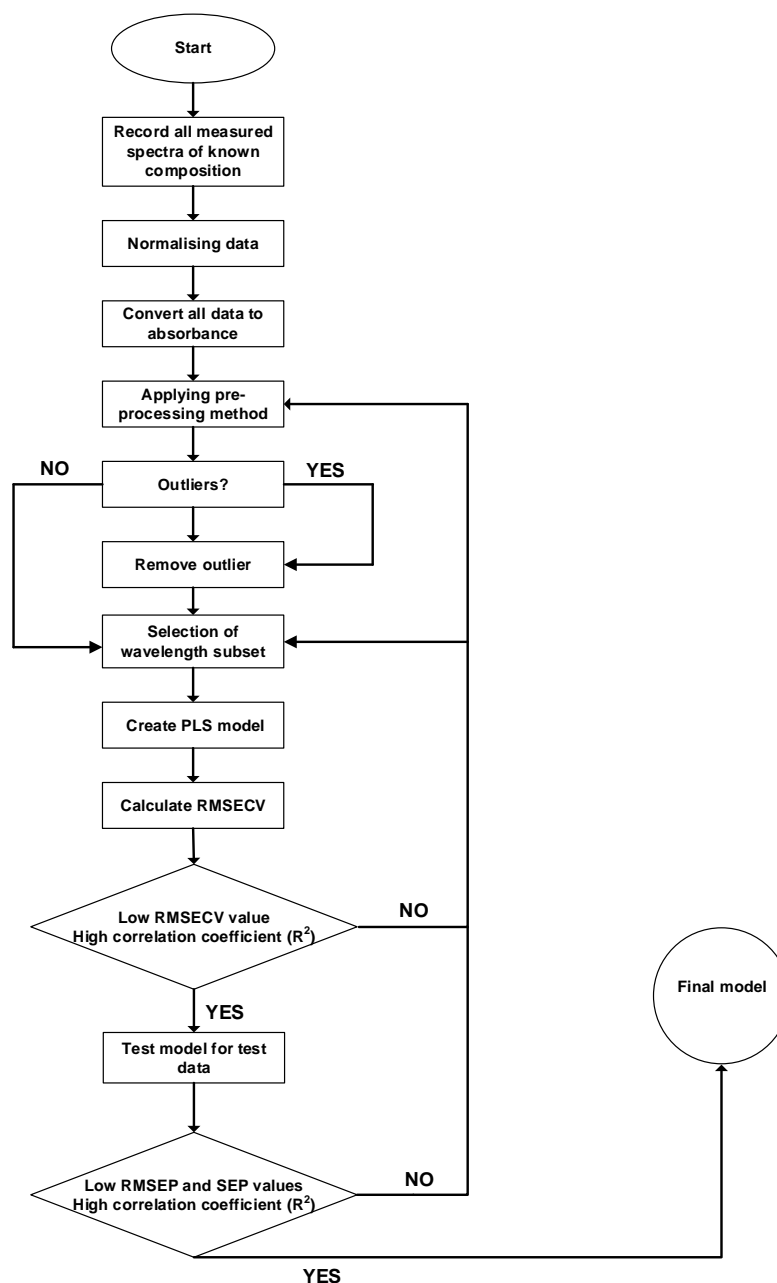


Figure 2.16. A flowchart showing the sequence of steps that followed to develop the final PLS models.

2.8.4 PLS results

After recording the FTNIR spectra of each sample (synthetic gas mixture) at specified pressure and temperature conditions, firstly the reference intensity (I_0 , vacuumed cell,) and the sample spectrum (I) were both normalised (maximum method) and then used to convert to absorbance unit ($A = \log(I_0/I)$). The reference intensity was recorded before starting of each measurement.

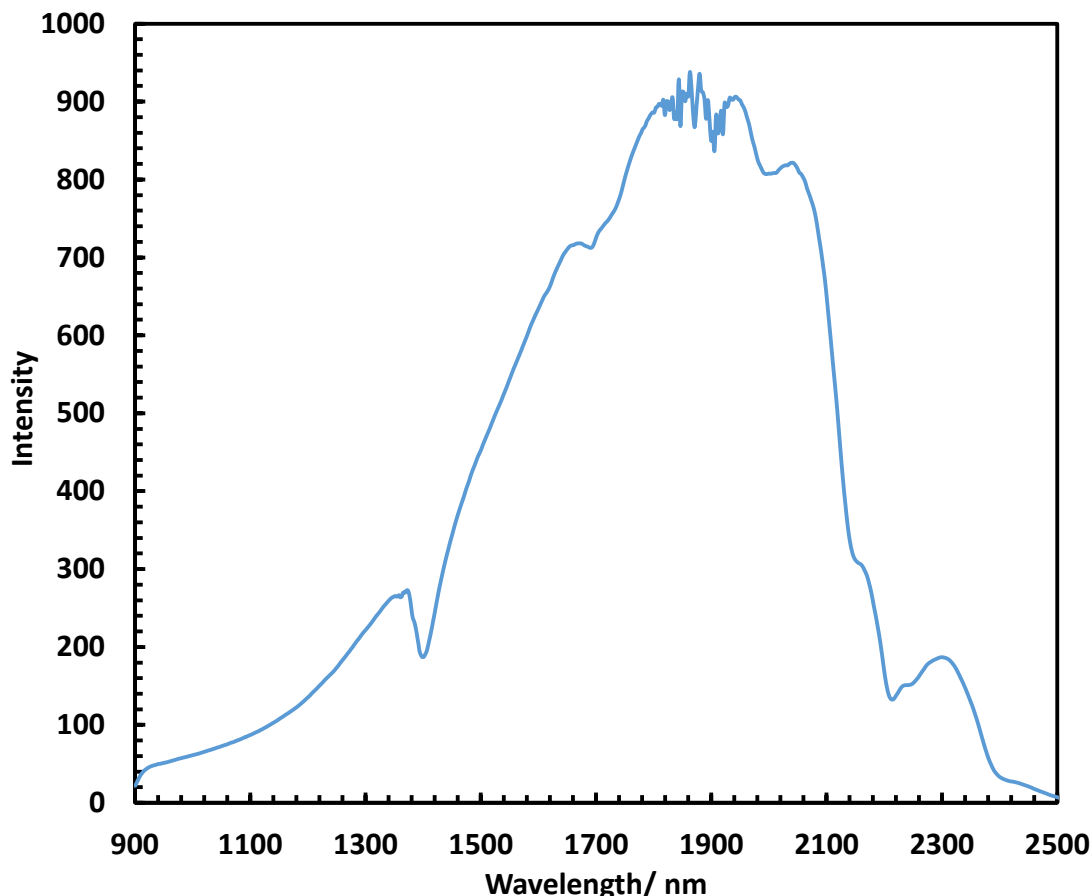


Figure 2.17. Reference intensity spectrum (background).

Various pre-processing methods were applied to the remained calibration data set to evaluate the effect of these techniques on the accuracy of the developed PLS model. As mentioned earlier, different pre-processing methods were applied the prior construction of the calibration models at various pressure and temperature conditions. In order to evaluate the accuracy of the developed model and select the best pre-processing method, RMSEC, RMSECV, RMSEP, SEP and R^2 of each created model were derived. In order to obtain an accurate prediction model, it is always required to have low RMSEP/SEP values, with fewer latent variables (LVs) while maintaining a high correlation (R^2) at the same time. A high coefficient of determination is a sign that there is good agreement between the values that acquired by the model compare to actual values. In this work, different pre-processing methods were applied to whole spectra and as mentioned earlier the range between 1670 to 1800 nm was selected as the final range for construction of calibration models for all the components. After construction of calibration models, the existence of outliers in the data set was examined and removed from the dataset. The outliers were identified by plotting Hotelling's T^2 versus Q residuals. Hotelling's T^2 is the square of the distance of the sample from the model mean that can be explained by normal

variations within the group and it used to detect situations where a process is operating outside normal conditions. The Q residuals mean the distance of the sample from the model that can be explained by random error[79]. Spectra in the 95% confidence interval for both Hotelling's T^2 and Q residuals are stored, and if the Hotelling T^2 and Q-residual statistics for measured spectra lie outside this specific region, they are selected as outliers. The existence of outlier in the dataset could be due to the error in FTNIR measurements or error in sample preparation.

As mentioned earlier, the main concept behind the pre-processing methods is to eliminate unwanted background data and reduce noise level before construction of the calibration model [54, 70]. Various pre-processing methods can be applied to the spectral data to improve the accuracy of the developed calibration model. In this study, the spectra were pre-treated using multiplicative scatter correction (MSC); standard normal variate (SNV); first and second Savitzky-Golay derivatives (SGD1 and SGD2); first Savitzky-Golay derivative followed by the orthogonal signal correction (SGD1 + OSC) and second Savitzky-Golay derivative followed by the orthogonal signal correction (SGD2 + OSC). The final RMSECV and the optimum number of latent variables values for all developed models for each component with different pre-processing methods at a pressure of 6.89 MPa and temperature of 293.15 K are presented in Table 2.4.

In order to find the optimum number of the smoothing points, different smoothing points were implemented to the spectra data using the Savitzky-Golay algorithm. The best results in terms of RMSECV values were observed when the first-Savitzky-Golay with five smoothing points were applied to the spectra data and regarding the second-Savitzky-Golay; the best results were found while 15 smoothing points had been implemented to the given spectra. A slight improvement was noted in the RMSECV values for all the components while OSC was applied to the spectra data after applying the first and second Savitzky-Golay algorithm. It should be highlighted that, in all cases, the pre-treated spectra were also mean-centred before developing of the PLS model. The RMSECV values obtained for both MSC and SNV are very similar for all the components. It can be seen the RMSECV values for methane, ethane, propane, i-butane and n-butane are reduced significantly while the first and second Savitzky-Golay derivative are applied to spectra. It can be seen from Table 2.4, the treatments of SG1 and SG2 are reduced the number of latent variables in some cases. The main improvement of SG1 and SG2 pre-processing methods on results are their influence on RMSECV values rather than a

number of latent variables. Similar results were obtained for all the developed models at different pressure and temperatures.

Table 2.4. Comparison of RMSECV and latent variables of different pre-processing methods at a pressure of 6.89 MPa and temperature of 293.15 K.

Components	Methane		Ethane		Propane		I-butane		N-butane	
Pre-processing method	LV	RMSECV	LV	RMSECV	LV	RMSECV	LV	RMSECV	LV	RMSECV
MSC	2	0.43	4	0.33	6	0.16	5	0.15	5	0.18
SNV	2	0.47	4	0.38	5	0.19	5	0.18	5	0.19
SG1	2	0.22	5	0.19	5	0.13	5	0.10	5	0.09
SG2	2	0.25	5	0.22	5	0.14	4	0.13	5	0.11
SG1 + OSC	2	0.20	5	0.18	5	0.12	4	0.09	5	0.07
SG2 + OSC	2	0.23	5	0.20	5	0.14	4	0.13	5	0.11

The optimum number of the latent variables for each component was selected on the basis of RMSECV values of different latent variables. Initially, the RMSECV value starts to decrease with an increase in a number of latent variable (starts from one to certain number). PLS extracts the latent variables based on the covariance between the independent matrix and dependent variables. Essentially, while no significant change is observed in RMSECV value from one number of latent variable to the next, the subsequent latent variables are not considered for developing of the calibration models because they may just describe some noise or irrelevant information. The procedure for selection of the optimum number of latent variables is illustrated in Figure 2.18.

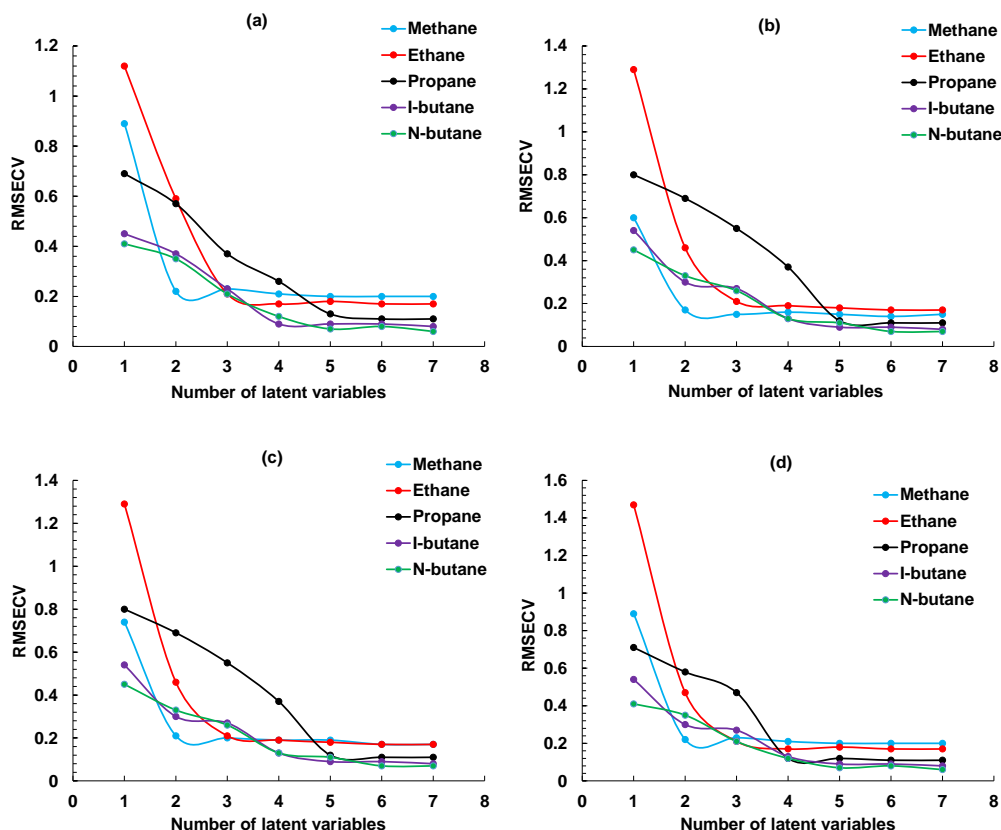


Figure 2.18. Comparison of RMSECV with respect to the number of latent variables for developed PLS model – SG1 + OSC pre-treatment, at a temperature of 293.15 K and various pressures (3.44 (a), 6.89 (b), 10.34 (c), and 13.78 (d) MPa).

Figure 2.18 shows the RMSECV values for all studied components versus the number of the latent variables that are employed for the construction of the PLS models at a temperature of 293.15 K and different pressures. For example, for propane at 6.89 MPa, the RMSECV value was found to be minimum when the PLS model developed with five latent variables, whereas the minimum prediction error for methane occurs while the PLS model is developed with two number of latent variables. It can be seen, no significant changes in RMSECV values for these two components are observed for a higher number of latent variables. Similar procedure was repeated for all the components at various pressures and temperatures to detect the proper number of latent variables. In summary, in order to develop accurate PLS models, the number of latent variables and the final spectra range that used in the PLS models should be considered carefully.

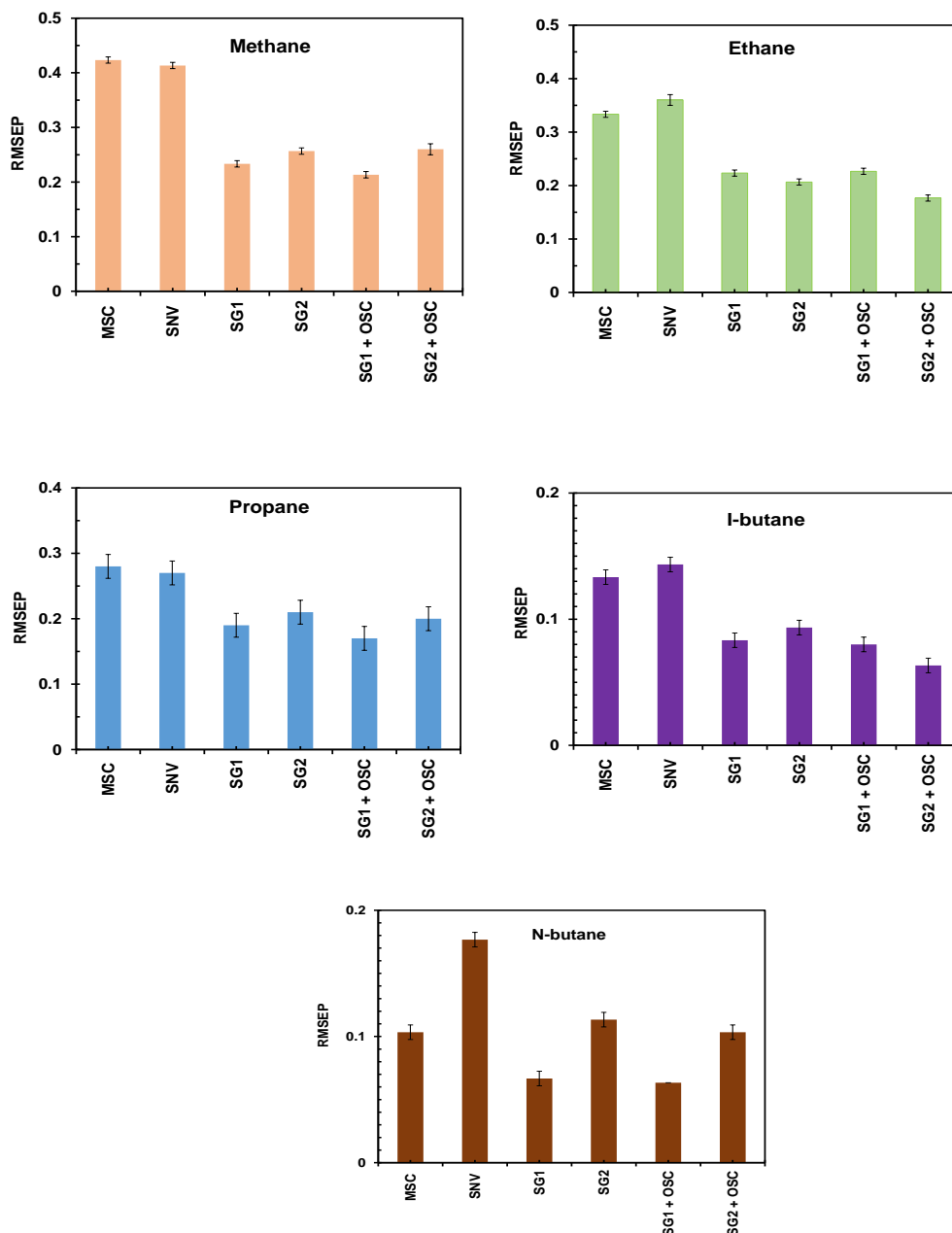


Figure 2.19. Comparison of RMSEP of different pre-processing methods for PLS developed models at a pressure of 6.89 MPa and temperature of 293.15 K.

Furthermore, the performance of various developed PLS models was investigated for prediction samples that are not included in the calibration data set. As one can see in Figure 2.19, the best results in terms of RMSEP value obtained again when the first Savitzky-Golay derivative (SGD1) with smoothing over 5 points plus orthogonal signal correction (OSC) were applied to the FTNIR spectra data. It should be noted that the number of components for OSC pre-treatment for all components is single because of their highest predictability compare to the higher number of components.

The NIR spectra after SG1 + OSC treatment for each component at a pressure of 6.89 MPa and temperature of 293.15 K are illustrated in Figure 2.20 and Figure 2.21.

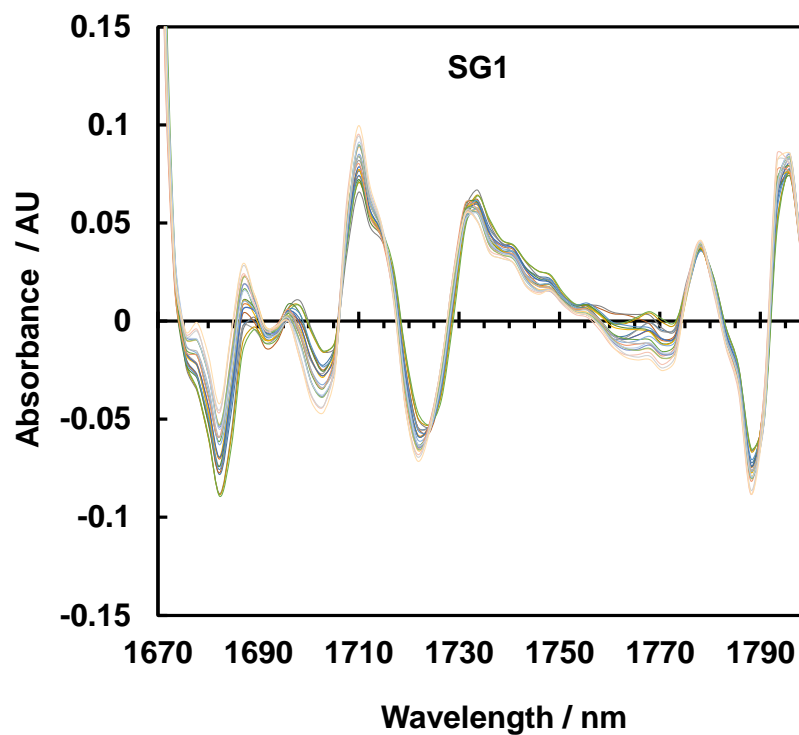


Figure 2.20. NIR spectra after SG1 pre-treatment for all the calibration samples.

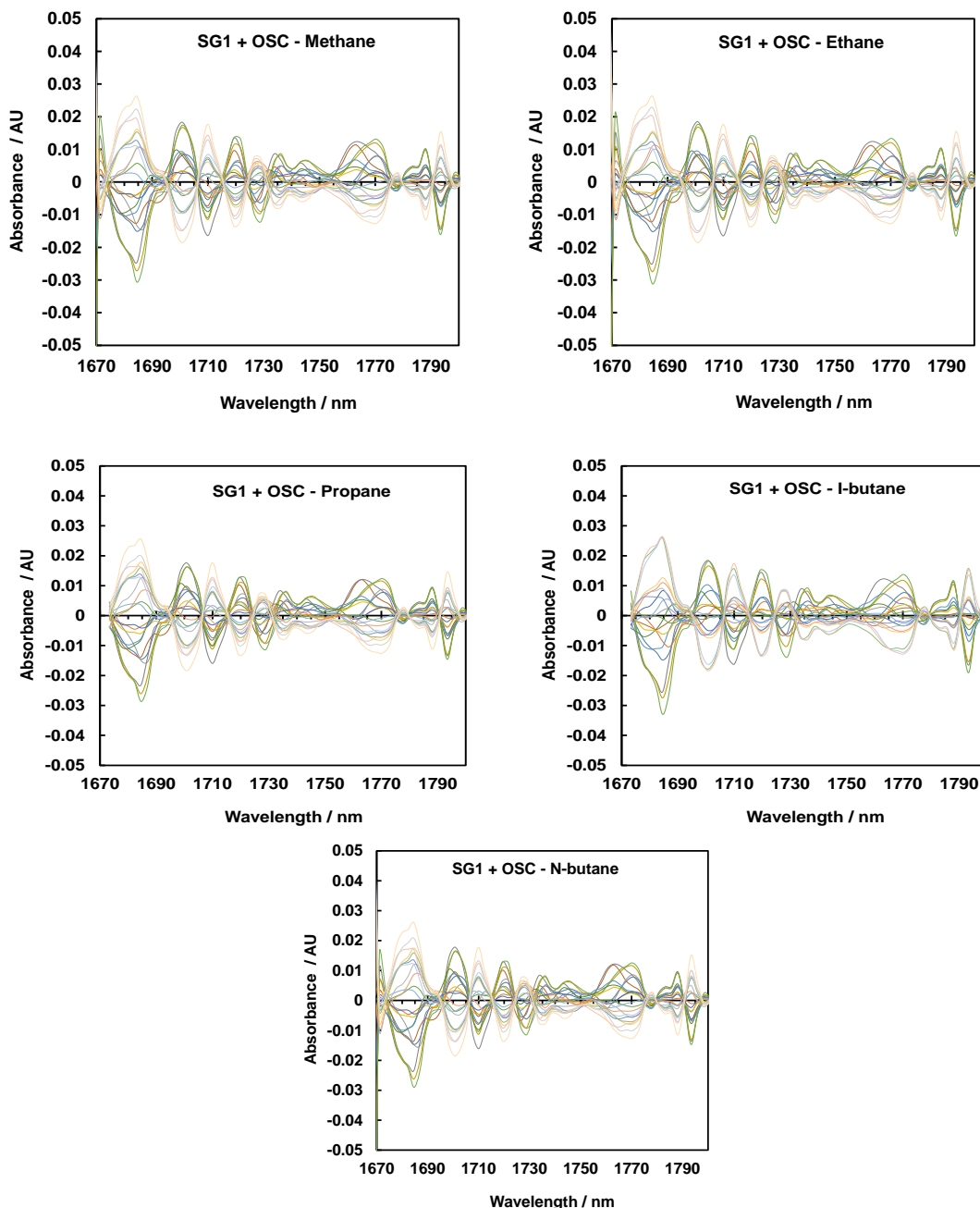


Figure 2.21. NIR spectra after SG1 + OSC treatment for methane, ethane, propane, i-butane and n-butane at pressure of 6.89 MPa and temperature of 293.15 K.

Additionally, the performance of each PLS model at different conditions is represented graphically through plots of FTNIR-predicted data derived from the PLS models versus the actual value (Figure 2.22 to Figure 2.24). As mentioned earlier, The SGD1-OSC method produced the best results in terms of root mean square of prediction (RMSEP) compare to other techniques and was used for data pre-treatment. This work, therefore, considers the results of PLS model using this technique at different T&P conditions. As can be seen, there is no significant difference between FTNIR predictive values and measured values, and the PLS-determined methane, ethane, propane, i-butane and n-

butane concentrations are so adjacent to the 0-error line which indicates the good predictive capability of the developed PLS models at different pressures and temperatures. Regarding RMSEP, results for methane, ethane, propane, i-butane and n-butane varied from 0.17 to 0.28, 0.14 to 0.23, 0.11 to 0.23, 0.06 to 0.13, and 0.06 to 0.12 mol%, respectively, indicating a small difference in comparison to the measured values at various pressure and temperature conditions. Furthermore, the R^2 statistic was calculated for individual samples and results show good agreement between predicted and measured values. The optimal number of latent variables for the PLS model was selected to be 2 for methane, 4 or 5 for ethane, propane and i-butane, and 5 or 6 for n-butane according to the target temperature and pressure of the system (Table 2.5 - Table 2.9). It can be seen all the developed PLS models have a good predictive statistics in terms of low RMSEP value, high R^2 value that indicates the capability of the proposed PLS models to determine the composition of samples. However, higher RMSEP values were observed for all the components at a pressure of 3.44 MPa compared to others. This may be attributed to the low absorbance of hydrocarbons at respective pressure compared to other calibration pressures. Totally, most of the models are performed very well in predicting samples not included in the calibration set.

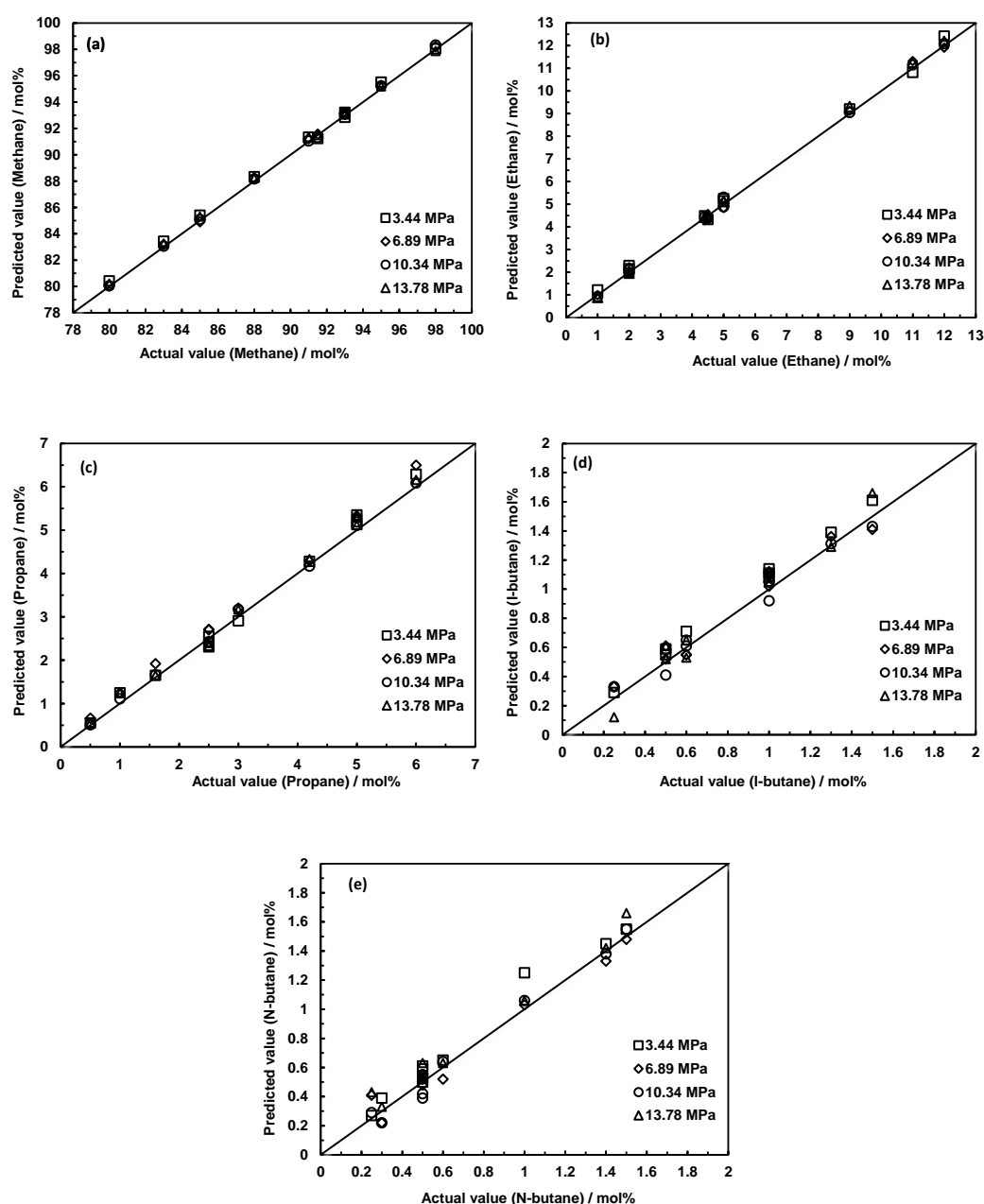


Figure 2.22. PLS regression plot of predicted versus actual concentration of methane (a), ethane (b), propane (c), i-butane (d) and n-butane (e) in synthetic gas mixtures (independent samples) at temperature of 278.15 K and various pressures.

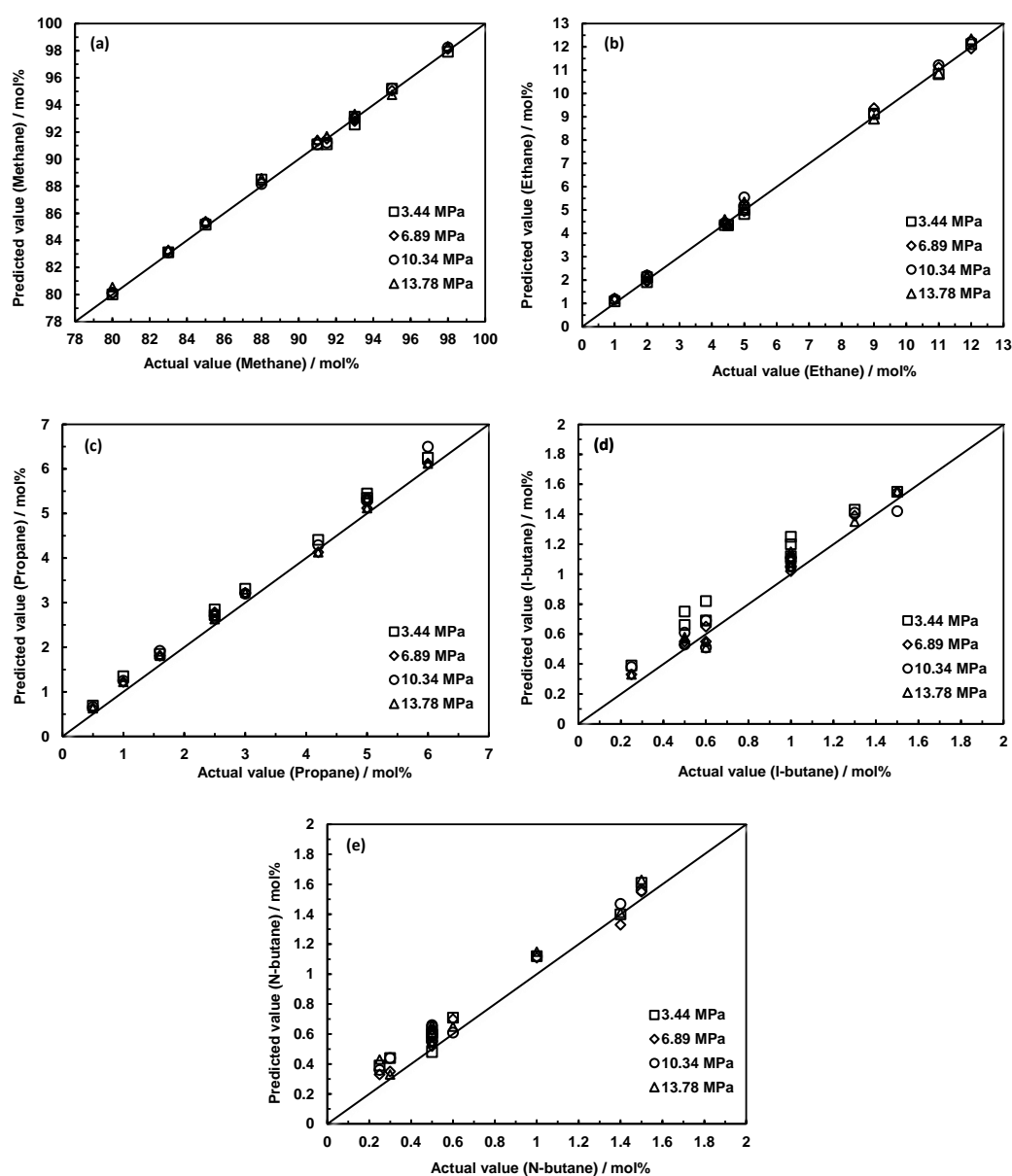


Figure 2.23. PLS regression plot of predicted versus actual concentration of methane (a), ethane (b), propane (c), i-butane (d) and n-butane (e) in synthetic gas mixtures (independent samples) at temperature of 293.15 K and various pressures.

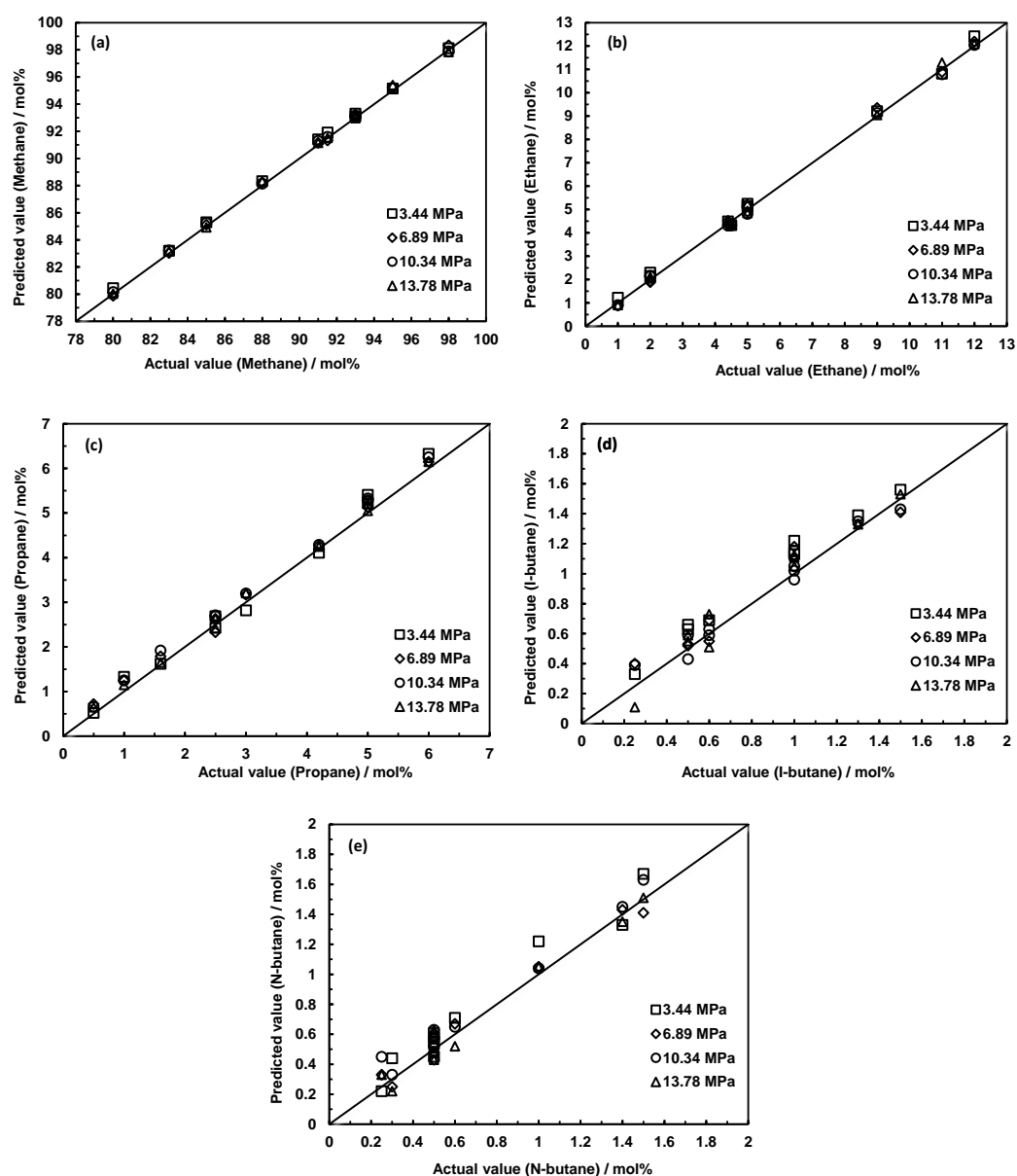


Figure 2.24. PLS regression plot of predicted versus actual concentration of methane (a), ethane (b), propane (c), i-butane (d) and n-butane (e) in synthetic gas mixtures (independent samples) at temperature of 313.15 K and various pressures.

Table 2.5. Results of the PLS model to estimate the concentration of methane (mol%) in synthetic gas mixtures at different temperatures and pressures (spectral region: 1670 – 1800 nm).

Calibration			Prediction						
Components	Temperature (K)	Pressure (MPa)	LV	RMSECV	R ²	RMSEP	R ²	bias	SEP
Methane	278.15	3.44	2	0.221	0.997	0.281	0.998	0.008	0.283
	293.15	3.44	2	0.222	0.996	0.252	0.999	0.007	0.253
	313.15	3.44	2	0.221	0.996	0.303	0.998	0.005	0.304
	278.15	6.89	2	0.213	0.996	0.174	0.998	0.009	0.175
	293.15	6.89	2	0.201	0.996	0.203	0.998	0.006	0.205
	313.15	6.89	2	0.213	0.997	0.194	0.999	0.007	0.195
	278.15	10.34	2	0.213	0.997	0.171	0.998	0.006	0.172
	293.15	10.34	2	0.212	0.997	0.209	0.998	0.007	0.210
	313.15	10.34	2	0.216	0.998	0.194	0.998	0.007	0.196
	278.15	13.78	2	0.213	0.997	0.222	0.999	0.007	0.224
	293.15	13.78	2	0.223	0.998	0.214	0.997	0.009	0.215
	313.15	13.78	2	0.204	0.998	0.245	0.999	0.009	0.246

Table 2.6. Results of the PLS model to estimate the concentration of ethane in synthetic gas mixtures at different temperatures and pressures (spectral region: 1670 – 1800 nm).

Calibration			Prediction						
Components	Temperature (K)	Pressure (MPa)	LV	RMSECV	R ²	RMSEP	R ²	bias	SEP
Ethane	278.15	3.44	5	0.192	0.996	0.231	0.996	0.005	0.232
	293.15	3.44	5	0.189	0.996	0.207	0.996	0.004	0.208
	313.15	3.44	5	0.182	0.996	0.235	0.997	0.004	0.236
	278.15	6.89	4	0.171	0.997	0.163	0.998	0.006	0.165
	293.15	6.89	5	0.185	0.996	0.185	0.997	0.005	0.186
	313.15	6.89	4	0.174	0.996	0.165	0.998	0.003	0.166
	278.15	10.34	4	0.193	0.996	0.145	0.998	0.006	0.147
	293.15	10.34	4	0.165	0.997	0.223	0.997	0.005	0.225
	313.15	10.34	4	0.162	0.997	0.151	0.998	0.004	0.152
	278.15	13.78	4	0.191	0.996	0.168	0.999	0.004	0.169
	293.15	13.78	4	0.171	0.997	0.176	0.998	0.004	0.177
	313.15	13.78	4	0.185	0.996	0.166	0.998	0.005	0.167

Table 2.7. Results of the PLS model to estimate the concentration of propane in synthetic gas mixtures at different temperatures and pressures (spectral region: 1670 – 1800 nm).

Calibration			Prediction						
Components	Temperature (K)	Pressure (MPa)	LV	RMSECV	R ²	RMSEP	R ²	bias	SEP
Propane	278.15	3.44	4	0.135	0.997	0.235	0.996	0.005	0.236
	293.15	3.44	5	0.154	0.996	0.209	0.997	0.001	0.209
	313.15	3.44	5	0.147	0.997	0.235	0.991	0.004	0.235
	278.15	6.89	4	0.159	0.996	0.202	0.997	0.004	0.203
	293.15	6.89	5	0.125	0.996	0.176	0.997	0.004	0.177
	313.15	6.89	4	0.129	0.996	0.195	0.997	0.003	0.195
	278.15	10.34	5	0.123	0.995	0.112	0.997	0.004	0.113
	293.15	10.34	4	0.121	0.995	0.175	0.998	0.006	0.176
	313.15	10.34	4	0.110	0.996	0.143	0.997	0.004	0.144
	278.15	13.78	4	0.121	0.995	0.175	0.994	0.004	0.176
	293.15	13.78	5	0.112	0.996	0.172	0.999	0.005	0.173
	313.15	13.78	5	0.142	0.995	0.196	0.995	0.004	0.196

Table 2.8. Results of the PLS model to estimate the concentration of i-butane in synthetic gas mixtures at different temperatures and pressures (spectral region: 1670 – 1800 nm).

Calibration			Prediction						
Components	Temperature (K)	Pressure (MPa)	LV	RMSECV	R ²	RMSEP	R ²	bias	SEP
I-butane	278.15	3.44	4	0.061	0.988	0.130	0.971	0.006	0.131
	293.15	3.44	4	0.072	0.983	0.135	0.969	0.003	0.136
	313.15	3.44	4	0.075	0.982	0.124	0.979	0.005	0.125
	278.15	6.89	4	0.091	0.980	0.083	0.965	0.005	0.084
	293.15	6.89	4	0.091	0.979	0.085	0.971	0.006	0.086
	313.15	6.89	5	0.111	0.982	0.102	0.963	0.007	0.104
	278.15	10.34	4	0.083	0.982	0.065	0.973	0.004	0.066
	293.15	10.34	4	0.104	0.981	0.064	0.969	0.007	0.065
	313.15	10.34	4	0.092	0.981	0.076	0.973	0.008	0.078
	278.15	13.78	5	0.102	0.985	0.095	0.974	0.005	0.096
	293.15	13.78	5	0.072	0.989	0.095	0.968	0.004	0.097
	313.15	13.78	5	0.093	0.981	0.091	0.963	0.007	0.093

Table 2.9. Results of the PLS model to estimate the concentration of n-butane in synthetic gas mixtures at different temperatures and pressures (spectral region: 1670 – 1800 nm).

Calibration			Prediction						
Components	Temperature (K)	Pressure (MPa)	LV	RMSECV	R ²	RMSEP	R ²	bias	SEP
N-butane	278.15	3.44	5	0.08	0.979	0.113	0.977	0.006	0.114
	293.15	3.44	5	0.07	0.982	0.102	0.979	0.007	0.104
	313.15	3.44	5	0.07	0.981	0.125	0.961	0.005	0.962
	278.15	6.89	6	0.07	0.984	0.079	0.973	0.006	0.080
	293.15	6.89	5	0.07	0.985	0.107	0.981	0.006	0.108
	313.15	6.89	5	0.07	0.985	0.085	0.967	0.005	0.086
	278.15	10.34	5	0.06	0.989	0.066	0.981	0.006	0.667
	293.15	10.34	5	0.07	0.985	0.112	0.978	0.004	0.112
	313.15	10.34	5	0.07	0.984	0.067	0.979	0.008	0.068
	278.15	13.78	5	0.09	0.982	0.092	0.981	0.005	0.093
	293.15	13.78	5	0.07	0.983	0.085	0.985	0.005	0.086
	313.15	13.78	6	0.08	0.983	0.090	0.981	0.004	0.091

One can see from above results that all the PLS developed models are performed well in predicting samples that are not included in the calibration samples. The procedure explained in section 2.6 was followed to estimate the LoD. The LoD value reported in Table 2.10 for each component is the average of calculated LoD values for all the developed PLS models at different T&P conditions.

Table 2.10 Calculated LoD for developed PLS models for each component (mol %)

Composition	LoD
Methane	0.85
Ethane	0.38
Propane	0.32
I-butane	0.13
N-butane	0.16

One tailed t-test was also carried out for all the components using Equation 2.37 for prediction samples to test the significance of bias that included in the final model. It was noticed that the relevant bias does not produce significant systematic errors since the $t_{\text{calculated}}$ for all the components was less than $t_{\text{critical}} = 1.725$ at a level of 95% confidence [75]. All of the models developed in this study had RPD value higher than 2.80, indicating created models can be trusted for monitoring the composition of main hydrocarbons in gas samples. The RPD values ranged from 20.85 to 24.59, 13.07 to 16.56, 11.24 to 14.96, 2.78 to 4.37 and 3.27 to 4.83 for methane, ethane, propane, i-butane and n-butane models respectively at different T&P conditions.

The results show that the restricted wavelength region from 1670 to 1800 nm can be used to develop accurate calibration models with high accuracy to predict the concentration of interested hydrocarbon components in synthetic gas mixtures. It is not required to use the full spectral range as the whole spectra contain some variables that provide unrelated information that weaken the performance of developed PLS models. Therefore, a cheaper NIR spectrometer with a reduced wavelength region between 1670 to 1800 nm with same resolution can be used to quantify the concentration of interested hydrocarbon components in gas samples.

2.8.5 ANN Results

In this section, the ability of ANN was investigated to measure the concentration of hydrocarbon components (methane through pentanes) in natural gas. ANN is one of the most important nonlinear calibration methods that can be employed when the relationship between independent data and variables are nonlinear. The important steps in developing a nonlinear ANN model is to select the appropriate training algorithm, the appropriate transfer function for hidden and output layers and finally find an optimal number of neurones in hidden layer and output layer. The ANN can be express mathematically as:

$$O_i = f \left[\sum_{n=1}^N w_n g \left(\sum_{j=1}^J w_{nj} x_{ij} + b_n \right) + b \right] \quad \text{Equation 2.38.}$$

In which N denotes the number of neurons in hidden layer that can be selected by user, w_{nj} represents the weights in the hidden layer, b_n are the biases in the hidden layer, x_{ij} are the variables (dependent data), f and g are the transfer functions used for hidden and output layers respectively and finally b is the bias in the output layer. Firstly, initial values

are created for weight and bias randomly, and backpropagation algorithm is used to update the weights and biases until the output is as close as possible to target value. The sum of square errors used as a criterion for adjustments of weights and biases. In this study, the hyperbolic tangent sigmoid transfer function was employed for the hidden layer for this aim all the input data were normalised in the range between -1 to +1 to fit the range of hyperbolic tangent function:

$$f(x) = \frac{2}{1 + e^{-2x}} - 1 \quad \text{Equation 2.39.}$$

In this work, firstly, the performance of two training algorithms, Bayesian regularization (BRANN) and Levenberg–Marquardt (LMANN), were investigated. The Bayesian regularization training algorithm shows slightly better performance compare to the Levenberg–Marquardt training algorithm (lower RMSEC and RMSEP values). LMANN is the commonly used training algorithm to model the NIR dataset, LMANN optimises the connected weight from input to hidden layer neurons and hidden layer neurons to output neurons, by minimising the error of output.

$$\delta = (J^T J + \lambda I)^{-1} \times J^T \times E \quad \text{Equation 2.40.}$$

$$\delta = w_{new} - w_{old} \quad \text{Equation 2.41.}$$

In which J is the Jacobian matrix of the first derivative of global errors in network with respect to the weights and bias, E stands for error of the network, λ is adjustment factor, E is error vector (difference between predicted value and set value of each vector), and δ is the weigh update vector. The disadvantage of this method is that it has the risk of overfitting particularly when we have small training dataset that results in poor performance of test cases. One of the alternative way to solve overfitting in data is using of Bayesian regularization in combination with Levenberg–Marquardt training algorithm (BRANN). BRANN considers all possible values of weights of a neural network weighted by the probability of each set of weights.

$$F = \beta E_d + \alpha E_w \quad \text{Equation 2.42.}$$

Where E_d is the sum of squared errors, and E_w is the sum of squared weights. α and β are the parameters that need to be optimised. Bayesian regularization minimises the combination of squared weights and errors in order to generate an ANN model to perform well. In this method not only the global error of the network is taken into consideration, but the value of each weight in the network also is taken into account. The details about the LMANN and BANN training algorithms can be found in other studies [80].

The ANN model was tested as nonlinear with a different number of neurons (1 to 10) for the hidden layer. The best results were obtained when the number of neurons in the hidden layer is set to five. The optimum number of hidden neurons is found out by trial-and-error approach. Different number of layers were tested to see which one works best. The schematic of the ANN model for all studied hydrocarbon components at different pressure and temperature conditions are illustrated in Figure 2.25.

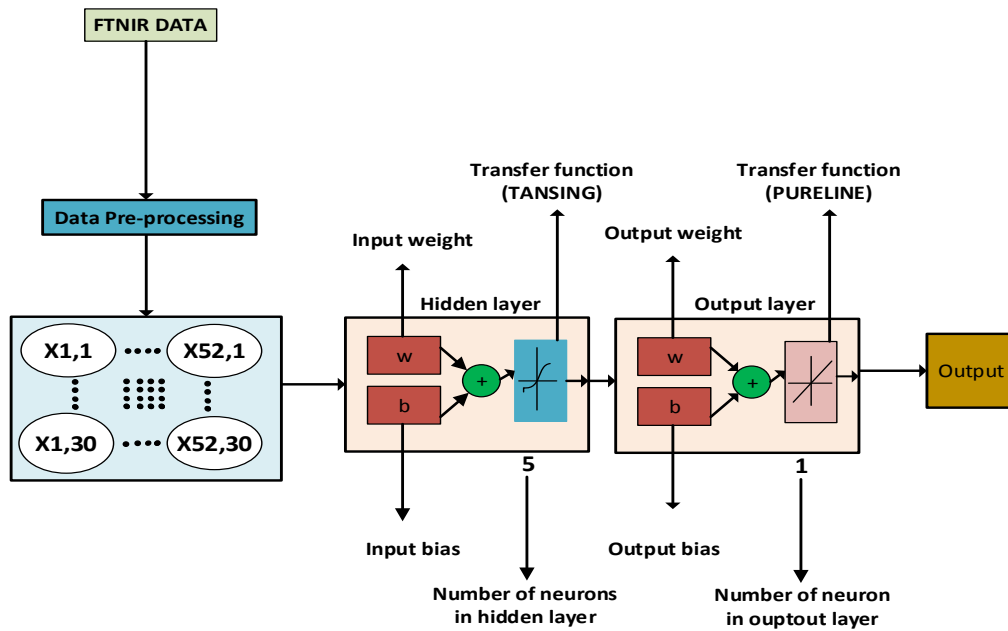


Figure 2.25. Schematic of the developed ANN models for all the hydrocarbon components at various pressures and temperatures.

Following the same procedure explained before, all the data were pre-treated using different pre-processing methods, and the pre-processed data were fed as inputs to ANN. Same as PLS, for each component, at each calibrated pressure and temperature condition, one separate model was developed. The model with lowest RMSEP value was selected

as a best model for each component at different temperature and pressures conditions. Again the best results were obtained when SG1 + OSC was applied to the given dataset at various pressure and temperatures. This section considers the results of ANN models using SG1+ OSC pre-processing method. Same calibration dataset and validation data set were used to construct the ANN calibration models and to evaluate the performance of developed models respectively. RMSEP was calculated for each component at different pressure and temperature conditions to assess the ability of developed models. The performance of each ANN model at different conditions is plotted graphically through plots of FTNIR-predicted data derived from the ANN models versus the actual value in following.

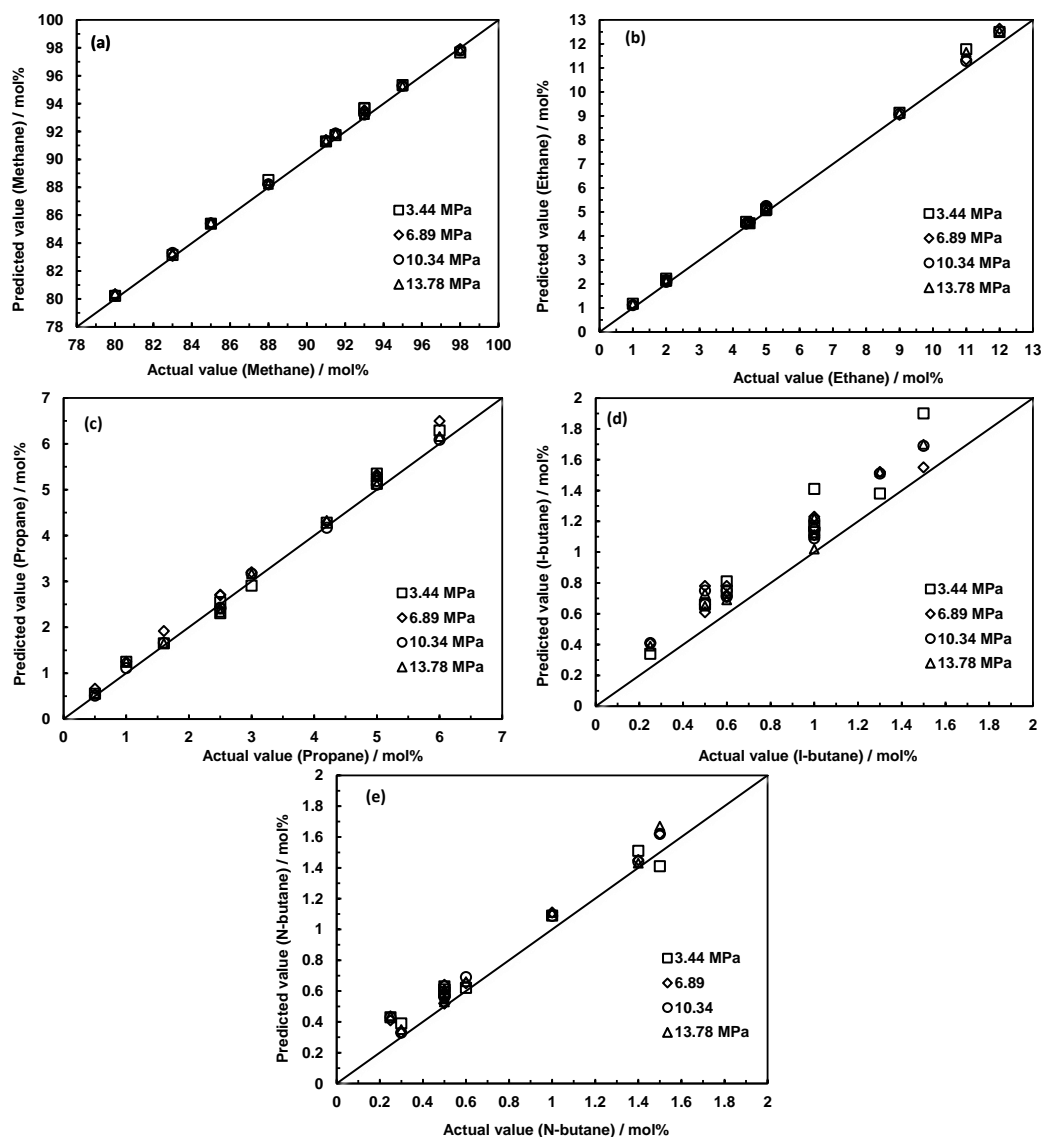


Figure 2.26. ANN regression plot of predicted versus actual concentration of methane (a), ethane (b), propane (c), i-butane (d) and n-butane (e) in synthetic gas mixtures (independent samples) at temperature of 278.15 K and various pressures.

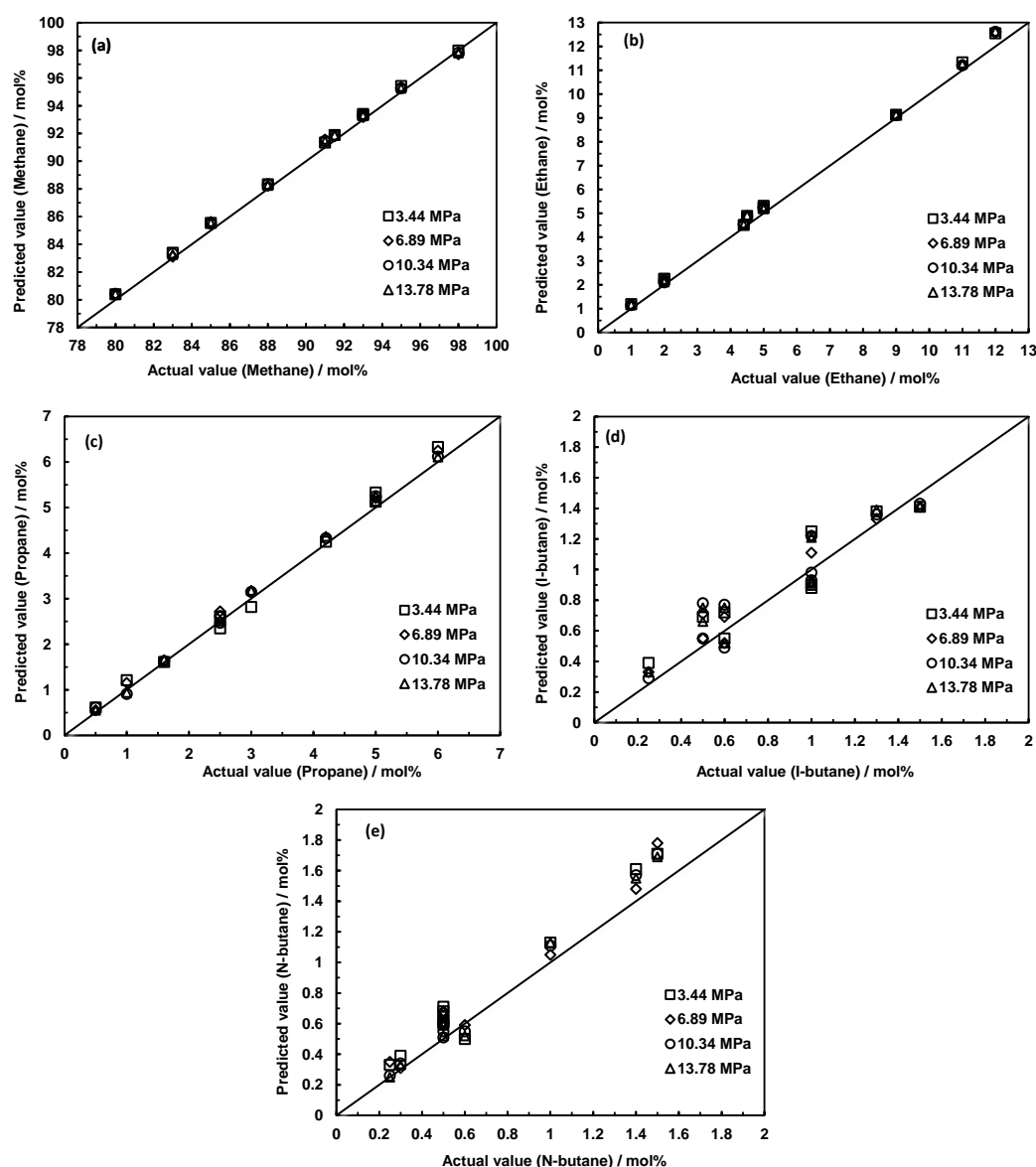


Figure 2.27. ANN regression plot of predicted versus actual concentration of methane (a), ethane (b), propane (c), i-butane (d) and n-butane (e) in synthetic gas mixtures (independent samples) at temperature of 293.15 K and various pressures.

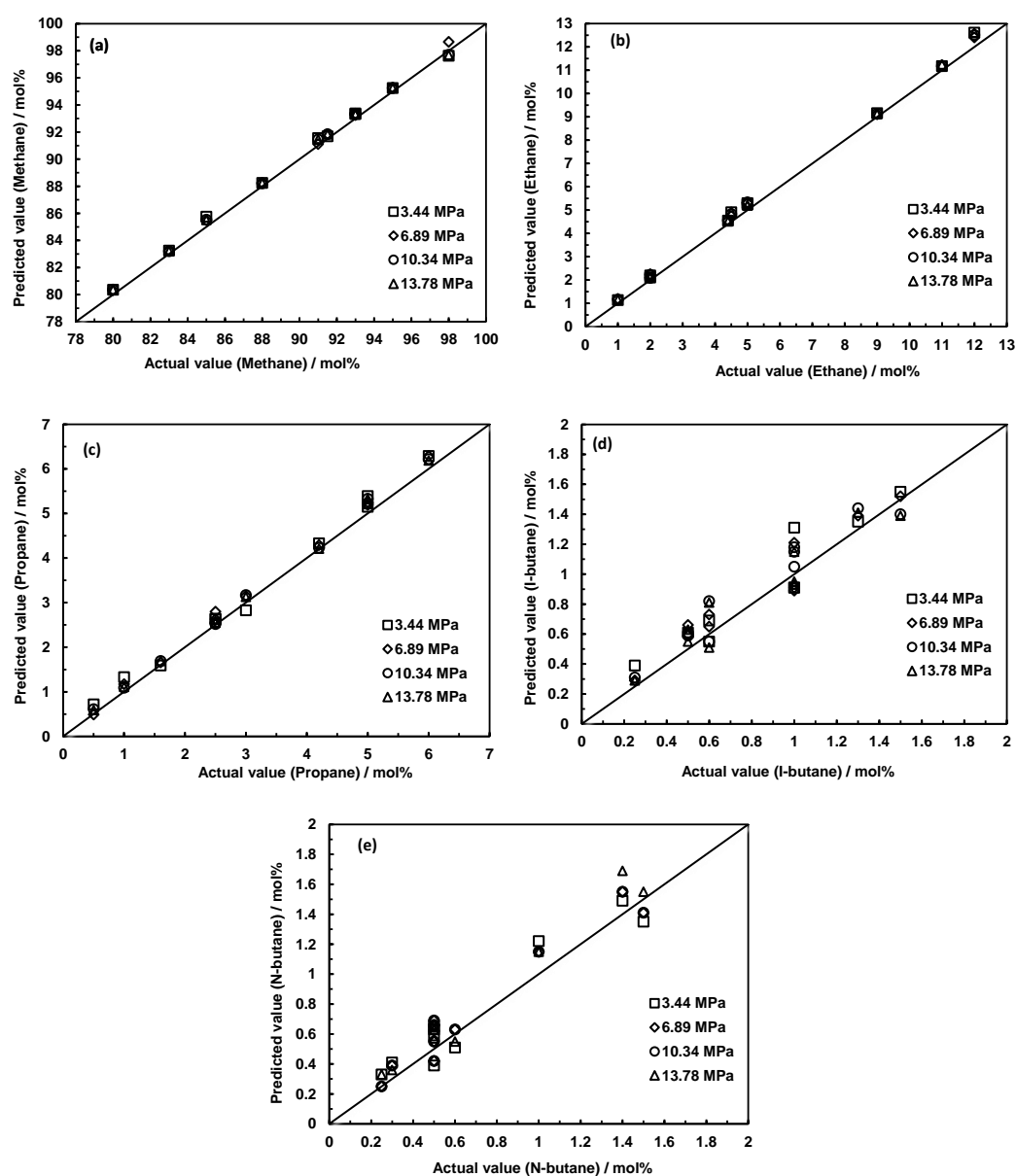


Figure 2.28. ANN regression plot of predicted versus actual concentration of methane (a), ethane (b), propane (c), i-butane (d) and n-butane (e) in synthetic gas mixtures (independent samples) at temperature of 313.15 K and various pressures .

Table 2.11. Results of the ANN model to estimate the concentration of methane in synthetic gas mixtures at different temperatures and pressures (spectral region: 1670 – 1800 nm).

Calibration			Prediction					
Components	Temperature (K)	Pressure (MPa)	RMSEC	R ²	RMSEP	R ²	bias	SEP
Methane	278.15	3.44	0.291	0.998	0.413	0.991	0.009	0.415
	293.15	3.44	0.282	0.997	0.394	0.994	0.008	0.396
	313.15	3.44	0.311	0.998	0.383	0.994	0.010	0.386
	278.15	6.89	0.231	0.997	0.333	0.991	0.009	0.336
	293.15	6.89	0.257	0.996	0.355	0.993	0.008	0.357
	313.15	6.89	0.221	0.996	0.313	0.998	0.008	0.315
	278.15	10.34	0.241	0.997	0.292	0.995	0.008	0.294
	293.15	10.34	0.235	0.997	0.305	0.993	0.009	0.308
	313.15	10.34	0.277	0.998	0.275	0.994	0.008	0.278
	278.15	13.78	0.244	0.998	0.299	0.999	0.007	0.301
	293.15	13.78	0.233	0.998	0.283	0.992	0.008	0.285
	313.15	13.78	0.262	0.998	0.262	0.998	0.008	0.264

Table 2.12. Results of the ANN model to estimate the concentration of ethane in synthetic gas mixtures at different temperatures and pressures (spectral region: 1670 – 1800 nm).

Calibration			Prediction					
Components	Temperature (K)	Pressure (MPa)	RMSEC	R ²	RMSEP	R ²	bias	SEP
Ethane	278.15	3.44	0.239	0.997	0.242	0.990	0.008	0.245
	293.15	3.44	0.228	0.995	0.253	0.991	0.008	0.255
	313.15	3.44	0.241	0.995	0.272	0.989	0.007	0.273
	278.15	6.89	0.212	0.997	0.192	0.989	0.010	0.195
	293.15	6.89	0.225	0.993	0.215	0.991	0.010	0.219
	313.15	6.89	0.193	0.996	0.236	0.995	0.009	0.238
	278.15	10.34	0.195	0.996	0.227	0.995	0.012	0.230
	293.15	10.34	0.187	0.996	0.202	0.992	0.011	0.205
	313.15	10.34	0.201	0.995	0.192	0.991	0.015	0.194
	278.15	13.78	0.221	0.996	0.222	0.993	0.009	0.225
	293.15	13.78	0.185	0.996	0.205	0.994	0.011	0.208
	313.15	13.78	0.216	0.996	0.221	0.996	0.012	0.223

Table 2.13. Results of the ANN model to estimate the concentration of propane in synthetic gas mixtures at different temperatures and pressures (spectral region: 1670 – 1800 nm).

Calibration			Prediction					
Components	Temperature (K)	Pressure (MPa)	RMSEC	R ²	RMSEP	R ²	bias	SEP
Propane	278.15	3.44	0.20	0.999	0.265	0.991	0.009	0.267
	293.15	3.44	0.20	0.991	0.267	0.989	0.007	0.269
	313.15	3.44	0.19	0.992	0.254	0.990	0.007	0.255
	278.15	6.89	0.17	0.993	0.213	0.990	0.009	0.215
	293.15	6.89	0.18	0.994	0.225	0.993	0.009	0.228
	313.15	6.89	0.21	0.994	0.212	0.992	0.008	0.215
	278.15	10.34	0.19	0.994	0.221	0.997	0.008	0.223
	293.15	10.34	0.20	0.994	0.222	0.993	0.010	0.225
	313.15	10.34	0.19	0.993	0.205	0.992	0.011	0.207
	278.15	13.78	0.22	0.994	0.191	0.992	0.008	0.194
	293.15	13.78	0.18	0.991	0.213	0.991	0.008	0.214
	313.15	13.78	0.19	0.996	0.221	0.990	0.007	0.222

Table 2.14. Results of the ANN model to estimate the concentration of i-butane in synthetic gas mixtures at different temperatures and pressures (spectral region: 1670 – 1800 nm).

Components	Calibration		Prediction					
	Temperature (K)	Pressure (MPa)	RMSEC	R ²	RMSEP	R ²	bias	SEP
I-butane	278.15	3.44	0.137	0.988	0.181	0.963	0.006	0.182
	293.15	3.44	0.141	0.983	0.179	0.963	0.005	0.180
	313.15	3.44	0.142	0.982	0.165	0.962	0.007	0.167
	278.15	6.89	0.123	0.980	0.151	0.959	0.009	0.154
	293.15	6.89	0.118	0.979	0.142	0.959	0.007	0.144
	313.15	6.89	0.117	0.982	0.153	0.962	0.006	0.155
	278.15	10.34	0.101	0.982	0.145	0.957	0.006	0.147
	293.15	10.34	0.111	0.981	0.146	0.963	0.005	0.148
	313.15	10.34	0.122	0.981	0.151	0.966	0.006	0.153
	278.15	13.78	0.131	0.985	0.161	0.961	0.007	0.164
	293.15	13.78	0.129	0.989	0.159	0.969	0.007	0.161
	313.15	13.78	0.131	0.981	0.139	0.964	0.009	0.142

Table 2.15. Results of the ANN model to estimate the concentration of n-butane in synthetic gas mixtures at different temperatures and pressures (spectral region: 1670 – 1800 nm).

Components	Calibration		Prediction					
	Temperature (K)	Pressure (MPa)	RMSEC	R ²	RMSEP	R ²	bias	SEP
N-butane	278.15	3.44	0.128	0.981	0.149	0.963	0.005	0.151
	293.15	3.44	0.131	0.985	0.161	0.963	0.005	0.163
	313.15	3.44	0.132	0.979	0.151	0.962	0.005	0.152
	278.15	6.89	0.135	0.982	0.123	0.959	0.005	0.124
	293.15	6.89	0.140	0.986	0.115	0.959	0.006	0.117
	313.15	6.89	0.119	0.979	0.131	0.962	0.004	0.132
	278.15	10.34	0.091	0.981	0.125	0.957	0.005	0.126
	293.15	10.34	0.111	0.975	0.150	0.963	0.006	0.151
	313.15	10.34	0.103	0.980	0.171	0.966	0.006	0.172
	278.15	13.78	0.102	0.981	0.121	0.961	0.006	0.123
	293.15	13.78	0.091	0.983	0.134	0.969	0.005	0.135
	313.15	13.78	0.112	0.984	0.182	0.964	0.005	0.184

The performance of all ANN models was evaluated using the coefficient of determination (R^2) and RMSEC, RMSEP and SEP. It should be noted that the same procedure like PLS was followed to find the appropriate wavelength subset. The whole spectral region and different wavelength subset were tested and same as the PLS models, according to calculated RMSEC, RMSEP and SEP values, the best results were obtained while the range between 1670 to 1800 nm was selected. When the spectral range between 1670 to 1800 nm were used to develop the calibration models, the RMSEP for methane, ethane, propane, i-butane and n-butane varied from 0.26 to 0.41, 0.19 to 0.25, 0.19 to 0.26, 0.13 to 0.18, and 0.11 to 0.18 mol%, respectively. Furthermore, high correlation coefficients were obtained for all the models, demonstrating that the developed models are performing well. The same prediction dataset that was used to evaluate the performance of the PLS

models were employed to assess the performance of created ANN models. For created ANN models like PLS, a one paired t-test was carried out to see whether the bias included in each ANN model is significant or not. The calculations were shown that $t_{\text{calculated}} > t_{\text{critical}}$ for all the developed models, indicating the bias included in each ANN model was not significant. For models developed using ANN approach, high RPD values ($\text{RPD} > 2.5$) were gained, indicating the high power of developed ANN models for monitoring the concentration of major hydrocarbons in the gas phase.

2.8.6 PLS vs. ANN

A comparison was made between all the models that developed using PLS and ANN approaches at different pressures and temperatures. Figure 2.29, Figure 2.30 and Figure 2.31 summarise the results obtained by these methods.

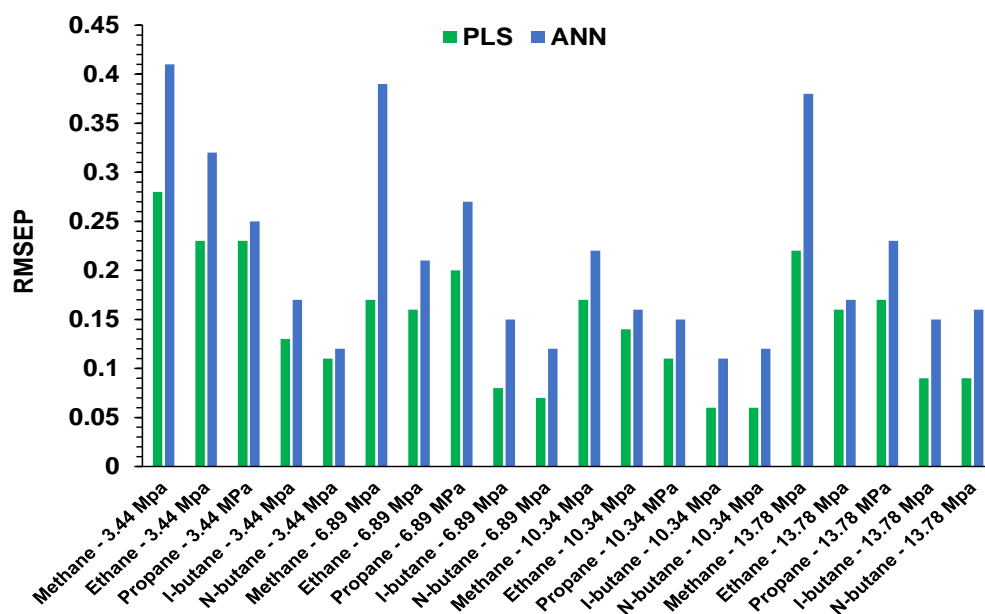


Figure 2.29. The comparison of developed PLS and ANN models at various pressures and temperature of 278.15 K.

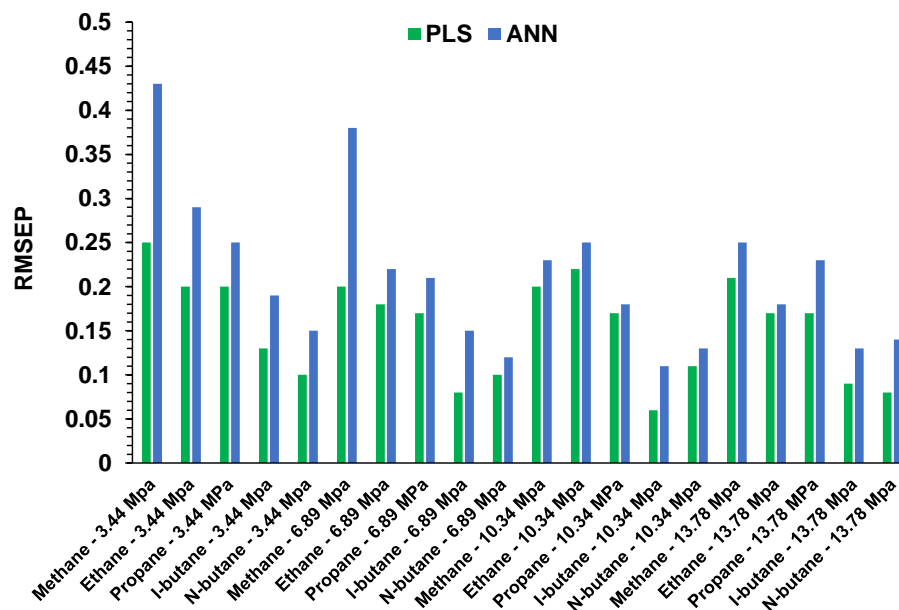


Figure 2.30. The comparison of developed PLS and ANN models at various pressures and temperature of 293.15 K.

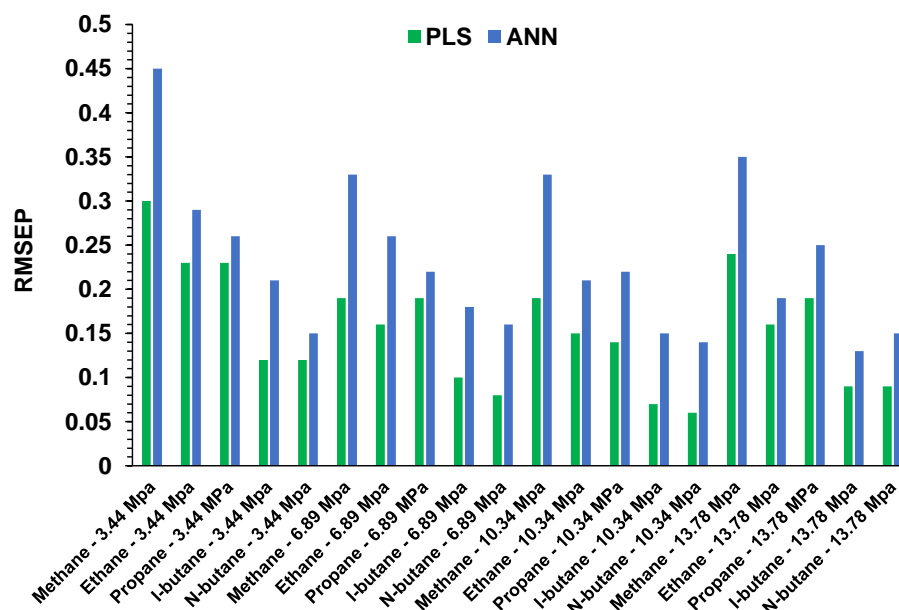


Figure 2.31. The comparison of developed PLS and ANN models at various pressures and temperature of 313.15 K.

The prediction ability of the external validation was assessed by RMSEP for all the developed models. As mentioned earlier same prediction sets were employed to evaluate the accuracy of created models. These figures highlight the superiority of the PLS

approach to ANN (lower RMSEP values found for PLS). All these results confirmed that all created PLS models pre-treated by the SG1-OSC algorithm produced the best results for all the studied components at various pressures and temperatures. It is noteworthy to mention that the ANN method was so complex and time consuming and it is required to vary a lot of model parameters in the optimisation process (i.e., number on hidden layers, transfer function, training algorithm)[81]. Therefore, the calibration and optimisation took a very long time. However, a PLS model requires less time to develop than an ANN model. A comparison of nonlinear methods on NIR spectroscopy data was examined by Balabin et al.[81], the result indicated that ANN approach is superior to a PLS (linear-PLS) method in accuracy and was suggested for practical applications. Although PLS plays a key role in NIR data mining, the main drawback this method is that only linear information can be extracted from the data [82]. However, in this work, results showed that PLS is superior to ANN approach. Generally, both methods provide low RMSEP values (see Figure 2.31), showing the consistency of both methods for measuring the concentration of hydrocarbons in the gas phase. Regarding ANN, it seems it is required to perform large number of individual test for each components to find the best solution and to reach to results as good as PLS in terms of RMSEP value.

2.8.7 Comparison of the gas compositions measured by GC and the FTNIR method

The prediction capability of the developed PLS models and ANN models at 293.15 K and various pressures were examined for two unknown natural gas mixtures that contain hydrocarbon components, carbon dioxide, and nitrogen against the gas chromatography as a conventional and reliable method for monitoring the concentration of hydrocarbons in gas mixtures. A Flame Ionisation Detector (FID) was used to detect the concentration of hydrocarbons in the gas samples, and the Thermal Conductivity Detector (TCD) was employed to detect the content of nitrogen and carbon dioxide. It is well-known that nitrogen as well as oxygen is not NIR active and does not absorb the emitted light. Moreover, carbon dioxide absorbs the NIR light at another region different from the region where used to construct the calibration models. Figure 2.32 illustrates carbon dioxide, methane, and nitrogen absorption spectra in the range between 1600 to 2100 nm that obtained by the FTNIR spectrometer at room temperature and 3.44 MPa.

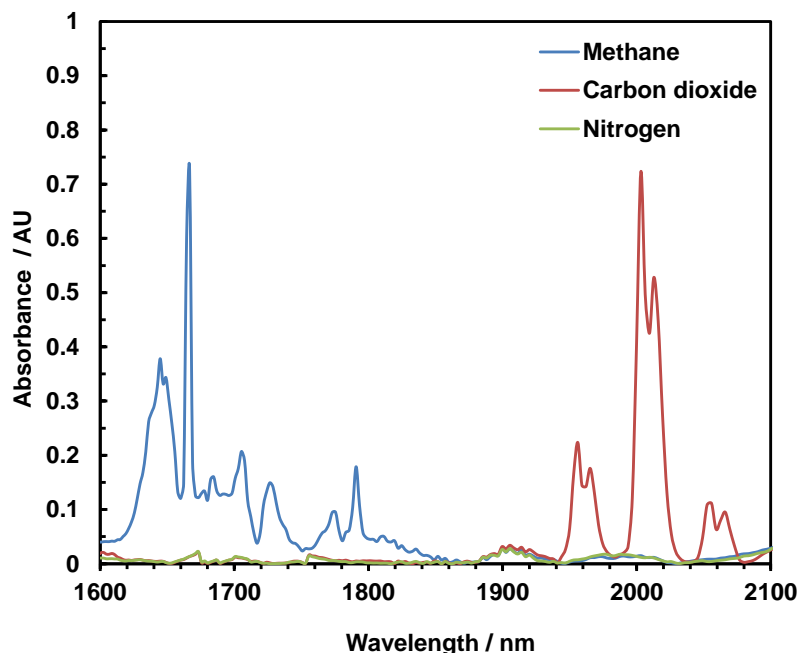


Figure 2.32. FTNIR spectra of pure carbon dioxide methane and nitrogen at a pressure of 3.44 MPa and room temperature from FTNIR spectrometer.

It is clear that carbon dioxide and methane (representative of hydrocarbons) absorb the NIR lights at two separate regions, and there is no interference between absorption spectra of hydrocarbons and carbon dioxide. It is expected that existence of these components in the sample do not affect the accuracy of the results. The objectives of these tests were to compare the NIR-measured values with those of GC analysis and to investigate the influence of the presence of nitrogen, CO₂, and other heavier hydrocarbons such as pentanes in the natural gas to confirm the accuracy and reliability of the developed PLS and ANN models. The spectra were recorded at 293.15 K and four different pressures. Then, the withdrawn samples were injected into the GC by means of the gas syringes with the volume of 500 μ l. Measurement time for GC and FTNIR analysis were about 15 minutes and 90 seconds, respectively. For both methods, the average value of three measurements was used as the final value. The results are summarised in Table 2.16 through Table 2.19. It should be noted that the measured values obtained by GC for nitrogen and carbon dioxide was removed from the results and the rest of the measured values by GC (i.e., measured hydrocarbon concentrations) were normalised to 100 mol%. Moreover, the uncertainty for all the measured components using the NIR analyser at various pressures and the GC at atmospheric pressure are calculated and reported in aforementioned tables.

Table 2.16. Comparison of the NIR results using developed PLS models at 293.15K and various pressures with GC for natural gas sample 1, average of three measurements, in mol%.

Components	GC	GC (normalized)	FTNIR 3.44 MPa	FTNIR 6.89 MPa	FTNIR 10.34 MPa	FTNIR 13.78 MPa
Methane	90.29	92.46 (± 0.11)	92.12 (± 0.12)	91.98 (± 0.11)	91.97 (± 0.10)	91.95 (± 0.11)
Ethane	5.48	5.61 (± 0.08)	5.73 (± 0.09)	5.78 (± 0.08)	5.79 (± 0.09)	5.74 (± 0.08)
Propane	1.35	1.38 (± 0.01)	1.47 (± 0.03)	1.48 (± 0.03)	1.45 (± 0.02)	1.51 (± 0.02)
I-butane	0.20	0.21 (± 0.006)	0.31 (± 0.03)	0.35 (± 0.01)	0.37 (± 0.02)	0.40 (± 0.01)
N-butane	0.25	0.26 (± 0.008)	0.37 (± 0.02)	0.41 (± 0.01)	0.42 (± 0.01)	0.40 (± 0.01)
I-pentane	0.05	0.05 (± 0.004)	N/A	N/A	N/A	N/A
N-pentane	0.03	0.04 (± 0.005)	N/A	N/A	N/A	N/A
Carbon dioxide	1.02	0.00	N/A	N/A	N/A	N/A
Nitrogen	1.32	0.00	N/A	N/A	N/A	N/A

Table 2.17. Comparison of the NIR results using developed ANN models at 293.15 K and various pressures with GC for natural gas sample 1, average of three measurements, in mol%.

Components	GC	GC (normalized)	FTNIR 3.44 MPa	FTNIR 6.89 MPa	FTNIR 10.34 MPa	FTNIR 13.78 MPa
Methane	90.29	92.46 (± 0.11)	91.83 (± 0.14)	91.85 (± 0.13)	91.89 (± 0.12)	91.90 (± 0.14)
Ethane	5.48	5.61 (± 0.08)	5.79 (± 0.11)	5.83 (± 0.12)	5.84 (± 0.11)	5.82 (± 0.11)
Propane	1.35	1.38 (± 0.01)	1.60 (± 0.05)	1.56 (± 0.06)	1.53 (± 0.05)	1.54 (± 0.05)
I-butane	0.20	0.21 (± 0.006)	0.38 (± 0.04)	0.38 (± 0.03)	0.33 (± 0.05)	0.39 (± 0.07)
N-butane	0.25	0.26 (± 0.008)	0.40 (± 0.04)	0.38 (± 0.03)	0.41 (± 0.05)	0.35 (± 0.06)
I-pentane	0.05	0.05 (± 0.004)	N/A	N/A	N/A	N/A
N-pentane	0.03	0.04 (± 0.005)	N/A	N/A	N/A	N/A
Carbon dioxide	1.02	0.00	N/A	N/A	N/A	N/A
Nitrogen	1.32	0.00	N/A	N/A	N/A	N/A

Table 2.18. Comparison of the NIR results using developed PLS models at 293.15 K and various pressures with GC for natural gas sample 2, average of three measurements, in mol%.

Components	GC	GC (normalized)	FTNIR 3.44 MPa	FTNIR 6.89 MPa	FTNIR 10.34 MPa	FTNIR 13.78 MPa
Methane	88.11	91.27 (± 0.11)	91.13 (± 0.13)	91.21 (± 0.10)	91.19 (± 0.11)	91.19 (± 0.11)
Ethane	5.91	6.12 (± 0.07)	6.05 (± 0.10)	6.09 (± 0.07)	6.11 (± 0.09)	6.12 (± 0.09)
Propane	1.92	1.99 (± 0.02)	2.05 (± 0.03)	1.95 (± 0.03)	1.97 (± 0.03)	1.96 (± 0.02)
I-butane	0.35	0.36 (± 0.005)	0.42 (± 0.03)	0.43 (± 0.02)	0.42 (± 0.02)	0.40 (± 0.02)
N-butane	0.25	0.26 (± 0.004)	0.35 (± 0.03)	0.32 (± 0.02)	0.31 (± 0.02)	0.33 (± 0.02)
Carbon dioxide	1.37	0.00	N/A	N/A	N/A	N/A
Nitrogen	2.09	0.00	N/A	N/A	N/A	N/A

Table 2.19. Comparison of the NIR results using developed ANN models at 293.15K and various pressures with GC for natural gas sample 2, average of three measurements.

Components	GC	GC (normalized)	FTNIR 3.44 MPa	FTNIR 6.89 MPa	FTNIR 10.34 MPa	FTNIR 13.78 MPa
Methane	88.11	91.27 (± 0.11)	91.41 (± 0.13)	91.33 (± 0.11)	91.35 (± 0.13)	91.33 (± 0.12)
Ethane	5.91	6.12 (± 0.07)	5.92 (± 0.12)	5.97 (± 0.11)	5.94 (± 0.12)	5.94 (± 0.10)
Propane	1.92	1.99 (± 0.02)	1.88 (± 0.04)	1.92 (± 0.4)	1.90 (± 0.06)	1.93 (± 0.06)
I-butane	0.35	0.36 (± 0.005)	0.44 (± 0.04)	0.43 (± 0.04)	0.46 (± 0.03)	0.44 (± 0.05)
N-butane	0.25	0.26 (± 0.004)	0.35 (± 0.05)	0.35 (± 0.04)	0.35 (± 0.04)	0.36 (± 0.05)
Carbon dioxide	1.37	0.00	N/A	N/A	N/A	N/A
Nitrogen	2.09	0.00	N/A	N/A	N/A	N/A

It can be seen that there is a good agreement between the predicted and measured values of hydrocarbons using NIR at all considered pressures and GC for the same components respectively. As it expected, the presence of nitrogen, carbon dioxide and very low concentration of pentanes in the natural gas does not affect the accuracy of the chemometric models. The difference between NIR and GC measurements can be defined by the accuracy of their measurements. These results suggest us that this method is insensitive to the components that are NIR inactive and also the components that do not contain carbon-hydrogen molecular bonds in their structures. These results confirmed that created PLS models are more accurate than developed ANN models. Hence, PLS models that are satisfying all the criteria were selected as a final model for future measurements. Figure 2.33 to Figure 2.37 illustrate the PLS models absolute residual distribution for all independent samples (unknown samples). More than 100 different independent samples were analysed by the developed FTNIR analyser at different pressure and temperature

conditions, and at the same time, all the composition of these samples were measured by means of GC (reference value) in order to evaluate the accuracy of NIR analyser. Part of these samples was prepared in the laboratory to evaluate the ability and accuracy of developed models and the rest are those that were analysed by the NIR analyser during to detect formation of gas hydrate based on the compositional change technique (See Chapter 3). All these data were gathered and presented graphically in following. It is obvious that the PLS model provides a good fit throughout the analytical ranges with a constant variance of the absolute residual values and low residues for all samples which were analysed.

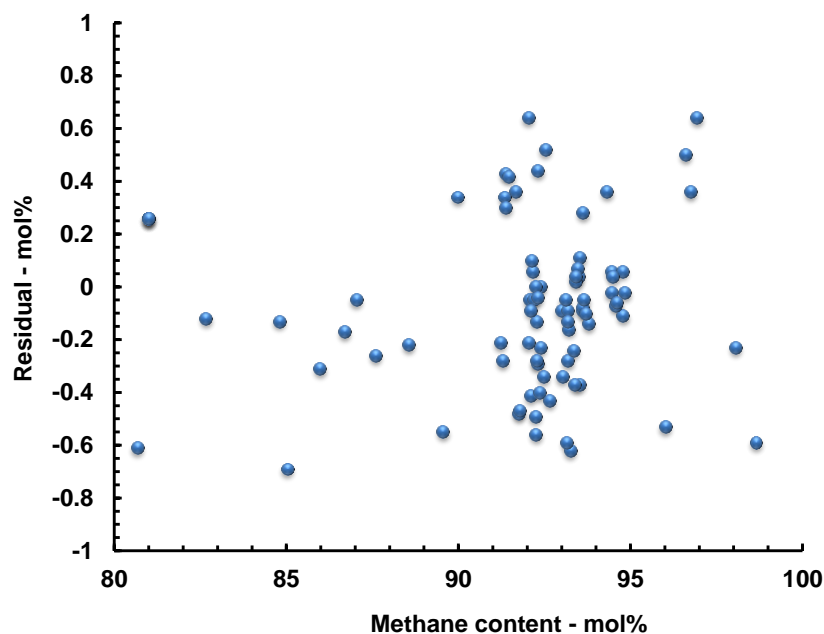


Figure 2.33. Absolute residual (Difference between GC and FTNIR measured values) distribution for methane.

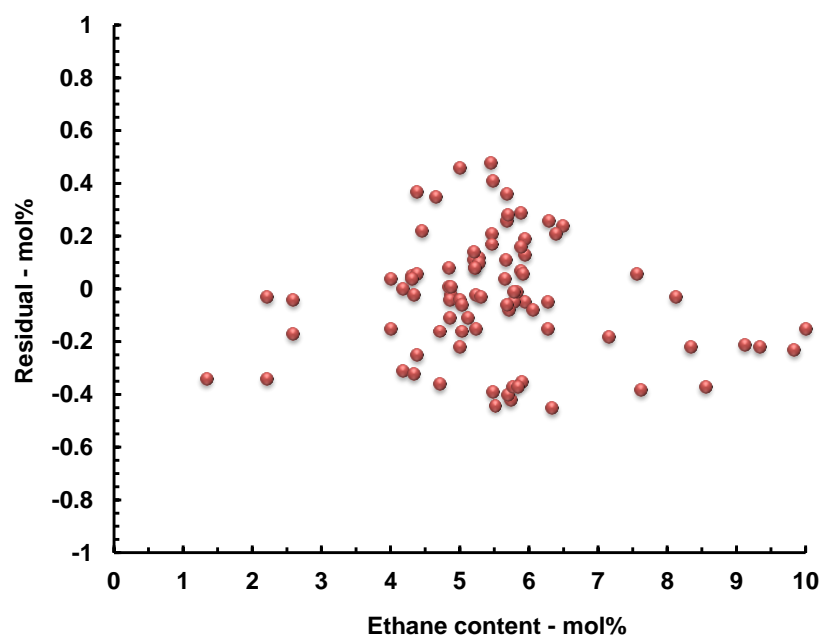


Figure 2.34. Absolute residual (Difference between GC and FTNIR measured values) distribution for ethane.

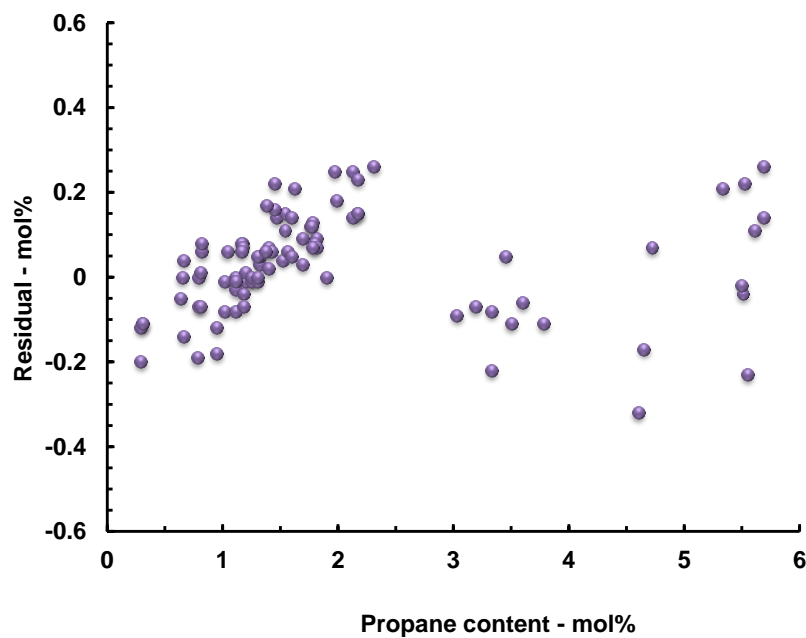


Figure 2.35. Absolute residual (Difference between GC and FTNIR measured values) distribution for propane.

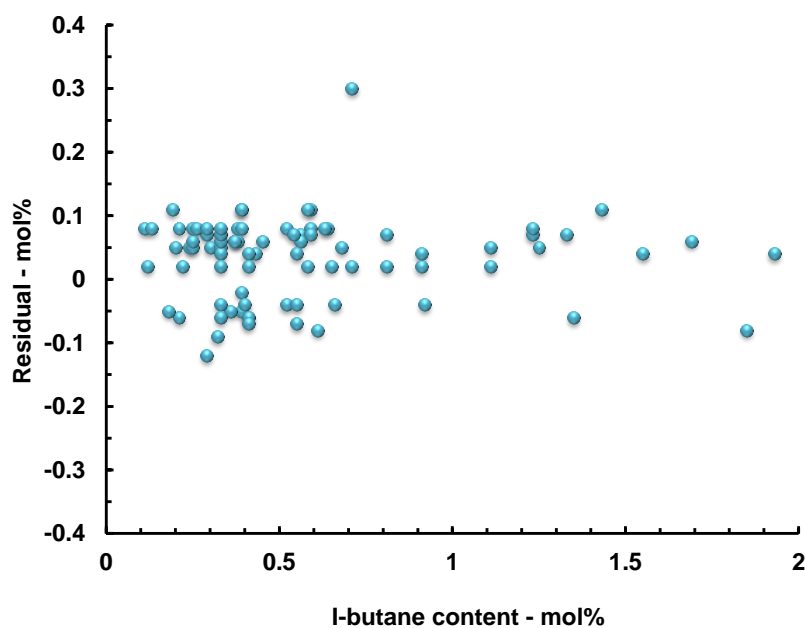


Figure 2.36. Absolute residual (Difference between GC and FTNIR measured values) distribution for i-butane.

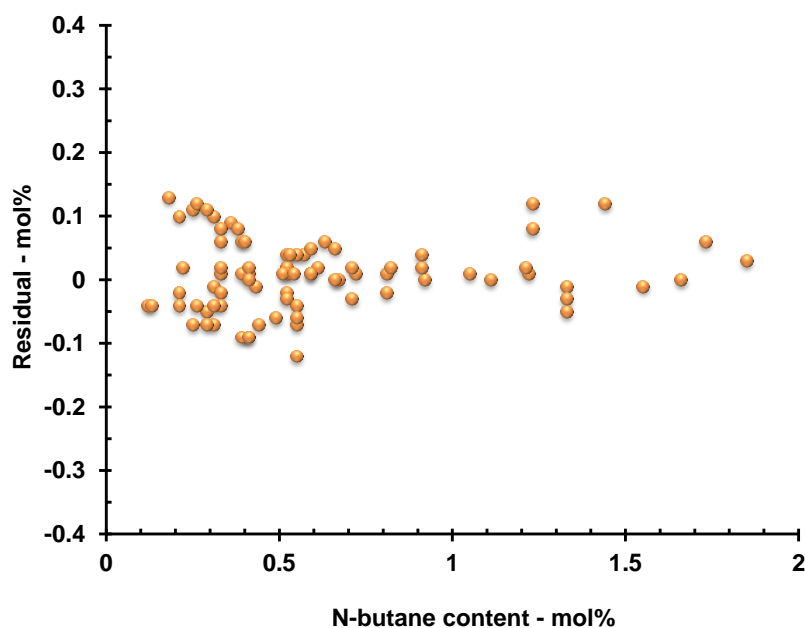


Figure 2.37. Absolute residual (Difference between GC and FTNIR measured values) distribution for n-butane.

Table 2.20. Summary of FTNIR analyser testing.

Component	Average Error	Maximum Error	RMSEP	R ²
Methane (80 - 100 mol %)	0.25	0.69	0.28	0.991
Ethane (0 - 12 mol %)	0.17	0.43	0.16	0.983
Propane (0 - 6 mol %)	0.09	0.32	0.13	0.976
I-butane (0 - 2 mol %)	0.06	0.30	0.10	0.973
N-butane (0 - 2 mol %)	0.04	0.13	0.10	0.969

2.8.8 Temperature and pressure sensitivity analysis for a specific PLS regression model

As mentioned in above, PLS approach showed better performance compare to ANN. In this section, the effect of a shift in pressure and temperature was examined for a specific PLS regression model. A series of experiments were conducted to characterise the sensitivity of the constructed PLS regression model at a pressure of 6.89 MPa and temperature of 293.15 K. To investigate the effect of pressure shift, firstly one synthetic gas sample containing methane, ethane, propane, i-butane and n-butane was introduced into the FTNIR cell, and the pressure and temperature of the cell were then set at 6.89 MPa and 293.15 K, respectively. The components concentration for each component was predicted using the developed PLS models, and the average of predicted values for three measurements for all the five components was utilised as the reference value. Then, the pressure of the gas sample in the cell was varied from 6.89 MPa to 7.58 MPa and from 6.89 to 6.20 MPa with a particular interval at the fixed temperature.

The components concentration of the sample was predicted using acquired spectra by using the developed PLS model at 293.15 K and pressure of 6.89 MPa and were subtracted from the reference values and then divided by the reference value to calculate the relative deviation. The results are presented Figure 2.38 through Figure 2.42. These results specified that the variation of the pressure affects the performance of the PLS model at the calibrated pressure. As shown, a negative systematic error was observed for propane, ethane, and n-butane while the pressure for the validation set was lower than the pressure of the calibration set whereas, a positive systemic error was found for i-butane and methane at pressures lower than calibration set. A contrariwise trend was observed for all the components while the measurement pressure was higher than the pressure of the calibration set. It is worthy to notice that our findings indicate that the error of PLS

models to predict the concentration of individual components is negligible when the shift is less than 0.14 MPa in the measurement pressure, which is just related to the uncertainty of measurement.

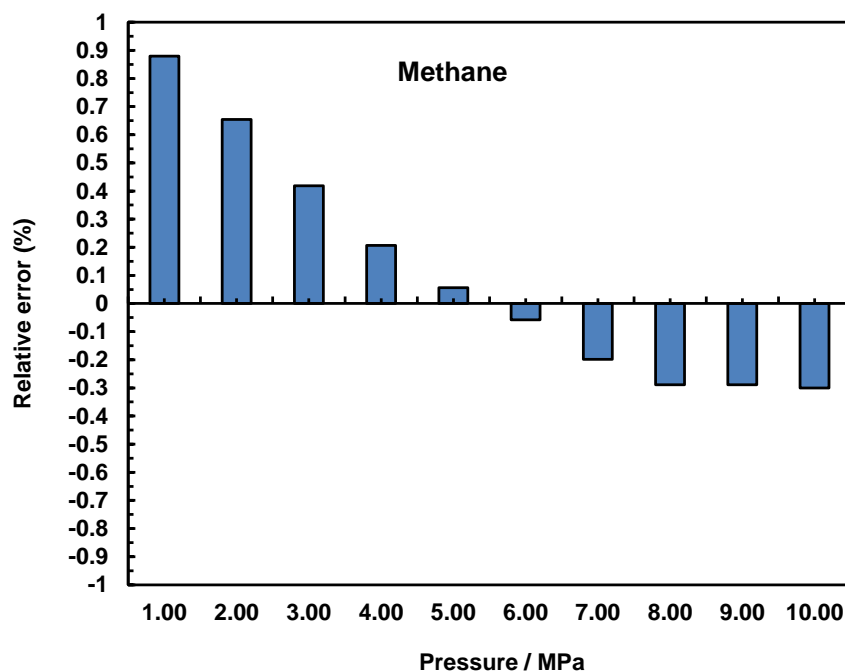


Figure 2.38. Effect of pressure variation on the FTNIR predicted values (mol%) for methane on the 293.15 K.

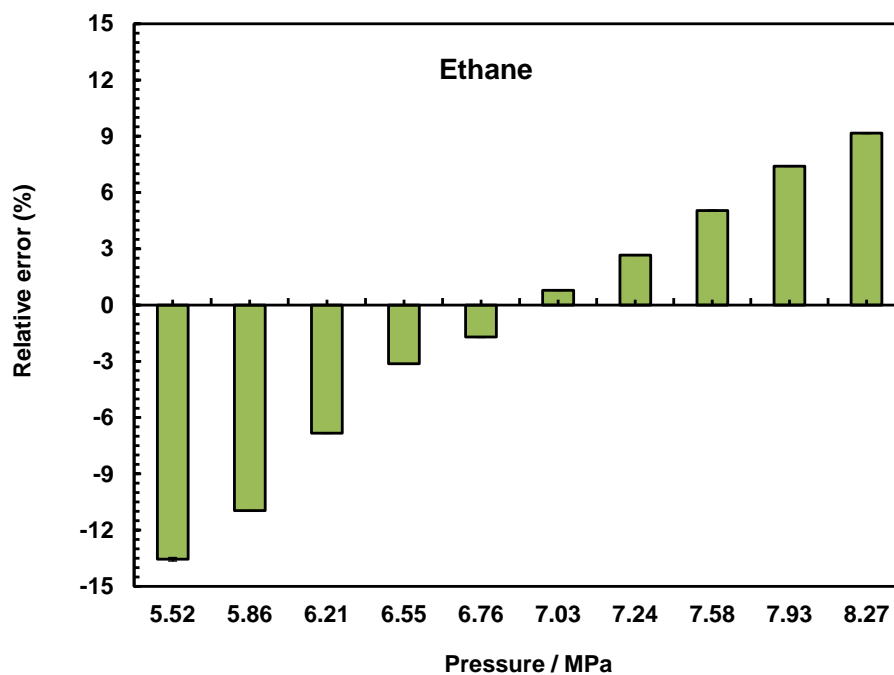


Figure 2.39. Effect of pressure variation on the FTNIR predicted values (mol%) for ethane on the 293.15 K.

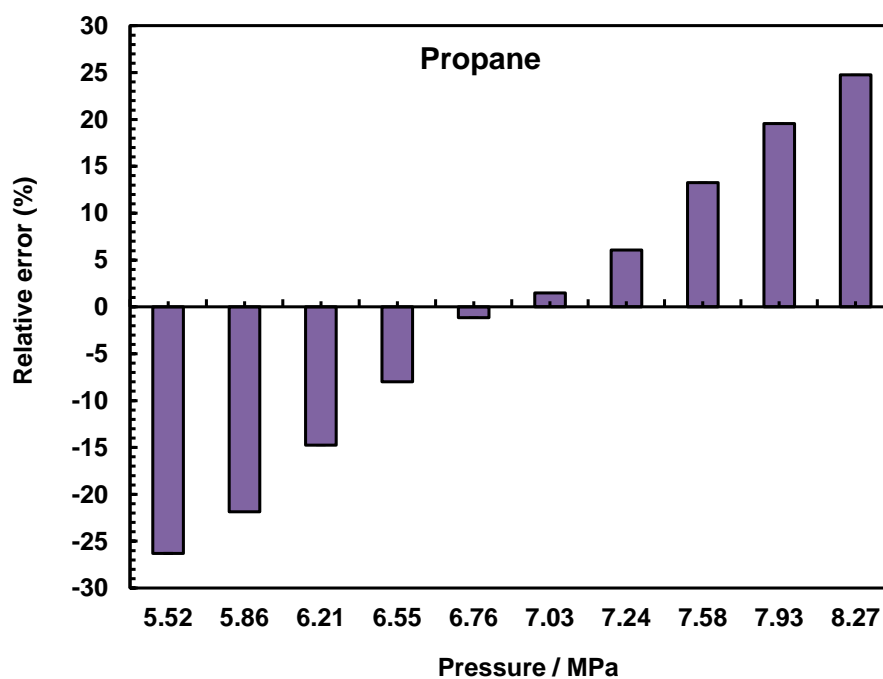


Figure 2.40. Effect of pressure variation on the FTNIR predicted values (mol%) for propane on the 293.15 K.

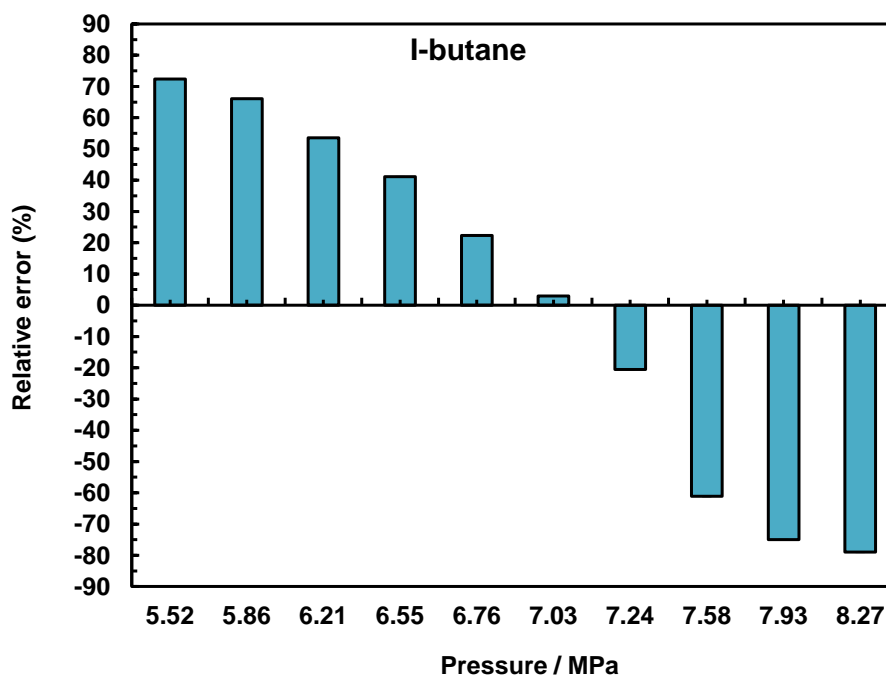


Figure 2.41. Effect of pressure variation on the FTNIR predicted values (mol%) for i-butane on the 293.15 K.

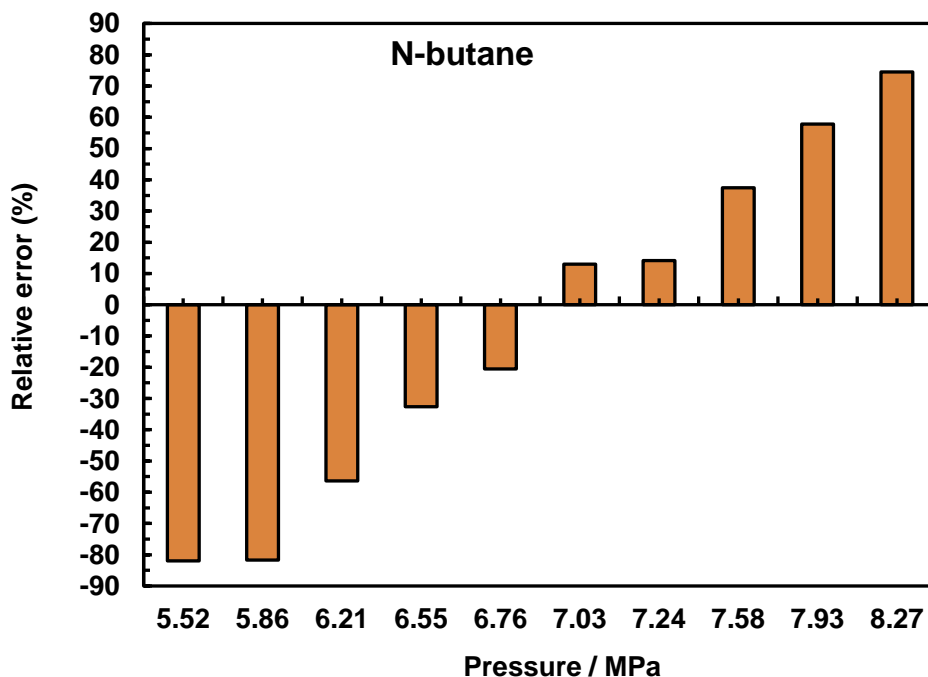


Figure 2.42. Effect of pressure variation on the FTNIR predicted values (mol%) for n-butane on the 293.15 K.

The accuracy of one of the developed PLS model ($P = 6.89$ MPa, $T = 293.15$ K) was also evaluated regarding the influence of sample temperature variation on the FTNIR predicted values. At this time, the pressure of the sample inside the cell was kept constant ($P = 6.89$ MPa) and the spectra were recorded at various temperatures. The deviation of the measured value for methane, ethane, propane, i-butane, and n-butane with respect to the actual value of the synthetic gas mixture (values measured at $P = 6.89$ MPa, $T = 293.15$ K) using the chemometric models is shown as a function of temperature in Figures 2.43 to 2.47.

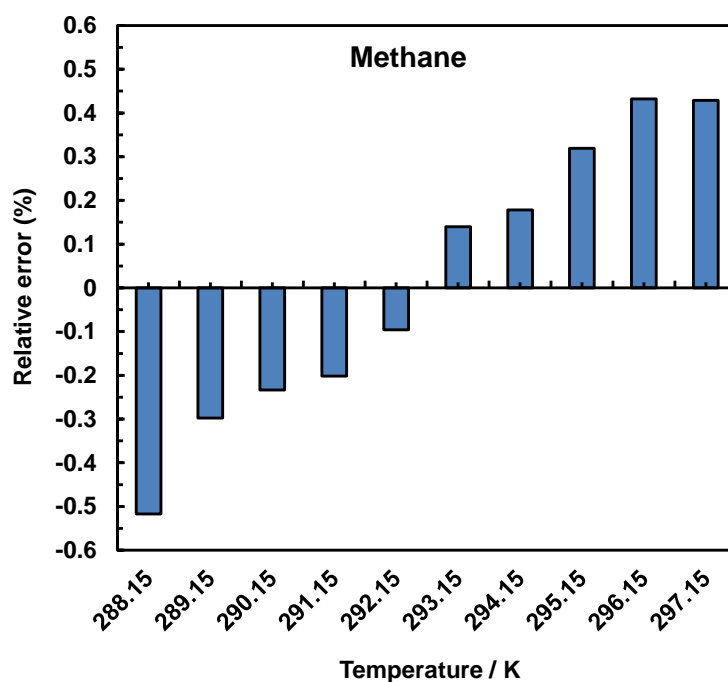


Figure 2.43. Effect of temperature variation on the FTNIR predicted values (mol%) for methane at a pressure of 6.89 MPa.

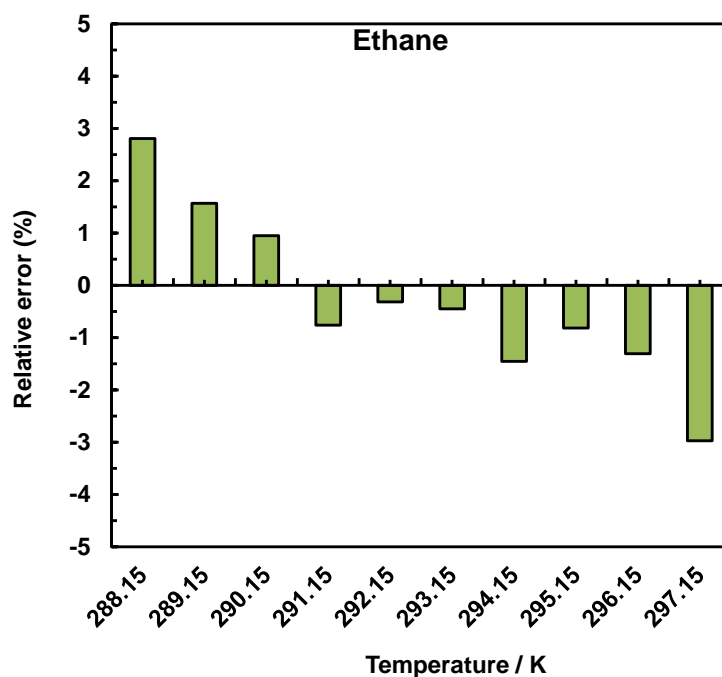


Figure 2.44. Effect of temperature variation on the FTNIR predicted values (mol%) for ethane at a pressure of 6.89 MPa.

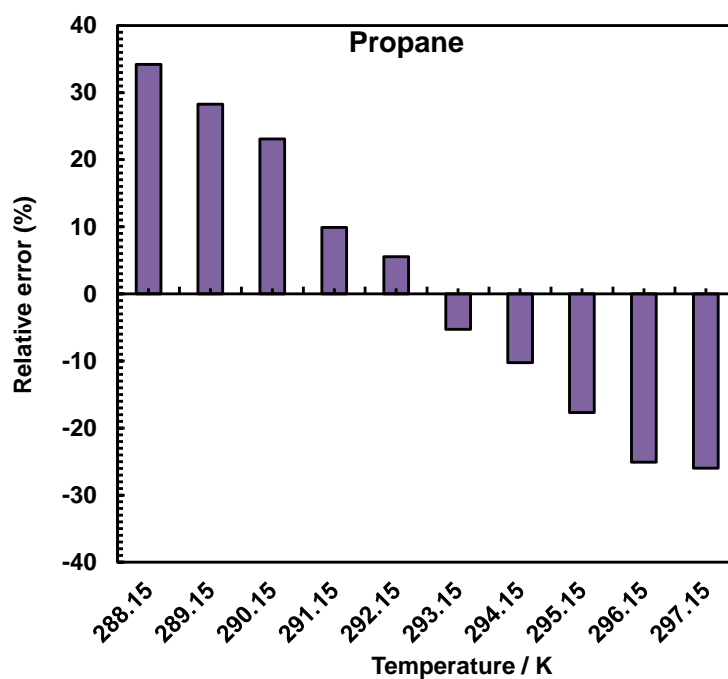


Figure 2.45. Effect of temperature variation on the FTNIR predicted values (mol%) for propane at a pressure of 6.89 MPa.

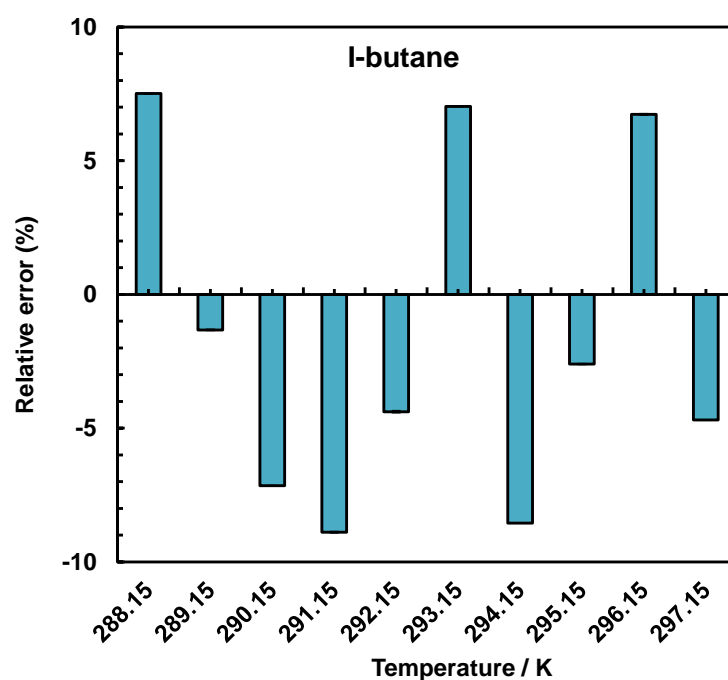


Figure 2.46. Effect of temperature variation on the FTNIR predicted values (mol%) for i-butane at a pressure of 6.89 MPa.

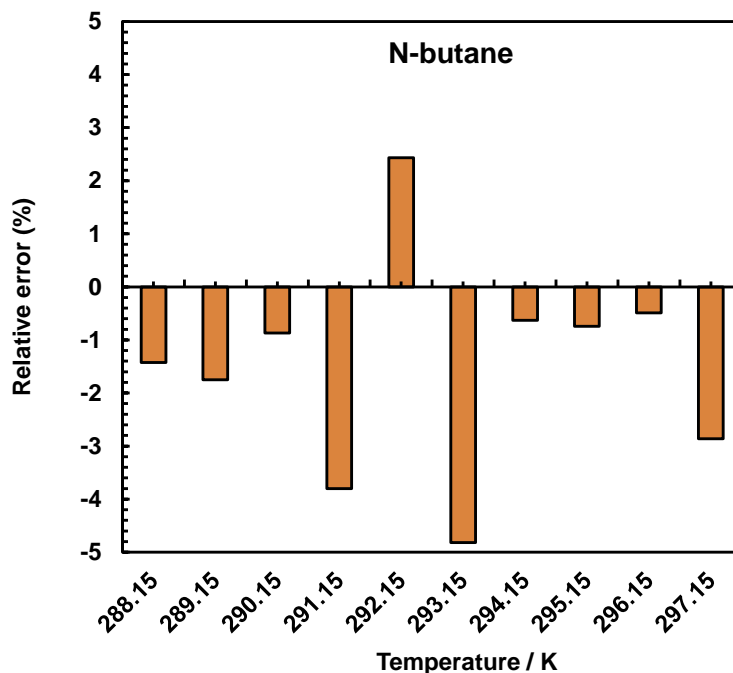


Figure 2.47. Effect of temperature variation on the FTNIR predicted values (mol%) for n-butane at a pressure of 6.89 MPa.

No significant variation in the concentration of methane, ethane and propane had been observed while the shift in temperature was less than 2 K. It should be noted that small errors in this range of temperature are within the uncertainty measurements of the models. Furthermore, negligible errors were noticed for i-butane and n-butane while the temperature was changed from 278.15 K to 288.15 K with 1 K interval. All these results confirmed that variation in pressure and temperature of the sample affect the accuracy of PLS models that created at specific pressure and temperature due to the effect of temperature and pressure of gas on the shape and amount of absorption. Therefore, it is necessary to maintain the temperature and pressure of the system to an accuracy of ± 2 K and ± 0.14 MPa to achieve accurate results.

2.9 Graphical User Interface (GUI) for FTNIR Prototype

A graphical user interface (GUI) was developed in the LabVIEW 2013 environment to control the FTNIR testing system that is shown in Figure 2.48. This GUI integrates the FTNIR setup into a prototype for online monitoring and real-time determination of methane, ethane, propane, i-butane, n-butane, and the ratio of methane to ethane and methane to propane. As it can be seen in Figure 2.49, changes in the concentration of methane, ethane, propane, i-butane, n-butane, and the ratios of methane to propane and methane to ethane can be monitored from the main window. Original spectrum and pre-

processed spectrum show the raw data recorded by the spectrometer and the spectrum after pre-processing, respectively.

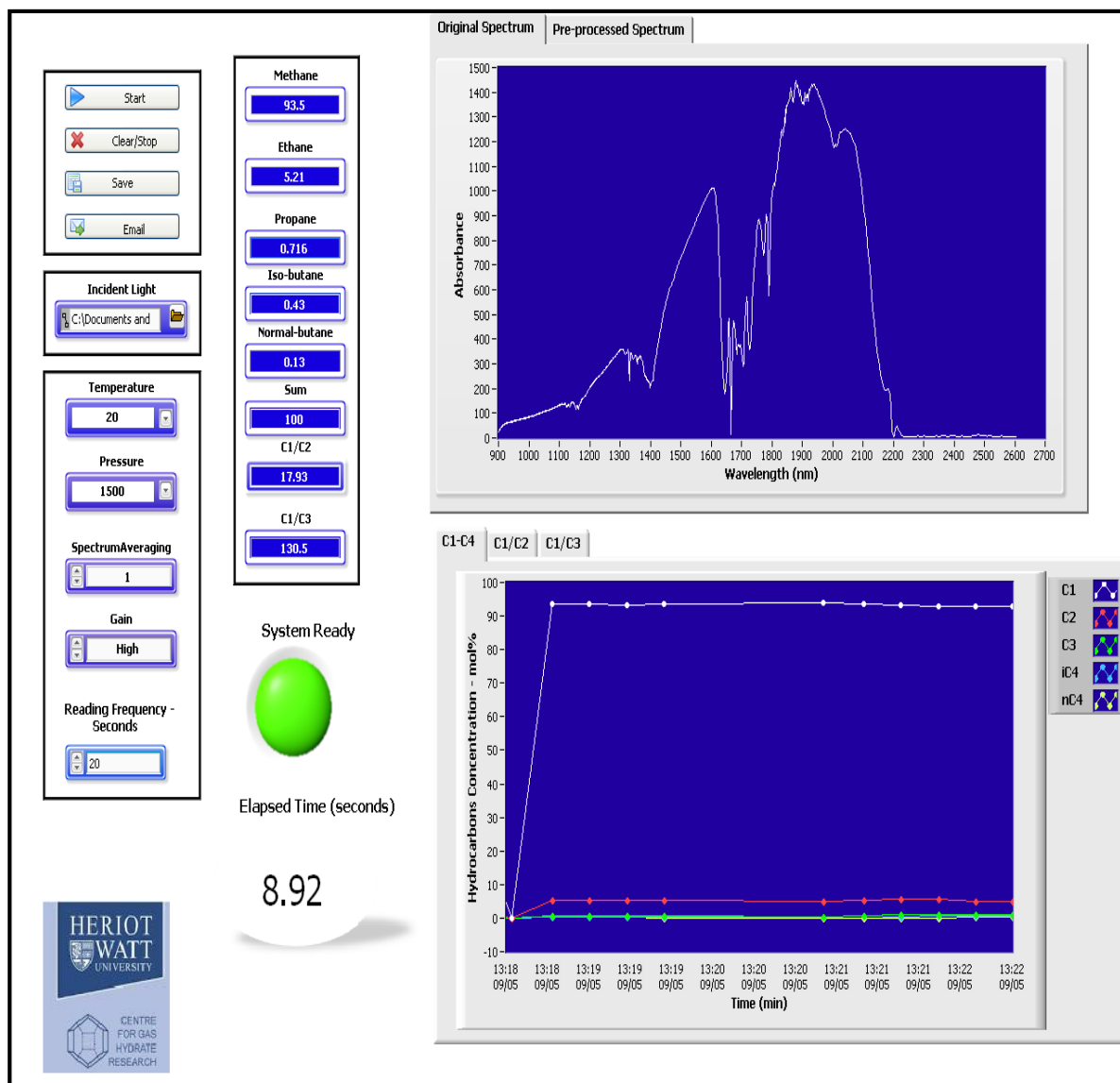


Figure 2.48. The main window of the FT-NIR analyser.

A data dashboard app for LabVIEW was further developed to be able to remotely monitor the concentration of methane, ethane, propane, i-butane, n-butane and changes in C_1/C_3 ratio using mobile phones or tablets. The app displays the values of network-published shared variables and/or web services on charts, gauges, text indicators, and LED. The data can be transferred or shared through a wireless network with the mobile phones or tablets in which the LabVIEW program was installed.

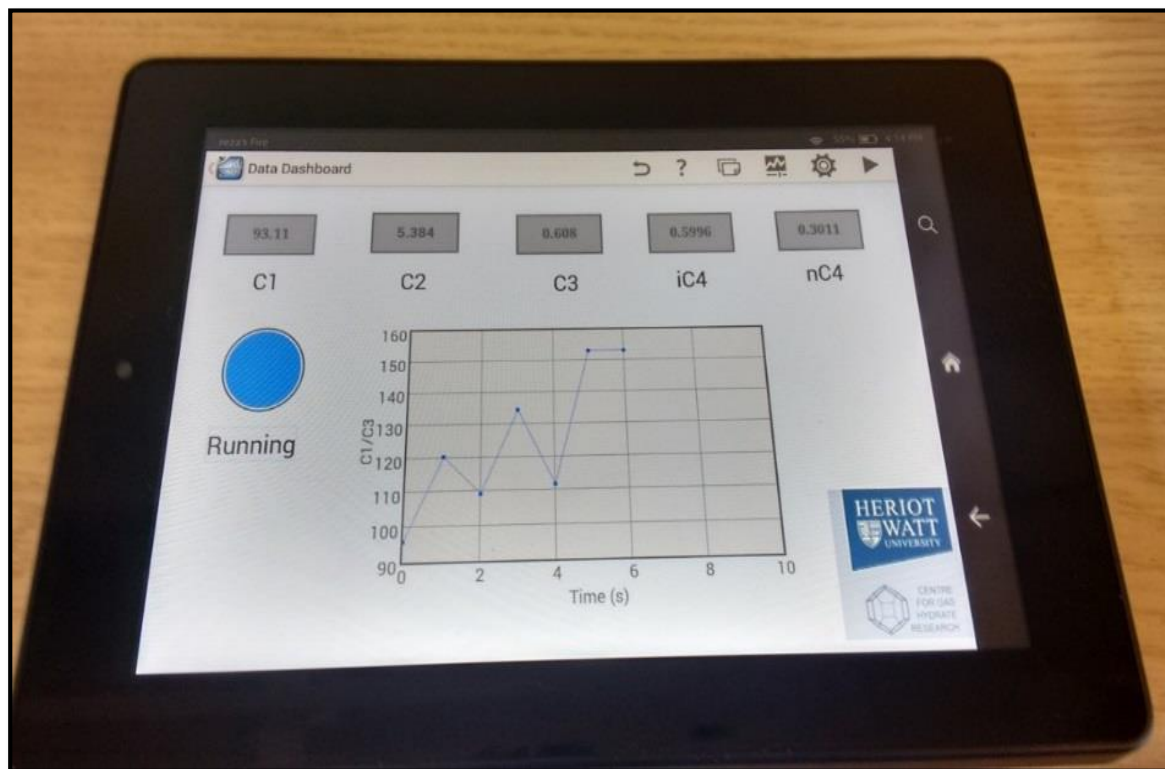


Figure 2.49. The Data Dashboard application for controlling and monitoring the compositional change in the gas sample.

2.10 Conclusions

The conclusions that can be made from the work presented in this chapter, aimed at developing and validating new spectroscopy method and setup for monitoring the composition of main hydrocarbons components in the gas phase quickly and accurately.

- The spectral region from 1667 to 1800 nm was selected as a final region for construction of the calibration models (PLS & ANN), as it provides lower error for all the studied components.
- Overall, the PLS models yielded reasonably lower RMSEP and SEP values for all the components compare to developed ANN models for all the components.
- The developed PLS models could provide sufficient measurement accuracy if the shift is less than 2 K in the measurement temperature and 0.14 MPa in the measurement pressure.
- The developed end-user interface allow the user to determine the concentration of methane, ethane, propane, i-butane and n-butane in mol% using LabView software in about 90 seconds and also make it easy to control .

Based on the available commercial devices in the industry for monitoring the composition of natural gas, advantages and disadvantages of developed spectroscopic setup are summarised in below:

- NIR analyser instrument is easy to install, operate and maintain (Rugged design).
- Fast Response (less than 90 seconds).
- No gas carrier or consumable compare to GC.
- Accurate results - Using high-resolution spectrometer accuracy of measurements can be improved, in this work, a spectrometer with a resolution of 2.5 nm was used.
- The composition of the gas sample can be analysed at high pressure and temperature.
- The system can be controlled and monitor remotely.

Disadvantages:

- Gas temperature and pressure strongly affect the measurement accuracy. Therefore, it is necessary to maintain the temperature and pressure within a certain range for high accuracy results.
- The existence of water in the system may affect the accuracy of the results as it is a strong NIR absorber [83].

To summarize, FTNIR spectroscopy is a fast, accurate and robust method to monitor and measure the composition of main hydrocarbons species simultaneously in the gas phase. Moreover, because of its capability to operate at high pressures, the FTNIR analyser can employed at in-situ pressure beside the gas outlet of the pipelines for online monitoring of hydrocarbon gas compositions without requiring any gas carrier and skilled operators in comparison with gas chromatography, which makes it easy to use with significant reduction in the operation costs.

CHAPTER 3: DETECTION OF INITIAL SIGNS OF HYDRATE FORMATION BY FTNIR SPECTROSCOPY TECHNIQUE

3.1 Introduction

Formation of gas hydrates from natural gas and water can lead to blockage in hydrocarbon transportation pipelines, causing extensive damage to the pipelines. Therefore, chemical additives known as hydrate inhibitors are employed to prevent hydrate blockage or reduce the risk of hydrate blockage. There is a need for improved techniques to reduce the risk of hydrate formation at an optimum cost and improve the reliability of the inhibitor-based techniques for preventing gas hydrate formation.

As it was explained in Chapter 1, gas hydrates are crystalline solid compounds that form when the guest molecules of a suitable size are embedded in the lattices of water under low temperature and elevated pressure conditions. Guest molecules such as methane, ethane, propane and i-butane and the other gases such as carbon dioxide, nitrogen and hydrogen sulphide are capable of occupying the cavities and forming gas hydrates.

It is believed that initial formation of gas hydrates do not result in hydrate blockage. In fact, when the initial hydrate formation is not detected and, hence, addressed, further hydrate formation can occur, and the resulting build-up of hydrates could cause pipeline blockage [34]. Hence, it is necessary to detect early signs of hydrate formation as an early warning method to prevent the formation of gas hydrate plugs inside the pipeline [20].

Small molecules such as methane prefer to form hydrate structure I (sI), while relatively large and round molecules such as propane and i-butane tend to form hydrate structure II (sII) [84]. Details about the structure of hydrates and their physical and chemical properties have been well-established in the literature [3]. Formation of hydrate structure II (sII) will result in an increase in the concentration of methane and decrease in concentration of heavier components like ethane, propane and i-butane in the gas phase [85]. This results in the reduction of propane and i-butane content in the gas phase. On the contrary, when the operating envelope is within sI hydrate stability zone, both sI and sII hydrate structure may form, resulting in a reduction of both light and heavy hydrocarbon contents in the gas phase [86]. Hence, a reduction in methane can be a sign of hydrate structure I formation and reduction in ethane, propane and i-butane content in the gas phase can be a sign of hydrate structure II formation. Furthermore, the formation

of gas hydrate can result in an increase in the concentration of salt and hydrate inhibitors in the liquid phase because of the reduction of water as a result of hydrate formation. When hydrates are formed, they exclude salts and other impurities from their structure, results in an increase in the concentration of salt in the remaining water [87]. Thereby, an increase in the salinity and hydrate inhibitor also could be a sign of formation of gas hydrates in pipelines, allowing the operator to react in time to avoid pipeline plugging.

Several research groups have reported experimental studies focusing on the evolution of gas composition in hydrate and vapour phases. The results of these studies indicate that as the formation of natural gas hydrates proceeds, the concentration of gas in both hydrate and gas phases changes significantly [88]. The rate of formation of propane hydrates has been investigated using modulated differential scanning calorimetry by Givarini *et al.* [89] and their results showed that liquefied petroleum gases (LPGs), which is mainly composed of propane and butane could form hydrate instantaneously with melting ice. The compositional changes in a mixture of methane, ethane, propane and i-butane in hydrate phase and gas phase have been investigated by Kawasaki *et al.* [90]. According to their results, after the onset of hydrate formation, the concentration of ethane, propane and i-butane in gas phase decreases significantly. In contrast, an increase can be observed in methane concentration in the gas phase, whereas opposite trend was observed in the hydrate phase. The results revealed a substantial reduction in methane concentration and a significant increase in propane and i-butane concentration in the hydrate phase. Uchida *et al.* [91] experimentally analysed the crystalline structures and hydrate-guest composition during hydrate formation using X-ray diffraction and Raman spectroscopy. They used high speed gas chromatograph (GC) to monitor the compositional changes in a gas mixture composed of methane and propane. Their results confirmed that as the hydrate formation progressed, the concentration of propane and methane in the vapour phase is lower and higher than those in the original gas composition, respectively.

In situ Raman spectroscopic experiments were carried out in an oceanic laboratory to analyse the structural characteristics of mixed hydrate when it is formed from natural gas in bulk water [92]. Based on these spectroscopic analyses, the consumption of propane and i-butane from the gas phase lead to vapour composition becoming rich in methane and results indicated that the formation of hydrate sII continued as long as the concentration of heavy sII forming molecules denudes from the gas phase and due to the enrichment of gas phase with methane there is a reasonable possibility of forming hydrate sI. Kondo *et al.* [35] also have studied the compositional evolution of natural gas mixtures

consisting of methane, ethane and propane in 90, 7 and 3 molar ratios during an isobaric semi-batch hydrate formation operation. These analyses revealed the coexistence of both sI and sII hydrates during the hydrate-formation process.

Monitoring the changes in the composition of hydrocarbons in the gas phase and changes in the concentration of salt and hydrate inhibitors in the aqueous phase can be a good sign of gas hydrate formation. In this chapter, the feasibility of FTNIR spectroscopic method was investigated based on the effect of hydrate formation on the gas composition in the vapour phase. Different methods were employed to monitor the changes in gas phase such as GasPT [93], the speed of sound and GC . The results obtained by our developed prototype were compared to those measured by GasPT and GC. Moreover, the developed FTNIR spectroscopy technique was integrated with the V-V_{tc} technique to monitor the changes in the concentration of hydrate inhibitors and salt in the aqueous phase as well as changes in the concentration of hydrocarbons in the gas phase at different conditions (before and after hydrate formation). The V-V_{tc} technique was developed based on measurement of acoustic velocity and its thermal coefficient. Details about this technique are explained in section 3.2.3. Finally, the compositional change method was field tested on one gas/condensate field in France in which one of the sponsors was involved. Results of this study are summarised in section 3.6.1.

3.2 Methods to Detect Early Signs of Gas Hydrate Formation

One of the main objectives of this study is to first investigate and examine the capability of FTNIR techniques to detect early signs of hydrate formation by monitoring changes in the concentration of hydrocarbons in the gas phase for different systems containing salt, methanol, MEG, KHI, gas condensate and deionised water. The developed calibration models (PLS and ANN) were employed at various pressure and temperature conditions. Then, the FTNIR prototype was evaluated for a salt-MEG system and a salt-methanol system by integrating with the GasPT and the V-V_{tc} prototype, respectively.

3.2.1 FTNIR

As explained in Chapter 2, a prototype was developed to determine the concentration of hydrocarbons (methane through butanes) in the gas phase. In this chapter, the changes in gas composition (e.g., C₃ and/or C₂ concentrations, C₁/C₃ and/or C₁/C₂ ratios) were monitored using the developed prototype before and after hydrate formation. A series experimental tests were conducted at four different pressures and three separate temperatures to examine the performance of the developed PLS and ANN models.

3.2.2 GasPT

Gas Properties Transmitter (GasPT) is commonly used in oil and gas industry (i.e., gas transportation and processing) for measuring different properties of gas mixtures [94]. A GasPT has the ability to estimate the concentration of gas components, by measuring various physical properties of a gas mixture [85]. It analyses pseudo gas compositions of methane, propane, CO₂ and N₂ by measuring the speed of sound and thermal conductivity at atmospheric pressure. As illustrated hereafter by an example, this device was used to detect initial signs of hydrate formation by monitoring the changes in the concentration of methane and propane in the gas phase.

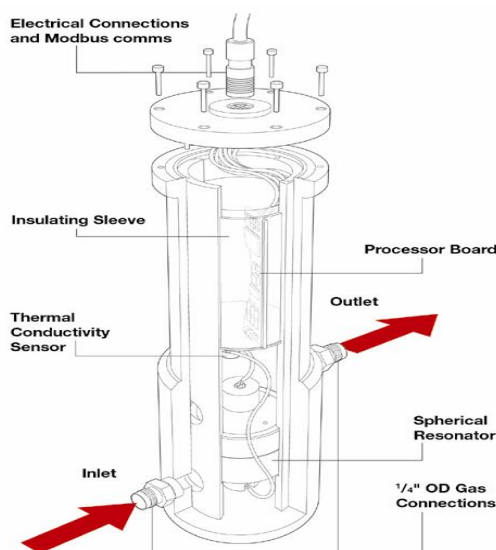


Figure 3.1. Schematic of GasPT.

A sample of the gas passes through the probe (in at the bottom, out near the middle is shown in Figure 3.1). The probe typically requires a flow of around 1 L/min at a pressure of less than 0.3 MPa. The sensors within the probe measure the speed of sound, thermal conductivity, temperature and pressure of the gas mixture. A microcontroller within the probe correlates the measured physical properties to the effective gas mixture and 'gas quality' parameters. Furthermore, the gas sample must be clean and dry because the existence of water in the gas sample may cause damage to internal components. Water will irrevocably damage the thermal conductivity sensor. In other words, any particulates within the gas would obviously coat the surface of the sensors, in the long run, may not provide accurate results as these impurities prevent the sensors from "seeing" the gas. In this work, although nitrogen and carbon dioxide will contribute to hydrate phase but our

main focus is on methane and propane content. Thereby, the output is normalised on only methane and propane.

3.2.3 V-V_{tc} technique

The V-V_{tc} technique was developed to determine concentrations of both salts and hydrate inhibitors. It is based on measurement of acoustic velocity and its change with temperature. Two acoustic velocities are measured at two different temperatures and identical pressure to determine the velocity change with temperature. For the two fixed temperatures, the two measured acoustic velocities with the measured pressure together can be used to identify concentrations of salts and hydrate inhibitors.

Figure 3.2 illustrates the principle of the V-V_{tc} technique. In this approach, two velocities at two different temperatures under an identical pressure are measured. The thermal coefficient of the acoustic velocity can be calculated according to the definition of the thermal coefficient Equation 3.1:

$$V_{tc} = \frac{\Delta V}{\Delta T} = \frac{V_2 - V_1}{T_2 - T_1} \quad \text{Equation 3.1.}$$

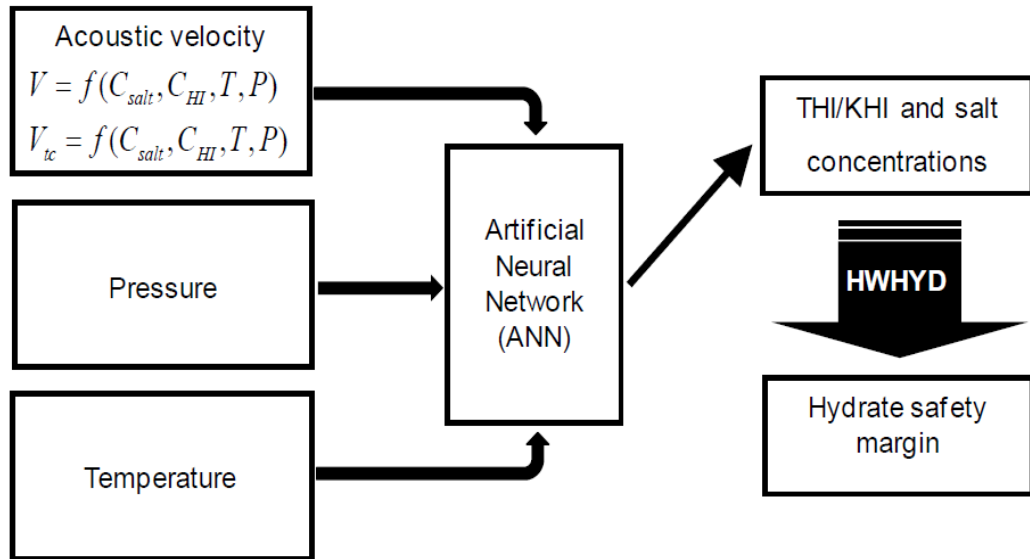


Figure 3.2. Flowchart of the V-V_{tc} technique.

For a certain temperature interval, the V-V_{tc} technique can determine both salt and hydrate inhibitor concentrations by directly using the measured velocities. The two measured velocities with the pressure together are fed to an ANN that was previously trained, validated, and tested. The ANN then determines both salt and hydrate inhibitor concentrations. Finally, the hydrate safety margin can be determined using the determined

salt and inhibitor concentrations by a thermodynamic model that is integrated with the $V-V_{tc}$. Figure 3.3 shows a picture of the developed $V-V_{tc}$ prototype. It consists of two sample cells equipped with thermoelectric heatsinks, a PID temperature controller including a switch power supply and a PID controller, an ultrasonic unit including a pulser/receiver and a digital storage oscilloscope that are installed in one instrument case, a T & P display box, and a GUI that is installed on a personal computer. The GUI acquires the measured travelling time, the cell temperature and pressure, and then determines the concentration of salts and inhibitors using the developed ANN models.



Figure 3.3. Picture of the developed $V-V_{tc}$ prototype.

3.3 Detection of Early Signs of Gas Hydrate Formation Using FTNIR Technique

3.3.1 Apparatus

Figure 3.4 shows a schematic diagram of the high pressure rig that used to form gas hydrate. It had a volume of 2230 cm^3 and can be used up to 40 MPa over 248 to 323 K. The cell was surrounded by a cooling jacket connected to a cooling/heating bath for temperature control purposes. To measure the pressure, a Druck pressure transducer were used with the accuracy of $\pm 0.03 \text{ MPa}$. Temperature measurement was done by using a PRT temperature probe with the accuracy of $\pm 0.1 \text{ K}$. In order to attain a fast

thermodynamic equilibrium and to provide a proper mixing of the fluids, a high pressure magnetic stirrer (Top Industry S.A. – wetted parts made of Hastelloy C276) was employed to mix the test fluids at around 300 RPM with a Rushton type impeller. This autoclave is connected to the FTNIR sample cell which is attached to the FTNIR setup for measuring the composition of the gas sample (Figure 3.5).

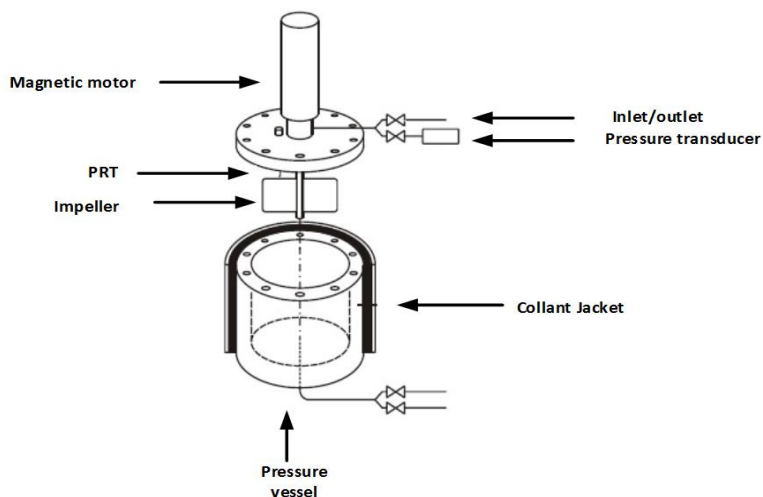


Figure 3.4. Schematic illustration of high pressure rig.

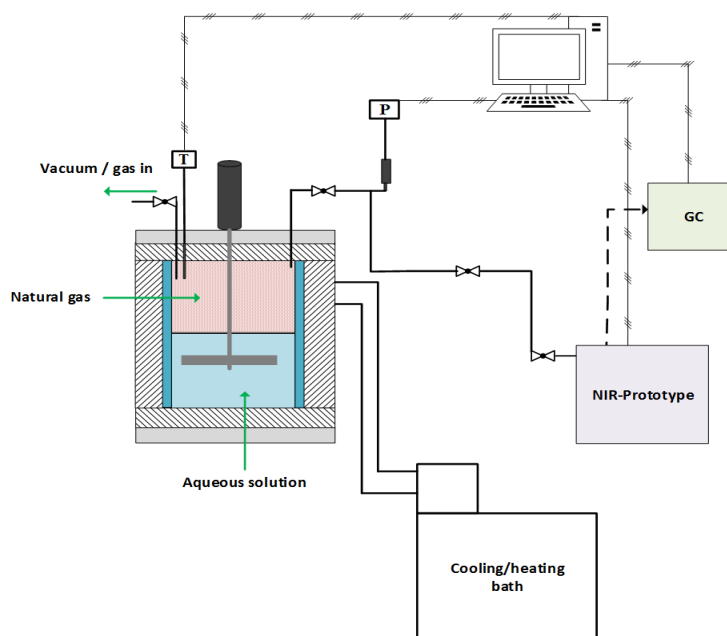


Figure 3.5. Schematic diagram of the experimental setup.

3.3.2 Experimental procedure

Experimental procedures consist of several steps. The high pressure rig was preloaded with about 400 ml of the aqueous liquid solution under test (The type and amount of solutions depend on the individual experiments), and the high-pressure rig was vacuumed before gas injection. Natural gas (NG) was injected to the rig until the desired pressure. The system was left at a temperature outside the hydrate stability zone overnight to allow thermodynamic equilibrium to be reached. This temperature depends on the amount of salt and/or inhibitors in the solution. For this purpose, the composition of the natural gas and the salt and/or inhibitor concentration were fed into a thermodynamic model called HydraFLASH. The thermodynamic model was developed in the Heriot-Watt University. The cubic-plus-association equation of state (CPA EoS) was used to determine hydrate phase boundary [7].

As mentioned above, the system was left at this temperature overnight to allow thermodynamic equilibrium and also to ensure there is no leakage in the system. The mixing rate was set at 300 RPM. The system was then cooled down with cooling rate of 0.5 K/min inside the sI hydrate stability zone and left for 24 hours and then at this point, a sample of gas phase was taken from the top of the rig and transferred to the FTNIR cell to evaluate the effect of formation of sI hydrate on the compositional change technique. The FTNIR spectrum was then acquired in the range 900 to 2600 nm as the average of 20 scans. After acquiring the FTNIR spectrum, the mixture was transferred to the GC sampling valve for chromatographic analysis. Then the hydrates were dissociated by heating up the system with a heating rate of 1 K/min to the targeted degree Kelvin inside hydrate structure I&II stability zone, inside the sII hydrate stability zone and outside the hydrate stability zone. For each sampling point, the system was left for at least 12 hours that depends on the experiment (to achieve the desired equilibrium pressure). All the samples were analysed and compared using GC and FTNIR. Furthermore, one test was carried out with much lower water: a gas ratio that to examine the sensitivity of compositional change technique using FTNIR spectroscopy. For this purpose, a new blade with longer length was designed and employed to agitate the sample fluid. The previous blade was not long enough to agitate the fluid sample. The Arcspectro FT ROCKET spectrometer is connected to a computer and provides communication through Arcspectro software [95].

3.3.3 Hydrate calculation

To roughly estimate the amount of water converted to hydrate at different P-T conditions, the pressure drop in the system (ΔP) was calculated at different sampling points, and the hydration number (H_n) is assumed constant and equal to 6.5. Hydration number is the number of water molecules per gas molecule at a given P-T condition. The amount of water converted to hydrate can be estimated using equation 3.2:

$$WCH\% = \frac{\Delta n_{water}}{n_w} \quad \text{Equation 3.2.}$$

$$\Delta n_{gas} = \frac{\Delta P}{P} n_{gas} \quad \text{Equation 3.3.}$$

n_{gas} and P are the number of gas moles in the gas phase and pressure of the system respectively, before formation of the gas hydrate. The water mole fraction can be determined by:

$$f_w = \frac{n_{water}}{n_{gas} + n_{water}} = \frac{n_{water}}{n_{tot}} \quad \text{Equation 3.4.}$$

The number of water moles used in hydrates (Δn_{water}) is then calculated using equation 3.6.

$$\Delta n_{gas} = \frac{\Delta P}{P} (1 - f_w) n_{tot} \quad \text{Equation 3.5.}$$

$$\Delta n_{water} = H_n \frac{\Delta P}{P} (1 - f_w) n_{tot} \quad \text{Equation 3.6.}$$

Then, WCH can be estimated using equation 3.7 in litre:

$$WCH \% = H_n \frac{\Delta P}{P} \frac{(1 - f_w)}{f_w} \quad \text{Equation 3.7.}$$

In this study, the amount of water converted to hydrate is expressed in bbl/MMscf unit. For this purpose, the amount of water converted in hydrate in gram is calculated by multiplying Δn_{water} by 18.01 gr/mol and converted to litre unit (the density of water is

assumed to be 1000 gr/L). The amount of water is then converted to U.S. barrel (bbl) by multiplying by 0.0086 and the volume of the gas in litre is estimated ($V = \frac{n_{gas}ZRT}{P}$, assuming standard condition $T = 288.70K$ and $P = 0.1$ MPa) and converted to million standard cubic feet (MMscf is a volume unit in the petroleum industry.) by multiplying by 0.0035.

3.3.4 Materials

Various natural gas compositions were used to evaluate the feasibility of the NIR analyser which is given in Table 3.1. All these gas mixtures were analysed by GC. Deionised water was used in all tests. Pure methanol, MEG and salt (Thermodynamic hydrate inhibitors, Purity > 99.9%) were provided by Sigma-Aldrich and Luvicap EG (Kinetic hydrate inhibitors) was supplied by BASF. Luvicap EG is composed of about 60 wt % ethylene glycol and 40 wt % of the Poly-nvinylcaprolactam (PVCap) [96].

Table 3.1. The composition of the natural gas used.

Components	NG-A (mol%)	NG-B (mol%)	NG-C (mol%)
Methane	90.29	88.09	89.40
Ethane	5.48	5.95	5.81
Propane	1.35	2.01	1.81
I-butane	0.20	0.22	0.20
N-butane	0.25	0.29	0.28
I-pentane	0.04	-	0.06
N-pentane	0.03	-	0.06
Carbone dioxide	1.01	1.94	0.78
Nitrogen	1.32	1.50	1.59

3.3.5 Results and discussions

In this section, the feasibility of compositional change method is investigated for different aqueous systems containing salt, alcohol and kinetic hydrate inhibitors using the FTNIR spectroscopic method for detecting early signs of hydrate formation. Meanwhile, the performance of our developed prototype was further examined with GC for hydrate early warning purposes.

It is known that gas hydrates can form more easily in a system that gas hydrates were already formed and dissociated under certain thermodynamic conditions [67]. This is attributed to a phenomenon that is named hydrate memory. In other words, gas hydrates

can form earlier with less degree of sub-cooling in a system that has resulted from dissociation of hydrates compared to a system that has not experienced hydrates (water is fresh and has no hydrate experience). In this study, the dependence of hydrate memory on different parameters was investigated, such as the retaining time and temperature outside the hydrate stability zone. Some experiments were carried out to examine the sustainability of hydrate memory in the presence of salt, various hydrate inhibitors and condensate.

1.1.1.1 Test 1: Natural gas + deionised water

In this test, hydrates were formed in the presence of natural gas (NG-A) and deionised water. To perform this experiment 400 cc of deionised water was injected and after vacuuming the system was pressurised with natural gas until the desired pressure. Then, the system was left at a specific temperature point outside the hydrate stability zone over night. Next day, the first sample was taken and transferred to the FTNIR cell. To flow the gas through the measurement cell, valves both side of measurement cell were gradually opened until the FTNIR cell reaches to desired pressure. The system pressure was dropped for each measurement about 0.3 to 0.7 MPa due to gas sampling. Average absorbance spectra for 20 scans were recorded for each sample for better accuracy in the FTNIR cell. All the recorded absorbance spectra of gas mixtures were analysed by using two different computational methods (PLS & ANN). Afterwards, little amount of gas in NIR cell was taken for GC analysis. Then, the system was cooled down to form hydrate at desired temperature and the second sample was taken for GC and FTNIR analysis. Hydrates were then dissociated by heating up the system to a sequence of the targeted temperature, and one sample was taken at each temperature step for monitoring the change in concentration of hydrocarbons in natural gas using FTNIR and GC. The GC and FTNIR analysis were performed with three replicates, and the standard deviation for each component is also added. In this test, five samples were taken.

- Sample 1: at 294.65 K and 12.49 MPa outside the hydrate stability zone
- Sample 2: at 277.25 K and 7.83 MPa inside the s-I and s-II hydrate stability zones.
- Sample 3: at 281.45 K and 7.77 MPa inside the s-I and s-II hydrate stability zones.
- Sample 4: at 291.15 K and 10.56 MPa outside the s-I hydrate stability zone and inside s-II hydrate stability zone.
- Sample 5: at 293.65 K and 11.21 MPa outside the hydrate stability zone.

As mentioned before, due to the effect of temperature and pressure of gas on the shape, amount of absorption and consequently the accuracy of the results, the NIR cell should control them to make them constant, in this test all the spectra were recorded at a pressure of 3.44 and 6.89 MPa and temperature of 293.15 K. In this section, the results for both PLS and ANN models are presented.

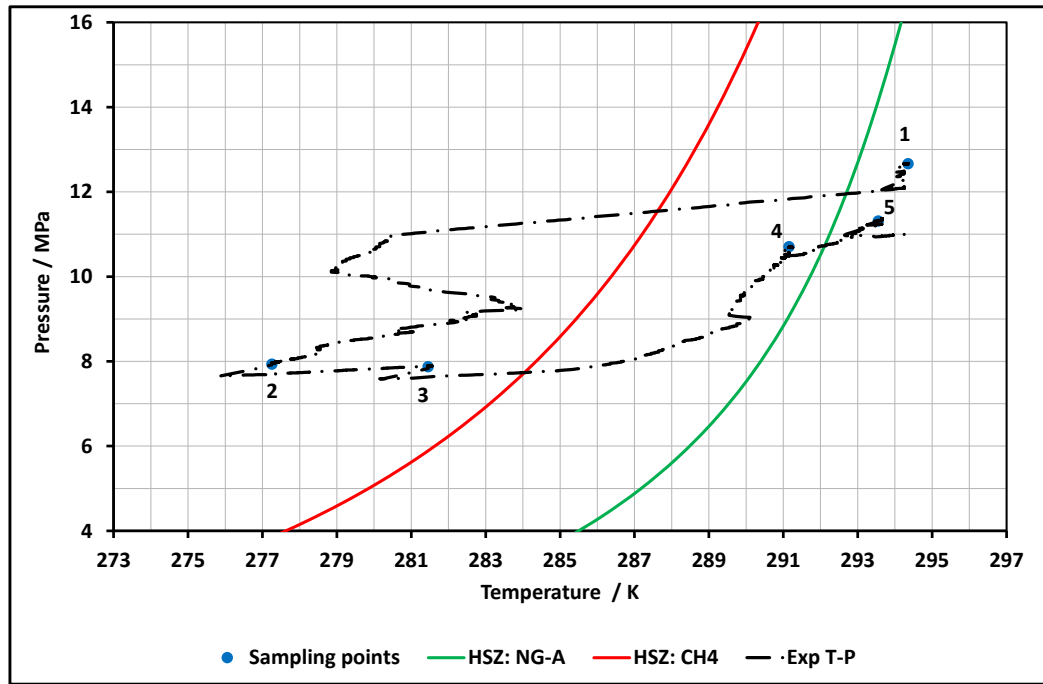


Figure 3.6. Temperature-pressure profile and sampling points for the system with NG-A and deionised water.

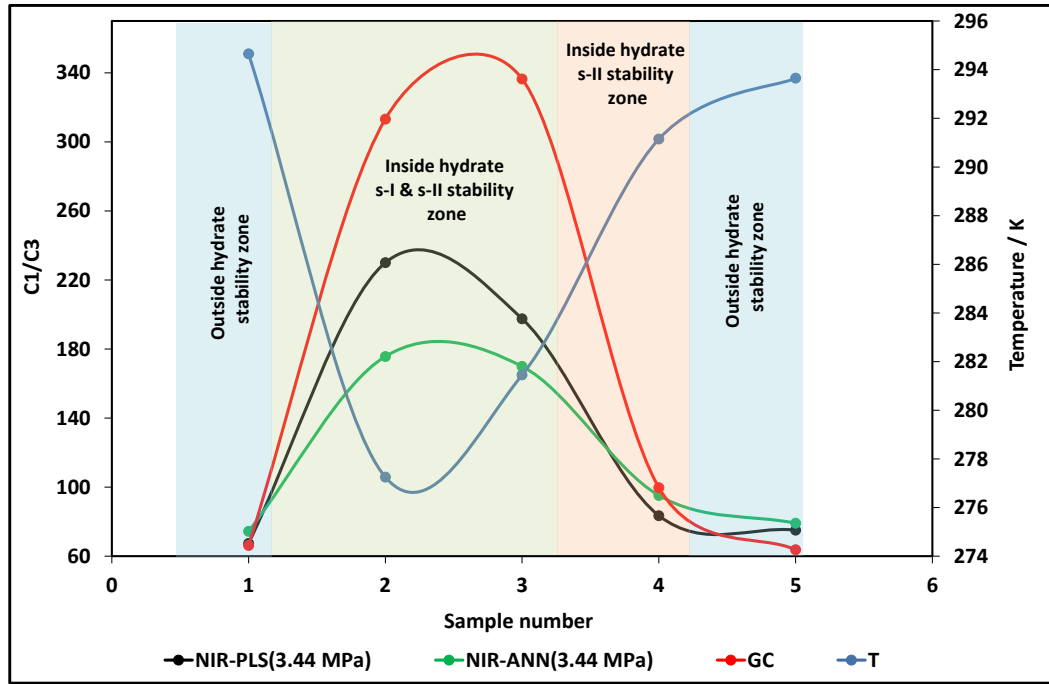


Figure 3.7. Compositional monitoring of C_1/C_3 ratio in the gas phase using GC and FTNIR at 3.44 MPa and 293.15 K. Connection trend between points are only for visual clarification.

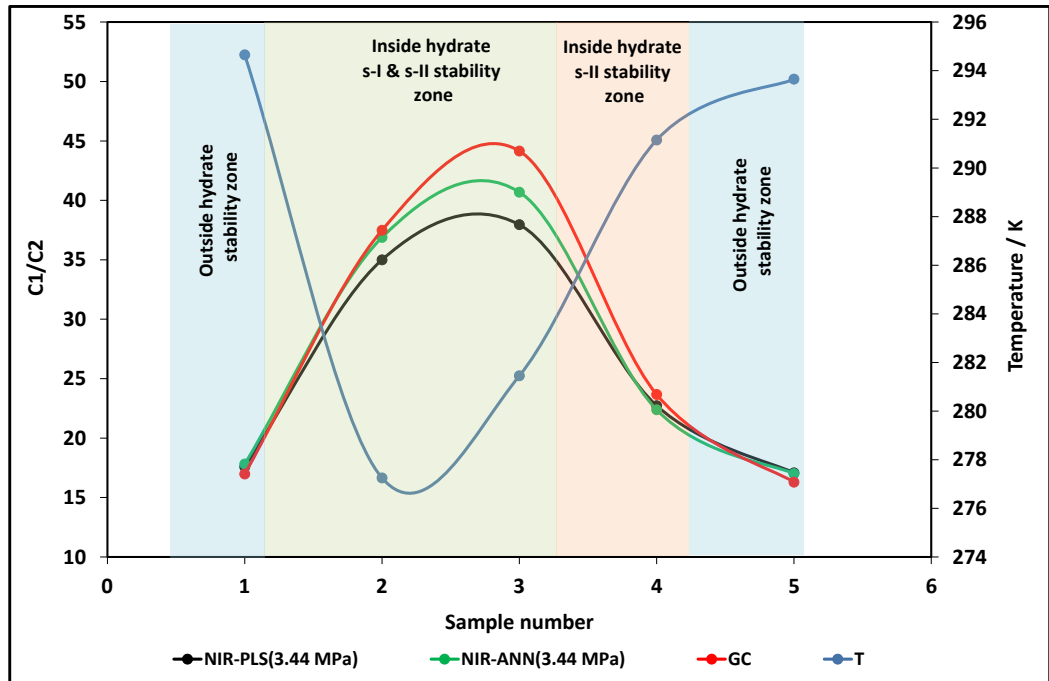


Figure 3.8. Compositional monitoring of C_1/C_2 ratio in the gas phase using GC and FTNIR at 3.44 MPa and 293.15 K. Connection trend between points are only for visual clarification.

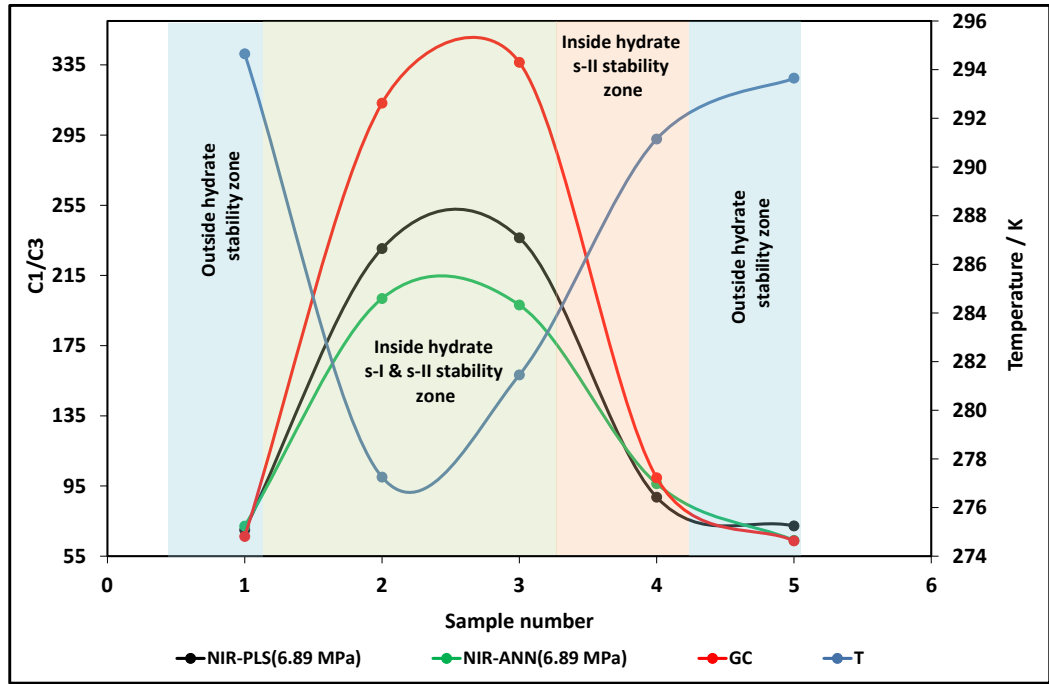


Figure 3.9. Compositional monitoring of C_1/C_3 ratio in the gas phase using GC and FTNIR at 6.89 MPa and 293.15 K. Connection trend between points are only for visual clarification.

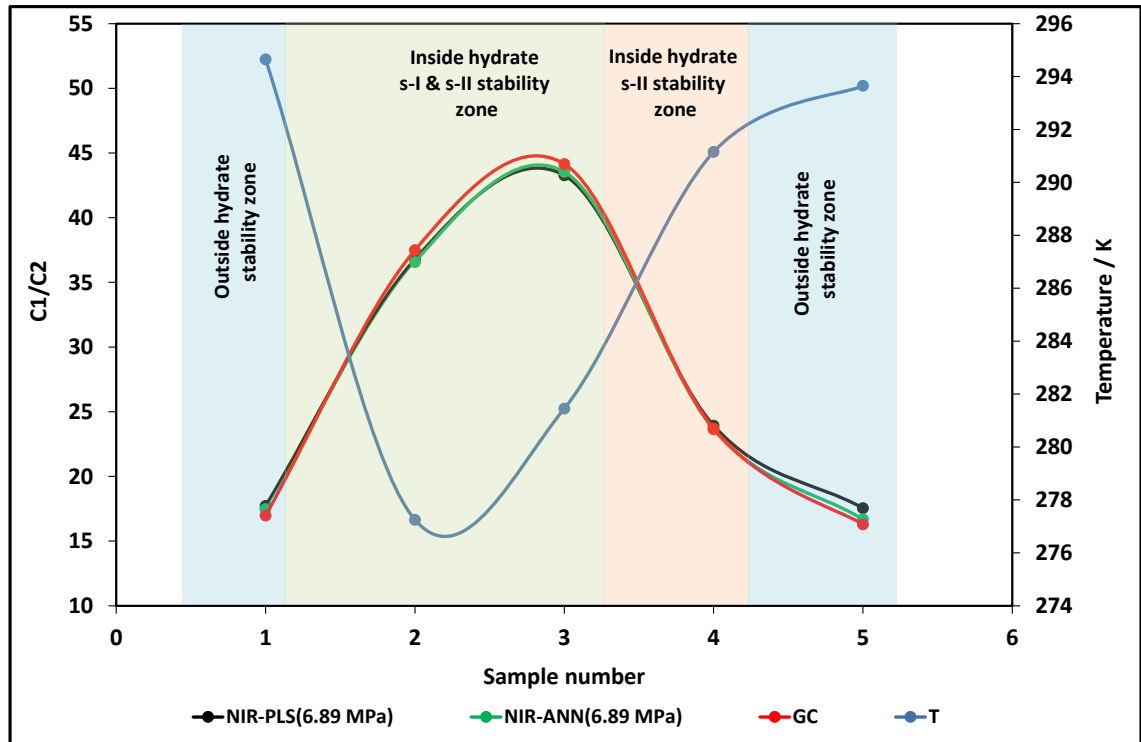


Figure 3.10. Compositional monitoring of C_1/C_2 ratio in the gas phase using GC and FTNIR at 6.89 MPa and 293.15 K. Connection trend between points are only for visual clarification.

Table 3.2. Evolution of C_1/C_3 ratio in vapour phase in the presence of NGA and deionised water.

T/K	P/MPa	Water in hydrate Barrel/MMscf	GC	PLS-6.89	PLS-3.44	ANN-6.89	ANN-3.44
294.65	12.49	-	66.2 (± 1.5)	69.9 (± 1.5)	67.4 (± 1.5)	72.2 (± 1.6)	74.4 (± 1.7)
277.25	7.83	182	313.2 (± 1.5)	230.3 (± 1.9)	230.0 (± 1.7)	201.9 (± 2.0)	175.7 (± 1.9)
281.45	7.77	162	336.4 (± 1.7)	236.4 (± 1.8)	197.5 (± 1.9)	198.2 (± 2.0)	169.9 (± 2.1)
291.15	10.56	32	99.6 (± 1.4)	88.5 (± 1.6)	83.5 (± 1.5)	96.3 (± 1.6)	95.2 (± 1.8)
293.65	11.21	0	63.7 (± 1.5)	72.2 (± 1.5)	75.1 (± 1.5)	64.0 (± 1.6)	79.1 (± 1.6)

Table 3.3. Evolution of C_1/C_2 ratio in vapour phase in the presence of NGA and deionised water.

T/K	P/MPa	Water in hydrate Barrel/MMscf	GC	PLS-6.89	PLS-3.44	ANN-6.89	ANN-3.44
294.65	12.49	-	16.9 (± 0.1)	17.7 (± 0.2)	17.6 (± 0.2)	17.5 (± 0.2)	17.8 (± 0.3)
277.25	7.83	182	37.5 (± 0.1)	36.8 (± 0.2)	35.0 (± 0.2)	36.6 (± 0.2)	36.9 (± 0.3)
281.45	7.77	162	44.1 (± 0.1)	43.3 (± 0.2)	38.0 (± 0.2)	43.5 (± 0.2)	40.7 (± 0.3)
291.15	10.56	32	23.7 (± 0.1)	23.9 (± 0.2)	22.7 (± 0.2)	23.7 (± 0.2)	22.4 (± 0.2)
293.65	11.21	0	16.3 (± 0.1)	17.6 (± 0.2)	17.1 (± 0.2)	16.7 (± 0.2)	17.0 (± 0.3)

One of the main objectives of these tests is first to characterise the accuracy of the NIR analyser relative to the GC measured values. The tables above summarises the results. As mentioned in the second chapter, the PLS made better predictions compared to ANN but based on the results presented hereafter; both methods are able to designate the changes in the concentration of gas phase as a result of hydrate formation. It can be seen there is a good agreement between the values that obtained between GC and NIR and it is apparent that all the calibration models follow the same trend that GC follows. This result has shown that the measurements from gas mixtures can be processed collectively using multivariate regression methods to predict the compositions of natural gas accurately. Multivariate regression modelling along with NIR spectroscopy and other gas measurement methods is a promising alternative technique to gas chromatography. As mentioned before, in these experiments hydrate was formed at different temperature and pressure conditions far inside hydrate structure I stability zone in order to see the effect of formation of hydrate structure I on compositional change technique. Figure 3.7 to Figure 3.10 show the results of this measurement for different calibration models. As one can see in Table 3.2 when the system is far inside sI hydrate stability zone the amount of water converted to hydrate is about 182 bbl/MMscf. It can be seen from aforementioned figures the methane to propane ratio and methane to ethane ratio start to increase, and it means that relatively more propane and ethane have been consumed during hydrate

formation which results in an increase in the concentration of methane that is a sign of sII hydrate formation. During hydrate dissociation, it is evident that the C_1/C_3 and C_1/C_2 ratios start to decrease while the system enters inside hydrate structure II and outside hydrate stability zone, it means that propane and ethane released from the aqueous phase and entered into the gas phase during hydrate dissociation. The results suggest that changes in C_1/C_3 and C_1/C_2 ratio are noticeable despite the formation of hydrate sI in the system. These results also show changes due to hydrate formation is significant enough to be detected with NIR spectroscopy. NIR could clearly detect the changes due to hydrate formation.

1.1.1.2 Test 2: Natural gas + deionised Water + 5 mass% NaCl

The second test was conducted for a system containing natural gas, deionised water, and 5 mass% NaCl. Figure 3.11 shows the temperature-pressure profile and the sampling points. In this test, 6 samples were taken, and all the spectra were recorded at a pressure of 6.89 MPa and temperature of 313.15 K.

- Sample 1: at 291.0 K and 12.79 MPa outside hydrate stability zone.
- Sample 2: at 276.90 K and 10.01 MPa inside the sI and sII hydrate stability zones.
- Sample 3: at 282.80 K and 10.0 MPa inside the sI and sII hydrate stability zones.
- Sample 4: at 286.50 K and 10.70 MPa outside the sI hydrate stability zone and inside sII hydrate stability zone.
- Sample 5: at 289.6 K and 11.27 MPa outside the sI hydrate stability zone and inside sII hydrate stability zone.
- Sample 6: at 290.7 K and 11.36 MPa outside hydrate stability zone.

As one can see in Figure 3.12 and Figure 3.13, by increasing the amount of water converted to hydrate, the ratio of methane to propane and methane to ethane is increased (more significantly in methane to propane ratio). Based on these results it can be concluded that, when the system is far inside sI hydrate stability zone for the even large amount of hydrate, the methane to propane and ethane to methane ratios will be increased. It means that if hydrate forms in a natural gas system, the methane to propane ratio will be more than that when the system never experienced hydrate. This property could be used for hydrate early warning system by monitoring the changes in the C_1/C_3 and C_1/C_2 ratio. Furthermore, all the hydrate formers will be released upon hydrate dissociation.

Although $i\text{-C}_4$ contributes to the formation of gas hydrates, changes in the concentration of $i\text{-C}_4$ was not accounted in this study due to low concentration of this component in the natural gas samples used in this work ($i\text{-butane} < 0.3 \text{ mol\%}$) and low accuracy of the NIR method while the concentration of the interested species in the gas phase is less than 0.2 mol\% ($\text{LoD} = 0.13 \text{ mol\%}$, see Table 2.10). As one can see from Figure 3.12, the C_1/C_3 ratio starts to decrease, while hydrate is dissociating. This is because of the liberation of propane from the aqueous phase, results in an increase in the concentration of propane in the gas phase.

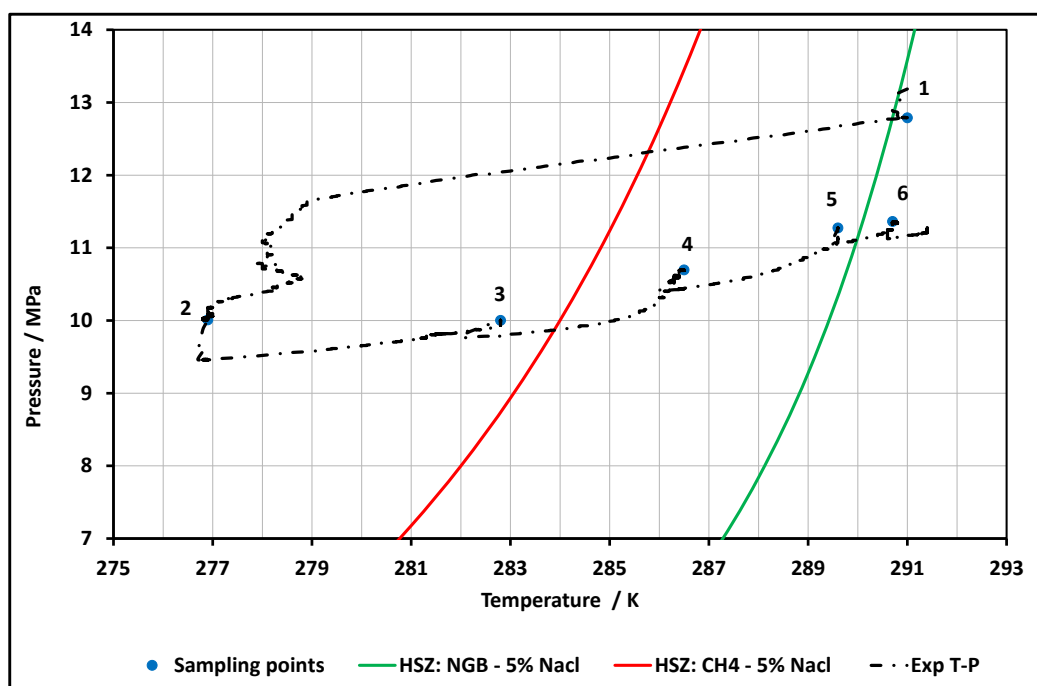


Figure 3.11. Temperature-pressure profile and sampling points for the system with NG-A, deionised water and salt.

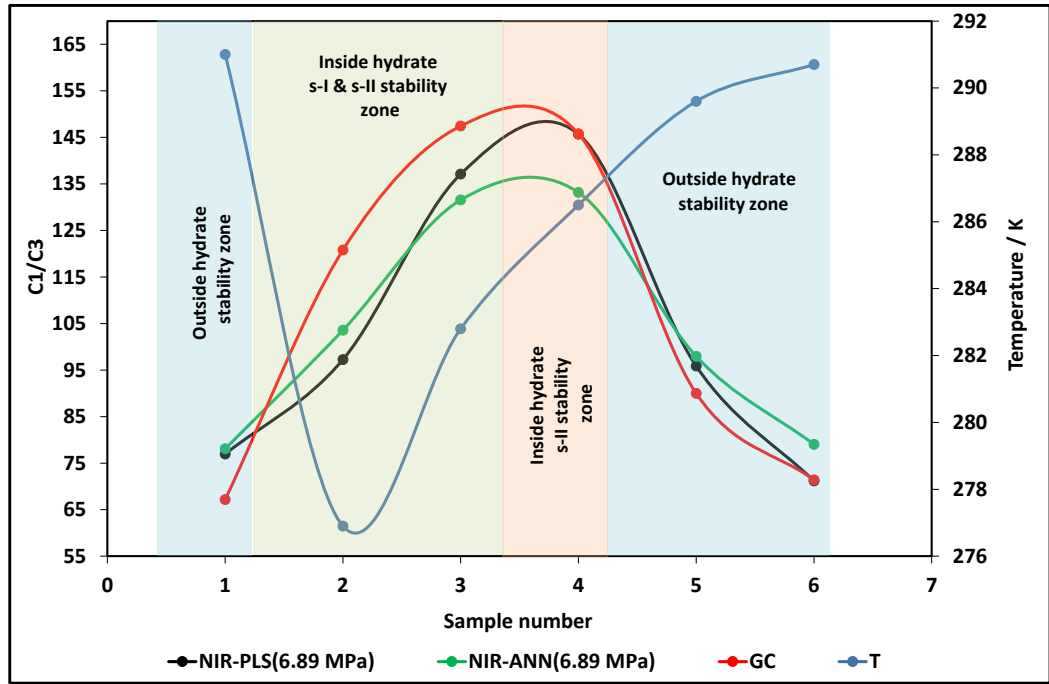


Figure 3.12. Compositional monitoring of C_1/C_3 ratio in the gas phase using GC and FTNIR at 6.89 MPa and 293.15 K. Connection trend between points are only for visual clarification.

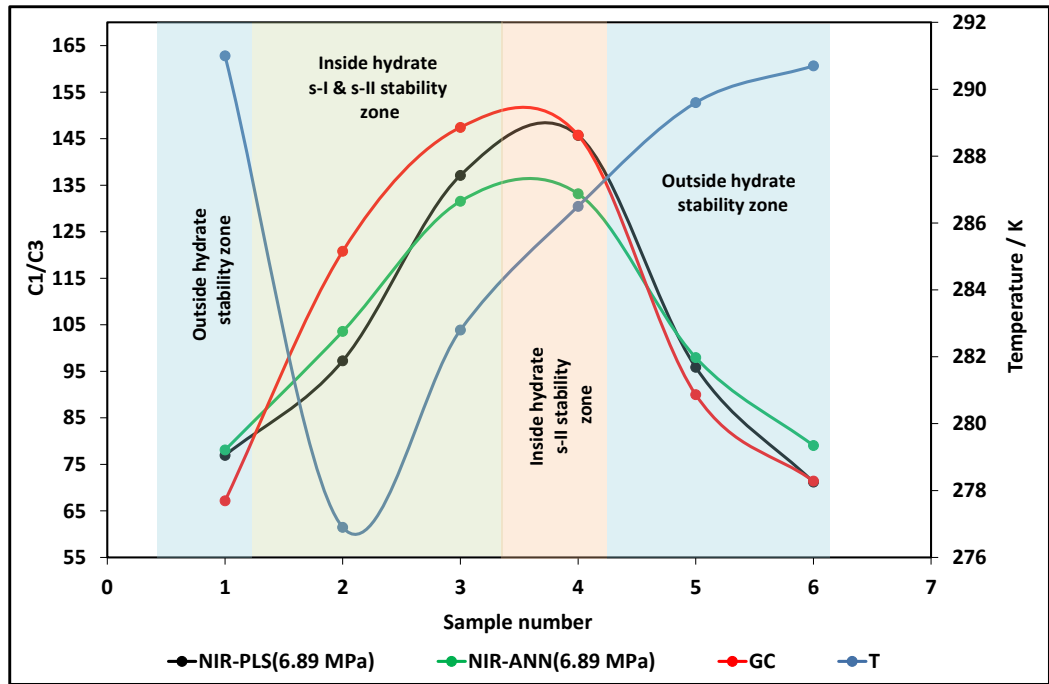


Figure 3.13. Compositional monitoring of C_1/C_2 ratio in the gas phase using GC and FTNIR at 6.89 MPa and 293.15 K. Connection trend between points are only for visual clarification.

Table 3.4. Evolution of C_1/C_3 ratio in the vapour phase in the presence of natural gas and deionised water and 5 mass% NaCl.

T/K	P/MPa	Water in hydrate Barrel/MMscf	GC	PLS-6.89	ANN-6.89
291.00	12.79	-	67.2 (± 2.1)	76.9 (± 2.2)	78.1 (± 2.1)
276.90	10.01	107	120.8 (± 1.8)	97.3 (± 2.5)	103.6 (± 2.2)
282.80	10.00	101	147.4 (± 2.2)	137.1 (± 3.1)	131.6 (± 3.3)
286.50	10.70	59.8	145.8 (± 2.8)	145.7 (± 3.3)	133.2 (± 2.3)
289.60	11.27	23.0	90.0 (± 2.0)	95.9 (± 2.2)	98.0 (± 2.0)
290.70	11.36	0	69.3 (± 1.9)	74.4 (± 2.0)	76.4 (± 2.1)

Table 3.5. Evolution of C_1/C_2 ratio in the vapour phase in the presence of natural gas and deionised water and 5 mass% NaCl.

T/K	P/MPa	Water in hydrate Barrel/MMscf	GC	PLS-6.89	ANN-6.89
291.00	12.79	-	16.9 (± 0.1)	18.4 (± 0.2)	18.3 (± 0.1)
276.90	10.01	107	20.3 (± 0.1)	21.9 (± 0.1)	23.0 (± 0.1)
282.80	10.00	101	21.2 (± 0.1)	22.4 (± 0.1)	22.6 (± 0.2)
286.50	10.70	59.8	21.7 (± 0.1)	23.7 (± 0.2)	23.0 (± 0.2)
289.60	11.27	23.0	18.7 (± 0.1)	20.7 (± 0.1)	20.9 (± 0.2)
290.70	11.36	0	17.1 (± 0.1)	18.8 (± 0.2)	19.0 (± 0.2)

Table 3.4 and Table 3.5 show comparisons of the C_1/C_2 ratio and C_1/C_3 ratio in vapour phase obtained with the FTNIR and the GC at a pressure of 6.89 MPa and temperature of 313.15 K. Results showed that changes in the gas composition could be detected for low amount of water converted to hydrate, indicating the capability of developed FTNIR prototype to detect initial signs of hydrate formation.

To investigate the effect of salt on hydrate memory, the system was left for 12 hours outside hydrate stability zone, and one sample (Sample 6) was taken. It was found that the concentration of propane and ethane were very close to the original composition before the formation of gas hydrate. These results suggested that presence of salt did not prolong the memory remaining time. As one can be seen from

Table 3.5, the C_1/C_2 ratio measured by NIR and GC was equal to 18.8 and 17.1 when the hydrate is fully dissociated, and these values are close to those measured by NIR and GC when the system has not experienced hydrates. Similar results were obtained for C_1/C_3

(see Table 3.4). This small difference in measured C_1/C_3 and C_1/C_2 ratios between the original value and the values measured while the hydrate was fully dissociated could be attributed to either uncertainty of the measurement or withdrawal of the gas samples during sampling from the system which removes more methane as propane and ethane contribute to gas hydrate formation (Table 3.6 through Table 3.8).

Table 3.6. Comparison of NIR results with GC for methane, average of three measurements, mol%

Sample	GC	PLS-6.89	ANN-6.89
1	92.67(±0.10)	93.10 (±0.11)	92.92 (±0.12)
2	94.22 (±0.11)	94.34 (±0.12)	94.25 (±0.13)
3	94.36 (±0.10)	94.61 (±0.12)	94.72 (±0.14)
4	94.75 (±0.10)	94.71 (±0.12)	94.55 (±0.13)
5	93.58 (±0.11)	93.94 (±0.11)	94.04 (±0.13)
6	92.82 (±0.11)	93.24 (±0.10)	93.27 (±0.12)

Table 3.7. Comparison of NIR results with GC for ethane, average of three measurements, mol%

Sample	GC	PLS-6.89	ANN-6.89
1	5.47 (±0.08)	5.06 (±0.09)	5.09 (±0.10)
2	4.65 (±0.09)	4.30 (±0.09)	4.09 (±0.11)
3	4.45 (±0.09)	4.23 (±0.09)	4.19 (±0.10)
4	4.37 (±0.09)	4.00 (±0.09)	4.12 (±0.11)
5	5.00 (±0.07)	4.54 (±0.08)	4.50 (±0.11)
6	5.44 (±0.08)	4.96 (±0.09)	4.90 (±0.11)

Table 3.8. Comparison of NIR results with GC for propane, average of three measurements, mol%

Sample	GC	NIR-6.89	ANN-6.89
1	1.38 (±0.03)	1.21 (±0.04)	1.19 (±0.05)
2	0.78 (±0.03)	0.97 (±0.04)	0.91 (±0.04)
3	0.64 (±0.03)	0.69 (±0.04)	0.72 (±0.04)
4	0.65 (±0.04)	0.65 (±0.03)	0.71 (±0.05)
5	1.04 (±0.03)	0.98 (±0.03)	0.96 (±0.05)
6	1.30 (±0.03)	1.31 (±0.04)	1.18 (±0.05)

1.1.1.3 Test 3: Natural gas + deionised water + 5 mass% NaCl + 10 mass% MEG

To study the effect of chemical additives on the performance of FTNIR method, MEG and methanol were used to examine this technique and also to study the sustainability of hydrate memory. This test was conducted for a system containing 5 mass% NaCl and 10 mass% MEG. In this test, the spectra were recorded at 293.15 K under 6.89 and 10.34 MPa, respectively. In this test, 8 samples were taken. Figure 3.14 shows the sampling points. The results are illustrated in Figure 3.15 to Figure 3.18 and tabulated in Table 3.9 and Table 3.10.

- Sample 1: at 290.6 K and 18.43 MPa outside hydrate stability zone.
- Sample 2: at 267.1 K and 13.75 MPa inside the sI and sII hydrate stability zones.
- Sample 3: at 283.6 K and 16.12 MPa inside the sI and sII hydrate stability zones.
- Sample 4: at 286.60 K and 16.23 MPa outside the hydrate sI stability zone and inside sII hydrate stability zone.
- Sample 5: at 288.0 K and 15.96 MPa outside the hydrate sI stability zone and inside sII hydrate stability zone.
- Sample 6: at 289.70 K and 16.12 MPa outside hydrate stability zone.
- Sample 7: at 291.40 K and 16.05 MPa outside hydrate stability zone.
- Sample 8: at 291.60 K and 15.71 MPa outside hydrate stability zone.

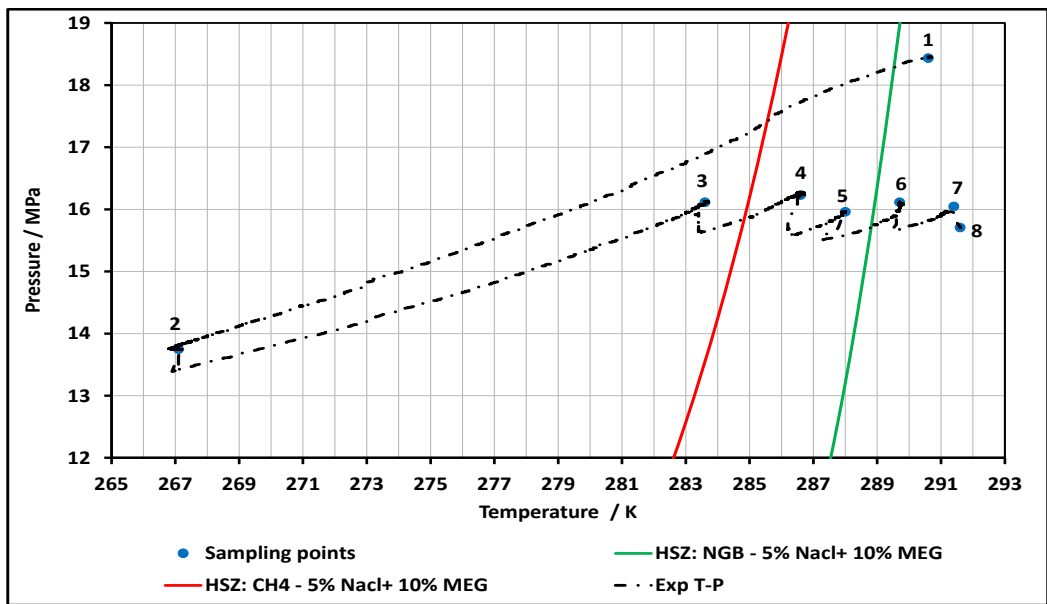


Figure 3.14. Temperature-pressure profile and sampling points for the system with NGB, deionised water, MEG and salt.

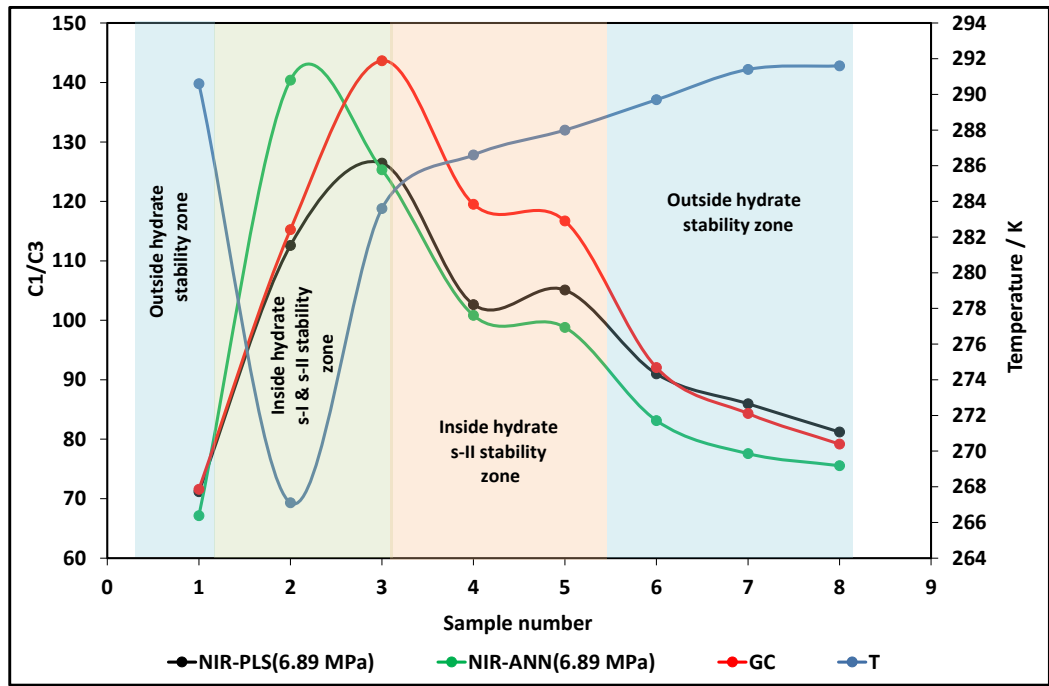


Figure 3.15. Compositional monitoring of C_1/C_3 ratio in the gas phase using GC and FTNIR at 6.89 MPa and 313.15 K. Connection trend between points are only for visual clarification.

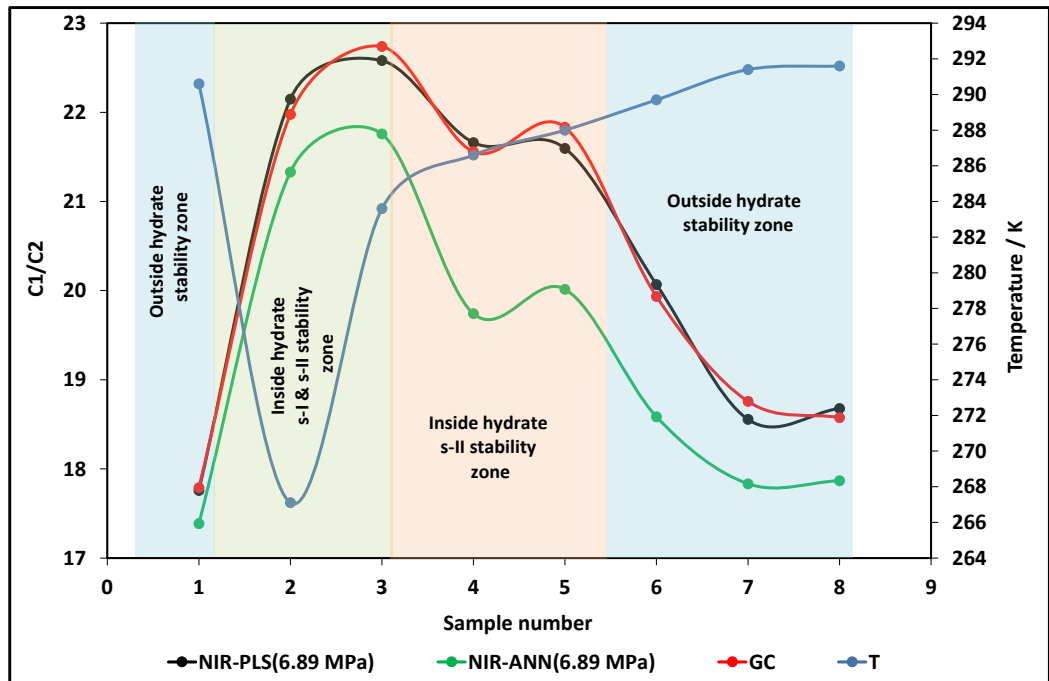


Figure 3.16. Compositional monitoring of C_1/C_2 ratio in the gas phase using GC and FTNIR at 6.89 MPa and 313.15 K. Connection trend between points are only for visual clarification.

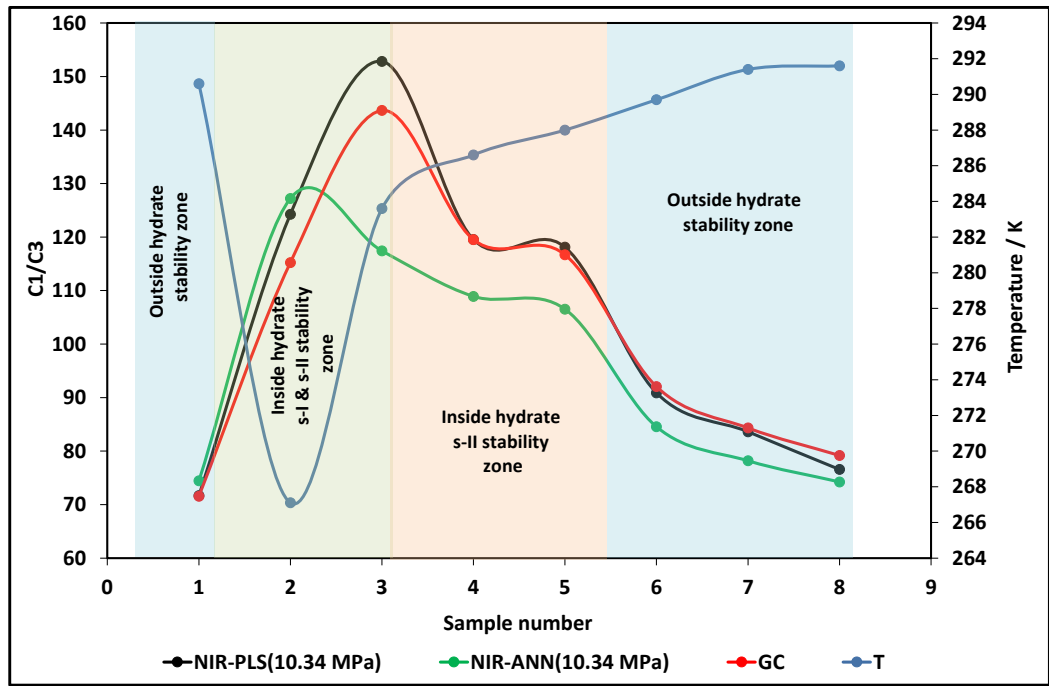


Figure 3.17. Compositional monitoring of C_1/C_3 ratio in the gas phase using GC and FTNIR at 10.34 MPa and 313.15 K. Connection trend between points are only for visual clarification.

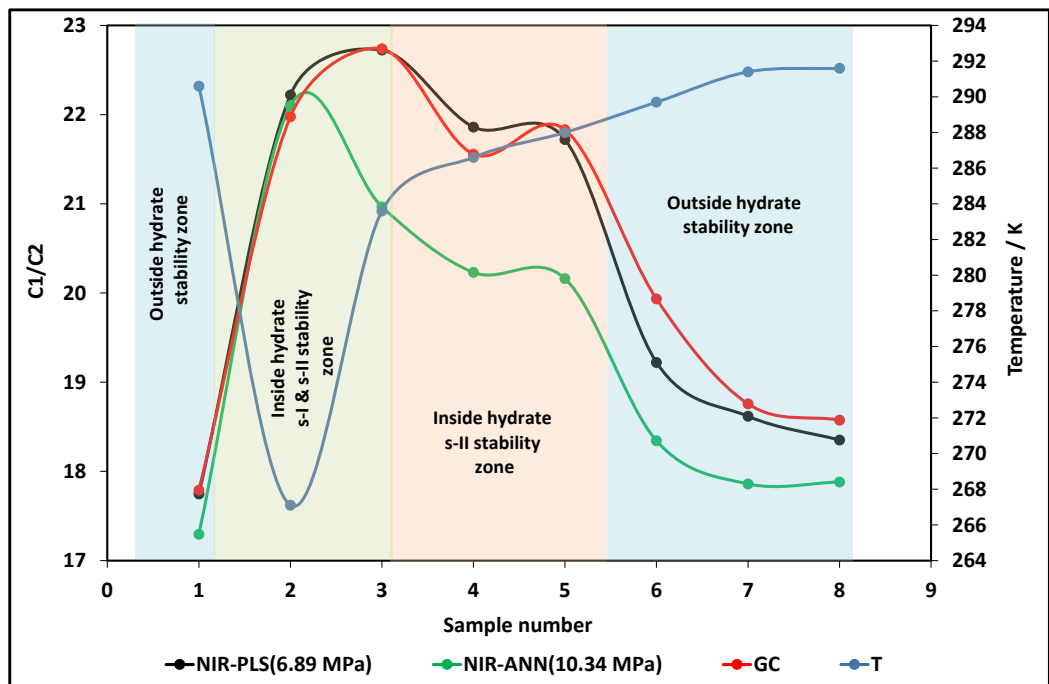


Figure 3.18. Compositional monitoring of C_1/C_2 ratio in the gas phase using GC and FTNIR at 10.34 MPa and 313.15 K. Connection trend between points are only for visual clarification.

Table 3.9. Evolution of C_1/C_3 ratio in the vapour phase in the presence of natural gas, deionised water, salt and MEG.

T/K	P/MPa	Water in hydrate Barrel/MMscf	GC	PLS-6.89	PLS-10.34	ANN-6.89	ANN-10.34
290.60	18.43	-	71.6	71.7 (± 1.8)	71.2 (± 2.0)	74.4 (± 1.9)	67.2 (± 2.0)
267.10	13.75	94.5	115.2	124.3 (± 1.7)	112.6 (± 2.1)	127.2 (± 2.0)	140.4 (± 1.9)
283.60	16.12	25.4	143.7	152.8 (± 1.9)	126.5 (± 2.0)	117.4 (± 2.0)	125.3 (± 2.1)
286.60	16.23	12.1	119.5	119.5 (± 1.8)	102.7 (± 2.0)	108.9 (± 1.9)	100.8 (± 2.0)
288.00	15.96	8.3	116.7	118.1 (± 1.8)	105.1 (± 2.0)	106.5 (± 1.8)	98.8 (± 1.9)
289.70	16.12	0	92.1	90.9 (± 1.9)	91.0 (± 1.8)	84.6 (± 1.9)	83.1 (± 2.1)
291.40	16.05	0	84.3	83.6 (± 1.8)	86.0 (± 2.0)	78.2 (± 2.0)	77.6 (± 1.9)
291.60	15.71	0	79.2	76.6 (± 2.0)	79.2 (± 1.8)	74.2 (± 1.9)	75.5 (± 2.0)

Table 3.10. Evolution of C_1/C_2 ratio in the vapour phase in the presence of natural gas, deionised water, salt and MEG.

T/K	P/MPa	Water in hydrate Barrel/MMscf	GC	PLS-6.89	PLS-10.34	ANN-6.89	ANN-10.34
290.60	18.43	-	17.8 (± 0.1)	17.8 (± 0.1)	17.8 (± 0.1)	17.3 (± 0.1)	17.4 (± 0.1)
267.10	13.75	94.5	22.0 (± 0.1)	22.2 (± 0.1)	22.2 (± 0.1)	22.1 (± 0.1)	21.3 (± 0.1)
283.60	16.12	25.4	22.7 (± 0.1)	22.7 (± 0.1)	22.6 (± 0.1)	21.0 (± 0.1)	21.8 (± 0.1)
286.60	16.23	12.1	21.6 (± 0.1)	21.9 (± 0.1)	21.7 (± 0.1)	20.2 (± 0.1)	19.7 (± 0.1)
288.00	15.96	8.3	21.8 (± 0.1)	21.7 (± 0.1)	21.6 (± 0.1)	20.2 (± 0.1)	20.0 (± 0.1)
289.70	16.12	0	19.9 (± 0.1)	19.2 (± 0.1)	20.1 (± 0.1)	18.3 (± 0.1)	18.6 (± 0.1)
291.40	16.05	0	18.8 (± 0.1)	18.6 (± 0.1)	18.6 (± 0.1)	17.9 (± 0.1)	17.8 (± 0.1)
291.40	15.71	0	18.6 (± 0.1)	18.4 (± 0.1)	18.7 (± 0.1)	17.9 (± 0.1)	17.9 (± 0.1)

The results show that it is possible to detect hydrate formation by monitoring the gas composition (e.g., C_3 and/or C_2 concentration, C_1/C_3 and/or C_1/C_2 ratio) despite the co-formation of sI and sII hydrates and high amount of water converted to hydrate.

The changes in the concentration of propane, ethane, and the methane to propane ratio and methane to ethane ratio in the gas phase were used to determine hydrate memory. After hydrate formation and dissociation, the system was first left 12 hours outside the hydrate stability zone. It was found that amount of propane and ethane still remained in the aqueous phase after about 12 hours (Sample 6). Hence, the temperature was increased to 291.40 K and system were left for 8 hours, and another sample was taken and analysed by GC and NIR. It was found that the C_1/C_3 and C_1/C_2 values measured by NIR prototype at a pressure of 6.89 MPa were decreased from 90.88 to 83.62 and 19.22 to 18.62

respectively, but they are still far from the original value. Then again the system was left at the same temperature for 12 hours and at this time changes were noticed in a C_1/C_3 ratio from 83.62 to 76.57 which is closer to the original value. It can be seen that the memory is still detectable. Table 3.11 shows the changes in the concentration of propane and ethane that were obtained from GC and FTNIR while the system is outside hydrate stability zone.

Table 3.11. Comparison of NIR results with GC for propane, mol%.

Sample	GC - propane	NIR - propane	GC - ethane	NIR - ethane
1	1.30	1.30	5.14	5.16
6	1.02	1.03	4.71	4.87
7	1.11	1.12	4.99	5.03
8	1.18	1.23	5.08	5.11

In general, increasing retaining time and the temperature outside hydrate stability zone expedited the hydrate memory disappearance which is different from the other systems. These results suggested that the presence of MEG in the system prolonged the hydrate memory.

1.1.1.4 Test 4: Natural gas + deionised water + 5 mass% NaCl + 15 mass% Methanol

In this test, hydrates were formed in the presence of deionised water, salt, methanol and natural gas (NG-C). In this test, the spectra of samples were recorded at a pressure of 6.89 and 10.34 MPa and temperature of 313.15 K. The test was conducted at 6 stages as explained in following:

- Sample 1: at 289.0 K and 19.82 MPa outside hydrate stability zone.
- Sample 2: at 268.70 K and 14.59 MPa inside the sI and sII hydrate stability zones.
- Sample 3: at 279.10 K and 16.08 MPa inside the sI and sII hydrate stability zones.
- Sample 4: at 282.0 K and 16.22 MPa outside the hydrate sI stability zone and inside sII hydrate stability zone.
- Sample 5: at 283.60 K and 16.21 MPa outside the hydrate sI stability zone and inside sII hydrate stability zone.
- Sample 6: at 286.60 and 16.51 MPa outside hydrate stability zone.

As it can be seen from Figure 3.20 to Figure 3.23, the changes in methane to propane ratio and methane to ethane ratio are noticeable when the system is far inside hydrate stability sI stability zone.

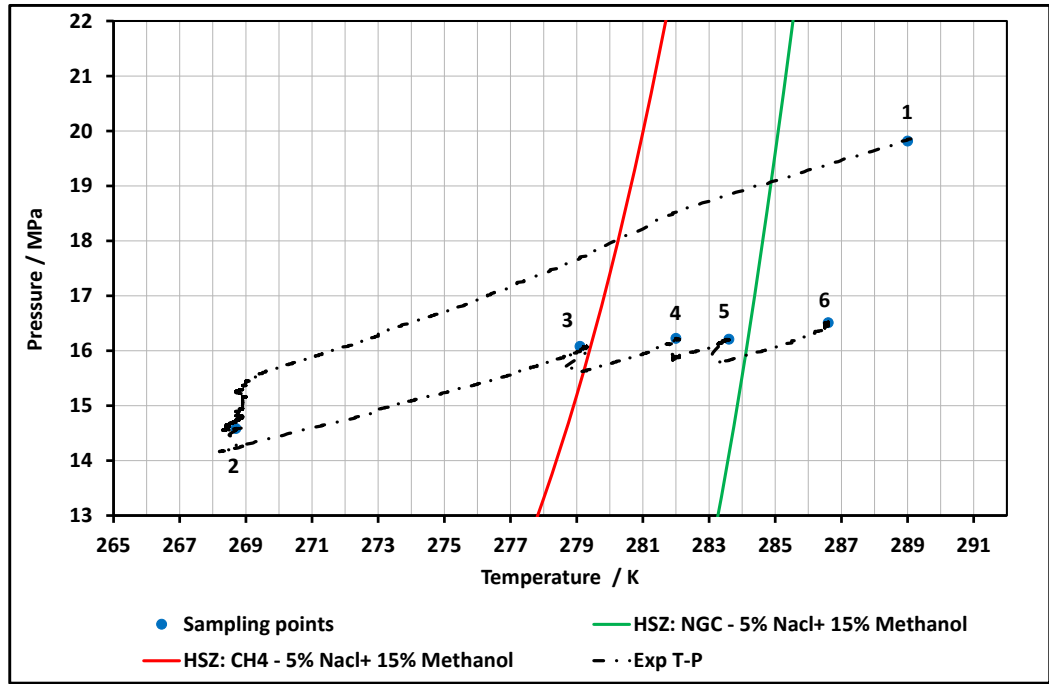


Figure 3.19. Temperature-pressure profile and sampling points for the system with NGB, deionised water, methanol and salt.

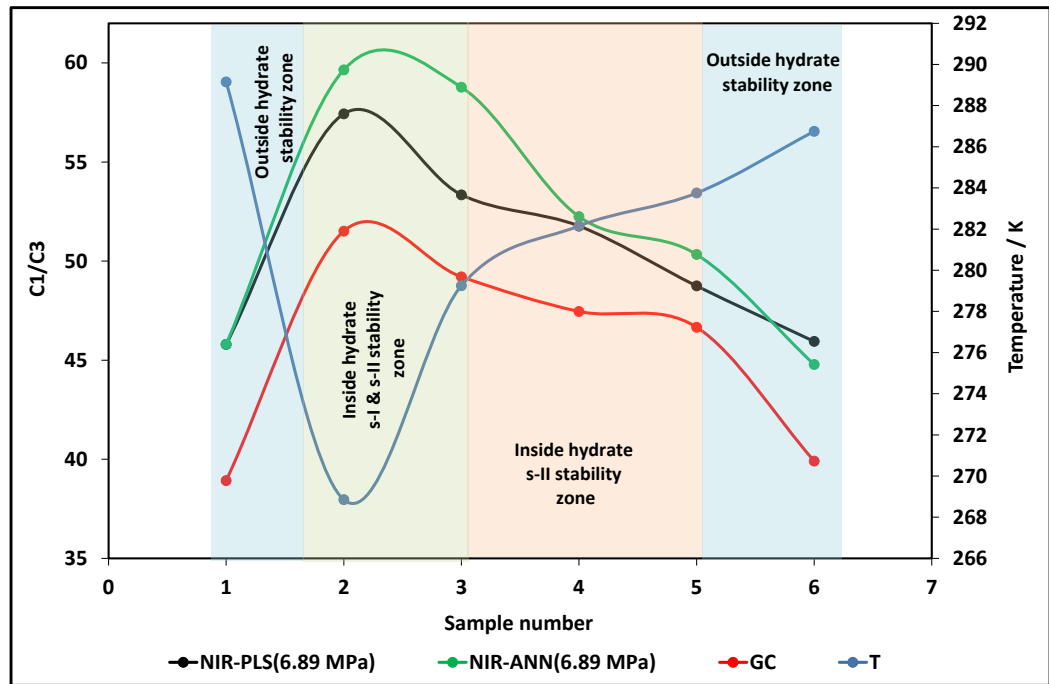


Figure 3.20. Compositional monitoring of C₁/C₃ ratio in the gas phase using GC and FTNIR at 6.89 MPa and 313.15 K. Connection trend between points are only for visual clarification.

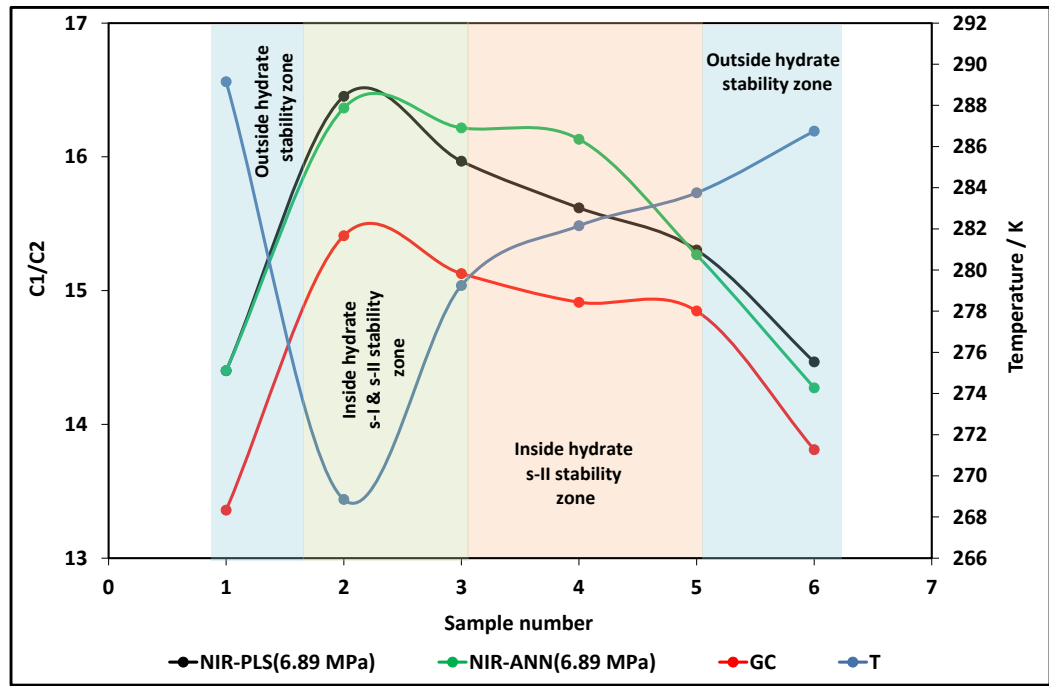


Figure 3.21. Compositional monitoring of C_1/C_2 ratio in the gas phase using GC and FTNIR at 6.89 MPa and 313.15 K. Connection trend between points are only for visual clarification.

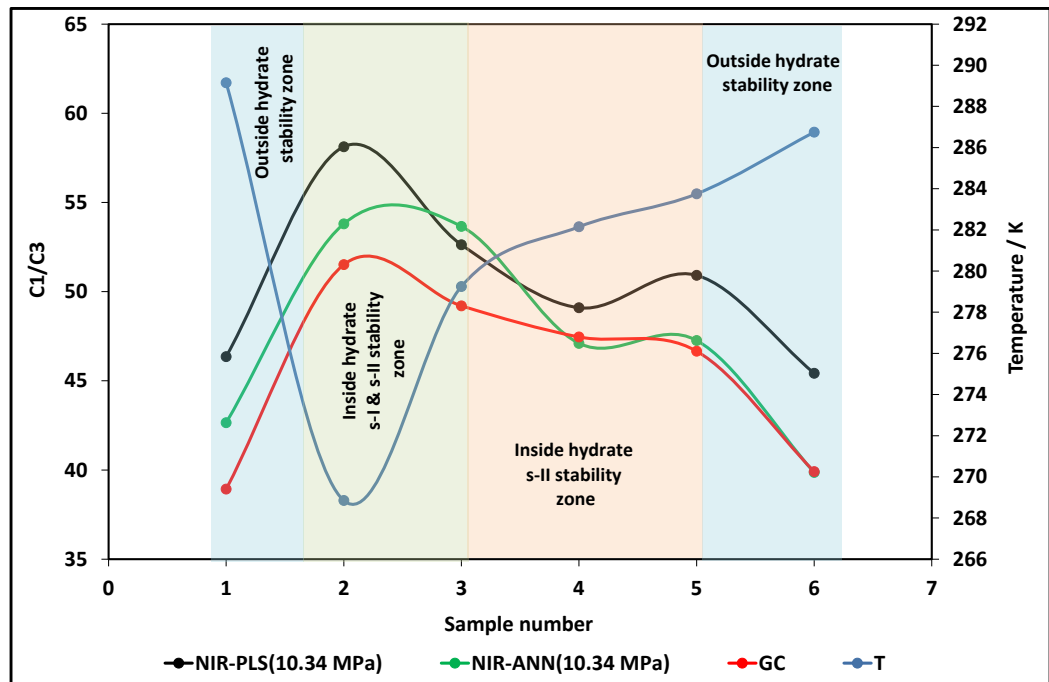


Figure 3.22. Compositional monitoring of C_1/C_3 ratio in the gas phase using GC and FTNIR at 10.34 MPa and 313.15 K. Connection trend between points are only for visual clarification.

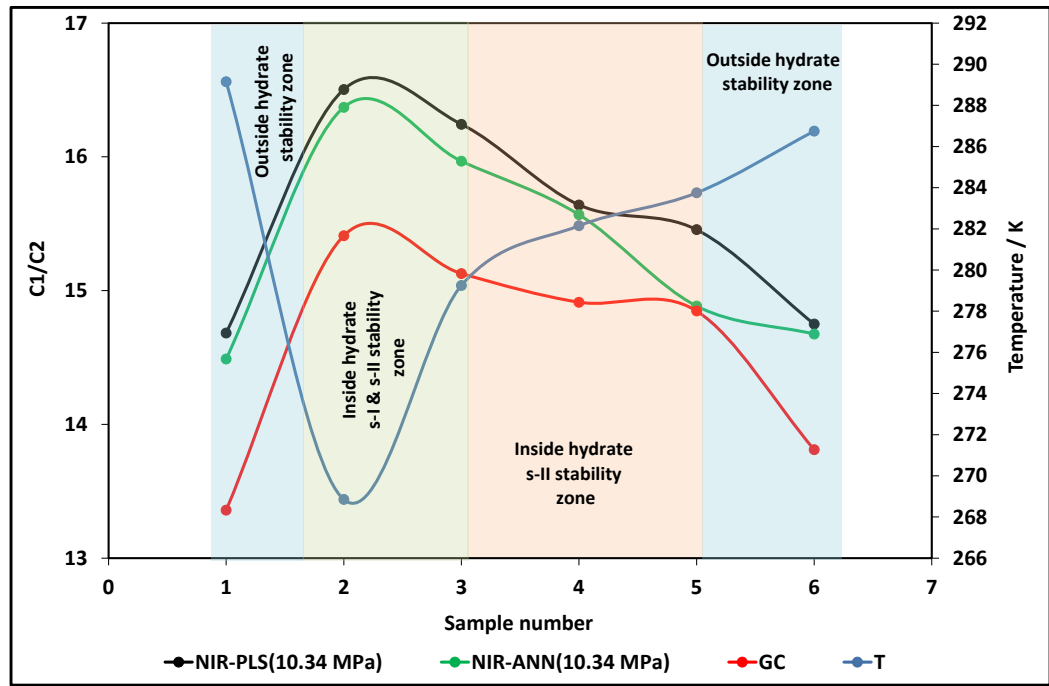


Figure 3.23. Compositional monitoring of C_1/C_2 ratio in the gas phase using GC and FTNIR at 10.34 MPa and 313.15 K. Connection trend between points are only for visual clarification.

Table 3.12. Evolution of C_1/C_3 ratio in the vapour phase in the presence of natural gas, deionised water, salt and methanol.

T/K	P/MPa	Water in hydrate Barrel/MMscf	GC	PLS-6.89	C1/C3 PLS-10.34	ANN-6.89	ANN-10.34
289.0	19.82	-	46.4 (± 1.1)	45.8 (± 1.2)	42.7 (± 1.1)	45.8 (± 1.3)	46.4 (± 1.1)
268.7	14.59	79.9	58.1 (± 1.2)	57.4 (± 1.0)	53.8 (± 1.3)	59.7 (± 1.3)	58.1 (± 1.3)
279.1	16.08	42.8	52.6 (± 1.1)	53.4 (± 1.2)	53.7 (± 1.3)	58.8 (± 1.2)	52.6 (± 1.4)
282.0	16.22	21.6	49.1 (± 1.0)	51.8 (± 1.1)	47.1 (± 1.2)	52.2 (± 1.5)	49.1 (± 1.2)
283.6	16.21	7.8	50.9 (± 1.0)	48.8 (± 1.2)	47.3 (± 1.2)	50.3 (± 1.1)	50.9 (± 1.2)
286.6	16.51	0	45.4 (± 1.0)	45.9 (± 1.2)	39.9 (± 1.1)	44.8 (± 1.2)	45.4 (± 1.2)

Table 3.13. Evolution of C_1/C_2 ratio in the vapour phase in the presence of natural gas, deionised water, salt and methanol.

T/K	P/MPa	Water in hydrate Barrel/MMscf	GC	PLS-6.89	C1/C2 PLS-10.34	ANN-6.89	ANN-10.34
289.0	19.82	-	13.4 (± 0.1)	14.7 (± 0.1)	14.4 (± 0.1)	14.5 (± 0.1)	14.4 (± 0.1)
268.7	14.59	79.9	15.4 (± 0.1)	16.5 (± 0.1)	16.5 (± 0.1)	16.4 (± 0.1)	16.4 (± 0.1)
279.1	16.08	42.8	15.1 (± 0.1)	16.2 (± 0.1)	16.0 (± 0.1)	16.0 (± 0.1)	16.2 (± 0.1)
282.0	16.22	21.6	14.9 (± 0.1)	15.6 (± 0.1)	15.6 (± 0.1)	15.6 (± 0.1)	16.1 (± 0.1)
283.6	16.21	7.8	14.9 (± 0.1)	15.5 (± 0.1)	15.3 (± 0.1)	14.9 (± 0.1)	15.3 (± 0.1)
286.6	16.51	0	13.8 (± 0.1)	14.8 (± 0.1)	14.5 (± 0.1)	14.7 (± 0.1)	14.3 (± 0.1)

Table 3.12 and Table 3.13 show comparisons of the C_1/C_2 ratio and C_1/C_3 ratio in vapour phase obtained with the NIR and the gas chromatograph. Similar trends are observed for all the presented method. After hydrate formation and dissociation, the system was left for 12 hours outside the hydrate stability zone (2 K outside the hydrate stability zone) and one sample was taken and analysed by GC and NIR. Based on the results, the C_1/C_2 and C_1/C_3 measured values by GC and NIR are very close to those measured by GC and FTNIR with the same system without hydrate memory. These results show that methanol does not prolong the hydrate memory remaining time and hydrocarbons were almost fully recovered from the gas phase.

1.1.1.5 Test 5: Natural gas + deionised water + 5 mass % NaCl + 2.5 mass % Luvicap

In this test, hydrates were formed in the presence of natural gas, deionised water and KHI inhibitor (Luvicap). The aim of this experiment was to study the effect of KHI on compositional change technique and their effect on the sustainability of hydrate memory. The experiments were conducted in the same procedure in the previous ones. In this test, 8 samples were taken. Figure 3.24 shows a typical temperature-pressure profile and the 8 sampling points.

- Sample 1: at 294.55 K and 22.11 MPa outside hydrate stability zone.
- Sample 2: at 269.75 K and 15.55 MPa inside the sI and sII hydrate stability zones.
- Sample 3: at 288.65 K and 18.94 MPa inside the sI and sII hydrate stability zones.
- Sample 4: at 290.25 K and 18.73 MPa outside the sI hydrate stability zone and inside sII hydrate stability zone.
- Sample 5: at 291.75 K and 18.86 MPa outside the sI hydrate stability zone and inside sII hydrate stability zone.
- Sample 6: at 294.65 K and 18.88 MPa outside the hydrate stability zone.
- Sample 7: at 294.65 K and 18.42 MPa outside the hydrate stability zone.
- Sample 8: at 296.65 K and 18.41 outside the hydrate stability zone.

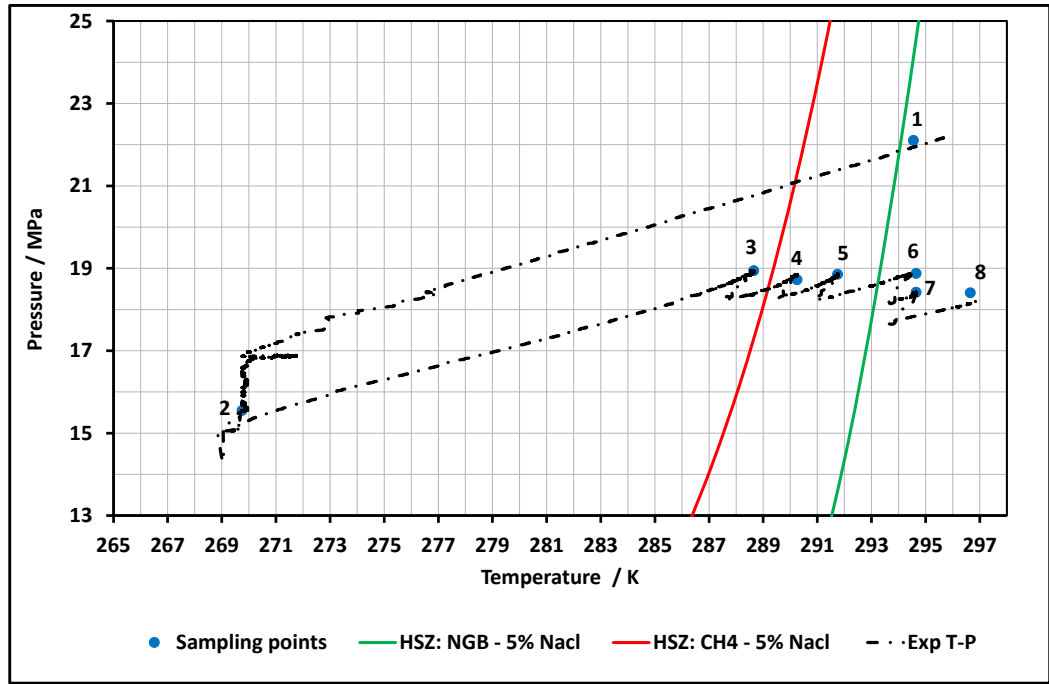


Figure 3.24. Temperature-pressure profile and sampling points for the system with NG-B, deionised water, Luvicap and salt.

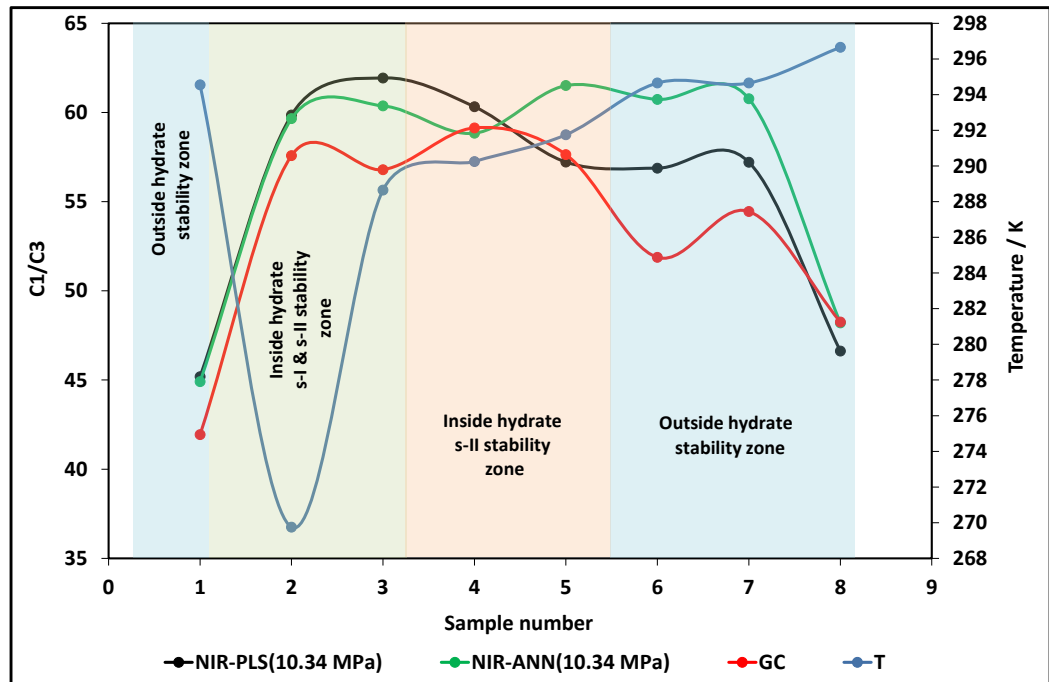


Figure 3.25. Compositional monitoring of C_1/C_3 ratio in the gas phase using GC and FTNIR at 10.34 MPa and 313.15 K. Connection trend between points are only for visual clarification.

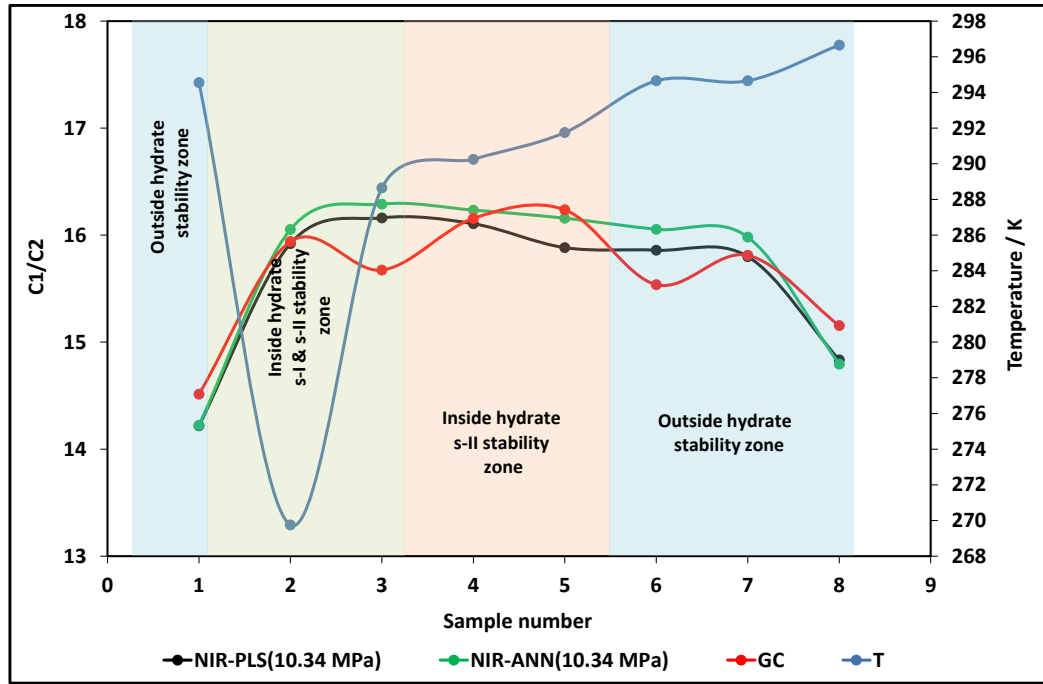


Figure 3.26. Compositional monitoring of C_1/C_2 ratio in the gas phase using GC and FTNIR at 10.34 MPa and 313.15 K. Connection trend between points are only for visual clarification.

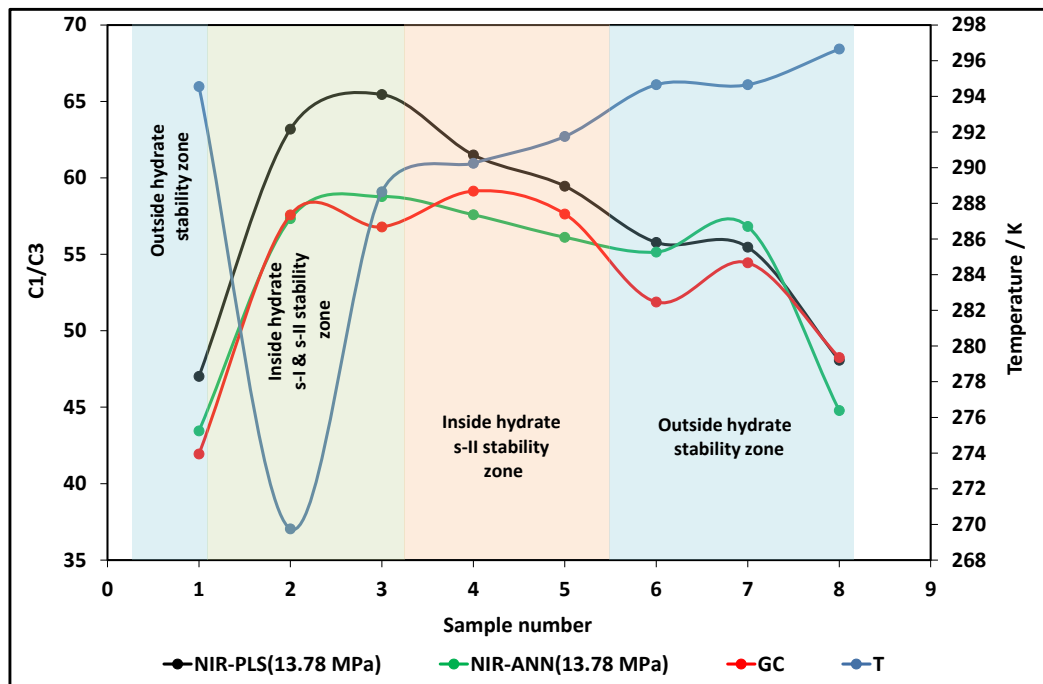


Figure 3.27. Compositional monitoring of C_1/C_3 ratio in the gas phase using GC and FTNIR at 13.78 MPa and 313.15 K. Connection trend between points are only for visual clarification.

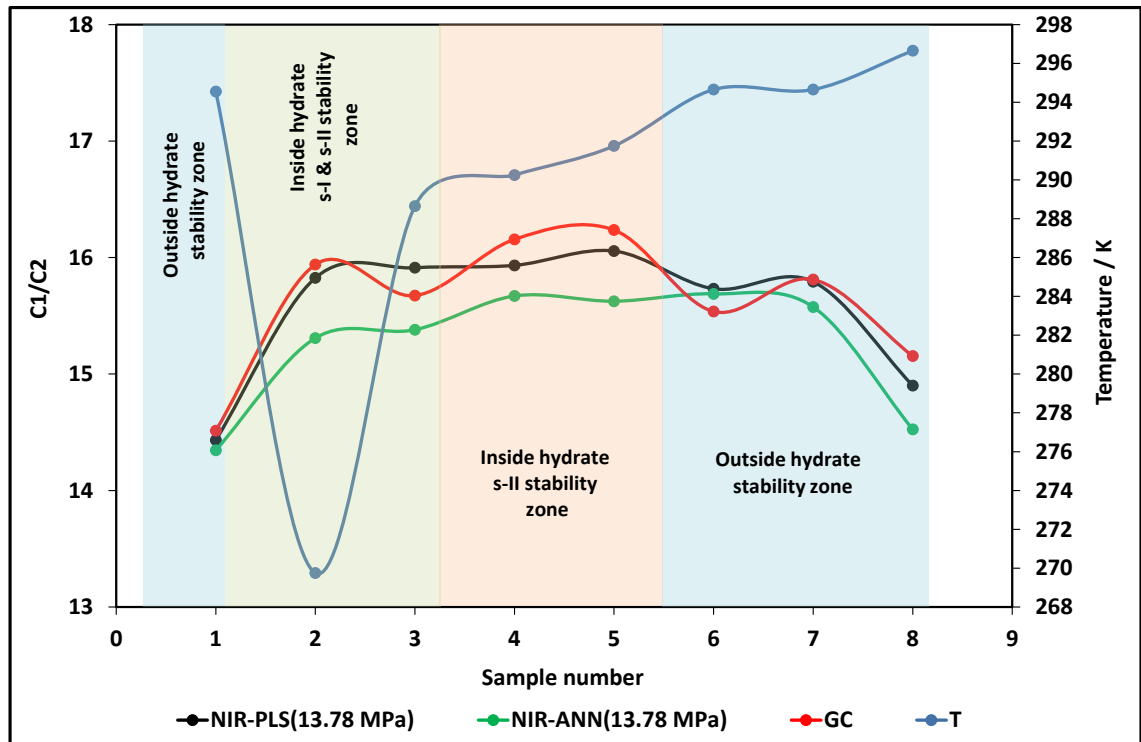


Figure 3.28. Compositional monitoring of C_1/C_2 ratio in the gas phase using GC and FTNIR at 13.78 MPa and 313.15 K. Connection trend between points are only for visual clarification.

Table 3.14. Evolution of C_1/C_3 ratio in vapour phase in the presence of natural gas, deionised water and Luvicap.

T/K	P/MPa	Water in hydrate Barrel/MMscf	C_1/C_2				
			GC	PLS-10.34	PLS-13.78	ANN-10.34	ANN-13.78
294.55	22.11	-	41.9 (± 1.2)	47.0 (± 1.8)	45.2 (± 1.7)	43.5 (± 1.6)	44.9 (± 2.0)
269.75	15.55	72.5	57.6 (± 1.4)	63.2 (± 1.9)	59.9 (± 1.9)	57.3 (± 1.5)	59.7 (± 1.9)
288.65	18.94	53.6	56.8 (± 1.5)	65.5 (± 2.0)	61.9 (± 1.9)	58.8 (± 1.8)	60.4 (± 1.9)
290.25	18.73	40.2	59.1 (± 1.5)	61.5 (± 1.9)	60.3 (± 1.8)	57.6 (± 1.9)	58.8 (± 1.9)
291.75	18.86	16.5	57.6 (± 1.6)	59.5 (± 1.9)	57.2 (± 1.8)	56.1 (± 1.9)	61.5 (± 1.9)
294.65	18.88	0	51.9 (± 1.4)	55.8 (± 1.8)	56.9 (± 1.6)	55.1 (± 1.8)	60.7 (± 1.9)
294.65	18.42	0	54.5 (± 1.4)	55.5 (± 1.8)	57.2 (± 1.8)	56.8 (± 1.8)	60.8 (± 2.0)
296.65	18.41	0	48.3 (± 1.4)	48.1 (± 1.8)	46.6 (± 1.8)	44.8 (± 1.8)	48.2 (± 1.9)

Table 3.15. Evolution of C_1/C_2 ratio in vapour phase in the presence of natural gas, deionised water and Luvicap.

T/K	P/MPa	Water in hydrate Barrel/MMscf	GC	PLS-10.34	PLS-13.78	ANN-10.34	ANN-13.78
294.55	22.11	-	14.5 (± 0.1)	14.4 (± 0.1)	14.2 (± 0.1)	14.4 (± 0.1)	14.2 (± 0.1)
269.75	15.55	72.5	15.9 (± 0.1)	15.8 (± 0.1)	15.9 (± 0.1)	15.3 (± 0.1)	16.1 (± 0.1)
288.65	18.94	53.6	15.7 (± 0.1)	15.9 (± 0.1)	16.2 (± 0.1)	15.4 (± 0.1)	16.3 (± 0.1)
290.25	18.73	40.2	16.2 (± 0.1)	15.9 (± 0.1)	16.1 (± 0.1)	15.7 (± 0.1)	16.2 (± 0.1)
291.75	18.86	16.5	16.2 (± 0.1)	16.1 (± 0.1)	15.9 (± 0.1)	15.6 (± 0.1)	16.2 (± 0.1)
294.65	18.88	0	15.5 (± 0.1)	15.7 (± 0.1)	15.9 (± 0.1)	15.7 (± 0.1)	16.1 (± 0.1)
294.65	18.42	0	15.8 (± 0.1)	15.8 (± 0.1)	15.8 (± 0.1)	15.6 (± 0.1)	16.0 (± 0.1)
296.65	18.41	0	15.2 (± 0.1)	14.9 (± 0.1)	14.8 (± 0.1)	14.5 (± 0.1)	14.8 (± 0.1)

The results are shown in Figure 3.25 to Figure 3.28 and Table 3.14 and Table 3.15. It is clear that the C_1/C_3 ratios measured by GC and FTNIR increase significantly while the system is far inside hydrate stability zone and this ratio decrease gradually during hydrate dissociation.

To evaluate the water memory method in the presence of Luvicap, the temperature was increased to 2 K outside hydrate stability zone for waiting 12 and 24 hours. It was found that amount of propane and ethane still remained in the aqueous phase after about 36 hours. GC analysis showed that concentration of ethane and propane changed from 1.60 mol% and 5.68 mol% to 1.77 mol% and 5.91 mol% when the system goes outside the hydrate stability zone after 12 hours (see Table 3.16). As mentioned in above, the system was left at the same temperature for more 12 hours, and no significant change was observed in the concentration of propane and ethane. Hence, the temperature was increased to 296.65 K (about 3 K outside the hydrate stability zone), and the system was left for 24 hours, and another sample was taken and analysed by GC and FTNIR. This time, it was noticed that the concentration of ethane and propane changed from 1.77 mol% and 5.68 mol% to 1.92 mol% and 6.05 mol%. Similar results were obtained for NIR as well.

It shows that waiting at 3 K outside the hydrate stability zone for even a long time outside hydrate stability zone didn't kill the memory. Therefore, the system was heated up to a higher temperature in order to remove the hydrate memory. These results show that KHI inhibitors could prolong the hydrate memory time.

Table 3.16. Comparison of NIR results with gas chromatograph for propane and ethane, mol%.

Sample	GC - propane	NIR - propane	GC - ethane	NIR - ethane
1	2.17	2.01	6.27	6.32
5	1.60	1.55	5.68	5.74
6	1.77	1.65	5.91	5.85
7	1.75	1.66	5.90	5.83
8	1.92	1.91	6.05	6.13

1.1.1.6 Test 6: Natural gas + deionised water + 5 mass% NaCl + 10 mass% Methanol + gas condensate

In this test, hydrates were formed in the presence of natural gas, deionised water, 5 mass% NaCl, 10 mass% methanol and 3 vol% gas condensate. The aim of this test was to investigate the effect of the presence of condensate on the sustainability of hydrate memory. In this test, 6 samples were taken. Figure 3.29 shows a typical temperature-pressure profile and the 6 sampling points.

- Sample 1: at 289 K and 24.03 MPa outside hydrate stability zone.
- Sample 2: at 266.4 K and 17.95 MPa inside the sI and sII hydrate stability zones.
- Sample 3: at 282 K and 21.25 MPa inside the sI and sII hydrate stability zones.
- Sample 4: at 284.9 K and 21.25 MPa outside the sI hydrate stability zone and inside sII hydrate stability zone.
- Sample 5: at 286.6 K and 21.14 MPa outside the sI hydrate stability zone and inside sII hydrate stability zone.
- Sample 6: at 286.6 K and 20.77 MPa outside hydrate stability zone.

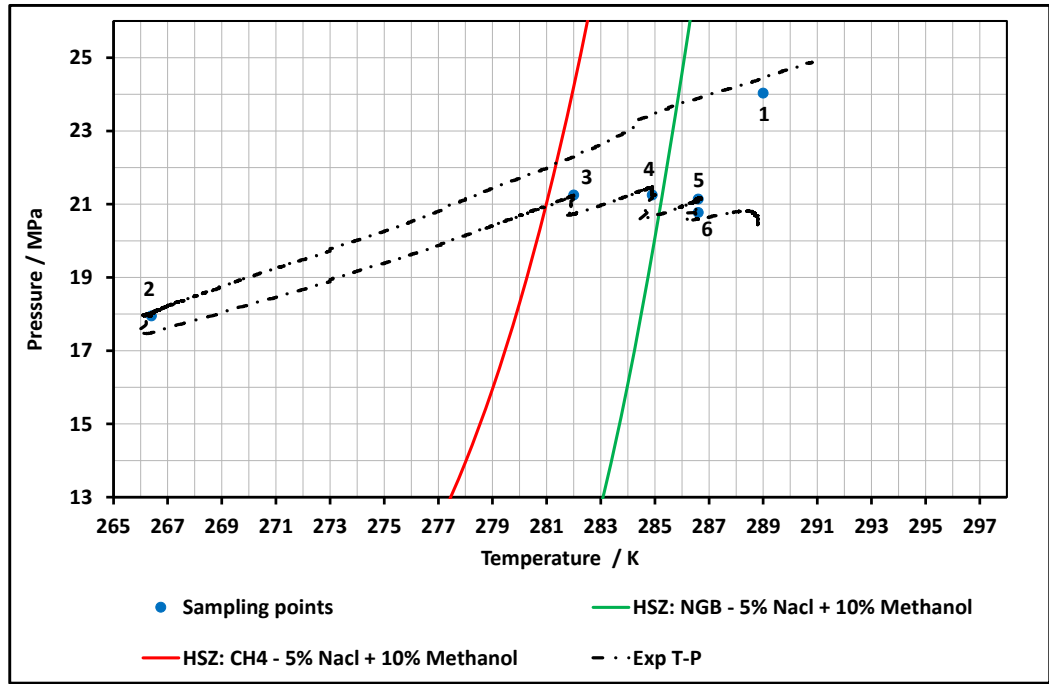


Figure 3.29. Temperature-pressure profile and sampling points for the system with NGB, deionised water, methanol, gas condensate and salt.

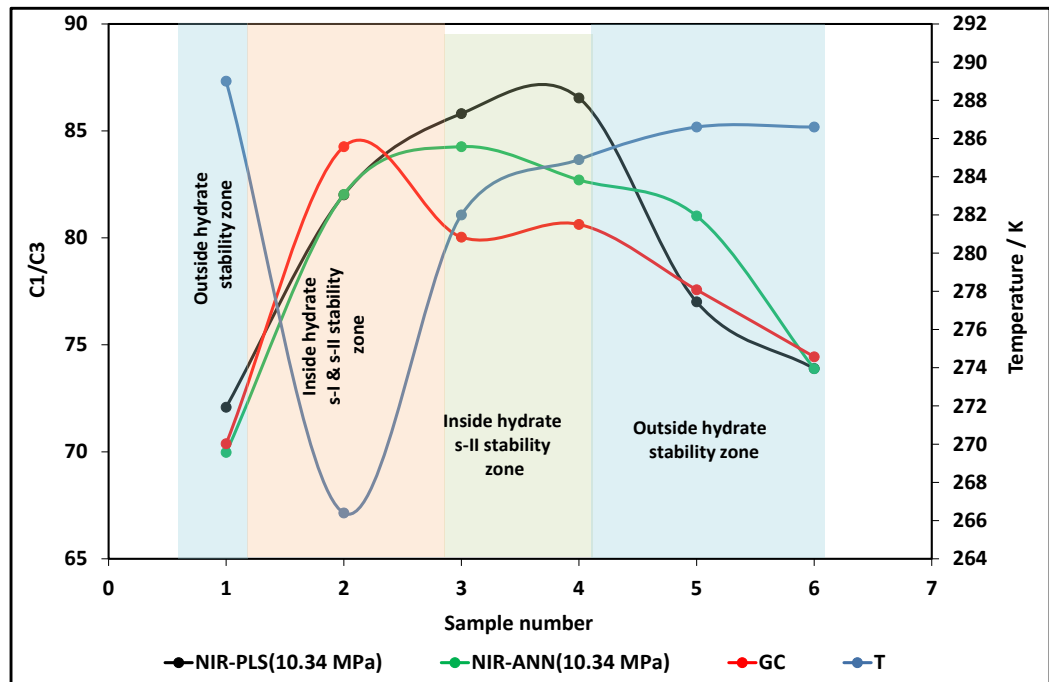


Figure 3.30. Compositional monitoring of C₁/C₃ ratio in the gas phase using GC and FTNIR at 6.89 MPa and 293.15 K. Connection trend between points are only for visual clarification.

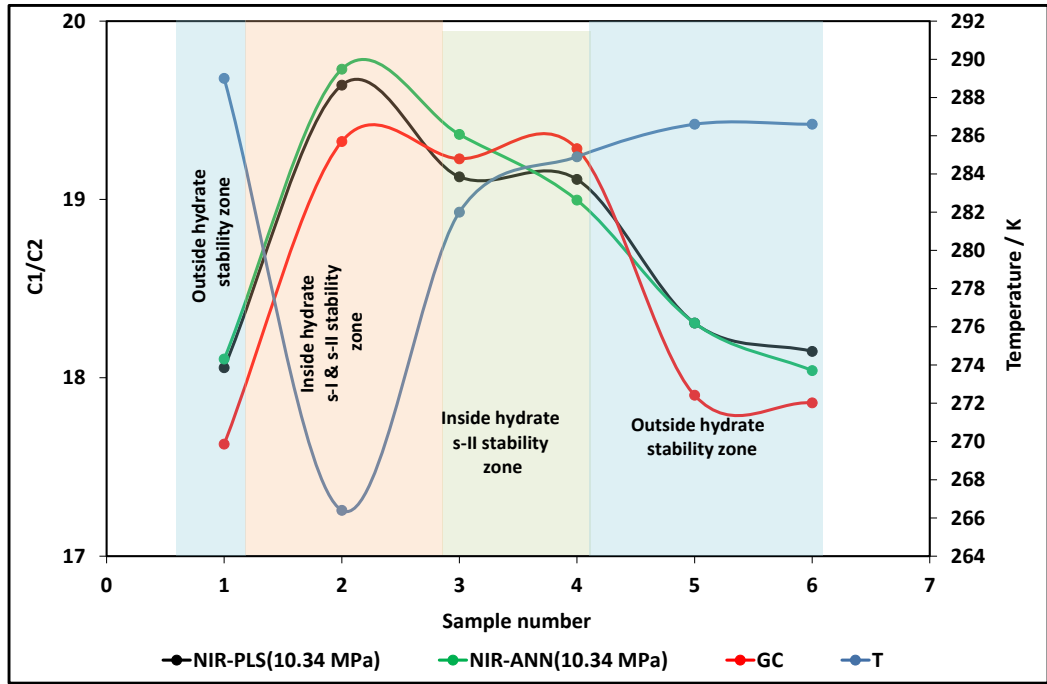


Figure 3.31. Compositional monitoring of C_1/C_2 ratio in the gas phase using GC and FTNIR at 6.89 MPa and 293.15 K. Connection trend between points are only for visual clarification.

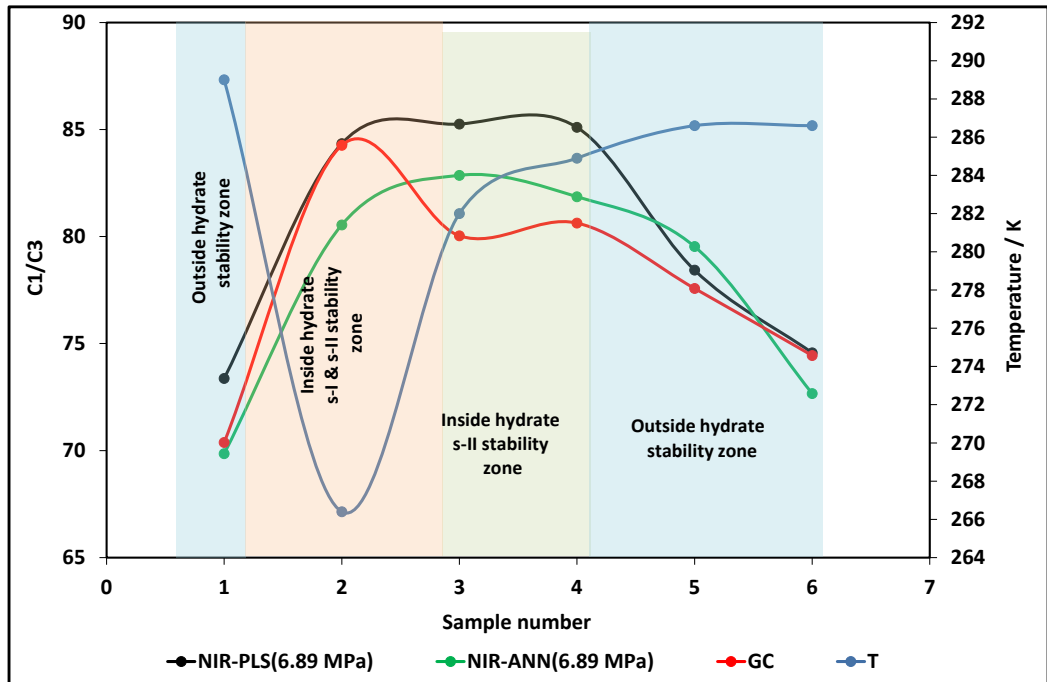


Figure 3.32. Compositional monitoring of C_1/C_3 ratio in the gas phase using GC and FTNIR at 10.34 MPa and 293.15 K. Connection trend between points are only for visual clarification.

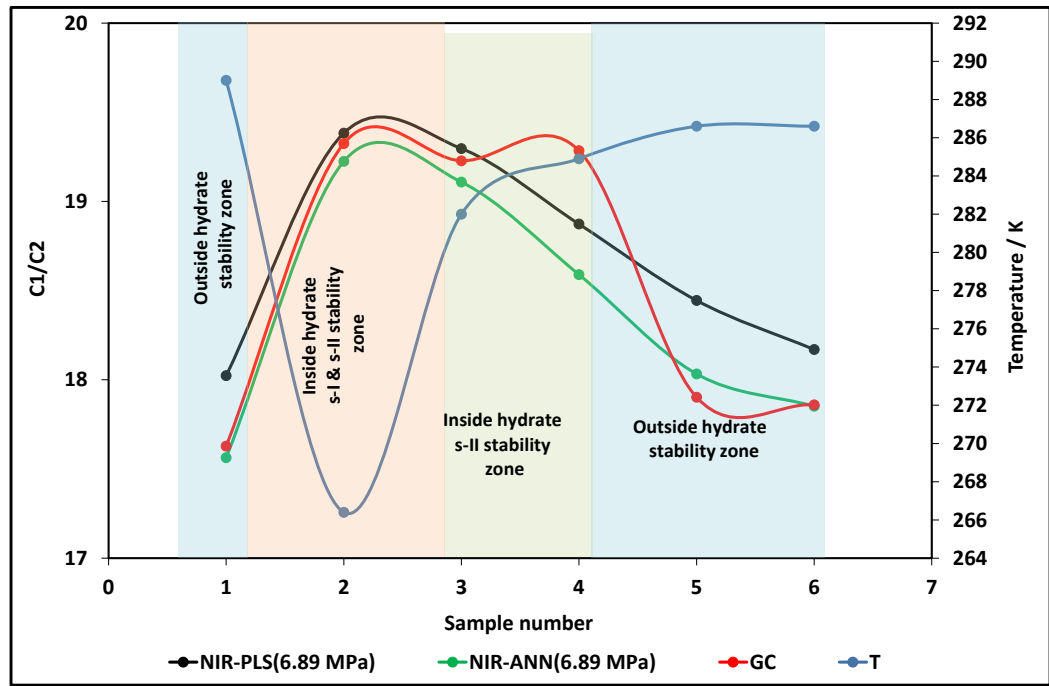


Figure 3.33. Compositional monitoring of C_1/C_2 ratio in the gas phase using GC and FTNIR at 10.34 MPa and 293.15 K. Connection trend between points are only for visual clarification.

Table 3.17. Evolution of C_1/C_3 ratio in vapour phase in the presence of natural gas, deionised water, salt, methanol and gas condensate.

T/K	P/MPa	Water in hydrate Barrel/MMscf	GC	PLS-6.89	PLS-10.34	ANN-6.89	ANN-10.34
289.0	24.03	-	70.4 (± 1.8)	72.1 (± 2.1)	73.4 (± 2.1)	69.9 (± 2.0)	70.0 (± 2.0)
266.4	17.95	59.9	84.3 (± 1.9)	82.0 (± 2.2)	84.3 (± 2.2)	80.5 (± 2.2)	82.0 (± 2.1)
282.0	21.25	39.3	80.0 (± 2.1)	85.8 (± 2.2)	85.3 (± 2.2)	82.9 (± 2.1)	84.3 (± 2.2)
284.9	21.25	9.1	80.6 (± 1.9)	86.5 (± 2.3)	85.1 (± 2.3)	81.9 (± 2.2)	82.7 (± 2.2)
286.6	21.14	0	77.6 (± 1.9)	77.0 (± 2.0)	78.4 (± 2.0)	79.5 (± 2.3)	81.0 (± 2.2)
286.6	20.77	0	74.4 (± 1.8)	73.9 (± 2.1)	74.6 (± 2.1)	72.7 (± 2.0)	73.9 (± 2.3)

Table 3.18. Evolution of C_1/C_2 ratio in vapour phase in the presence of natural gas, deionised water, salt, methanol and gas condensate.

T/K	P/MPa	Water in hydrate Barrel/MMscf	GC	PLS-6.89	PLS-10.34	ANN-6.89	ANN-10.34
289.00	24.03	-	17.6 (± 0.1)	18.1 (± 0.1)	18.0 (± 0.1)	17.6 (± 0.1)	18.1 (± 0.1)
266.40	17.95	59.9	19.3 (± 0.1)	19.6 (± 0.1)	19.4 (± 0.1)	19.2 (± 0.1)	19.7 (± 0.1)
282.00	21.25	39.3	19.2 (± 0.1)	19.1 (± 0.1)	19.3 (± 0.1)	19.1 (± 0.1)	19.4 (± 0.2)
284.90	21.25	9.1	19.3 (± 0.1)	19.1 (± 0.1)	18.9 (± 0.1)	18.6 (± 0.1)	19.0 (± 0.1)
286.60	21.14	0	17.9 (± 0.1)	18.3 (± 0.1)	18.4 (± 0.1)	18.0 (± 0.1)	18.3 (± 0.1)
286.60	20.77	0	17.9 (± 0.1)	18.2 (± 0.1)	18.2 (± 0.1)	17.9 (± 0.1)	18.0 (± 0.1)

The presence of methanol and condensate makes the hydrate memory disappear much earlier than MEG system. As shown in Table 3.17 and Table 3.18, when the system was remained about 2 K outside with a waiting time of 12 hours, the value of C_1/C_3 ratio was very close to those measured by GC before gas hydrate formation. These results show that with about 12 hours waiting time, hydrate memory was almost disappearing and hydrocarbons were mostly recovered from the aqueous phase.

1.1.1.7 Test 7: Natural gas + deionised water + salt (low water to gas ratio)

In this test, hydrates were formed in the presence of natural gas and brine. 100 cc of brine with 5 mass% NaCl was loaded to the cell. After vacuuming the system was pressurised with natural gas until the desired pressure. As mentioned earlier, the experiment focuses mainly on examining the sensitivity of compositional change technique using the FTNIR spectroscopy on low water: gas ratio in the system especially in the presence of gas hydrate. Figure 3.34 highlights the sampling points collected during the duration of the experiment. In this test, 7 samples were taken.

- Sample 1: at 293.70 K and 16.41 MPa outside hydrate stability zone.
- Sample 2: at 279.70 K and 14.11 MPa inside the sI and sII hydrate stability zones.
- Sample 3: at 284.90 K and 14.23 MPa inside the sI and sII hydrate stability zones.
- Sample 4: at 287.50 K and 14.33 MPa inside the sI and sII hydrate stability zones.
- Sample 5: at 289.90 K and 14.37 MPa outside the sI hydrate stability zone and inside sII hydrate stability zone.

- Sample 6: at 291.50 K and 14.18 MPa outside the sI hydrate stability zone and inside sII hydrate stability zone.
- Sample 7: at 292.0 K and 13.87 MPa outside hydrate stability zone.

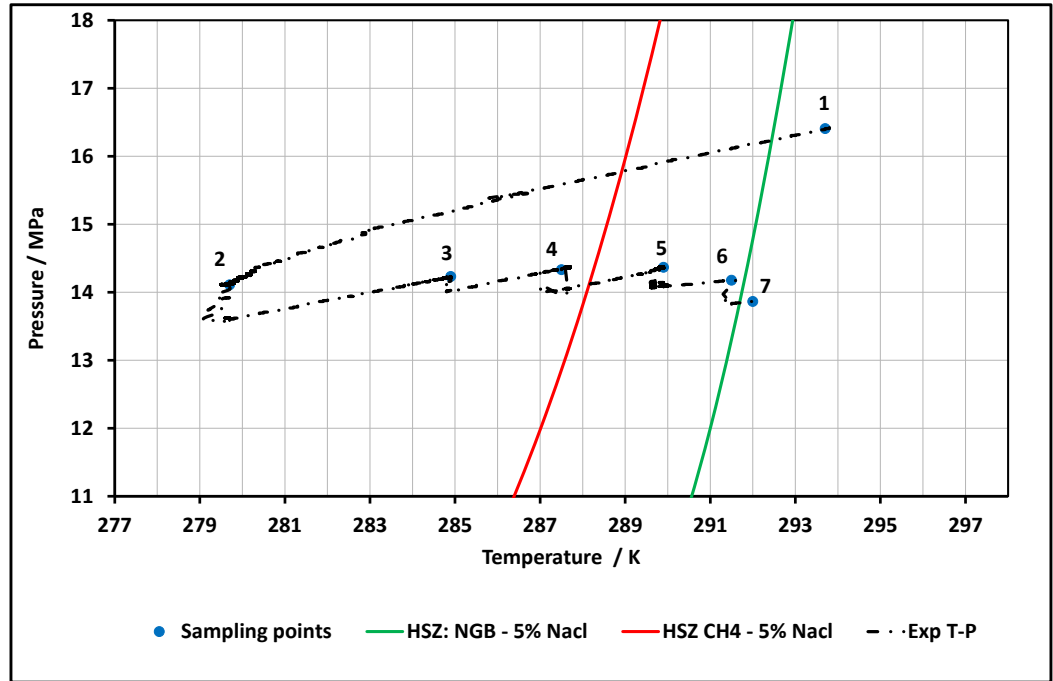


Figure 3.34. Temperature-pressure profile and sampling points for the system with NGB, deionised water and salt.

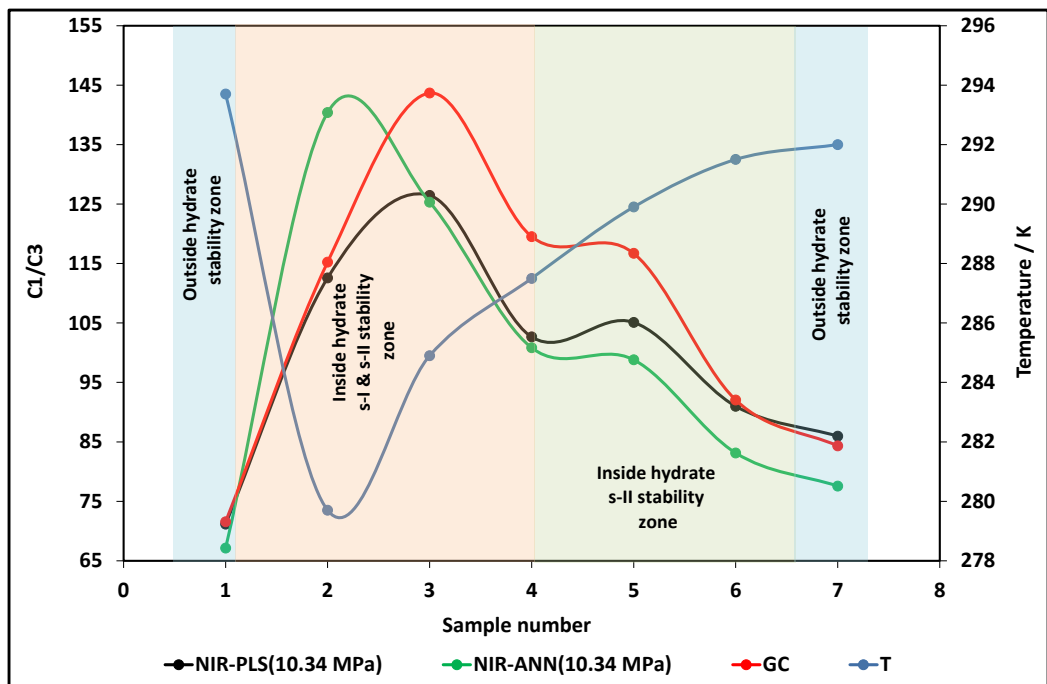


Figure 3.35. Compositional monitoring of C₁/C₃ ratio in the gas phase using GC and FTNIR at 6.89 MPa and 293.15 K. Connection trend between points are only for visual clarification.

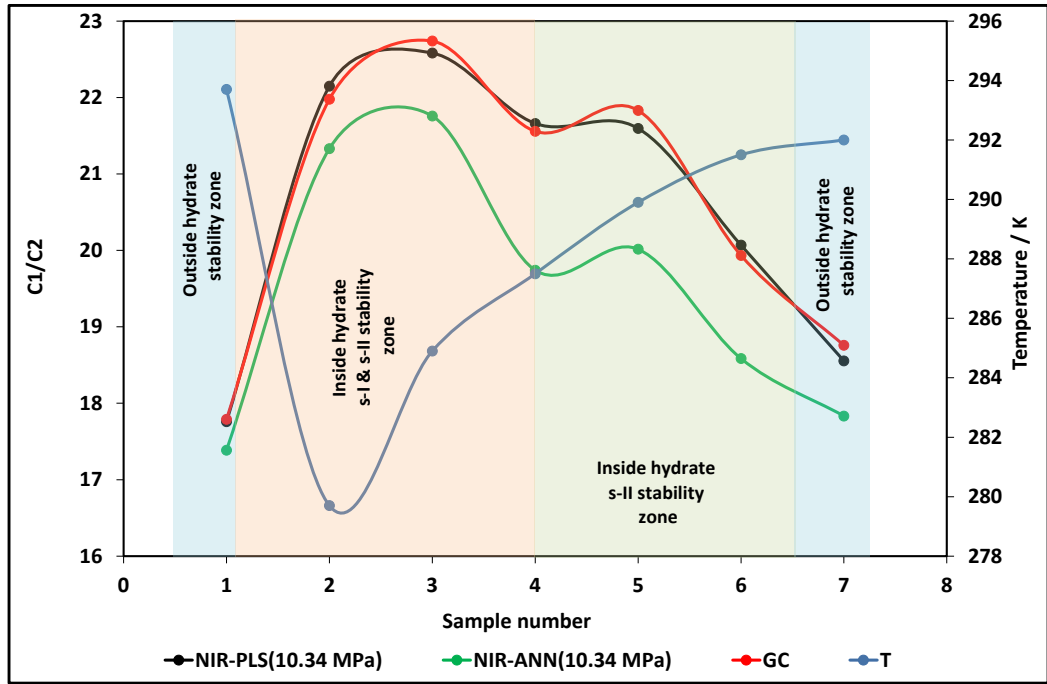


Figure 3.36. Compositional monitoring of C_1/C_2 ratio in the gas phase using GC and FTNIR at 6.89 MPa and 293.15 K. Connection trend between points are only for visual clarification.

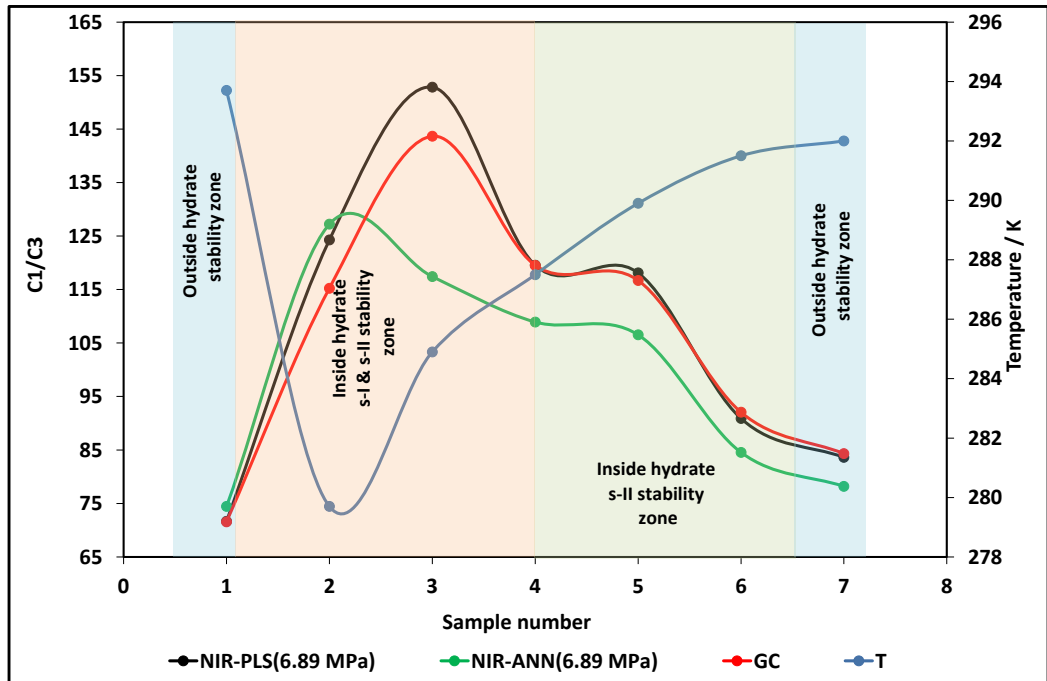


Figure 3.37. Compositional monitoring of C_1/C_3 ratio in the gas phase using GC and FTNIR at 10.34 MPa and 293.15 K. Connection trend between points are only for visual clarification.

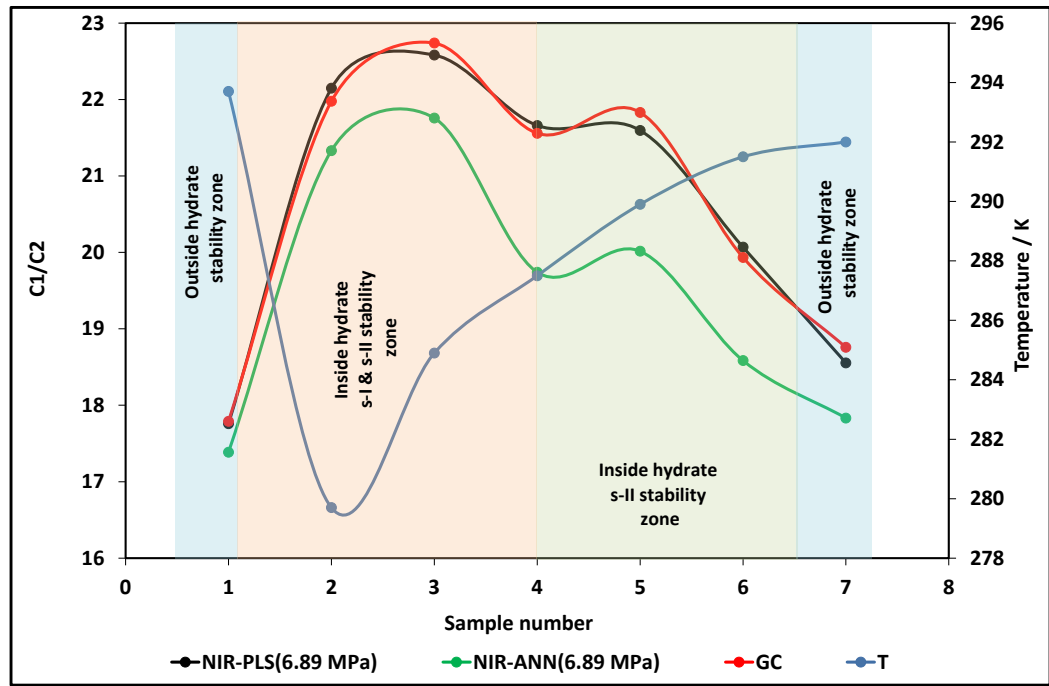


Figure 3.38. Compositional monitoring of C_1/C_2 ratio in the gas phase using GC and FTNIR at 10.34 MPa and 293.15 K. Connection trend between points are only for visual clarification.

As mentioned before, in these experiments hydrate was formed at different temperature and pressure conditions far inside sI hydrate stability zone in order to see the effect of formation of hydrate sI on compositional change technique.

Figure 3.35 to Figure 3.38 show the results of this measurement for different calibration models. It is apparent that the methane to propane ratio and methane to ethane ratio start to increase because propane and ethane were consumed during hydrate formation, which is a sign of sII hydrate formation. During hydrate dissociation, it is noticeable that the C_1/C_3 and C_1/C_2 ratios start to decrease while the system enters inside sII hydrate and outside hydrate stability zone. It means that propane and ethane released from the aqueous phase into the gas phase during hydrate dissociation. The results suggest that this method is sensitive with even low water/gas ratios.

Table 3.19. Evolution of C_1/C_3 ratio in vapour phase in the presence of natural gas, deionised water and salt.

T/K	P/MPa	Water in hydrate Barrel/MMscf	GC	PLS-6.89	PLS-10.34	ANN-6.89	ANN-10.34
293.70	16.41	0.00	71.6 (± 2.1)	71.7 (± 2.1)	71.2 (± 2.0)	74.4 (± 2.2)	67.2 (± 2.2)
279.70	14.11	31.87	115.2 (± 2.1)	124.3 (± 2.1)	112.6 (± 2.2)	127.2 (± 2.3)	140.4 (± 2.3)
284.90	14.23	32.52	143.7 (± 2.2)	152.8 (± 2.1)	126.5 (± 2.2)	117.4 (± 2.3)	125.3 (± 2.3)
287.50	14.33	23.94	119.5 (± 2.3)	119.5 (± 2.1)	102.7 (± 2.3)	108.9 (± 2.4)	100.8 (± 2.3)
289.90	14.37	15.75	116.7 (± 2.0)	118.1 (± 2.1)	105.1 (± 2.3)	106.5 (± 2.3)	98.8 (± 2.3)
291.50	14.18	9.54	92.1 (± 2.0)	90.9 (± 2.1)	91.0 (± 2.0)	84.6 (± 2.4)	83.1 (± 2.4)
292.00	13.87	0	84.3 (± 2.0)	83.6 (± 2.1)	86.0 (± 2.0)	78.2 (± 2.1)	77.6 (± 2.2)

Table 3.20. Evolution of C_1/C_2 ratio in vapour phase in the presence of natural gas, deionised water and salt.

T/K	P/MPa	Water in hydrate Barrel/MMscf	GC	PLS-6.89	PLS-10.34	ANN-6.89	ANN-10.34
293.70	16.41	0.0	17.8 (± 0.1)	17.8 (± 0.1)	17.8 (± 0.1)	17.3 (± 0.1)	17.4 (± 0.1)
279.70	14.11	31.8	22.0 (± 0.1)	22.2 (± 0.1)	22.2 (± 0.1)	22.1 (± 0.1)	21.3 (± 0.1)
284.90	14.23	32.5	22.7 (± 0.1)	22.7 (± 0.1)	22.6 (± 0.1)	21.0 (± 0.1)	21.8 (± 0.1)
287.50	14.33	23.9	21.6 (± 0.1)	21.9 (± 0.1)	21.7 (± 0.1)	20.2 (± 0.1)	19.7 (± 0.1)
289.90	14.37	15.7	21.8 (± 0.1)	21.7 (± 0.1)	21.6 (± 0.1)	20.2 (± 0.1)	20.0 (± 0.1)
291.50	14.18	9.5	19.9 (± 0.1)	19.2 (± 0.1)	20.1 (± 0.1)	18.3 (± 0.1)	18.6 (± 0.1)
292.00	13.87	0.0	18.8 (± 0.1)	18.6 (± 0.1)	18.6 (± 0.1)	17.9 (± 0.1)	17.8 (± 0.1)

This experimental test was repeated several times with different amount of water converted into hydrates in order to investigate the sensitivity of the compositional change technique using FTNIR and GC. These tests were conducted following the same procedure. The same amount of brine with 5 mass% NaCl was preloaded in the equilibrium cell. After removal of air from the system by vacuuming, natural gas was injected into the cell to reach the desired pressure. The system temperature was kept at this condition for a day to reach equilibrium. The system was then cooled down about 3 or 4 K inside the sII hydrate stability zone and outside sI hydrate stability zone to form

only sII hydrate. The mixing rate was increased to 1000 RPM to be able to initiate hydrate formation under the low sub-cooling. As can be seen from Table 3.21, the compositional changes are detectable even if only a few barrels of water was converted into gas hydrates per MMscf.

Table 3.21. Changes in gas composition due to hydrate formation, C_1/C_3 ratio.

Water in hydrate Barrel/MMscf	GC	PLS-1000	PLS-1500	ANN-1000
0	85.5 (± 1.1)	83.7 (± 1.4)	83.0 (± 1.4)	84.1 (± 1.7)
7.68	90.5 (± 1.5)	89.3 (± 1.5)	88.5 (± 1.5)	88.3 (± 1.7)
11.5	98.2 (± 1.6)	97.2 (± 1.6)	90.3 (± 1.8)	91.0 (± 1.7)
14.3	102.8 (± 1.5)	105.5 (± 1.7)	102.2 (± 1.8)	105.2 (± 1.8)
16.1	115.2 (± 1.7)	117.9 (± 1.7)	114.3 (± 1.9)	121.2 (± 1.9)
21.5	125.8 (± 1.8)	123.2 (± 1.9)	122.1 (± 1.7)	127.2 (± 1.9)
27.8	137.7 (± 1.8)	138.1 (± 1.9)	141.7 (± 1.9)	143.6 (± 2.0)

3.4 Integration of the FTNIR Spectroscopy and GasPT Techniques

The compositional change was analysed by the developed NIR prototype, GasPT and GC. The main objective was to compare results that were obtained by the NIR prototype to those measured by the GasPT and GC.

3.4.1 Apparatus

Figure 3.39 shows the schematic of the setup. A large piston vessel of 8.3 L was used to form gas hydrate. The piston in the vessel can be driven by a syringe pump within a movement range of 320 mm, which makes it possible to maintain the system pressure constant during draining gas through the GasPT and NIR which can simulate the pipeline condition. The system temperature is controlled by a cooling bath that circulates coolant through a cooling jacket surrounding the test cell. The gas stream flows in, a tube cylinder and the GasPT, finally a gas meter. The gas meter is used to monitor the flow rate, and the tube cylinder collects any condensed water to prevent condensed water from directly getting in the GasPT sensor. The GasPT measures the equivalent composition of the gas in the system. The system temperature and pressure are recorded by a personal computer.

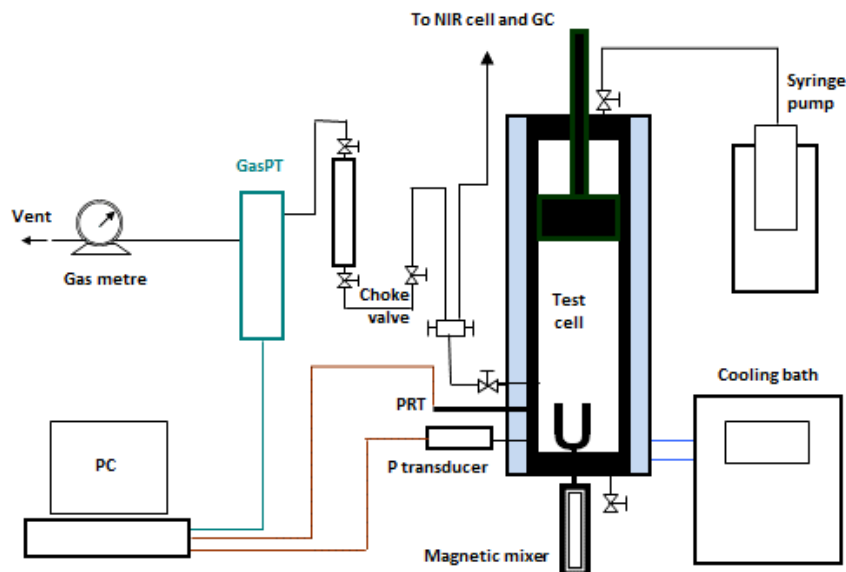


Figure 3.39. Temperature and pressure profiles and test points in the test of the integrated water content (re-calibrated HMT360)-compositional change (NIR prototype, GasPT and GC) system.

3.4.2 Experimental procedure

An aqueous solution of about 500 ml containing 3 mass% NaCl + 10 mass% MEG was loaded to the cell. After vacuuming the same natural gas was injected into the cell until the system was pressurised to the desired pressure. The natural gas composition is shown in Table 3.22. The magnetic mixer was set at 300 RPM. The system was cooled down in steps and left overnight at each test temperature to allow thermodynamic equilibrium.

Table 3.22. Composition of the natural gas.

Component	CO ₂	N ₂	C ₁	C ₂	C ₃	i-C ₄	n-C ₅	i-C ₅	n-C ₅
Concentration (mol%)	1.32	1.02	90.29	5.48	1.35	0.20	0.25	0.20	0.10

The choke valve was gently open, allowing the gas to flow through the GasPT at atmospheric pressure. The choke valve was adjusted to control the flow rate at about 1 L/min which was required by the GasPT. Meanwhile, water was injected behind the piston by the syringe pump to maintain the cell pressure. Compositional data measured by the GasPT were logged to a personal computer and gas flowing was stopped once the GasPT readings became stable.

3.4.3 Results and discussion

The test was conducted at 7 stages, as shown in Figure 3.40.

- Sample 1: at 289.05 K and 10.29 MPa, starting point outside the hydrate stability zone.

- Sample 2: at 285.65 K and 10.06 MPa, about 3 K inside the HSZ but no hydrates formed.
- Sample 3: at 277.05 K and 9.24 MPa, hydrate formed.
- Sample 4: at 285.65 K and 9.72 MPa, some hydrate dissociated.
- Sample 5: at 288.15 MPa and 10.06 MPa, after hydrate fully dissociated.
- Sample 6: at 289.15 K and 10.14 MPa, overnight at about 1.5 K outside the HSZ.

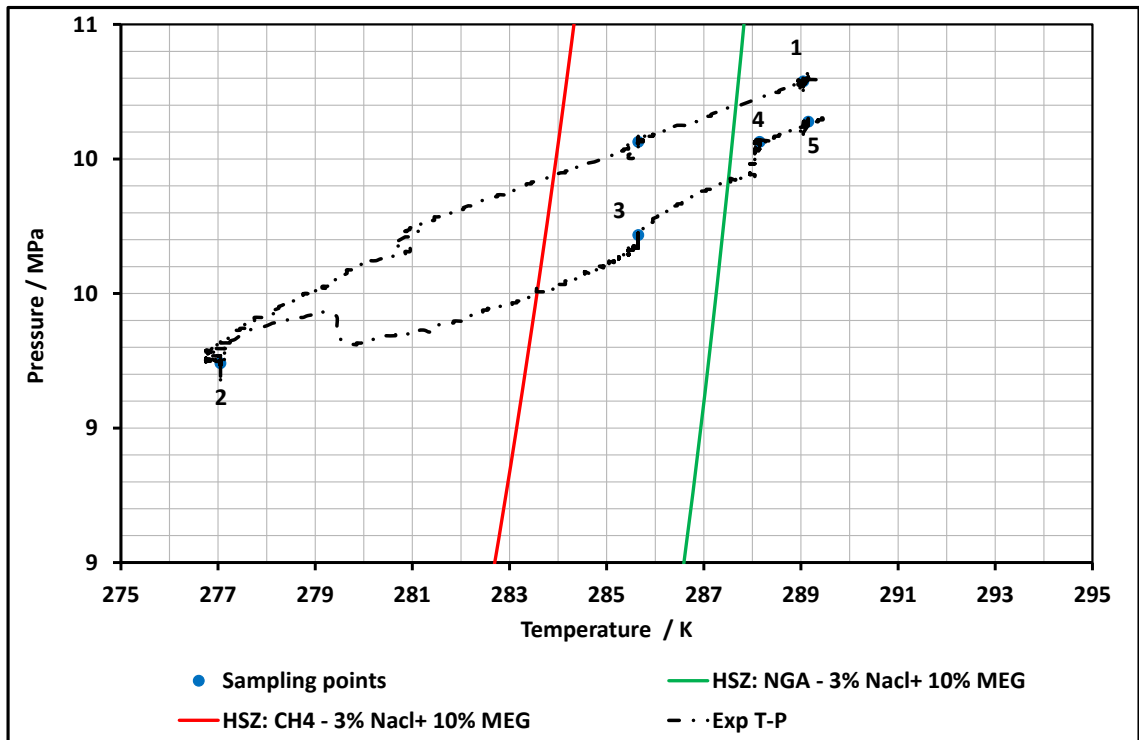


Figure 3.40. Temperature and pressure profiles and test points in testing of the integrated water content (HMT360)-compositional change system (GasPT).

Table 3.23 shows the testing results. At Stages 1 and 2 where no hydrates were formed, although the system was 3 K inside the HSZ at Stage 2, the gas composition measured by the GasPT did not have meaningful change. At Stages 3 and 4 where gas hydrates presented in the system, the propane to methane ratios was measurably smaller because relatively more propane molecules were taken in the hydrate cages compared to methane. At Stage 5 where the hydrates were fully dissociated overnight at about 0.5 K outside the HSZ, the methane to propane ratio seemed slightly greater than those before hydrate formation (i.e., at Stages 1 and 2), but measurably greater than those at Stages 6 and 7. This suggests that some propane molecules were still trapped in water after the hydrates

were completely dissociated overnight. The full recovery of the propane to methane ratio indicates that the hydrate memory disappeared at Stages 6 and 7, which means that hydrate memory may become undetectable if the pipeline operation conditions are far outside the HSZ. For instance, for a typical offshore production system the fluid conditions at the wellhead are normally outside the hydrate stability zone as the temperature and pressure of the wellhead is higher than downstream.

Table 3.23. Test results of compositional change techniques (NIR prototype, GasPT and GC) system (C_1/C_3 ratio in vapour phase).

P / MPa	T / K	Water in hydrate Barrel/MMscf	NIR	GC	GASPT
296.65	10.66	0	71.4 (± 1.2)	73.5 (± 1.2)	18.6
289.05	10.29	0	68.5 (± 1.4)	75.2 (± 1.2)	18.5
285.65	10.06	13.5	128.2 (± 1.3)	107.5 (± 1.3)	21.7
277.05	9.24	12.0	120.5 (± 1.4)	85.5 (± 1.2)	21.4
285.65	9.72	0.3	98.0 (± 1.4)	75.2 (± 1.2)	18.8
289.15	10.14	0	70.9 (± 1.4)	71.4 (± 1.4)	18.4

3.4.4 NIR vs. GasPT

According to the results that were presented in Table 3.23, NIR and GasPT are both viable approaches that can be employed to detect initial signs of hydrate formation based on changes in the composition of some preferential components in the gas phase. Hence, both methods with slight modifications can be used for monitoring the compositional changes along the pipelines. However, they have their own advantages and disadvantages. GasPT can operate at pressures close to atmospheric pressure (up to 0.3 MPa) and is so sensitive to water [93]. Hence, a pre-conditioning system needs to be applied to the GasPT setup in order to reduce the pressure of the gas sample to a specific range and remove water from the sample. The main advantage of the developed NIR prototype to the developed GasPT is that it can operate in pressure ranges from about 3.40 to 13.80 MPa which is within the range of operating pressure of the pipelines. It is known that water strongly absorbs the NIR light, thereby the presence of water in a direction that light passes through the sample may affect the accuracy of the measurement. Hence, it is required to apply some modification to the setup in order to avoid accumulation of water in the NIR cell. To overcome this problem, prior starting any measurement, nitrogen or air can pass through the NIR cell to dry the cell and remove the water droplets from the sapphire windows or a drain valve can be located beneath the cell to remove the water from the cell. Moreover, NIR can measure the real concentration of main hydrocarbons (methane through pentanes) in the gas phase, whereas GasPT measure pseudo gas composition of methane, propane, carbon dioxide and nitrogen.

3.5 Integration of NIR Spectroscopy Technique with V-V_{tc} Technique

The V-V_{tc} technique determines the concentration of salts and hydrate inhibitors in aqueous phase hence the hydrate safety margin by measuring acoustic velocity and its change with temperature. This test is to evaluate the integration of the compositional change technique and the V-V_{tc} technique to form a gas hydrate warning and monitoring system. Our extensive experiments have demonstrated that the developed V-V_{tc} technique is acceptably accurate, reliable, and robust, although measurements of aqueous samples may lead to several hours of time lag behind the gas phase in pipelines.

3.5.1 Apparatus

Figure 3.41 shows a schematic diagram of the integrated compositional change NIR-V-V_{tc} system. The gas composition was analysed by the developed NIR spectroscopy prototype which is reported in Chapter 2. The concentration of salts and hydrate inhibitors was determined by the developed V-V_{tc} prototype. The gas composition analysis (NIR) was performed at a fixed temperature and pressure (e.g., 293.15 K and 6.89 MPa), and inhibitor concentration determination (V-V_{tc}) was conducted at two fixed temperatures (278.15 and 298.15 K) and variable pressure from the atmosphere to 20 MPa.

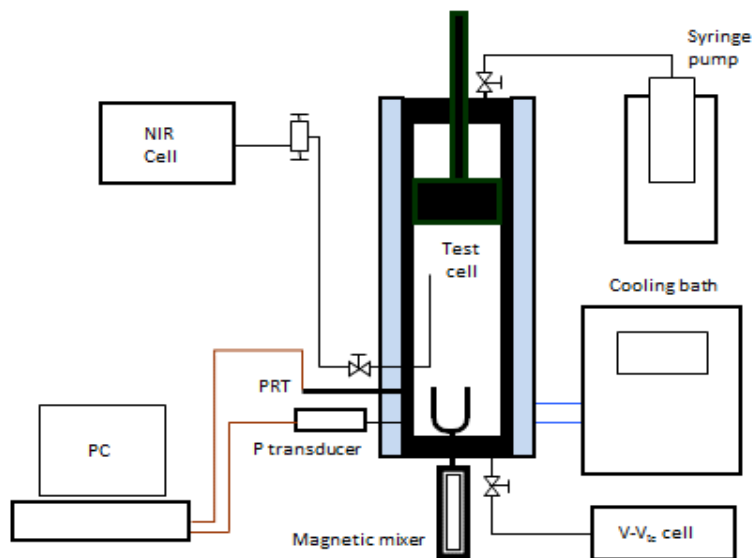


Figure 3.41. Schematic of the experimental setup for testing the integrated NIR spectroscopy and V-V_{tc} system.

3.5.2 Experimental procedure

The test was conducted with about 2600 ml of aqueous solution containing 3 mass% NaCl and 10 mass% methanol and natural gas. It was carried out in 5 temperature stages. At

each stage, the pressure of the large vessel was maintained constant by a syringe pump. The pressure of vessel can be adjusted by injection/withdrawal of water behind the piston. For NIR analysis, the gas samples were transferred from top of the large vessel to the NIR cell. To measure the concentration of salt and methanol using V-V_{tc}, prior to loading the aqueous sample, the V-V_{tc} cells were pressurised by injecting N₂ to avoid the appearance of gas bubbles during transferring the aqueous sample. Aqueous samples were loaded into the V-V_{tc} cells by slowly displacing the N₂ with the aqueous solution from the large vessel. It should be stated that, in in-situ pipelines, there is a continuous supply of produced water under a certain pressure so that no pre-pressurization will be needed. Figure 3.42 illustrates the temperature and pressure profiles and the testing stages compared to the natural gas and methane hydrate phase boundaries.

- Sample 1: at 293.15 K and 12.94 MPa, starting point
- Sample 2: at 278.05 K and 10.39 MPa, hydrate formed
- Sample 3: at 283.65 K and 11.53 MPa, some hydrate dissociated
- Sample 4: at 288.15 K and 12.46 MPa, overnight at about 2 K outside the HSZ
- Sample 5: at 293.95 K and 13.01 MPa, overnight at about 7 K outside the HSZ

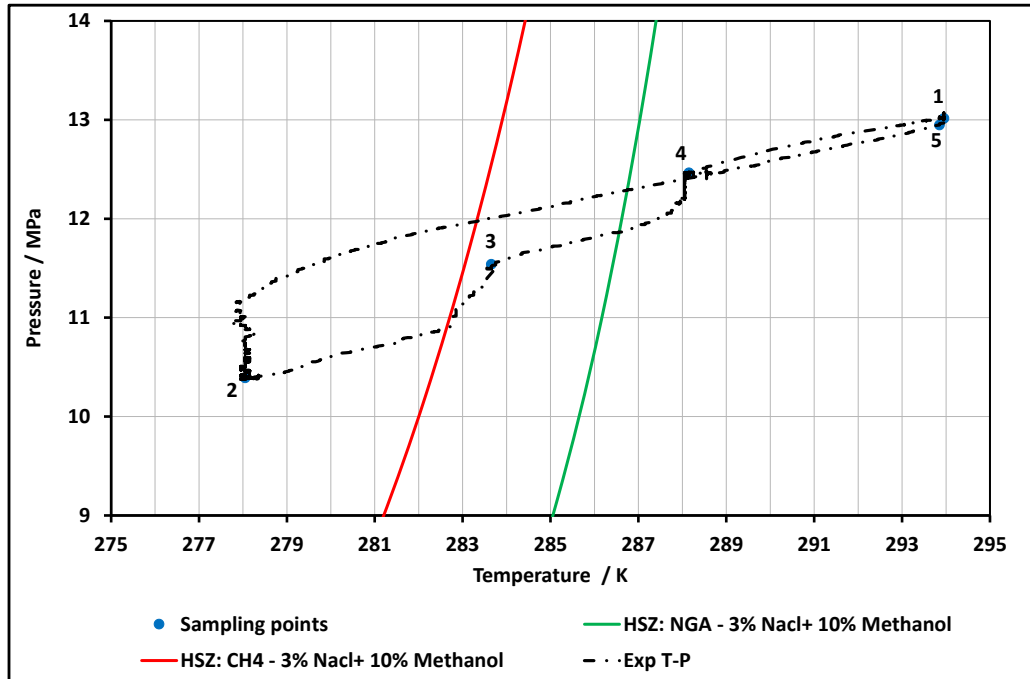


Figure 3.42. Temperature and pressure profiles and test points in the test of the integrated NIR spectroscopy technique and the V-V_{tc} technique.

3.5.3 Results and discussions

Table 3.24 shows the test results. As observed early in Section 3.4, the propane to methane ratio measured by the NIR spectroscopy technique reflects the presence of both natural gas hydrate and hydrate memory after the hydrate was fully dissociated overnight at 288.15 K and 12.46 MPa (Stage 4, about 2 K outside the HSZ). Hydrate memory became undetectable overnight at Stage 5 (293.95 K and 13.02 MPa, around 7 K outside the HSZ).

Table 3.24. Test results of the integrated NIR-V-V_{tc} system.

T K	P MPa	Water in hydrate Barrel/MMscf	C ₁ /C ₃ NIR	NaCl (mass%)		MeOH (mass%)	
				Exp	V-V _{tc}	Exp	V-V _{tc}
293.85	12.95	0	89.3 (±1.7)	3.0	10.0	10.0	10.3
278.05	10.39	160	333.3 (±1.8)	4.2	13.4	13.4	13.7
283.65	11.54	65	111.1 (±1.9)	3.6	10.8	10.8	12.4
288.15	12.46	0	96.2 (±1.8)	2.8	9.4	9.4	12.4
293.95	13.02	0	90.9 (±1.6)	2.8	9.4	9.4	10.1

Both salt concentration and methanol concentration were determined by the V-V_{tc} prototype, which is listed in the column that is marked “V-V_{tc}” in Table 3.24, while the column “Exp” represents the methanol concentrations that were calculated by taking into account the reduction of water due to hydrate formation. As shown in Table 3.24, the V-V_{tc} measured salt (NaCl) concentrations are in good agreement with the experimental/actual values and the deviations are less than 0.2 mass%. At Stage 1 (before hydrate formation) and Stage 2 (before hydrate dissociation), the V-V_{tc} measured are agreeable with the experimental values in about 0.3 mass% of measurement deviation. However, after the hydrate started dissociation, the measured methanol concentrations become obviously lower than the experimental values, which is opposite to what was anticipated. It was expected that, in the presence of gas hydrates, withdrawal of the aqueous solutions of the system would remove relatively more methanol and salt as the hydrate formation excludes methanol from hydrate formation. If this is the case, the methanol concentration should be reduced after the hydrates were dissociated, just like the reduction in the salt concentration. The opposite change in the methanol concentration has not been fully understood. One possibility could be some of the methanol molecules took part in the hydrate formation with the hydrocarbon molecules together which is beyond of the scope of this work and it needs to be further investigated in future.

3.6 Field Test Results of Monitoring Hydrates Formation by Gas Composition

Changes during Gas/Condensate Production with AA-LDHI

This section presents field test results from the LANOT4 well of the MEILLON sour gas field in France using a monitoring tool to detect early signs of hydrate formation. The

technique is based on monitoring changes in the gas composition as a consequence of hydrate formation. In this specific field, continuous injection of AA-LDHI into the production system was used to avoid hydrate blockage while operating inside hydrate P&T zone. An online Gas Chromatograph (GC) was installed at separator gas outlet to monitor the composition of gas continuously.

3.6.1 Presentation of MEILLON field

MEILLON is a very mature sour gas condensate on-shore field located in South-Western France close to the giant LACQ field producing for 50 years (around 250 Gm³ produced since first gas). One of a few remaining production wells called LANOT04 is still producing through non-optimised production scheme resulting from successive modifications of the whole field development which is more oriented towards field closure for quite a few years. A buried 10" flow line transfers the LANOT4 well streams to a separator some 1.6 km away operated at around 1.5 MPa, where gas and liquid are separated before being transported to the main Processing Centre 20 kilometers away through a 10" gas line and 6" liquid line. The conditions inside the surface separator can be inside the hydrate stability zone during the mild winter season nights. As consequences of successive field modifications and significant increase of water production with years, this LANOT04 well was regularly closed in winter time for 2/3 months due to hydrate plug formation inside the production system (mitigation strategy in place by design from start-up turned impossible to implement). Hydrate plug always occurred at the level of the separator liquid outlet, where the liquid is temporary pumped (around 10 minutes per hour) through 100 µm mesh filters protecting export pumps towards Process Plant.

In order to maintain production of LANOT4 well, the implementation during winter 2012/2013 of a continuous injection of a Low Dose Hydrate Inhibitor of Anti-Agglomerant type (LDH-AA) at the well-head was implemented. This occurred for the last winter before the well was closed and decommissioned.

The use of AA implies that hydrates do form and are transported through the production system as a low viscous liquid. This AA injection at LANOT4 wellhead turned to be fully efficient and no well closure was faced despite production inside the separator into hydrate stability zone during some cold nights (which always resulted in liquid outlet line hydrate plugging in the absence of any AA). It was decided to use this opportunity and examine the feasibility of monitoring changes in the gas composition as a consequence of hydrate formation for the first time. The objective of this monitoring technique being

to try using these gas composition changes as an “early warning” that hydrates are forming upstream.

1.1.1.8 LANOT4 well production data

The production data from the well during the test are the following: GCR=14,000 Sm³/Sm³, condensate=14 Sm³/d, water cut=50%, water salinity = around 1% NaCl equ.

Table 3.25. Composition of the natural gas.

Component	CO ₂	H ₂ S	C ₁	C ₂	C ₃	C ₄	C ₅	C ₆	C ₇
Concentration (mol%)	10.86	10.88	72.80	2.57	0.66	0.57	0.28	0.20	0.10

1.1.1.9 Gas composition analyser installed on-site

An online GC Micro GC SRA Instruments R3000 was installed at the gas outlet of the separator. The composition of the gas was analysed routinely as well as recording the system pressure and temperature.

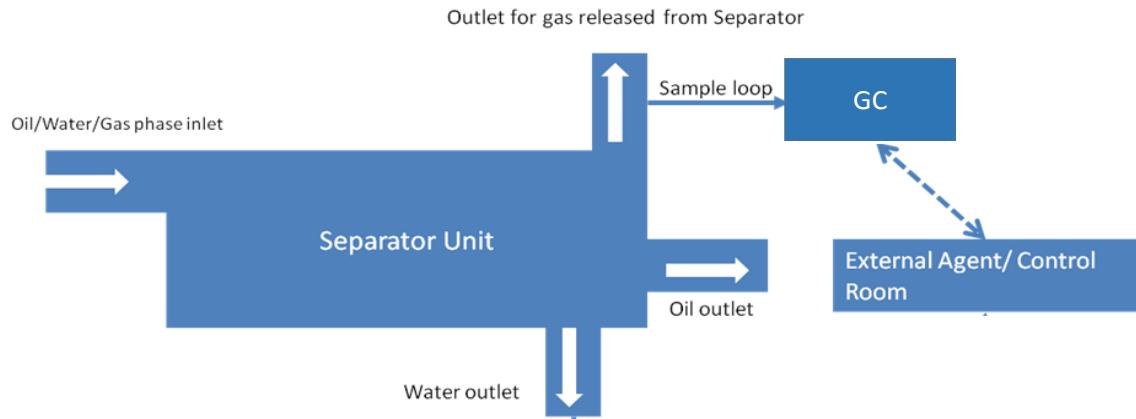


Figure 3.43. Schematic diagram of the separator unit.

3.6.2 Results and discussions

The LANOT4 hydrate formation curve of sI and sII, as well as operating system pressure and temperature, is represented in Figure 3.44. Monitoring the operating pressure and temperature are two important parameters to predict the risk of hydrate formation. For a given pressure, once the hydrate formation temperature is known, the hydrate subcooling temperature can be calculated by the difference between hydrate formation temperature and in situ gas temperature in the separator (DTHYD).

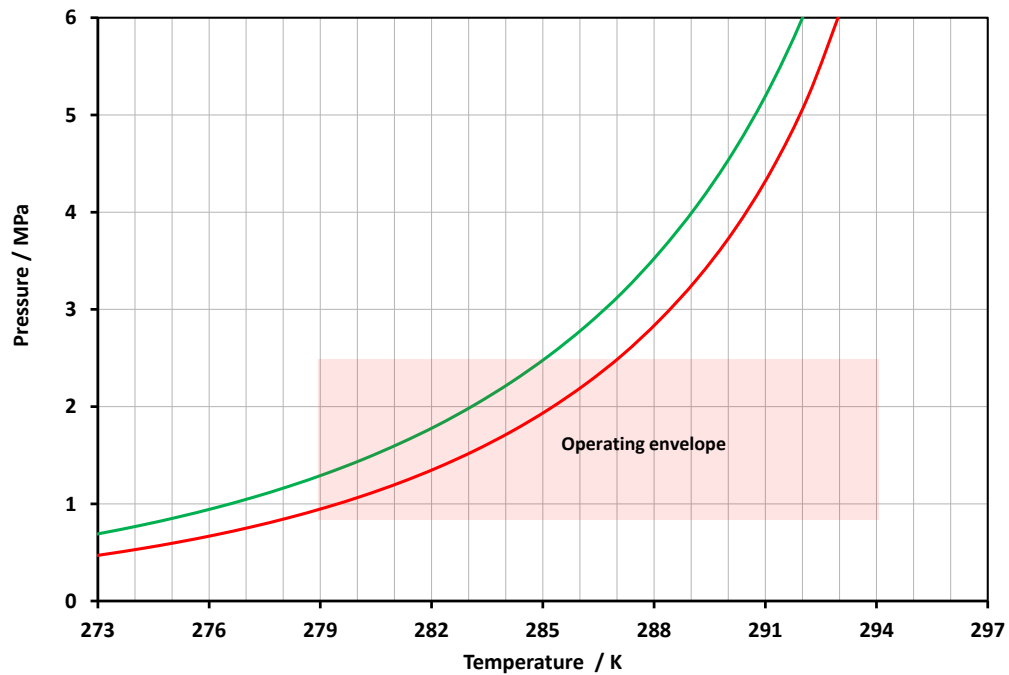


Figure 3.44. Predicted hydrate phase boundaries for the structure I and II hydrates for LANOT4 well. The red line represents hydrate phase boundary sII, and the green line represents hydrate phase boundary sI.

Therefore, a positive DTHYD means that the operating envelope is inside the hydrate risk area, while a negative value illustrate that system is outside hydrate stability region and there is no risk of hydrate formation as shown in Figure 3.45. The data presented in Figure 3.45 show the conditions inside the separator obtained from March 7 to 13. Fluctuations between day and night are evidenced. It demonstrates that while the difference between the hydrate formation temperature and the local fluid temperature is approximately less than 1.8 K and greater than 0 K (Red region); the operating envelope at the separator is inside hydrate sII stability zone. Thus the pressure and temperature in the separator meet the requirements to form hydrate sII. Furthermore, during night, with cooler temperatures, the degree of subcooling increased by up to 4.6 K where the operation conditions lie inside hydrate sI and sII stability zone (Blue region). This could result in the formation of sI hydrates together with sII hydrates. At points lower than zero, the system is in the hydrate safe zone (Tan region). Another point to note is that the separator pressure and temperature operating conditions are normally outside the hydrate zone during the day.

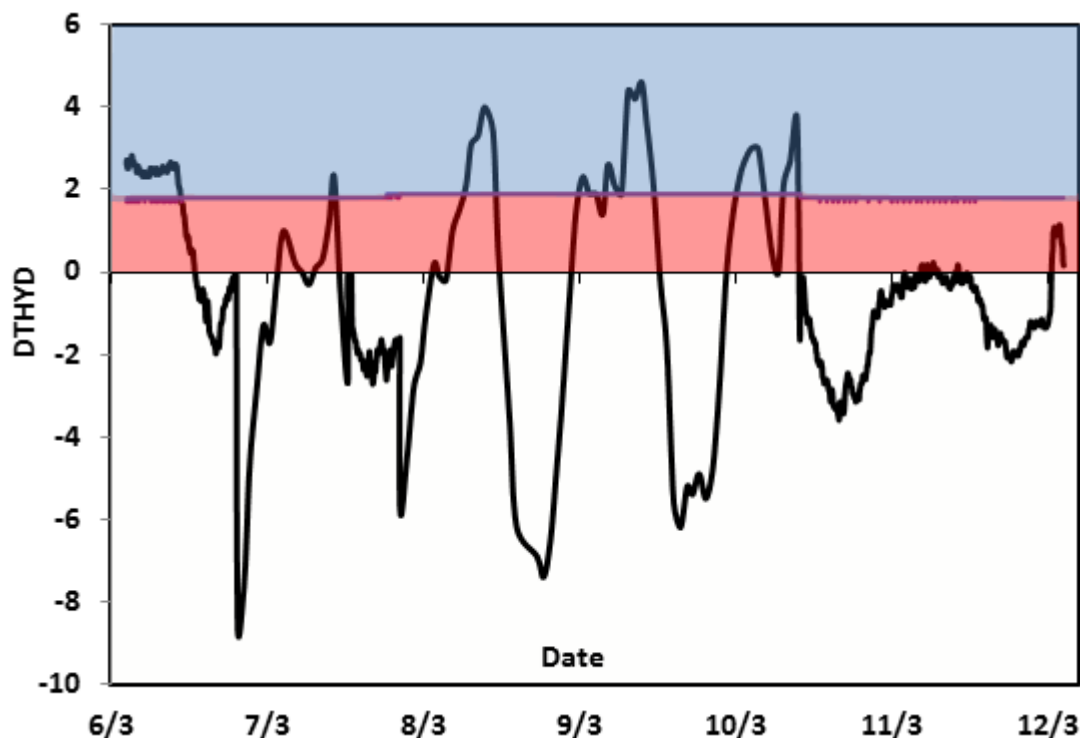
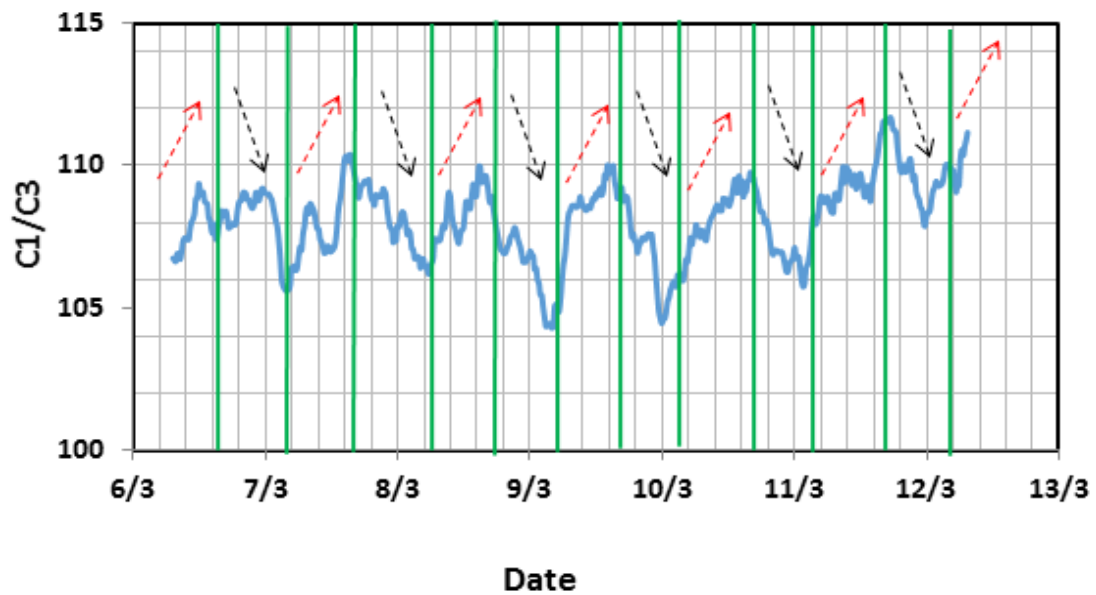


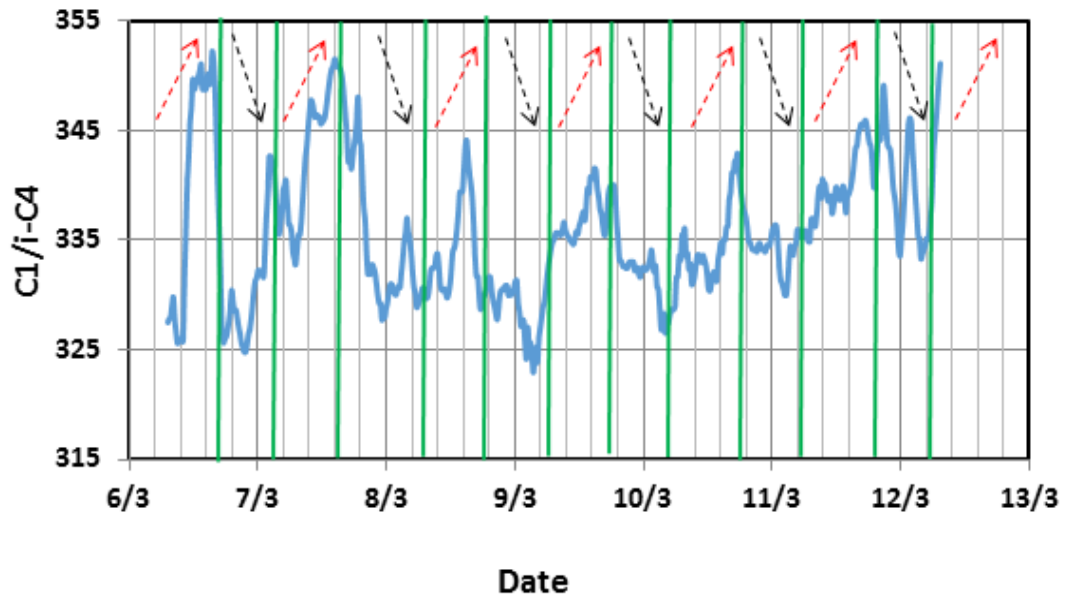
Figure 3.45. Hydrate subcooling temperature. White region: system is outside hydrate stability zone, red region: system is inside hydrate sII and outside hydrate sI stability zone and blue region: system is inside hydrate sI and sII stability zone.

To study the effect of variation in the concentrations of various components of the produced gas, the compositions of the gas phase inside the separator were measured by GC every 15 minutes to detect early signs of hydrate formation. For this aim, evaluations of the C_1/C_3 and $C_1/i-C_4$ ratios were monitored in the gas phase. It is known that naturally, hydrate structure sII will always be formed for the majority of gas and gas condensate compositions and there is a possibility of formation of hydrate sI simultaneously with hydrate sII if the temperature and pressure of operating condition shift inside the hydrate sI and sII stability zone. As one can see in Figure 3.46a, when the system is inside the hydrate stability zone during night, the methane to propane ratio will increase. This increase is for the loss of propane in gas phase due to the formation of hydrate structure II. Conversely, when the system is outside the hydrate stability zone during day, opposite results could be observed for the methane to propane ratio in the gas phase which is related to the liberation of propane after hydrate dissociation. The same results are observed for the methane to i-butane ratio as shown in Figure 3.46b. It can be seen that the methane to i-butane ratio is continuously increasing during night due to hydrate formation. In other word, the methane to propane ratio and methane to i-butane ratio in the gas phase increased at night (colder) and dropped in day-time (warmer). The results showed that gas hydrate were forming at nights, which resulted in relatively more propane and i-

butane got into hydrate crystals. In daytime the warmer ambient environment moved the T&P conditions outside the HSZ and no hydrate was forming, therefore, the gas composition (i.e., the methane to propane ratio and methane to i-butane ratio) dropped. This result suggests that, for the specific LACO4 well, it may be possible to reduce/stop the AA injection during day time. A moving-average technique is used with the aim of reducing the random variations in C_1/C_3 and $C_1/i-C_4$ ratios to detect the trends clearly and eliminate the noise. These results also show changes due to hydrate formation in the content of propane and iso-butane in the gas phase could be a method for detecting signs of hydrate formation. Furthermore an investigation was conducted to determine the relative changes in the composition of the gas phase due to preferential solubility of some components in the liquid phases due to changes in the system P&T. Results showed that solubility changes in C_1/C_3 and $C_1/i-C_4$ ratios are negligible and it might slightly affect the results.



(a)



(b)

Figure 3.46. Gas compositional changes due to hydrate formation indicated by the GC analysed C_1/C_3 (a) and $C_1/i-C_4$ (b) ratios.

Although the field trial can be regarded as successful, the main drawback of this method is the formation of hydrate sI. It should be noted that some inconsistencies can be observed in C_1/C_3 and $C_1/i-C_4$ ratios, this may be due to the operating conditions going inside the hydrate sI stability zone which concurs with Seo *et al.* [97] reporting that sI and sII hydrates could form simultaneously during the operation. When sII hydrates form, they use sII hydrate formers, hence shifting the hydrate stability zone for sI to the right. Therefore when the calculations show the system is on the hydrate stability zone for sI or near sI phase boundary, it could be inside the hydrate stability zone of sI hydrates. As previously mentioned, the phase boundary of hydrate structure I and structure II are very close. Hence the proximity of sI and sII phase boundaries increase the probability of nucleation of hydrate sI along with sII hydrate. In this work, a fixed composition was used to calculate sI and sII phase boundary while in fact the composition changes as hydrates are formed. Ideally, it is required to use instantaneous gas composition and system pressure and temperature for calculations. If the conditions are on the hydrate stability zone of one or both structures, it means that (those) structure(s) is (are) forming. If the system goes inside the hydrate stability zone, then it could mean that some degree of subcooling is required or water has been used up or salt concentration has increased as a result of hydrate formation. Further study is required before the validity of this assumption can be confirmed. Furthermore, the results show that although it is possible

to detect early signs of hydrate formation by monitoring variations in gas composition, quantifying the concentration of hydrates in the aqueous phase will depend on several other factors, notably the mole fraction of water in the pipeline (i.e., water hold up) and relative gas and aqueous phase velocities. Due to the fact that one volume of water in the pipeline will come into contact with several volumes of gas because of difference in velocity of the gas and liquid phase along the pipeline, the change in the gas composition cannot give an accurate account of the amount of water converted into hydrates.

3.7 Conclusions

The results from work presented in this chapter, aimed at validating the developed NIR spectroscopy setup as a new early warning method to detect initial signs of formation of gas hydrates. The main findings of this study are summarized in below:

- Results confirmed that it is possible to detect hydrate formation by monitoring the changes in gas composition (e.g., C_3 and/or C_2 concentrations C_1/C_3 and/or C_1/C_2 ratios) using the NIR setup and sII hydrate formation results in a reduction in the concentration of some preferential components in the gas phase.
- It was shown the NIR prototype is able to detect the changes due to the formation of gas hydrates as well as available commercial devices such (i.e., GC and GasPT).
- The feasibility of this method was investigated to study the sustainability of hydrate memory (i.e., how fast the gas composition could get back to the initial value.) by taking into account the retaining time and temperature outside the hydrate stability zone for different fluid systems.
- The integrated compositional change-V- V_{tc} system with the developed NIR prototype and the V- V_{tc} prototype was tested for a fluid system containing natural gas and 3 mass% NaCl and 10 mass% methanol. The results suggest that the NIR spectroscopy technique and the V- V_{tc} technique can be integrated to form a reliable hydrate early warning and monitoring system.
- This opportunity was seized to examine the feasibility of monitoring changes in the gas composition as a means for detecting hydrate formation at one of the sponsor's field. For this purpose, a GC was installed close to the separator in order to monitor the composition of the gas every 15 minutes. The results showed that gas hydrates were forming at nights, which resulted in relatively more propane

and i-butane into hydrate crystals. This process was reduced as soon as the sub-cooling was getting too strong and entering the structure I hydrate stability zone (as C3 & iC4 do not form structure I hydrate). In the daytime the warmer ambient environment moved the P&T conditions outside the hydrate stability zone, stopping any hydrate formation but very probably also triggering the dissociation of the trapped hydrates remaining in the stagnant liquid inside the separator. This field trial provided evidence that the compositional change technique is capable of detecting hydrates formation in a live system.

CHAPTER 4: INTEGRATED FTNIR AND UV SPECTROSCOPY TECHNIQUE FOR DETERMINATION OF BOTH THIS AND KHIS

4.1 Introduction

Currently, different types of hydrate inhibitors are used to prevent the formation of gas hydrates in hydrocarbons transport pipelines. Thermodynamic inhibitors (THIs, i.e., alcohols and glycols) are the most commonly used hydrate inhibitors in the industry since 1930[1]. However, in the last two decades, interest has been shown in using low dosage hydrate inhibitors (LDHIs) such as kinetic hydrate inhibitors (KHIs) and Anti-agglomerants (AAs). LDHIs, as their name implies, are injected in a small quantity (0.5 to 2 mass %) compared to THIs which are injected into the stream of hydrocarbons in high concentration (up to 60 mass %), depending on the operation conditions (i.e., pressure, temperature and water cut). Hydrate safety margin is defined as the temperature difference between the actual fluid temperature and the hydrate dissociation temperature at a given pressure. If at the given pressure the system temperature is inside hydrate stability zone there is a risk of hydrate formation. Otherwise, the formation of gas hydrate is not expected. Hence, to predict the hydrate stability zone and calculate the hydrate safety margin according to pipeline pressure and temperature operation conditions, it is necessary to know the concentration of hydrate inhibitors and salt as well as hydrocarbon compositions. However, we should keep in mind that unexpected issues such as a change in water cut, human errors, equipment breakdown, etc., could affect the actual concentration of organic inhibitors in real field application. It is usual that high dosage of inhibitors has to be applied to minimise the risk of hydrate blockages, which cause more operation cost and severe environmental damage. Monitoring the concentration of hydrate inhibitors in the pipeline can help the operator to determine the hydrate safety margin accurately, optimising inhibitor injection rate (i.e., ensuring adequate inhibition or avoiding over inhibition).

Several studies were carried out to measure the concentration of THIs, KHIs and salt in aqueous solutions. Henning *et al.* [98] reported the use of an acoustic multi-sensor for measuring the concentration of alcohols such as methanol and ethanol in aqueous solutions in the absence of salt. Sandengen *et al.* [99] provided an equation to calculate the concentration of salt and MEG by measuring the conductivity and density of the water

sample at a temperature of 298.15 K and 293.15 K respectively. Based on their results, the accuracy of the calculated MEG concentration was within ± 2 mass %, whereas an estimated accuracy of (5 to 6) % was reported for NaCl. Recently, a new hydrate inhibition monitoring/optimising system called conductivity-velocity (C-V) method based on a change in the acoustic velocity and electrical conductivity measurements of an aqueous sample were developed by Yang *et al.* [87]. An artificial neural network model (ANN) was created utilising the measured conductivity and velocity data and used to determine the concentration of the hydrate inhibitors in the presence of the salt in THIs (MEG/ Methanol)-salt or KHIs (Luvicap EG)-salt systems.

A few research projects have been carried out to measure the concentration of salt in water samples using near-infrared (NIR) spectroscopy. It is known that salt does not absorb the NIR light. However, the presence of salt in the water sample can cause an alteration in the structure of water by perturbation of the hydrogen bond network, which results in an overall change in the measured spectrum. This phenomenon was used by researchers to monitor and measure the concentration of different types of salt in water. In 1993, Lin *et al.* [100] determined the concentration of salt (up to 35 mass%) in seawater by employing NIR spectroscopy. They used the range between 1100 to 1900 nm for the construction of the calibration models. The accuracy of the measurement was believed to be within 0.22%. Grant *et al.* [101] also used NIR spectroscopic technique to measure the concentration of sodium hydroxide, sodium carbonate and sodium chloride in aqueous solutions in a range of concentrations from 0 to 15 mass%. In the other study, Gowen *et al.* [102] revealed that NIR spectroscopy is capable of determining low concentrations of salt in the order of 1000 ppm in solutions containing water and salt. They selected the spectral range from 1300 to 1600 nm as the final range for developing of the partial least square regression model as it provides lower error values for the prediction data set. Furthermore, vibrational spectroscopy methods such as NIR and UV spectroscopy can provide information about the evolution of KHI and THI contents in various fluid systems. Several studies were carried out to measure the concentration of ethanol and methanol in gasoline by combining NIR and chemometric methods [103-105]. Anderson *et al.* [106] utilised a UV-visible spectrometer to detect the concentration of type of KHI inhibitors (PVCap) in distilled water. They reported a detection limit of PVCap in the order of about 0.003 mass% in a solution containing PVCap and distilled water. Gibsson *et al.* [107] utilised a UV-Vis spectrometer to measure the concentration of various types of polymers in water. They could detect the concentration of different polymers in water

samples with a detection limit of 0.5 mg/L using single wavelength calibration in the ranges 200-220 nm.

To our knowledge, there have been no studies done on using NIR and UV spectroscopy together to identify the concentration of hydrate inhibitors (THIs and KHIs) and salt simultaneously. In this chapter, we investigate the potential of NIR and UV spectroscopic methods associated with partial least square (PLS) method to predict the concentration of hydrate inhibitors and NaCl in aqueous solutions at a temperature of 293.15 K and atmospheric pressure.

4.2 Spectroscopy Technique

Vibrational spectroscopic techniques are attractive technologies for measuring the concentration of chemical species in fluid samples because they are non-invasive/destructive, typically offer fast response times, minimum sample preparation, and minimum sample volume is required, and the modern instrumentation has a minimum footprint. In comparison, other conventional methods, for example, Gas chromatography (GC), colorimetric and gravimetric methods, are time-consuming, require a high degree of analytical skill, and have large footprints that are not amenable to developing portable analytical instruments. Utilizing the NIR region of the spectrum (800 to 2500 nm) and offers the ability to discriminate absorption features of organic species (e.g. Alcohols) from those of water, which is a very strong absorber across the majority of the infrared spectrum (see Figure 4.1). It is apparent that molecules of water absorb the NIR light strongly at two different regions. In Figure 4.1, we show the NIR response from water across the wavelength region of 1000 - 2100 nm, noting the main features at approx. 1450 and 1900 nm, which correspond to the first overtone and combination bands of O-H bonds, respectively [102]. The solvated salt ions, specifically Na^+ and Cl^- , are themselves transparent to the infrared light. However, the presence of salt in the water sample can cause an alteration in the structure of water by perturbation of the hydrogen bond network in the combination and overtone regions which results in an overall change in the measured spectrum. The extent of these perturbations depends upon the properties of the solute, such as size and ionic strength. These changes can be detected in the measured spectra and hence used to determine the concentration of salt in water samples. Methanol and MEG absorb the NIR light in the NIR region, according to the structure of their molecules. Methanol molecules contain one methyl group ($-\text{CH}_3$) and one hydroxyl group ($-\text{OH}$), whereas MEG molecules have two methylene groups ($-\text{CH}_2$) and two hydroxyl

groups. The NIR spectra of pure methanol, pure MEG and deionised water in the range of 1000 to 2200 nm are shown in Figure 4.1. The absorption bands in the range between 1450 and 1600nm are related to the first overtone of O-H bond, while the absorption bands between 1600 to 1850 belong to first overtones of the CH₃ (methyl) and CH₂ (methylene) groups. It is clear that there are some interferences between spectra of alcohols (Methanol and MEG) and water in almost the NIR entire region. The calibration models were developed and evaluated in different spectral ranges between 1400 to 1850 nm. The ranges higher than 1850 nm were excluded from the analysis due to very high absorption of water which produced large errors on methanol and MEG predictions. In the region comprised between 1000 and 1400 nm, the spectra of the water, MEG and methanol do not show any particular absorption feature, and they removed from the dataset.

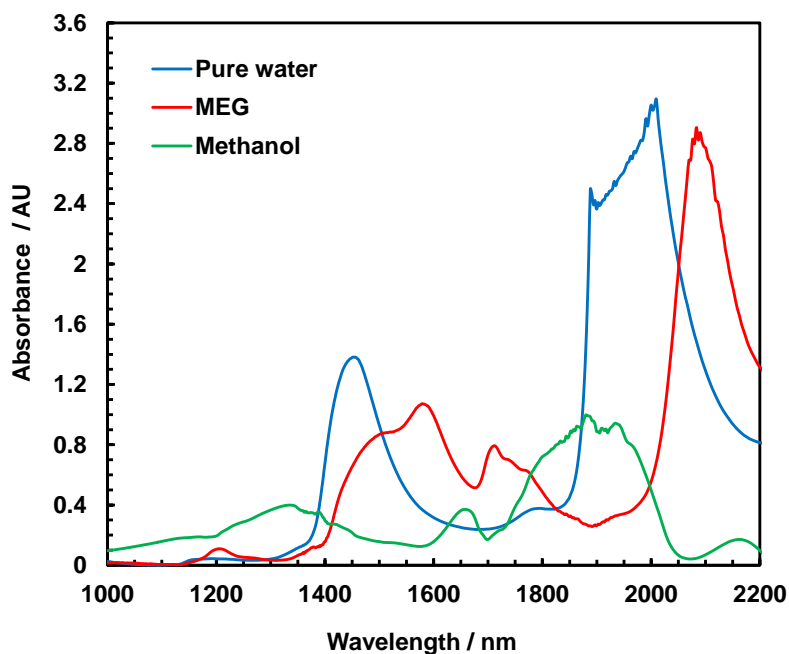


Figure 4.1. FTNIR Spectra of the pure water, methanol and MEG in a cuvette with a pathlength of 1 mm at atmospheric pressure and 293.15 K that captured by the FTNIR spectrometer.

UV region can provide some valuable information regarding the evolution of polymer contents in aqueous solutions. It was noticed that the absorbance values increase significantly between 300 and 400 nm while the concentration of PVCap in deionised water is varying from 0.5 to 3 mass% (Figure 4.2). A linear relationship was observed between the concentration of PVCap and absorbance. In this study, the NIR region was employed to determine the concentration of NaCl and THIs whereas UV region was used

to detect the changes in the concentration of PVCap which is low molecular weight polymers.

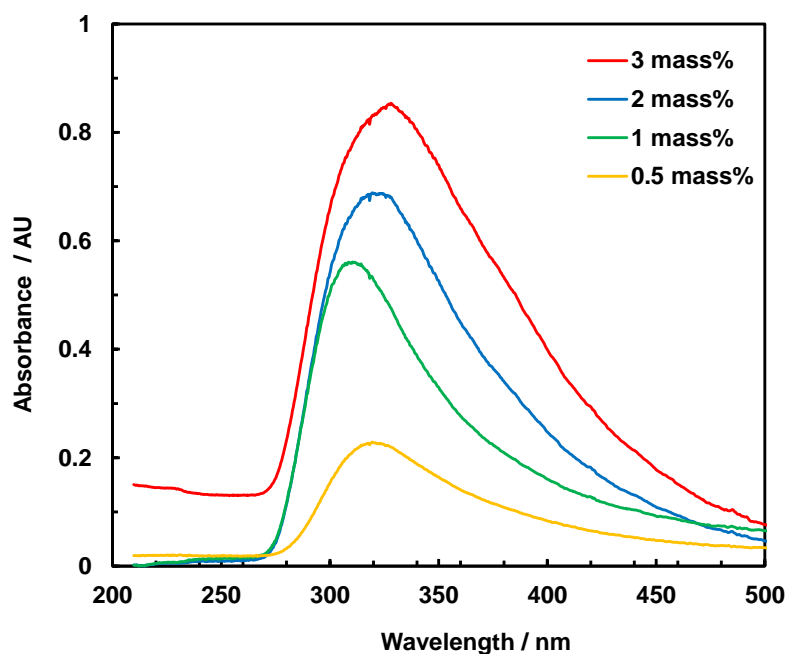


Figure 4.2. UV spectra of solutions with various PVCap concentrations captured by the UV-Vis-NIR spectrometer.

4.2.1 Partial Least Squares Model

Different partial least square (PLS) regression models were developed to predict the concentration of hydrate inhibitors and salt in the aqueous solutions. Before construction of the calibration models, all the spectra were first normalised and converted to absorbance unit (AU). Before construction of calibration models pre-processing methods had been implemented to the spectral data. In this study, the spectra were pre-treated using first Savitzky-Golay derivative with a different number of window points from 3 to 21. Root mean square of cross validation (RMSECV), root mean square of prediction (RMSEP), number of latent variables (LVs) and standard error of prediction (SEP) were used to evaluate the performance of the developed PLS models. It should be noted that the leave-one-out cross-validation was employed to develop the PLS model. Outliers were detected by plotting Hotelling's T^2 versus Q residuals. More detailed description of PLS, RMSECV, RMSEP, LVs and SEP could be found in Chapter 2. All the analysis were performed in Unscrambler® X10.3 (CAMO, Oslo, Norway).

4.3 Experimental Methodology

4.3.1 Experimental equipment

Figure 4.3 illustrates a schematic of the experimental apparatus. A broadband, 20 W tungsten-halogen light source (HL-2000-FHSA, Ocean Optics) and UV/VIS/NIR light source (L10290, Hamamatsu) were guided to an FT-NIR spectrometer (Arcoptix) and UV-VIS-NIR spectrometer (C10082MD, Hamamatsu Ltd.) respectively via a fibre optic cables. For NIR analysis, samples were scanned in a cuvette with a pathlength of 1 mm and internal volume of 350 μL and a cuvette with a pathlength of 5 mm and internal volume 1750 μL was used for UV analysis. The cuvettes were mounted in a metallic jacket that was temperature controlled by circulating fluid from a circulating water bath. The FT-NIR spectrometer can cover the spectral range of 900 – 2500 nm and the UV-Vis-NIR spectrometer covers the range between 200 to 1100nm. The absorption of wavelengths across this range is measured relative to a reference spectrum measured with air. The FT-NIR spectrometer has USB connectivity for control and data acquisition.

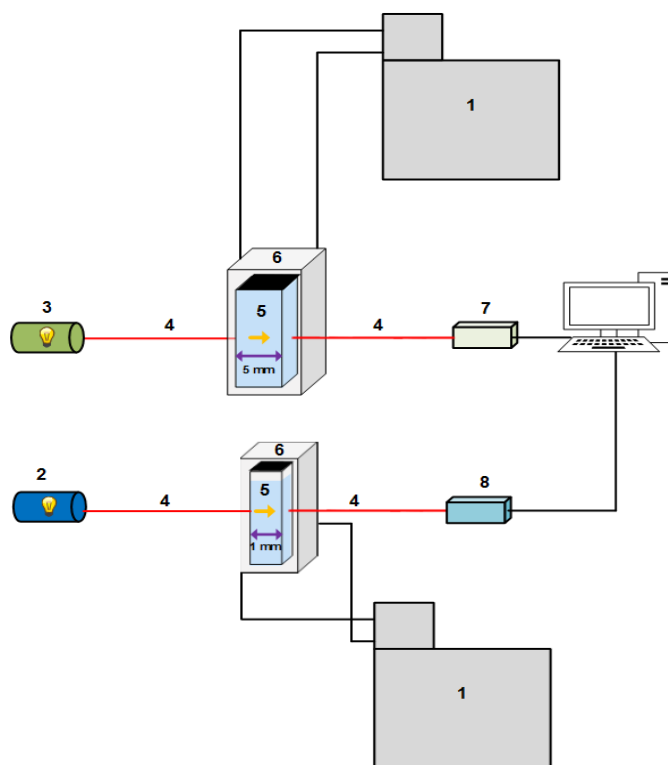


Figure 4.3. Schematic diagram of the spectroscopy setup, 1: Cooling / heating bath, 2: FT-NIR source, 3: UV-Vis-NIR source, 4: Fibre optic, 5: Cuvette, 6: Cuvette holder with a metallic jacket, 7: NIR detector and 8: UV-Vis detector.

4.3.2 Experimental procedure

Before starting each measurement, the cuvette was cleaned using deionised water and acetone and compressed air was used to dry the cuvette. Then, the sample was placed into a cuvette and mounted in the metallic jacket. The system was left for 2 minutes to reach thermal equilibrium. For measurements of test samples, an average of thirty spectra was recorded, and the same test sample was measured typically three times using three different aliquots of the sample. The temperature was set to 293.15 K in all cases.

4.3.3 Experimental material

Chemicals used in these experiments were mono-ethylene glycol (MEG) and methanol (MeOH) with 99.5% purity, and NaCl salt which was 99.5% pure. Poly-nvinylcaprolactam (PVCap) used as the KHI inhibitor which supplied by BASF. Three comprehensive calibration and prediction data sets were prepared using about 300 solutions covering the concentrations shown in Table 4.1. All samples were prepared gravimetrically using deionised water.

Table 4.1. Range of concentrations for the three calibration series.

Species	Calibration range #1 / mass%	Calibrated range #2 / mass%	Calibrated range #3 / mass%
MEG	0 – 50	-	0 - 50
Methanol	-	0-50	-
PVCap	-	-	0 - 3
NaCl	0 – 7	0 - 7	0 - 7

4.4 Result and Discussions

After applying the first Savitzky-Golay derivative (SG1) with different smoothing points to calibration data set, different PLS models were developed by employing different wavelength regions in the ranges 1400-1850 nm. To examine the performance of the models at first and second overtone regions, three spectral regions were selected for the construction of the calibration models: “A” (1400-1850 nm), “B” (1400-1600 nm), “C” (1600-1850). Same regions were also used to determine the concentration of salt according to the changes in absorption of water, MEG and methanol as a result of variation in concentration of NaCl. Regarding the PVCap, all the PLS models were developed in the range between 300 and 350 nm. It should be noted that all the solutions that were used as calibration data set contain different concentrations of NaCl and MEG. Hence, a single wavelength in UV region cannot be used to create a linear regression

model for measuring the concentration of the PVCap in the solution as the presence of other solutes in the solution affect the accuracy of the linear regression model. The appropriate wavelength region and the best pre-processing method for all the developed models were found according to the calculated RMSEP and SEP values, and finally, the model which provides the lower prediction errors was select as a final model.

4.4.1 MEG Systems with NaCl

The maximum concentration for MEG and salt was set to 50 and 8 mass% respectively. The NIR spectra of the calibration data set used for developing of the PLS models is shown in Figure 4.4. In this study, the spectra were pre-processed using Savitzky-Golay first derivative (SGD1) with different smoothing points. The best results in terms of RMSECV, RMSEP and SEP values were obtained while the SGD1 with 5 smoothing points was applied to the dataset. 35 samples were used for calibration, and 20 independent samples within the calibration range were used to assess the accuracy of the developed calibration models. The NIR spectra of calibration solutions after SGD1 treatment are illustrated in Figure 4.5.

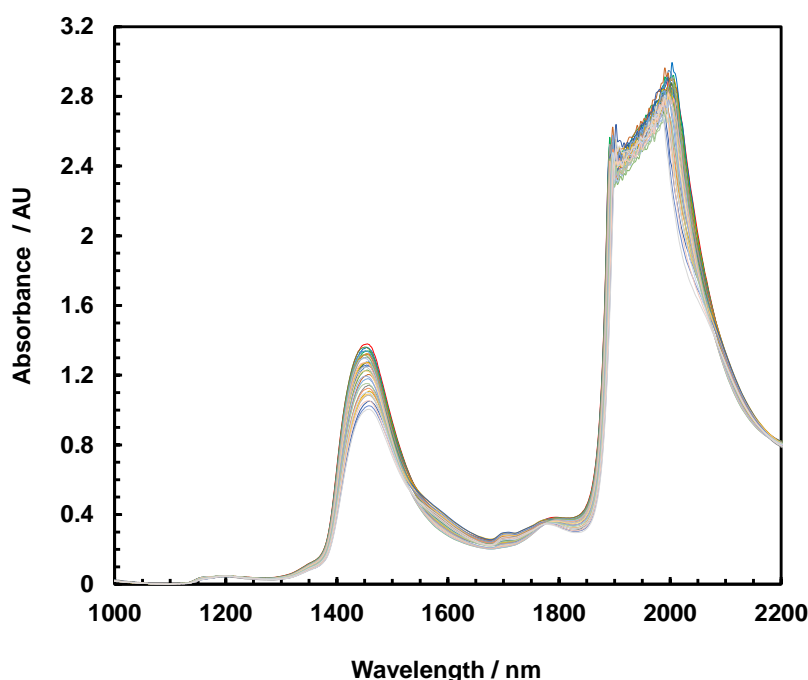


Figure 4.4. NIR Spectra of 35 water samples with different MEG and salt concentrations without applying any pre-processing method in the wavelength range from 900 to 2500 nm.

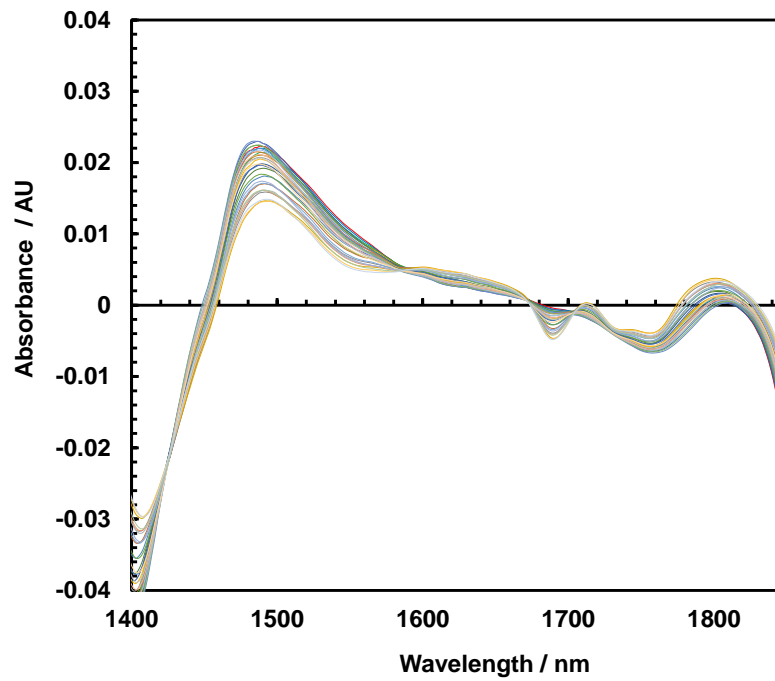


Figure 4.5. NIR Spectra of 35 water samples with different MEG and salt concentrations after applying the Savitzky-Golay pre-treatment in the wavelength range from 1400 to 1850 nm.

The performance of each PLS model at various spectral ranges is presented graphically through plots of NIR-predicted data obtained from the PLS models versus the measured value. Figure 4.6 and Figure 4.7 show the goodness of the fit, presented by plotting the measured and predicted values for MEG and NaCl in water samples.

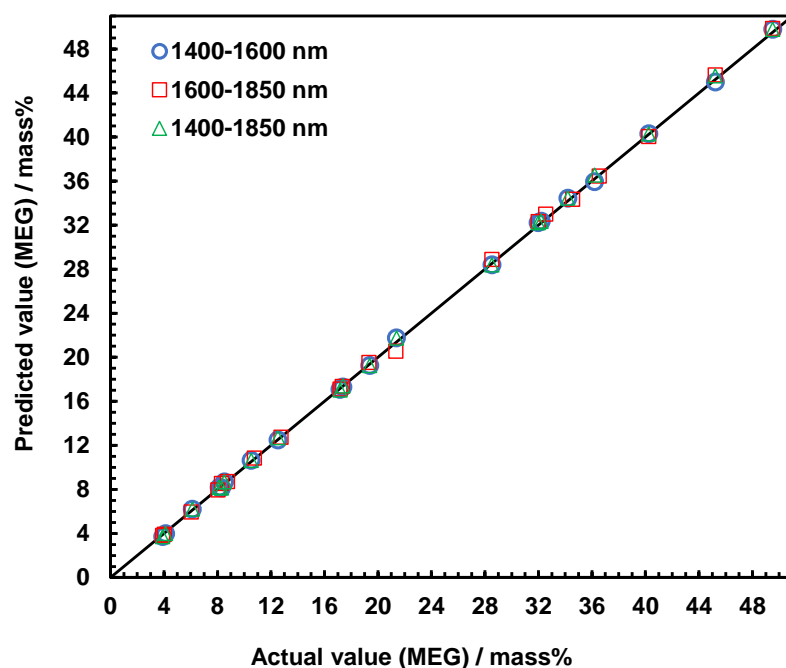


Figure 4.6. PLS regression plot of predicted versus actual concentration of MEG at different wavelength ranges.

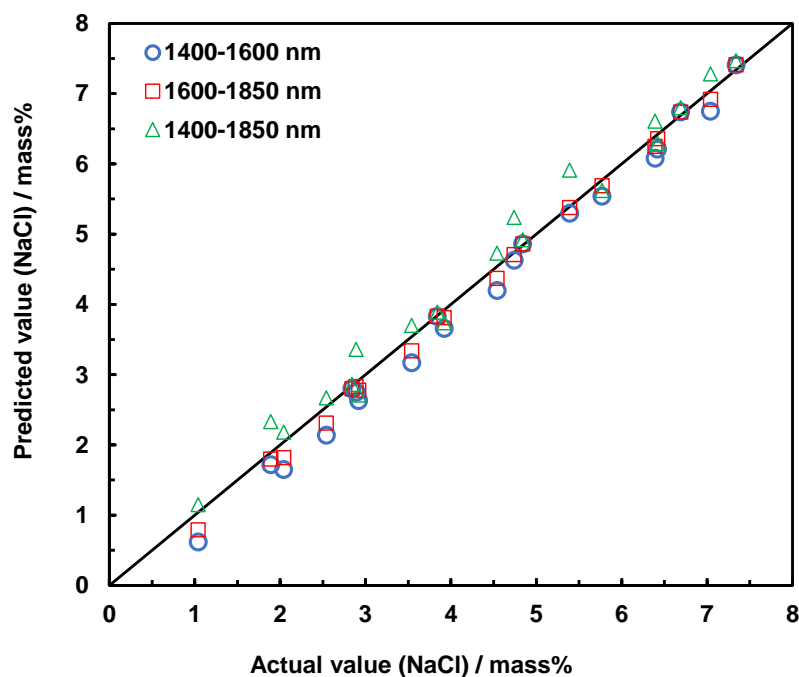


Figure 4.7. PLS regression plot of predicted versus actual concentration of NaCl at different wavelength ranges.

Table 4.2. Summary of results for calibration and prediction sets for MEG and NaCl in the water samples using NIR spectra and PLS.

Component	Range	LV	RMSECV	R ²	RMSEP	R ²	Bias	SEP
MEG	A(1400-1850)	4	0.147	0.999	0.192	0.999	-0.009	0.201
	B(1400-1600)	4	0.186	0.999	0.195	0.999	-0.010	0.203
	C(1600-1850)	5	0.202	0.999	0.281	0.999	-0.011	0.285
NaCl	A(1400-1850)	4	0.163	0.995	0.134	0.995	-0.008	0.142
	B(1400-1600)	4	0.219	0.991	0.249	0.995	-0.008	0.263
	C(1600-1850)	4	0.203	0.991	0.249	0.994	-0.010	0.251

Table 4.2 reports the results obtained for calibration and prediction sets. All of the models performed very well in predicting the concentration of MEG and NaCl in water samples not included in the calibration set. The R² for predicted samples ranged from 0.991 to 0.999 with SEP ranging from 0.29 to 0.14 mass%. Regarding MEG, the best results in terms of RMSEP and SEP values were found for models that were created in the regions “A” and “B”. A slight increase was noticed in the RMSEP and SEP values in the region “C”, showing that the PLS model is not capable of predicting the MEG content in solutions containing MEG, water and NaCl as accurate as region “A” and “B”. Region “A” is related to the first overtone region of OH bond and first overtone of the C-H stretching for CH₂ bond, whereas the changes in absorption bands in region “B” is attributed to only first overtone region of OH bond. It can be seen from Table 4.2, the developed PLS model for MEG in region “A” shows slightly lower RMSEP and RMSECV values than one created in the region “B”.

For NaCl, the best results were found when the wider spectral range (“A”) was employed for the construction of the calibration model. The calculated RMSECV, RMSEP and SEP values in region “A” were 0.16%, 0.13% and 0.14% respectively for the created NaCl prediction model. In fact, NaCl does not absorb the NIR light, but the presence of the NaCl in the aqueous solution can cause distortion in the regions that water absorbs the NIR light due to a perturbation that sodium and chloride ions create on the hydrogen bond network. All these results confirm that NIR spectroscopy technique can predict the concentration of MEG and NaCl simultaneously in water samples.

The RMSEP values of all the developed models are plotted as a function of wavelength range (Figure 4.8). It is apparent that the PLS models that developed in 1400-1850 nm wavelength range provide the lowest SEP values.

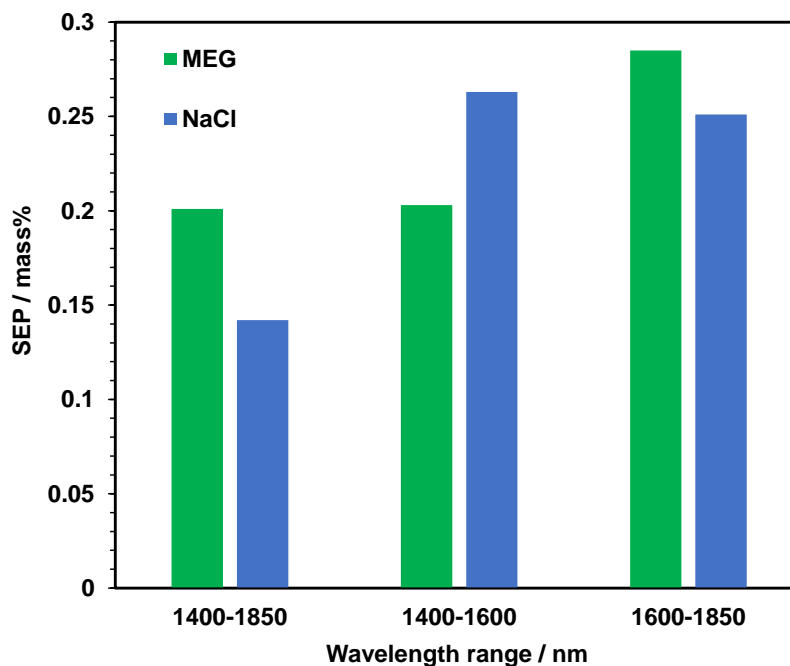


Figure 4.8. The comparison of root mean square of prediction (RMSEP) for MEG and NaCl at various wavelength ranges.

Finally, the limit of detection (LoD) was calculated for the best calibration model. To calculate the LoD, the spectra of ten samples of water without any solute and the spectra of 10 samples with the highest value of MEG (50 mass %) and salt (7 mass %) were measured. Then, the final PLS regression models were employed to predict the concentration of MEG and NaCl. Then, the average standard deviation of the predicted values was calculated for each model and was multiplied by 10/3 to roughly estimate the LoD.

Table 4.3. Calculated LoD for developed PLS models by using a Savitzky–Golay derivative pre-treatment with 5-point moving window in 1400-1850 nm wavelength range.

Composition	LoD (mass%)
MEG	0.53
NaCl	0.29

Furthermore, the t-test with 95% confidence and n-1 degree of freedom was carried out separately for the final PLS models based on the bias of each model. For MEG the $t_{\text{calculated}}$ was equal to 0.25 and for salt $t_{\text{calculated}}$ was 0.37 which were less than $t_{\text{critical}} = 1.725$, indicating the bias included in each PLS model was not significant and does not produce a systematic error.

4.4.2 Methanol systems with NaCl

Methanol has been used for hydrate inhibition in many fields and is the most common hydrate inhibitor. In this section, the ability of spectroscopic technique was investigated to predict the concentration of methanol and NaCl in water samples. Same as MEG-NaCl system the wavelengths less than 1400 and higher than 1850 nm are removed from the dataset. Regions “A”, “B” and “C”, were used to develop PLS models to predict the concentration of methanol and NaCl simultaneously in aqueous solutions. 35 samples were prepared as calibration samples, whereas 20 samples were prepared to evaluate the performance of the developed calibration models. All the sampled were placed into quartz cuvette with a pathlength of 1mm. The SGD1 with 5-points moving window was applied to all the raw data. Results are corroborated by the graph of predicted versus actual values obtained using the PLS model for independent samples in Region “A”, “B” and “C” (Figure 4.9 and Figure 4.10).

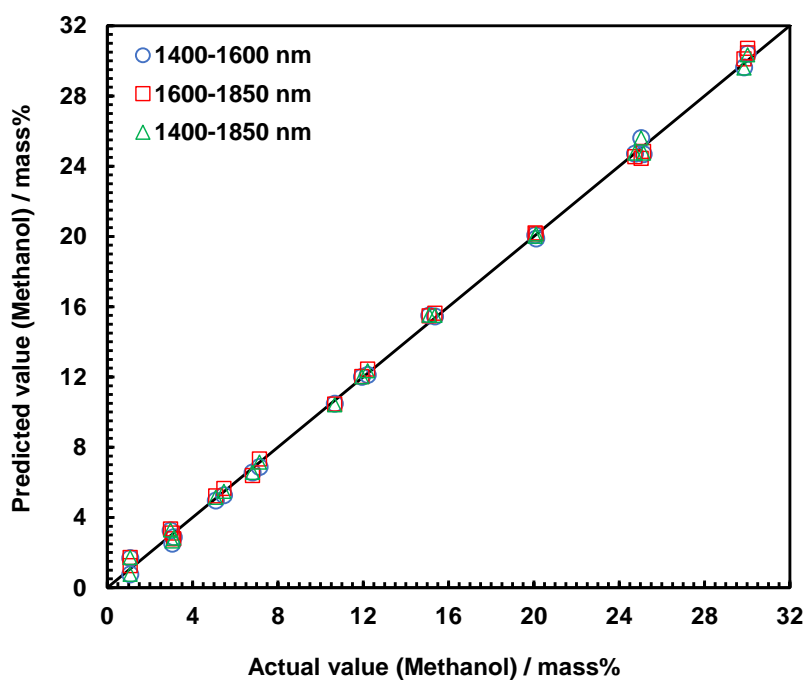


Figure 4.9. PLS regression plot of predicted versus actual concentration of methanol at different wavelength ranges.

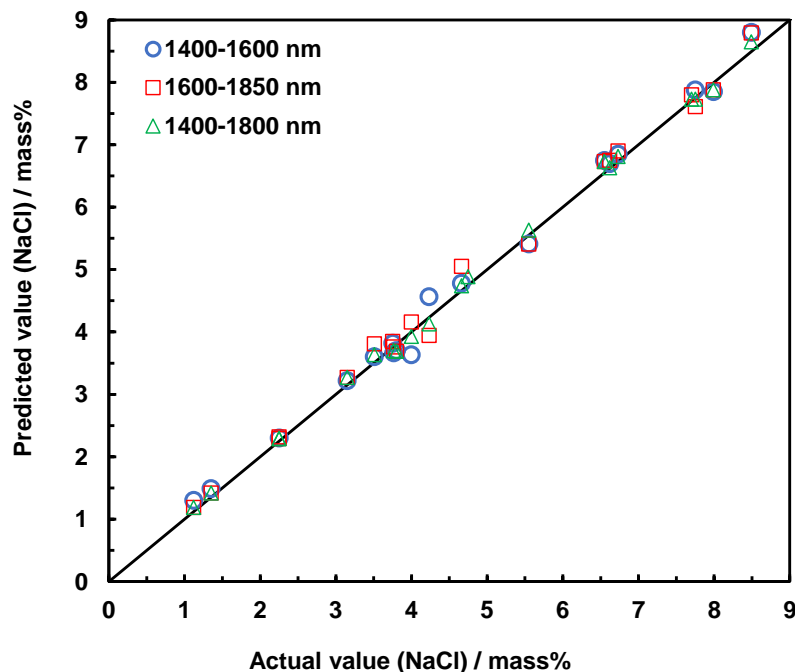


Figure 4.10. PLS regression plot of predicted versus actual concentration of NaCl at different wavelength ranges.

Good agreement was obtained between the values that predicted from developed PLS models and experimental values, demonstrating the adequate performance of created models for determining the concentration of methanol and NaCl in aqueous solutions.

Table 4.4. Calculated RMSECV and RMSEP in mass% and latent variables for developed PLS models by using a Savitzky–Golay derivative pre-treatment with a second-order polynomial and a 5-point moving window.

Component	Range	LV	RMSECV	R ²	RMSEP	R ²	bias	SEP
Methanol	A(1400-1850)	5	0.249	0.999	0.232	0.999	-0.009	0.228
	B(1400-1600)	4	0.251	0.999	0.241	0.999	-0.010	0.239
	C(1600-1850)	4	0.311	0.999	0.292	0.999	-0.012	0.301
NaCl	A(1400-1850)	5	0.163	0.995	0.134	0.995	-0.009	0.165
	B(1400-1600)	4	0.219	0.991	0.249	0.995	-0.008	0.225
	C(1600-1850)	4	0.203	0.991	0.249	0.994	-0.009	0.209

Table 4.4 shows the spectral range that utilised for each calibration model. It can be seen that all the models are performing well. Region “A”, which corresponds to the first overtone region of OH bond and first overtone region of C-H stretching for CH₃ bond was shown the best results in terms of RMSECV, RMSEP and SEP values. Same results were obtained for NaCl, and the created PLS model at region “A” has produced the lowest SEP value compare to other spectral regions.

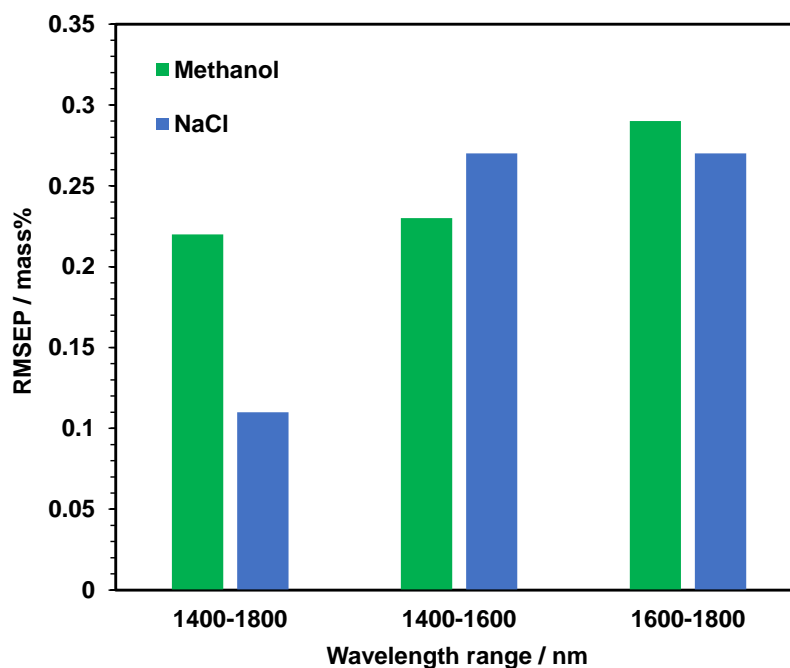


Figure 4.11. The comparison of root mean square of prediction (RMSEP) for MEG and NaCl at various wavelength ranges.

The LoD were calculated for the PLS model that constructed in the range from 1400 to 1850 nm and are tabulated in below.

Table 4.5. Calculated LoD for developed PLS models by using a Savitzky–Golay derivative pre-treatment with 5-point moving window in 1400-1800 nm wavelength range.

Composition	LoD (mass%)
Methanol	0.72
NaCl	0.31

One tailed t-test was carried out for both methanol and NaCl using the prediction samples to test the significance of bias that included in the final model. It was noticed that the relevant bias does not produce significant systematic errors, since the $t_{\text{calculated}}$ for methanol and salt were 0.38 and 0.12 which is less than t_{critical} at a level of 95% confidence.

4.4.3 MEG-PVCap systems with NaCl

In the last decade, using of low dosage inhibitors (LDHIs) such as KHIs has become popular in the oil and gas industry. The objective of this section is to investigate the ability of spectroscopy methods for predicting the concentrations of KHI and salt in aqueous

solutions simultaneously. Very low concentrations of KHI inhibitors are usually injected at the upstream of the pipelines. A number of companies are thinking of swapping from thermodynamic hydrate inhibitors such as MEG and methanol to LDHIs hydrate inhibitors. In the transition procedure, both thermodynamic and kinetic inhibitors are being injected [67]. After injecting both inhibitors for a period of time, they start to decrease the concentration of thermodynamic inhibitors gradually and hence both LDHI and thermodynamic inhibitor will exist in aqueous solution. Moreover, it is well-known that KHIs can only operate under some level of subcooling. Excess subcooling could lead to the KHI failure to delay nucleation and formation of gas hydrates. Therefore, a combination of a thermodynamic inhibitor with a KHI is accepted as an alternative option. Considering this fact that, in reality, salt is present in produced water. In this work the PVCap was used as KHI inhibitor. As polymers could absorb the UV light strongly and PVCap is a low molecular weight polymer, UV spectroscopy was used to determine the concentration of PVCap. To determine the concentration of PVCap, NaCl and MEG simultaneously all the calibration and prediction samples were analysed using both UV-VIS and NIR spectrometer and the interested spectral ranges were selected for the construction of the calibration models. To generate the necessary database for developing the PLS models a concentration range from 0 to 2 mass% KHI, 0 to 50 mass% MEG and 0 to 7 mass% NaCl was selected. All the measurements were carried out at a temperature of 293.15 K. The calibration solutions were aliquoted into a cuvette with a pathlength of 1 mm and 5 mm for NIR and UV analysis respectively. After data analysis, different PLS models were created and evaluated using independent data. The procedure for construction of the calibration models for MEG and salt was same as what explained in the previous sections. The presence of PVCap in the solutions does not allow us to employ the calibration models that already developed for MEG-NaCl systems as NIR is susceptible to either impurities or solutes that were not accounted for the construction of the calibration models. It should be mentioned that presence of a very low concentration of solutes (ppm level) would not affect the accuracy of the PLS models in this study as we are not interested to predict the low concentration of hydrate inhibitors in aqueous solutions. As mentioned in above, the PVCap calibration sample was defined in the concentration range of 0-3 mass%. Thus, it is necessary to develop new calibration models for MEG-NaCl-PVCap system to remove the effect of PVCap on the accuracy of the PLS models in the NIR region. 175 samples were prepared as calibration samples, and 20 samples were prepared to assess the performance of the calibration models. Figure

4.12, Figure 4.13 and 4.14 illustrate the agreement of the measured MEG, NaCl and PVCap contents of water samples with the predicted values in the same samples using the optimal model respectively.

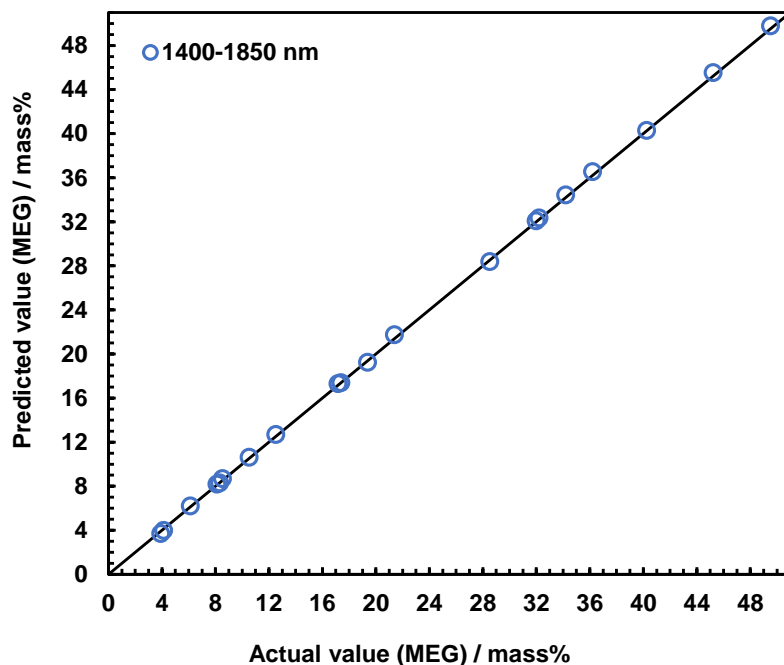


Figure 4.12. PLS regression plot of predicted versus actual concentration of MEG.

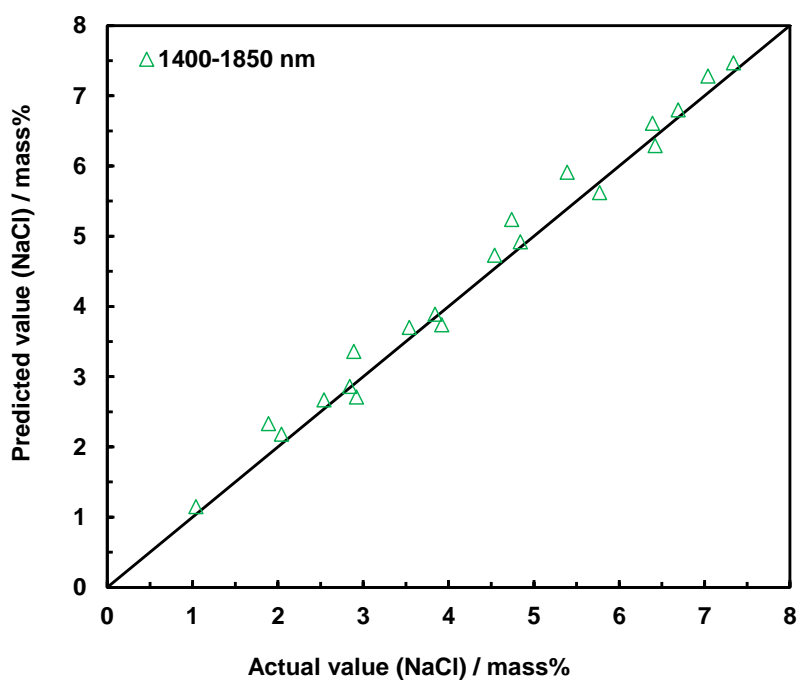


Figure 4.13. PLS regression plot of predicted versus actual concentration of NaCl.

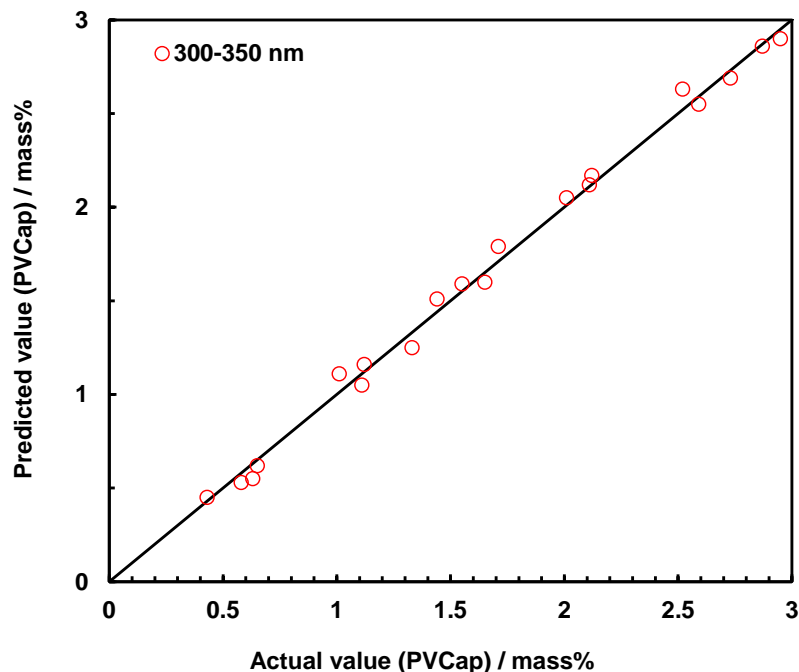


Figure 4.14. PLS regression plot of predicted versus actual concentration of PVCap.

The calibration models based on PLS for MEG and salt were developed at NIR regions between 1400 to 1850 nm and for PVCap the range between 300 to 350 nm were selected to develop the PLS model. It should be mentioned that all the UV spectra were pre-treated by applying SGD1 with 5 moving-point windows. The results obtained for the calibration models for all the components are shown in Table 4.6. The PLS models for PVCap determination indicated in Table 4.6 had RMSECV of 0.062 for calibration set and SEP value of 0.095 for prediction sets. The correlation coefficient for the prediction set was 0.991 and was obtained using 4 latent variables, showing the consistency of the developed model. Similar results to those for the MEG-NaCl system were observed for MEG and NaCl while PVCap presence in the calibration and prediction solutions. The LoD were calculated by following the procedure explained in section 4.4.1 for final models and tabulated in Table 4.7.

Table 4.6. Calculated RMSECV and RMSEP in mass% and latent variables for developed PLS models by using a Savitzky–Golay derivative pre-treatment with a second-order polynomial with 5-point moving windows.

Component	Range / nm	LV	RMSECV	R ²	RMSEP	R ²	bias	SEP
MEG	A(1400-1850)	4	0.15	0.999	0.20	0.999	-0.005	0.20
	B(1400-1600)	5	0.192	0.999	0.182	0.999	-0.008	0.203
	C(1600-1850)	5	0.201	0.999	0.275	0.999	-0.005	0.285
NaCl	A(1400-1850)	4	0.161	0.996	0.128	0.995	-0.009	0.142
	B(1400-1600)	4	0.215	0.993	0.229	0.997	-0.011	0.263
	C(1600-1850)	4	0.208	0.993	0.235	0.995	-0.007	0.251
PVCap	300-350	4	0.062	0.989	0.091	0.991	-0.011	0.095

Table 4.7. Calculated LoD for developed PLS models by using a Savitzky–Golay derivative pre-treatment with 5-point moving window in 1400-1850 nm wavelength range.

Composition	LoD (mass%)
MEG	0.55
NaCl	0.28
PVCap	0.10

Furthermore, to assess the impact of each bias on its PLS model, the t-value was calculated at a confidence level of 95%. Results revealed that the PLS models don't produce any significant inherent systematic errors as the calculated t-value is less than the t critical.

In summary, the results for the MEG-PVCap-salt system show good agreement between the PLS outputs and the experimental data, further confirming the applicability of the NIR method for KHI systems.

4.5 Evaluation of the Spectroscopic Techniques

In this section, the developed spectroscopic method was evaluated for the MEG-NaCl system. Figure 4.15 shows the schematic of the setup. A vessel of 2.3 L was used to form gas hydrate. The system temperature is controlled by a cooling bath that circulates coolant through a cooling jacket surrounding the test cell. The test was conducted with about 500 ml of aqueous solution containing 6.67 mass% NaCl and 10 mass% MEG and natural gas. After vacuuming natural gas was injected into the cell until the system was pressurised to the desired pressure. The natural gas composition is shown in Table 4.8. The magnetic mixer was set at 300 RPM. The system was cooled down in steps and left overnight at each test temperature to allow thermodynamic equilibrium.

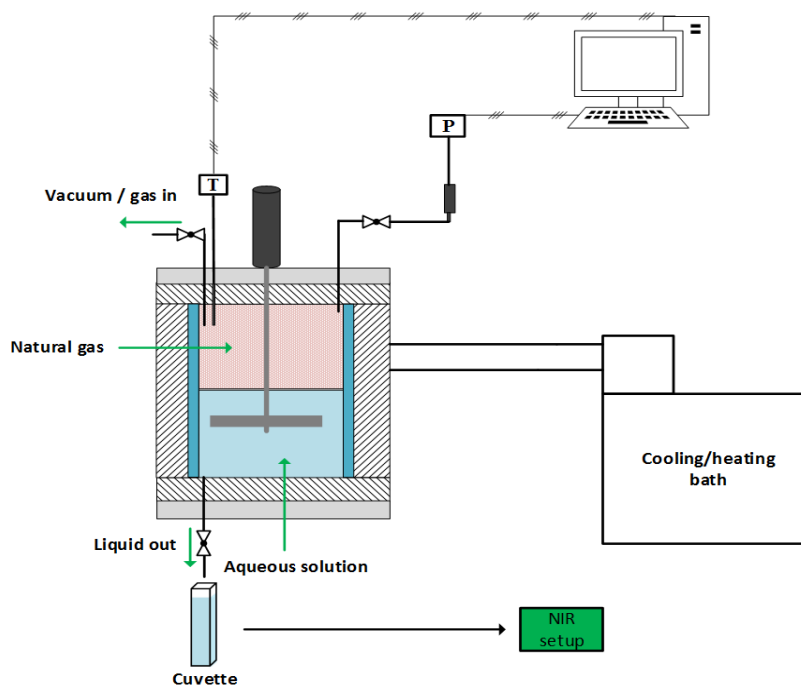


Figure 4.15. Schematic of the experimental setup.

Table 4.8. Composition of the natural gas.

Component	CO ₂	N ₂	C ₁	C ₂	C ₃	i-C ₄	n-C ₅	i-C ₅	n-C ₅
Concentration (mol%)	1.32	1.02	90.29	5.48	1.35	0.20	0.25	0.20	0.10

The experiment focuses mainly on determining the concentration of MEG and NaCl especially in the presence of gas hydrate. Initially, one sample was taken when the system was outside hydrate stability zone; then the system was directly cooled down to the target temperature to form gas hydrates with cooling rate of 0.5 K/min. After hydrate formation, the system was heated up with heating rate of 0.5 K/min to dissociate the hydrates. The hydrate dissociation process was carried out stepwise. The system was kept at each temperature for about 24 hours, and at each temperature, liquid sample was taken from the bottom of the cell (Figure 4.15), which normally resulted in about 0.01 MPa drop in the system pressure. All these liquid samples were placed into a quartz cuvette and analysed using the NIR spectrometer. The developed PLS models then used to predict the concentration of MEG and NaCl in the aqueous solutions. Figure 4.16 highlights the sampling points collected during the duration of the experiment.

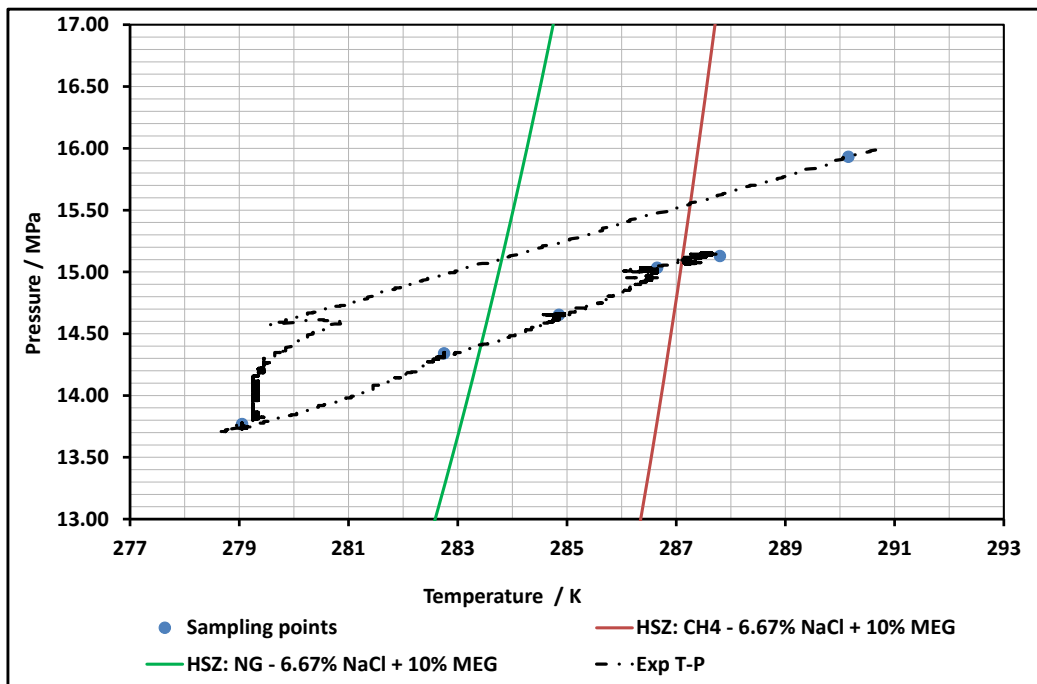


Figure 4.16. Temperature-pressure profile and sampling points for the system with natural gas, deionised water, MEG and NaCl.

- Sample 1: at 290.15 K and 15.93 MPa outside hydrate stability zone
- Sample 2: at 279.05 K and 13.77 MPa inside the sI and sII hydrate stability zones.
- Sample 3: at 282.75 K and 14.34 MPa inside the sI and sII hydrate stability zones.
- Sample 4: at 284.85 K and 14.65 MPa outside the sI hydrate stability zone and inside sII hydrate stability zone.
- Sample 5: at 286.65 K and 15.03 MPa outside the sI hydrate stability zone and inside sII hydrate stability zone.
- Sample 6: at 287.25 K and 15.13 MPa outside hydrate stability zone.

Table 4.9 shows the test results. Both salt concentration and MEG concentration were measured using the developed PLS models, which is listed in the column that is marked “NIR”, while the column “Exp” signifies the actual salt and MEG concentrations. The experimental values were calculated with regards to the reduction of water because of formation of gas hydrates. The procedures to calculate the amount of water converted to hydrate were explained in section 3.3.3. Therefore, at each sampling point the amount of water converted to hydrate was calculated to find the amount of free water and hydrate

inhibitor (experimental values). These values then used for comparison with the values measured by the NIR.

As shown in Table 4.9, the NIR measured salt (NaCl) concentrations are in good agreement with the actual values, and the deviations are less than 0.2 mass%, indicating the accuracy of the developed method. Hydrates exclude salt from their structures, therefore upon hydrate formation the concentration of salt in the remaining free water increases. Furthermore, the increase in the concentration of salt is proportional to the amount water converted into hydrates. Also, hydrates exclude water from their structures; hence water resulting from hydrate dissociation should have a lower salinity. It can be seen from Table 4.9, the concentration of salt was increased after formation of gas hydrates, and this value was started to decrease due to an increase of water concentration as a result of hydrate dissociation. At Stage 1 (before hydrate formation) and Stage 2 to 5 (during hydrate dissociation), the MEG measured values are also in good agreement with the experimental values in about 0.2 mass% of measurement deviation.

Table 4.9. Test results of the NIR method.

T K	P MPa	Water in hydrate Barrel/MMscf	NaCl (mass%)		MEG (mass%)	
			Exp	NIR	Exp	NIR
290.2	15.93	0	6.31	6.67	10.0	10.05
279.1	13.77	115.2	8.72	8.82	12.64	12.56
282.75	14.34	75.50	8.59	8.68	12.58	12.81
284.85	14.65	25.21	8.10	8.17	12.01	12.14
286.65	15.03	7.12	7.81	7.70	11.29	11.14
287.25	15.13	0	6.29	6.71	9.96	10.24

From these results it can be concluded, the NIR method could be applied for determining the concentration of thermodynamic inhibitors and salt in aqueous solutions and can be used as a reliable hydrate monitoring system. However, it is necessary to test more systems with different fluid systems to confirm the reliability of this method.

In Chapter 3, it was confirmed the NIR spectroscopy technique could detect the presence of natural gas hydrates and hydrate memory. Furthermore, based on the results that obtained in this chapter, it can be concluded that the combination of NIR and UV spectroscopy techniques can be employed to determine the concentration of both NaCl and hydrate inhibitors (LDHIs & THIs). Thus, a combination of these two developed techniques could provide a reliable and practical hydrate early warning and monitoring system.

4.6 Conclusions

In this chapter a new spectroscopy technique was developed for some inhibition systems: a) MEG-NaCl system, b) methanol-NaCl system and c) KHI-MEG-NaCl system. We demonstrated that NIR spectroscopy in combination with PLS method could be employed to predict the concentration of MEG/Methanol and NaCl simultaneously.

- According to reported results, NIR and UV spectroscopy techniques are promising techniques for detection of NaCl and hydrate inhibitors in water samples. Given the promising results reported herein, further work should be carried to extend this technology for other inhibition systems (i.e. Ethanol-NaCl system, Anti-agglomerants (AAs)-NaCl system) and make this method applicable in vast ranges of temperature as variation in temperature can affect the accuracy of the developed PLS models that calibrated at a single temperature.
- This method was tested for one typical inhibition system (MEG-salt system) before and during hydrate formation and dissociation. The results showed that the developed method could determine the concentration of NaCl and MEG with an acceptable accuracy.

In conclusion, the described system is suited for determining the composition of hydrate inhibitors as well as NaCl. As measurement times in the order of seconds (including data acquisition and evaluation) can be realised, the system is capable of providing online liquid characterization. Based on the results obtained in this study the spectroscopy methods are capable of predicting the concentration of NaCl and hydrate inhibitors and can be used as a suitable method for monitoring hydrate safety margin with a high level of confidence.

CHAPTER 5: SPECTROSCOPIC AND ELECTROMETRIC pH MEASUREMENTS AND pH MODELLING

5.1 Introduction

Atmospheric concentration of CO₂ has increased steadily from around the time of the industrial era. This increase in concentration of CO₂ can cause serious global warming and climate change issues. Hence, expanding the methods for CO₂ reduction in the atmosphere has become an important topic. In the last decades, this issue has prompted researchers to identify methods to combat global warming.

Carbon Capture and Storage (CCS) is currently one of the most widespread technologies aimed at alleviating the increase of CO₂ in the atmosphere. Currently, injecting CO₂ at high pressures in deep geologic formations, such as oil and gas reservoirs and deep saline aquifers, is the main alternative strategy for permanent or mid-term disposal of CO₂ instead of releasing it into the atmosphere.

A CCS cycle normally consists of three stages: capture, transportation and storage. The process comprises of the separation of CO₂ from the industrial sources, transport to a storage location and then long-term isolation from the atmosphere. To reduce the emission of CO₂, the carbon dioxide in flue gas of the feedstock in industrial processes must be captured and separated to produce the high-purity CO₂ for the storage purposes or enhanced oil recovery. There are various technologies available to capture and separate emitted CO₂ from at power stations, industrial sites or even directly from the air. The capture of CO₂ is more focused on large CO₂ emission sources, such as industries, energy-related sources and human activities [108]. There are three main carbon technologies; pre-combustion, post-combustion and oxyfuel. These technologies are briefly explained in following. In pre-combustion method, coal is combined with oxygen (O₂) to produce gas (synthetic gas) using a gasifier. The synthetic gas is mainly made up of carbon monoxide (CO) and hydrogen (H₂) [109]. However, the composition of the synthetic gas is rest on the gasifier conditions and the coal characteristics. In the next step, the synthetic gas is passed through a water gas shift reactor (WGSR) to converts the CO present in the gas mixture into H₂ and CO₂. The CO₂ can be safely captured and compressed to transport to storage site, while the H₂ is burned to drive turbine and generate electricity. In post combustion process, the fossil fuel is burned as normal and the flue gas passes through an absorber. Re-generable solvents such as amine and mono-ethanol-amine (MEA) are

commonly used to absorb the CO_2 [110]. The CO_2 is subsequently separated from the absorbing solution at high temperatures using steam, letting the absorbing solution to be recycled again for capture and the CO_2 can be compressed and transported to storage site. The last of the capture method is oxyfuel process. In this method, before combustion, the N_2 is separated from the O_2 using an air separator and the leftover O_2 is then combusted with the fossil fuel and produce CO_2 , water vapour and little amount of sulphur dioxide (SO_2) and nitrogen dioxide (NO_2). The safe transport of CO_2 from the capture point to the storage location is a crucial step in the carbon capture and storage chain. Transporting CO_2 takes place daily in many parts of the world by truck and ship, however, for CO_2 captured from large scale power plants or chemical processes significant investment in transportation infrastructure such as the construction of CO_2 pipeline networks are required. Pipelines are used to transport CO_2 -rich fluids or acid gases in liquid or dense-phase state from the emission sources for disposal in suitable geological storage sites. CO_2 originating from capture processes is generally not pure and can contain impurities such as N_2 , H_2 , O_2 , H_2S , CO , etc. and water. Similarly, acid gases can vary greatly in composition. The nature of these fluids combined with compression and potentially long distance transportation could lead to challenging engineering and flow assurance issues. The presence of water may result in corrosion, ice and/or gas hydrate formation and pipeline blockage, so the fluid system should meet certain dehydration requirements. There are several potential options for storing captured CO_2 ; it can be sequestered either in deep geological formations or in the form of mineral carbonates [111] or used for CO_2 -enhanced oil recovery (EOR). The most important concern in subsurface storage and dissolution methods is possible CO_2 leakage to ocean and/or atmosphere [112], which could potentially cause serious damage to the marine environment due to natural ocean circulation and the mobility of the CO_2 dissolution [113] as well as compromising CCS as a climate change mitigation option. Currently, injecting CO_2 at high pressures in deep geologic formations such as oil and gas reservoirs and deep saline aquifers are the main strategy for permanent or mid-term disposal of CO_2 instead of releasing it into the atmosphere. Deep saline aquifers are an attractive option for CO_2 sequestration particularly in the North Sea due to the large storage capacity. Knowledge of the mutual solubility of CO_2 and water and the knock-on effect of impurities are therefore critical. As the formation water in deep geological formations (i.e., deep saline aquifers) contains salt, measuring the pH with high accuracy in saline water is a prerequisite to characterise the properties of solutions. Hence, it is required to understand the interactions between CO_2 and brine at downhole wellbore conditions (high pressure and temperature) to

prevent the formation of scale and corrosion in pipelines as well as for safety concerns in the downhole/wellbore region.

The electrometric technique is typically the most common method for pH measurement. Different types of high pressure and high temperature glass electrodes are commercially available to determine pH of aqueous samples under relevant conditions of temperature and pressure. These glass electrodes require careful handling, particularly during depressurization. Significant amounts of CO₂ can dissolve into the electrode filling solution when CO₂ is injected into the high pressure cell. Therefore it is necessary to depressurise the system slowly to avoid electrode damage because of a sudden drop in pressure. Furthermore, liquid junction potential is still one of the main drawbacks of this type of measurement, particularly when the sample comprises a large amount of salt. When two different electrolyte solutions come into contact with each other, liquid junction potential may occur between these solutions resulting in an inaccurate pH measurement [114]; several methods have been suggested for decreasing the liquid junction potential [115, 116]. Another disadvantage of this approach is that it is necessary to calibrate the glass electrode frequently before each measurement using buffer solutions, making this method an unsuitable technique for in-situ measurements.

Spectroscopic techniques are the alternative technique for precise measurement of pH in CO₂-H₂O and CO₂-H₂O-NaCl systems. However, this technique requires the introduction of a specific quantity of dye indicator into the aqueous phase for both calibration and testing samples. Furthermore, each dye indicator covers a limited pH range; nonetheless mixtures of dye indicators at specific concentrations can be prepared, in order to cover the required pH range. Unlike the electrometric method, in the spectroscopic method it is not necessary to calibrate the system for pH measurement each time before the measurement using buffer solutions.

A number of researchers have shown that optical and electrometric techniques can be used to measure the pH of CO₂ in water and brine at high pressures and temperatures with high accuracy. Meyssami *et al.* [117] measured the pH of CO₂ in various fluid systems using a pH probe that was placed inside a high-pressure vessel. They performed all the measurements at pressures up to 35 MPa and temperatures from 305 K to 315 K. An experimental investigation was carried out by Rosenqvist *et al.* [118] to measure the pH of water and mineral suspension solution containing dissolved CO₂ using a pH probe at pressures up to 1 MPa and temperature of 294 K. The measured pH values in deionised water were in good agreement with those reported in the literature. Schaef *et al.* [119]

reported the use of an electrometric technique to determine the pH of both CO₂ saturated H₂O and NaCl systems at pressures up to 11 MPa and temperatures up to 343 K. In this study, the molarity of the NaCl solution varied from 1 to 4 mol.L⁻¹. Molarity (M) is number of moles of solute that dissolved in one litre of solution, whereas Molality (m) is number of moles of solute that dissolved in one kilogram of solvent. Recently, the pH of the CO₂-H₂O system was measured at temperatures between 308 K and 423 K and pressures up to 15 MPa by Peng *et al.* [120]. They used a commercially-available pH and Ag/AgCl electrode mounted inside a high-pressure/high-temperature equilibrium cell. All the measured values were compared with a chemical equilibrium model, and a good agreement was obtained between the experimental and simulated data.

The applicability of ultraviolet-visible spectrometer to determine the pH of different fluid systems was investigated by a few research groups. Toews *et al.* [121] developed a spectrometer analyser to determine the pH in the CO₂-H₂O system by observing the change in the spectra of the dye indicator (Bromophenol Blue, BPB hereafter) at two specific wavelengths (430 and 590 nm). Measurements were performed at pressures up to 20 MPa and 343K. In this study, the effect of a change in pressure on dissociation constant was neglected for pH calculation. Parton *et al.* [122] also employed UV-Vis spectroscopic technique to determine pH in the CO₂-H₂O system at different pressure and temperature conditions. Several spectroscopic studies have been carried out to measure the pH in seawater in high temperature and high salinities at low pressures. The pH of natural seawater is limited to a range between 7.5 to 8.5 [123]. Millero *et al.* [24] reported the use of spectrometric techniques by dissolving m-cresol purple indicator in NaCl solutions to measure dissociation constants as a function of NaCl molality (0 to 5.08 m) and temperatures (278 to 318 K) at atmospheric pressure. They have provided an equation to calculate the pH based on dissociation constant of m-cresol purple in brine. These results confirmed the applicability of the spectroscopic method to measure the pH at high level salinities at high temperatures.

As a result of injecting the CO₂ in deep geological formations, the pH value could decrease to low values, depending on the temperature, pressure and salinity of the system [124]. Recently, Shao *et al.* [125] employed the UV-Visible spectrometer to measure the pH in the CO₂-H₂O and CO₂-H₂O-NaCl systems at elevated pressures in the presence of two chromophores, BPB and bromocresol green (BCG) which can cover the pH range between 2.5 and 5.2. The experimental values were in good agreement with those obtained through geochemical models. The maximum difference of the experimental data

from four different models was found to be 0.16 pH units [126]. They led to the conclusion that by selecting a suitable calibration procedure and appropriate dye indicators the spectroscopic technique can provide an accurate and precise pH value for the CO₂-H₂O-NaCl systems. Truche *et al.* [127] reported the pH values in the CO₂-H₂O and CO₂-H₂O-NaCl in a 1.4 molal (m) NaCl solution systems by combining the Raman spectroscopy and the electrometric techniques at temperatures up to 553.15 K and pressures up to 15 MPa. Furthermore, they introduced a new thermodynamic model by revising the Pitzer coefficients for formatted Pitzer.dat thermodynamic database. Good agreement was obtained between the model and the experimental data for the CO₂-H₂O-1.4 m NaCl system at elevated pressures and temperatures.

The aim of the present research is to; (1) measure the pH of the CO₂-H₂O solutions at pressures around 5.5 MPa and at temperatures up to 353.15 K using a commercially-available pH and glass electrode; (2) spectroscopic measurement of pH in different fluid systems (i.e., CO₂-H₂O and CO₂-H₂O-NaCl) using bromophenol blue indicator which typically cover the appropriate range for our pH working range at pressures up to 6 MPa and temperatures up to 323.15 K; (3) investigate the performance of spectroscopic technique to measure the pH in the CH₄-CO₂-N₂-H₂O and multi-components mixtures at pressures up to 15 MPa ; (4) finally, compare all the experimental results from both methods and the literature data with the developed thermodynamic model.

5.2 Theory of Spectrophotometric for pH Measurement

Changes in the colour of the dye indicator will result in a change in the absorbance spectra of protonated (HI⁺) and deprotonated (I²⁻) of the dye indicator. These indicators could exist in both the acid and base form, and the absorbance of light varies while the pH of the solution changes within a certain range of the pH value. The equilibrium between the protonated (acid) and deprotonated (base) of the dye indicator is utilised to measure the pH of the solution.



$$pH = pk_a + \log \frac{[B]}{[A]} \quad \text{Equation 5.2.}$$

Where A is the acid form of the dye indicator and B represents the indicator's base form and pK_a is the dissociation constant of the dye indicator and is equal to $-\log K_a$. BPB solutions exhibit clear changes in their absorbance while the pH value is changing in the interested pH range. It was observed that BPB absorbs the visible part of spectrum maximally at a wavelength of 440 nm (λ_1) when it is in the acid form and the base form of BPB absorbs the visible light maximally at a wavelength of 590 nm (λ_2). Change in the pH of the solution that containing BPB results in a change in the relative heights of the absorption peaks at these two wavelengths that one corresponds to the concentration of the acid form and other corresponds to the concentration of the base form of the dye in the solution. Equation 5.2 must be modified based on the spectral measurements. The absorbance spectrum of BPB in the acid form overlaps with the absorbance spectrum of BPB in the base form at a wavelength of 440 nm. Thus, it is required to consider the small amount of the base form in the acid wavelength. The same modification requires being considered for the base wavelength. This can be performed by applying the Beer-lambert Law.

$$C_{Total} = C_A + C_B \quad \text{Equation 5.3.}$$

C_A and C_B are the concentration of the acid form and the base form of the dye indicator into the sample in mol.kg^{-1} .

$$A(\lambda_1) = \varepsilon_A^{\lambda_1} \cdot C_A \cdot l + \varepsilon_B^{\lambda_1} \cdot C_B \cdot l \quad \text{Equation 5.4.}$$

$$A(\lambda_2) = \varepsilon_A^{\lambda_2} \cdot C_A \cdot l + \varepsilon_B^{\lambda_2} \cdot C_B \cdot l \quad \text{Equation 5.5.}$$

$$R_{\lambda_1}^{\lambda_2} = \frac{A(\lambda_2)}{A(\lambda_1)} \quad \text{Equation 5.6.}$$

$$\frac{[B]}{[A]} = \frac{R_{\lambda_1}^{\lambda_2} \left(1 - \frac{\varepsilon_A^{\lambda_2}}{\varepsilon_A^{\lambda_1} \times R_{\lambda_1}^{\lambda_2}} \right)}{\frac{\varepsilon_B^{\lambda_2}}{\varepsilon_A^{\lambda_1}} \left(1 - \frac{\varepsilon_A^{\lambda_1} \times R_{\lambda_1}^{\lambda_2}}{\varepsilon_B^{\lambda_2}} \right)} \quad \text{Equation 5.7.}$$

Where $A(\lambda_2)$ and $A(\lambda_1)$ are the absorbance wavelength for the base and acid form respectively, $\varepsilon_A^{\lambda_i}$ and $\varepsilon_B^{\lambda_i}$ are the molar absorptivity of the acid and base form at wavelengths of 440 nm and 590 nm. l is the path length, the distance that light travels through the sample. By modifying Equation 5.2, one can calculate the pH of a buffer solution using the following equation:

$$pH = -\log[H^+]_m = pK_a(t, p, \mu) + \log \frac{R - e_1}{e_2 - R e_3} \quad \text{Equation 5.8.}$$

pK_a is defined as a function of temperature, pressure and ionic strength. The sensitivity of temperature and ionic strength on the dissociation constant can be examined experimentally. The effect of pressure on the dissociation constant can be derived using following equation.

$$\frac{RT}{(P-1)} \ln \frac{K_a(t, p, \mu)}{K_a(t, 1, \mu)} = -\Delta V + \Delta k \frac{P-1}{2} \quad \text{Equation 5.9.}$$

Where $K_a(t, 1, \mu)$ is the dissociation constant of BPB at atmospheric pressure. R is the gas constant and, P and T are the pressure and temperature at standard state respectively. The value of volume changes (ΔV) and compressibility changes (Δk) for BPB were reported by Usha and Atkinson [128]. Using these values, one can solve Equation 5.9 to get the dissociation constant of the BPB at various pressures.

e_1 , e_2 and e_3 are the ratio of the molar absorptivity of the protonated (acid) and deprotonated (base) of BPB at two wavelengths (λ_1 & λ_2). They are defined as:

$$e_1 = \frac{e_a^{\lambda_2}}{e_a^{\lambda_1}} \quad e_2 = \frac{e_b^{\lambda_2}}{e_a^{\lambda_1}} \quad e_3 = \frac{e_b^{\lambda_1}}{e_a^{\lambda_1}} \quad \text{Equation 5.10.}$$

These values can be measured experimentally. The absorbance spectra of both acid and base forms of BPB were recorded Figure 5.1, and e -values were calculated using the equations given in above.

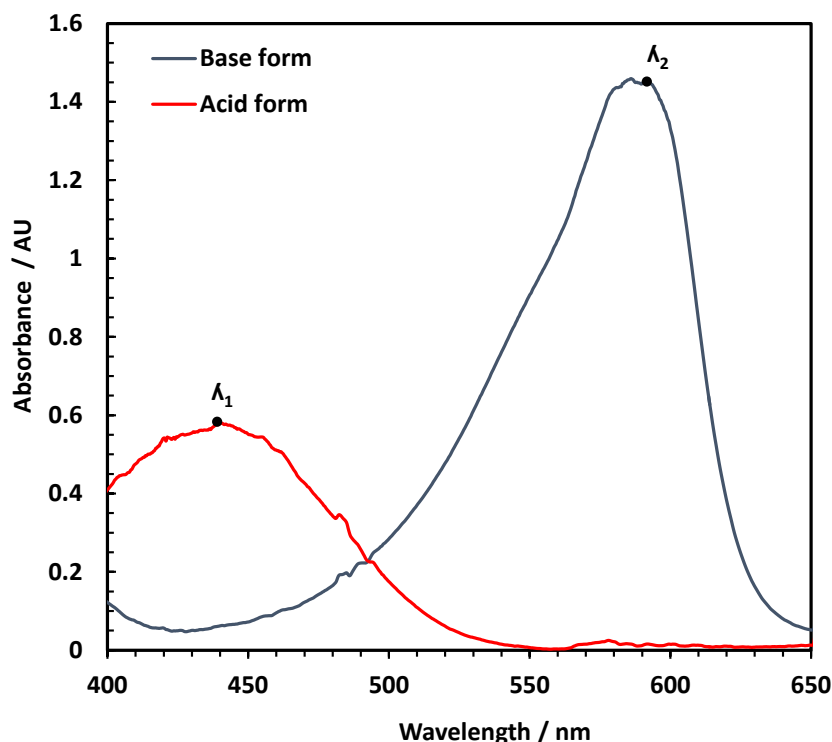


Figure 5.1. The absorbance spectrum of BPB solutions at pH of 7 (Base form) and pH of 1.5 (Acid form) using the UV-Visible spectrometer (1.4 cm path length).

5.2.1 Experimental

5.2.1.1 Materials

High purity research grade CO₂ (99.995%) was purchased from Air Products. All the solutions were prepared using deionised water. BPB indicator used in this study was provided by Sigma-Aldrich. The pH meter was calibrated using certified buffer solutions (pH 4 & pH 7) in order to determine the pH value of calibration samples. Buffer solutions were provided by Sigma-Aldrich and Hanna instruments. Nitrogen and deionised water were used for cleaning purposes. Prior to the start of each measurement, the system was cleaned by passing deionised water through the lines and then the cell. In order to dry the spectrophotometric cell, nitrogen was passed through the vessel.

5.2.1.2 Apparatus

An UV-Vis-NIR spectrometer (C10082MD, Hamamatsu Ltd.) equipped with an UV/VIS/NIR light source (L10290, Hamamatsu) was used for spectra acquisition between 200 to 1100 nm. The light source was mounted to one end of a spectroscopic cell through a fibre optic cable. Each end of the cell is fitted with windows to allow the light to pass through the sample. The cell windows are designed to work at elevated pressures. All the samples were placed in the high pressure cell which can operate at pressures up to 30 MPa. The setup has been designed to have maximum working temperature of 353

K. The test cell has an effective optical path length of approximately 1.4 cm and an internal diameter of 5.0 cm and internal volume of about 27 cm³. The cell is housed in a metallic jacket with fluid circulating through it from a cooling/heating bath. The pressure is measured using a Druck pressure transducer with a pressure range up to 60 MPa and previously calibrated against a dead weight pressure balance. This calibration procedure ensures a standard uncertainty of $u(P) = 0.04$ MPa. The temperature inside the cell is measured by a high precision PRT probe inserted into the cell, which is long enough to ensure the direct contact with the fluid. The temperature is regularly calibrated against a Prema 3040 precision thermometer. This calibration procedure ensures standard uncertainties of ± 0.05 K for the temperature readings. A schematic of the apparatus is shown in Figure 4.3.

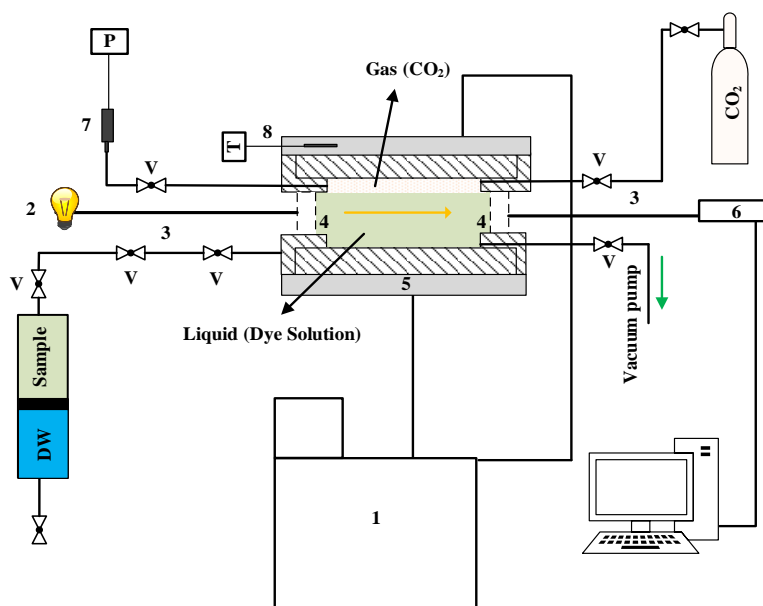


Figure 5.2. Schematic diagram of the spectroscopy setup for pH measurements, 1: Cooling / Heating bath, 2: Deuterium and tungsten light sources, 3: Fibre optic, 4: Sapphire windows, 5: High pressure cell, 6: Spectrometer, 7: Pressure transducer, 8: Temperature probe and V: Valve.

5.2.1.3 Experimental Procedure

The experimental procedure consists of several steps. First, all the buffer solutions were prepared by combining a specific amount of 0.1 m solution of citric acid and 0.1 m solution of trisodium citrate dihydrate. Various amounts of these stock solutions were combined together in order to reach target pH values. Sodium chloride was used to set the ionic strength of the buffer solutions to molality of 1, 2 and 3 mol.kg⁻¹. The pH of all the prepared buffer solutions with various ionic strengths at atmospheric pressure and the

test temperatures were measured using a pH meter (Hanna, HI-2002 Edge®) with a glass electrode. All the solutions for calibration were prepared in a pH range between 2.70 and 4.30 (Figure 5.3). After preparing the solutions with different pH and ionic strength values, the high pressure cell was first vacuumed, and 25 ml of each solution was placed into the cell. Then, the temperature of the cell was set at desired temperature, and the spectrum was recorded as a blank spectrum when the desired equilibrium temperature was reached. Afterwards, the BPB dye indicator was dissolved in the same solution at a concentration of $2 \times 10^{-5} \text{ mol.kg}^{-1}$ and the solution was then injected into the cell. A spectrum of the sample was recorded at the same temperature.

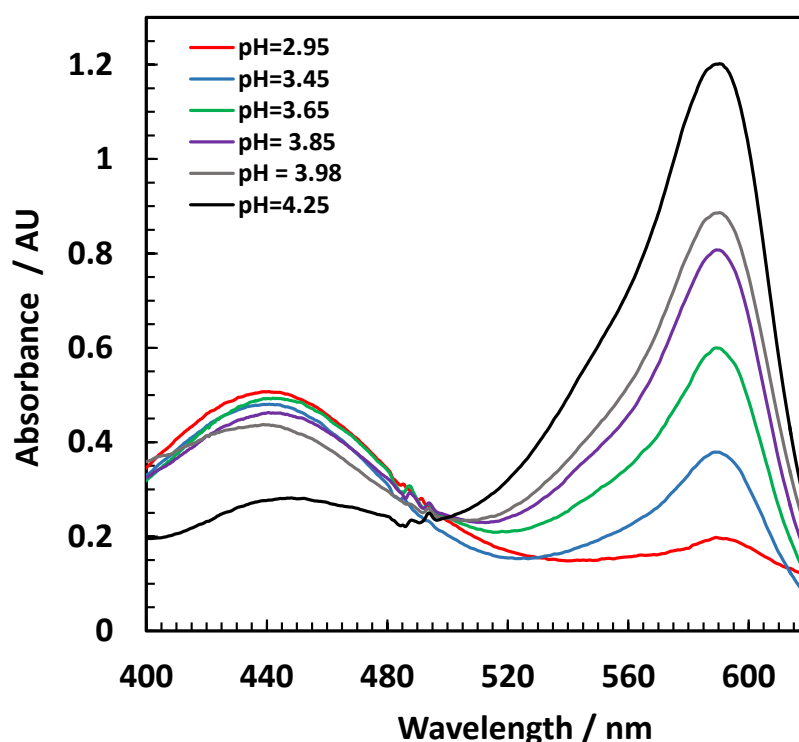


Figure 5.3. Spectra of BPB solutions with different pH values at a pressure of 0.1 MPa, the temperature of 298.15 K and zero ionic strength.

In order to measure the value of e_i (Equation 5.10) experimentally, the pH of the base solution was adjusted to 7 and the pH of the acid solution set to approximately 1.5 [126]. The concentration of BPB in the base and acid solution was adjusted to about $3 \times 10^{-5} \text{ mol.kg}^{-1}$ to obtain the maximum absorbance for BPB. Then, the samples were injected into the cell, and the spectra of the samples were recorded. In order to record the spectra of different systems, first, the cell was filled with deionised water or brine solutions. A headspace was left at the top of the cell to allow the gas sample to enter into the cell and dissolve easily into the fluid. When the system reached the desired equilibrium temperature, the spectrum was recorded as a blank. Then, the cell was vacuumed, and it

filled with deionised water or brine with a BPB concentration of $2 \times 10^{-5} \text{ mol.kg}^{-1}$. Pure CO_2 was then injected to achieve the desired equilibrium pressure. Equilibrium is assumed to have been reached when the total pressure remains unchanged within 0.007 MPa during a period of 30 minutes. To accelerate the thermodynamic equilibration process, the cell was placed on a pivotal axis, allowing the cell to rock using a compressed air-driven mechanism for each equilibrium condition; the spectrum was recorded three times in order to verify the measurements repeatability and to calculate the standard deviations of e_i and pK_a .

5.3 Electrometric Technique for pH Measurements

In this section, the electrometric technique is briefly described. The electrometric technique is one of the most popular methods for pH measurement in aqueous samples. pH is measured using a pH meter of a glass electrode. pH fundamentally represents the value of hydrogen ion activity in solutions. The principal of electrometric technique is based on the Nernst equation [129].

$$E = E^\circ + 2.3026 \left(\frac{RT}{F} \right) \text{pH} \quad \text{Equation 5.11.}$$

Where R and F are the molar gas constant ($8.3144 \text{ J mol}^{-1} \text{ K}^{-1}$) and the Faraday constant ($96.485 \text{ kC.mol}^{-1}$) respectively, T stands for the absolute temperature, E° is the standard electrode potential and E is measured e.m.f. in the presence of solution [120]. Different kinds of pH electrode are available commercially that are suitable for pH measurement over wide ranges of temperature and pressure. The glass electrode system measures the electrical potential difference between reference electrode and the pH measurement electrode within the glass membrane. The pH probe used in this study was a combination electrode, which combines both glass and reference electrode in one body. The reference electrode provides a constant electrical potential and the electrical potential of the glass electrode varies according to the solution that it is immersed in. The important part is the glass membrane which allows hydrogen ions to diffuse into the glassy membrane and this sets up an electrical potential between the inner buffer layer of the glass and the measured solution outside the glass membrane. The potential difference depends on the difference in the concentration of hydrogen ions inside and outside of the glassy membrane and the hydrogen ions will begin to diffuse from the lower activity part to the higher part; this

difference can be measured and used for the determination of pH for the solution. Before starting the measurement, it is necessary to calibrate the probe against the solutions of known pH at the operating temperature. One advantage of this method compared to spectrophotometric method is that the calibration procedure is very easy and fast but the glass electrode need to be calibrated frequently. Picture and schematic diagram of the glass electrode that used in this study are shown in Figure 5.4 and Figure 5.5.

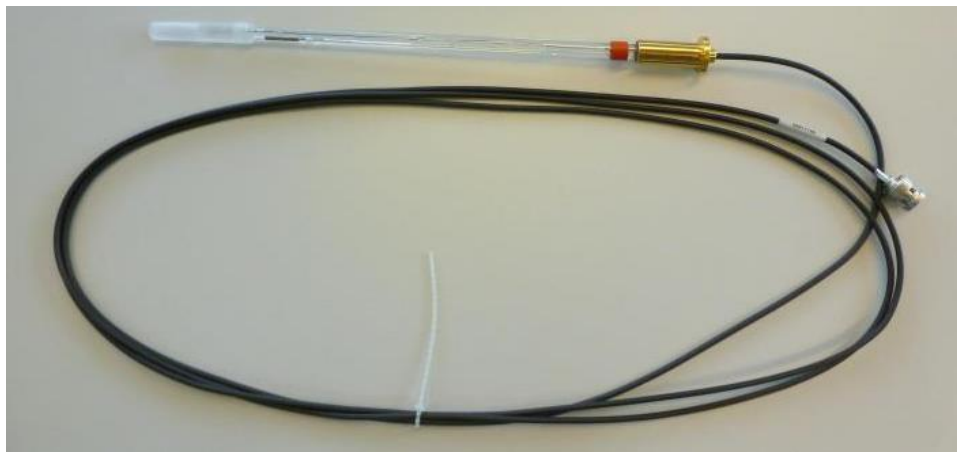


Figure 5.4. Picture of glass and reference electrode.

Although the pH glass measuring electrode responds very selectively to hydrogen ions, sodium, lithium, and, potassium ions can produce some interference in the pH measurement. The amount of this interference related to the size of the ion. Sodium ions cause the most significant interference. Lithium ions are not typically into solutions and potassium ion does not make considerable interference. In fact, sodium ions penetrate into glass electrode silicon-oxygen molecular structure, creating an offset in measured pH value, by varying the potential difference between the outer and inner surfaces of the electrode. Hydrogen ions replace with sodium ions, causing a decrease in hydrogen ion activity. Temperature is another factor that increases the error of the measurement when the concentration of sodium ions is high in the solution. Hence, the error of measurement increases as the temperature of sample increases. Depending on the glass formulation is used for measurement, sodium ion interference may shift to higher or lower pH. No glass formulation presently is presented that has zero sodium ion error. However, some methods like introducing salt bridges have been introduced to diminish the effect of sodium interference on pH measurement.

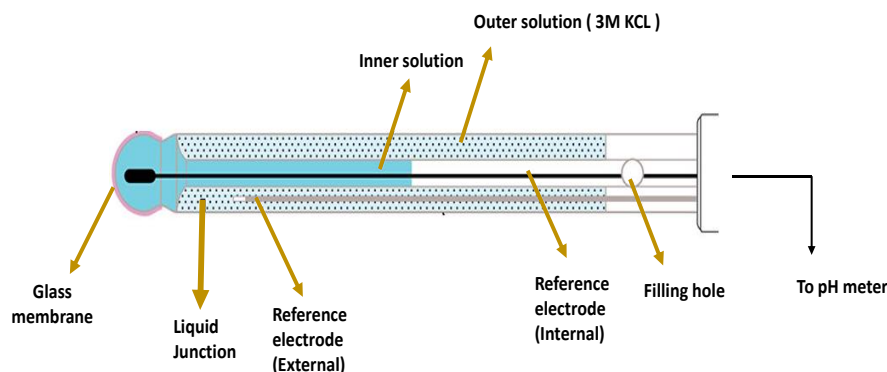


Figure 5.5. Schematic diagram of the glass and reference electrode.

5.3.1 Experimental

5.3.1.1 Apparatus

A high pressure vessel was purchased from Buchiglasuster as pictured in Figure 5.6. The cell volume is about 500 cm^3 , and it is constructed from Hastelloy which ensures that the wetted parts are resistant to acid. The cell was designed to operate at pressures up to 6 MPa, and it is capable of being used at temperatures up to 383 K. The pH probes were mounted through the closure of the vessels as shown in Figure 5.7. A pressure transducer was mounted directly on the top of the cell. A pressure transducer with a range up to 6 MPa was employed. The system allows real-time readings and storage of pressures during pH measurement. A high pressure magnetic stirrer was used to agitate the test fluids in order to accelerate the process of achieving thermodynamic equilibrium. The cell was surrounded by a cooling jacket connected to a cooling/heating bath for temperature control purposes. A temperature probe was used to monitor the cell temperature. The pH and temperature probes were connected to a controller box that records and displays both pH and temperature. The pressure transducer was calibrated by the manufacturer (ESI technology Ltd). The pressure transducer was designed for pressure up to 6 MPa with the uncertainty of $\pm 0.002 \text{ MPa}$. The cell temperature was measured by a PT100 temperature probe which is located on the upper level of the high pressure cell as seen in Figure 5.7. The accuracy of the measured temperature was $\pm 0.05 \text{ K}$. The temperature probe was calibrated against a Prema 3040 precision thermometer. Certified buffer solutions (pH 7 & pH 4) were used to calibrate the glass electrode. The calibration was performed at atmospheric pressure and room temperature. To investigate the influence of pressure on the accuracy of calibration, a buffer solution with known pH was placed into the high pressure vessel, and nitrogen was injected to reach the maximum operating pressure. No

significant change was noticed on the pH value of the buffer solution, showing that pressure does not affect the accuracy of pH measurements.



Figure 5.6. Picture of the autoclave for pH measurements.

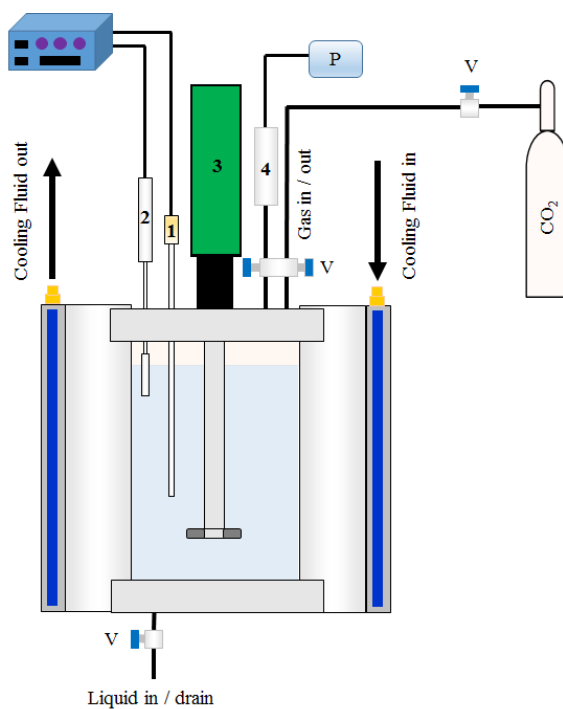


Figure 5.7. Schematic diagram of the high pressure setup for pH measurements using the glass electrode, 1: pH probe 2: Temperature probe, 3: Magnetic stirrer, 4: Pressure transducer and V: Valve.

5.3.1.2 Experimental Procedure

Prior to starting the experiments, the entire system was cleaned with deionised water and nitrogen passed through the system avoiding the accumulation of moisture inside the cell, line and valves. Then, the cell was vacuumed, and deionised water was then injected. The cell was initially filled with about 450 cm³ deionised water. In the next step, CO₂ was introduced to the system. CO₂ was injected slowly at a low rate into in order to avoid electrode damage. A magnetic stirrer was located in the cell in order to agitate the sample to achieve a fast thermodynamic equilibrium. The stirrer was set at a low rate (RPM < 100). A data acquisition unit is managed by data acquisition software which also allows adjustment of the rate of data acquisition. The pressure, temperature values were monitored and recorded every 5 seconds. It is worthy of note that the stirrer was stopped when no significant change was observed in the pressure. Once the pH and pressure remained constant; the value of the pH was recorded. Strictly speaking, the temperature of the vessel was set constant, and pressure was increased gradually and slowly to reach the required pressure and the final pH value recorded while the pressure, temperature and pH remained constant for a period of 30 minutes. All the experimental procedures were the same as those in the pH measurement experiment described in above.

5.4 Modelling Approach

In general, most of the recent models have focused on describing the non-ideal behaviour of the systems that arise at HPHT conditions, including both gaseous solubility and description of chemical equilibria of ionic species in solution. In this work the Cubic-Plus-Association Equation of State (CPA EoS) [130, 131] was selected for determining the solubility of acid gases (CO₂) in pure water and brines at HPHT conditions and the well-known Pitzer's equations [132, 133] were coupled for calculating the deviations to the ideality of each ionic species in the liquid phase.

The CPA parameters used for H₂O were taken from Kontogeorgis *et al.* [134]. Water was modelled using the 4C association scheme [135]. Critical properties of carbon dioxide were taken from Poling *et al.* [136]. Binary interaction coefficients (k_{ij} s) within the framework of this EoS were estimated from temperature-dependents functions established in previous works ($k_{\text{CO}_2\text{-H}_2\text{O}}$ [137, 138]). Carbon dioxide assumed to be able to cross-associate with water (solvation). The effect of salts on the solubility of CO₂ and H₂O are taken into account using the approach proposed by Aasberg-Petersen *et al.* [139] and extended to the CPA EoS [140, 141].

The basic equation used to calculate the pH is defined by:

$$pH = -\log_{10}(a_{H^+}) = -\log_{10}(m_{H^+}) - \log_{10}(\gamma_{H^+}) \quad \text{Equation 5.12.}$$

where a_{H^+} is the activity (in mol.L⁻¹), x_{H^+} is the molar concentration (in mol.L⁻¹), and γ_{H^+} is the activity coefficient (dimensionless) of hydrogen ions.

The equilibrium reactions considered for the systems of interest are as follows:

Pure water and carbon dioxide phase equilibria,



Salts equilibria,



The thermodynamic equilibrium constants for these reactions are:

$$K_{H_2O} = m_{H^+}(aq) m_{OH^-}(aq) \frac{\gamma_{H^+}(aq) \gamma_{OH^-}(aq)}{a_{H_2O}(aq)} \quad \text{Equation 5.17.}$$

$$K_{CO_2,1} = \frac{m_{H^+}(aq) m_{HCO_3^-}(aq)}{m_{CO_2}(aq)} \frac{\gamma_{H^+}(aq) \gamma_{HCO_3^-}(aq)}{\gamma_{CO_2}(aq) a_{H_2O}(aq)} \quad \text{Equation 5.18.}$$

$$K_{CO_2,2} = \frac{m_{H^+}(aq) m_{CO_3^{2-}}(aq)}{m_{HCO_3^-}(aq)} \frac{\gamma_{H^+}(aq) \gamma_{CO_3^{2-}}(aq)}{\gamma_{HCO_3^-}(aq)} \quad \text{Equation 5.19.}$$

$$K_{NaCl} = m_{Na^+}(aq) m_{Cl^-}(aq) \gamma_{Na^+}(aq) \gamma_{Cl^-}(aq) \quad \text{Equation 5.20.}$$

In order to calculate the pH with Equation 5.12, the concentration (m_{H^+}) and activity coefficient of the hydrogen (γ_{H^+}) ions need to be determined. Whereas the molality of the ionic species is uniquely given by equilibrium constants of pertinent reactions, the activity coefficients are influenced by all the remaining factors.

In this work, we have followed the Pitzer's formalism [132, 133] to determine the activity coefficients present in Equations (5.17 to 5.20). The Pitzer's model for electrolytes was derived from the Debye-Hückel's method in which the ionic strength and concentration of all ionic species in solution are combined to take into account electrostatic interactions between ionic species. The expressions corresponding to this approach will not be addressed here. A detailed description of this methodology can be referred to Pedersen *et al.* [142].

The amount of each component in solution is determined by the equilibrium stoichiometric constants and Equations (5.17 to 5.20). An accurate estimation of these quantities depends on the values considered for the stoichiometric constants. These constants were here determined at each temperature of interest using adjusted mathematical expressions taken from Pedersen *et al.* [142] and the effect of pressure on these values was neglected. The amount of CO₂ (aq) and the effect of salts on these quantities were calculated with our PVT model based on the CPA EoS.

The concentration and activity coefficients for each ionic species are calculated together with the resolution of the equation for electro neutrality, considering no mineral precipitation has occurred, defined as follows:

$$m_{H^+(aq)} - \frac{K_{H_2O} a_{H_2O(aq)}}{m_{H^+(aq)} \gamma_{H^+(aq)} \gamma_{OH^-(aq)}} - \frac{K_{CO_2,1} m_{CO_2(aq)} \gamma_{CO_2(aq)} a_{H_2O(aq)}}{m_{H^+(aq)} \gamma_{H^+(aq)} \gamma_{HCO_3^-(aq)}} - 2 \frac{K_{CO_2,2} m_{HCO_3^-(aq)} \gamma_{HCO_3^-(aq)}}{m_{H^+(aq)} \gamma_{H^+(aq)} \gamma_{CO_3^{2-}(aq)}} = 0 \quad \text{Equation 5.21.}$$

The amount of hydrogen ion (m_{H^+}) is calculated by solving Equation 5.21 with a Newton-Raphson iteration method and pH determined with Equation 5.12.

5.5 Results and Discussions

5.5.1 Spectroscopic Technique – (The dissociation constant of BPB, molar absorptivity coefficients of BPB)

As mentioned before, in the spectroscopic method, the measurements were performed at pressures up to 6 MPa and temperatures of 293.15 K and 323.15 K. Some experiments were carried out to investigate the e_i rate dependence on pressure, temperature and ionic strength. In order to find the influence of pressure on e_i , firstly, the spectra of the acid and base solutions in the presence of BPB were measured. Then, nitrogen was introduced to

the system to measure the spectra of the acid and base samples at various pressures (up to 6 MPa). A very small dependence of ϵ_i values to pressure was noticed and not accounted for the pH calculations. It should be noted that the molar absorptivity coefficients were measured at the calibrated temperatures (293.15 & 323.15 K). To examine the influence of a change in salinity on ϵ_i values, the spectra of two buffer solutions with the same pH value and different ionic strength (0 & 3 m) at fixed temperature and atmospheric pressure were measured. Results revealed that the changes in the ϵ_i values are negligible at different ionic strengths and these small changes can be attributed to the uncertainty of the measurement. In terms of the dissociation constant (pK_a), various buffer solutions with different ionic strengths (0 to 3 m) were prepared within the range of study. Spectra of all these solutions in the presence of BPB were measured at the atmospheric pressure and two different temperatures. Then, for each isotherm and ionic strength, the pK_a was calculated using Equation 5.8 by extracting λ_1 and λ_2 from the recorded spectra of all the buffer solutions. It should be noted that all the spectra were baseline corrected between the ranges from 340 to 655 nm before any calculation to overcome baseline shift during measurement. The results for ϵ_i and pK_a at different temperatures and ionic strengths at atmospheric pressure are listed in Table 5.1.

Table 5.1. Measured pK_a , ϵ_1 , ϵ_2 and ϵ_3 of BPB at atmospheric pressure and different temperatures and ionic strengths.

T/K	$m_{NaCl} / \text{mol.kg}^{-1}$	pK_a	ϵ_1	ϵ_2	ϵ_3
293.15	0	4.115 ± 0.005	0.014 ± 0.005	2.682 ± 0.009	0.022 ± 0.005
	1	3.671 ± 0.005			
	2	3.651 ± 0.007			
	3	3.643 ± 0.008			
323.15	0	4.145 ± 0.004	0.018 ± 0.006	2.712 ± 0.009	0.0381 ± 0.008
	1	3.751 ± 0.005			
	2	3.741 ± 0.008			
	3	3.732 ± 0.007			

The pK_a values obtained at 293.15 K and 323.15 K were close to those reported by Shao *et al.*[126]. However, the pK_a values measured in this study for BPB solutions with various ionic strengths were different from those reported by the same author. No significant change was observed in pK_a value with an increase in ionic strength from 1 m to 3 m for both calibrated temperatures. Calculated values for pK_a and ϵ_i were used to determine the value of pH using the spectra that collected for the $\text{CO}_2\text{-H}_2\text{O}$ and $\text{CO}_2\text{-H}_2\text{O-NaCl}$ systems at a temperature of 298.15 K and 323.15 K and pressures up to 6 MPa.

5.5.2 Equilibrium pH of CO₂ in Contact with Water and Brine

In this section, the results obtained experimentally by both the UV-Vis spectroscopic and electrometric techniques with the available data in the open literature within the range of our study are evaluated and compared. Three isotherms for the CO₂-H₂O system were studied in the temperature range of 293.15 to 353.15 K and pressures up to 5.5 MPa using the electrometric technique. A consistent trend was not observed for different CO₂-H₂O-NaCl systems using the electrometric technique at high pressures, thereby the results for this technique in brine systems are not reported in this communication. This may be attributed to sodium interference between the reference solution into the glass electrode and the sample solution outside the glass electrode due to the increase of sodium ions in the solution. For the spectroscopic technique, the pH was measured in the CO₂-H₂O, and CO₂-H₂O-NaCl systems at pressures up to 6 MPa and temperatures up to 323.15 K. The pH results obtained for both the spectroscopic and electrometric techniques in the CO₂-H₂O system are tabulated in Table 5.2 and Table 5.3 and depicted in Figure 5.8 and Figure 5.9, respectively.

Table 5.2. Measured and predicted pH values (electrometric technique) in the CO₂-H₂O system.

T/K	P/MPa	pH (Experimental)	pH (Model)
293.15	0.23	3.78	3.77
	0.74	3.53	3.52
	1.45	3.39	3.37
	2.15	3.32	3.29
	3.44	3.23	3.20
	5.07	3.18	3.13
323.15	0.23	3.88	3.86
	0.74	3.61	3.60
	1.45	3.48	3.46
	2.15	3.41	3.38
	3.44	3.32	3.28
	5.07	3.17	3.20
353.15	0.23	4.00	4.02
	0.74	3.70	3.73
	1.45	3.54	3.57
	2.15	3.46	3.49
	3.44	3.36	3.39
	5.07	3.28	3.31

Table 5.3. Measured and predicted pH values (spectroscopic technique) in the CO₂-H₂O system.

T/K	P/MPa	pH (Experimental)	pH (Model)
T = 293.15	0.60	3.58	3.65
	1.51	3.44	3.45
	2.25	3.36	3.27
	2.94	3.28	3.31
	4.41	3.19	3.23
	5.24	3.17	3.20
T = 323.15	1.14	3.59	3.51
	2.16	3.46	3.38
	3.25	3.40	3.29
	4.02	3.31	3.25
	5.51	3.27	3.19

Moreover, all the results were compared with selected data from the literature. As can be seen in Figure 5.8, the results that were measured using the pH probe are in quite good agreement with those obtained by Peng *et al.* [120], indicating the consistency of this method for pH measurements in CO₂ saturated water. It is apparent that, for all studied isotherms, the pH value decreases sharply with increasing pressures while the operating pressure is less than 3 MPa. This reduction in pH values is less for pressure higher than 3 MPa. For instance, in this study, pH decreased from 3.88 to 3.41 when the pressure was increased from 0.23 to 2.15 MPa at 323.15 K. However the pH value at the same temperature reduced by 0.15 units from 3.44 MPa to 5.07 MPa. This reduction in the pH value is expected to be less at higher pressures due to the steep increase in the composition of CO₂ in the liquid phase. A similar trend was observed by Peng *et al.* [120] at T = 323.0 K, pH decreased by 0.40 units from 0.38 to 2.43 MPa due to the high solubility of CO₂ in this range of pressure, whereas the pH value fell by 0.22 units while the pressure was increased from 2.43 to 6.23 MPa. Moreover, the results obtained in this study for the spectroscopic technique were compared with the available literature data for the same method within the range of the P–T conditions studied. As illustrated in Figure 5.9, the general trend in this method is in good agreement with the data that reported by Shao *et al.* [126] and Parton *et al.* [122]. The measured pH values in this work were close to values obtained by Shao *et al.* [126], however, pH results reported at a pressure higher than 2 MPa and T = 308.15 K by Parton *et al.* [122] are about 0.2 units lower than values measured in this study at T = 293.15 K. This difference is even higher as they measured the pH at slightly higher temperature (pH values at T = 293.15 K in this study was compared to pH values at T = 308.15 K) which results in an increase in pH value due to

the lower solubility of CO₂ at higher temperature. This difference in pH value may be attributed either to the procedure that was followed to calculate the pH or error of measurement. Overall, results obtained in this study by either the spectroscopic and electrometric method for the CO₂-H₂O system follow a similar trend, fast drop in pH value while pressure is less than 3 MPa and lower changes in pH values at a pressure higher than 3 MPa.

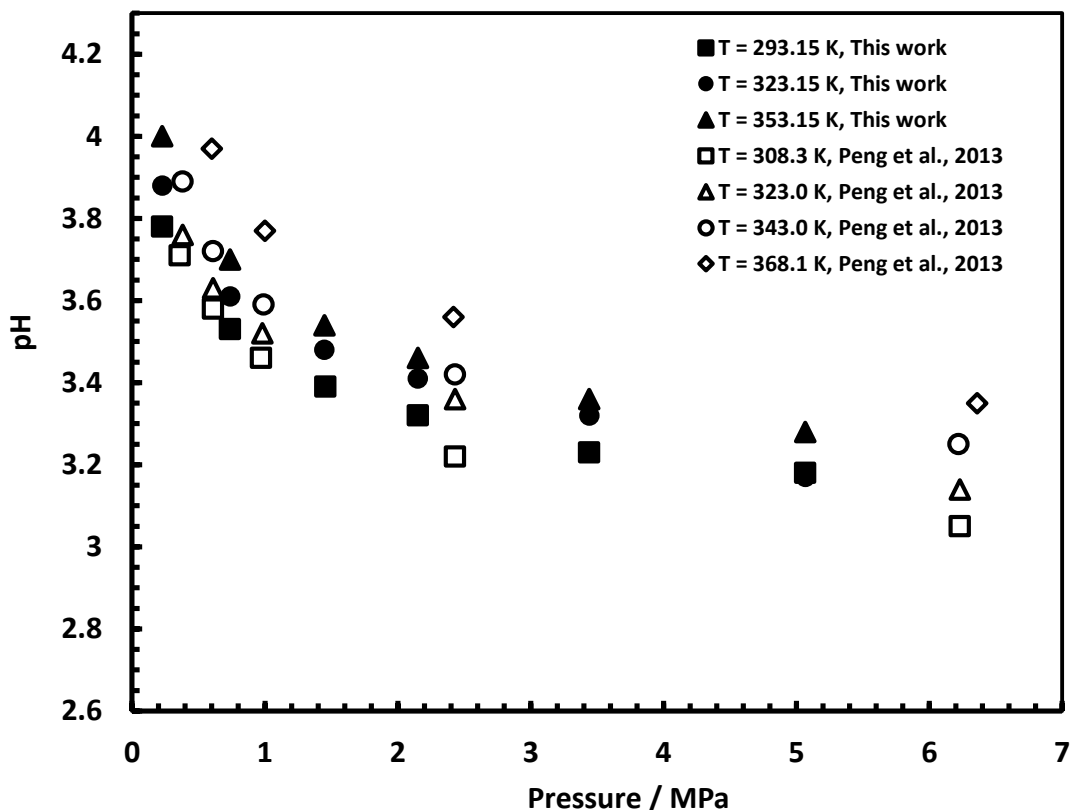


Figure 5.8. pH of CO₂ saturated solutions as a function of pressure in the CO₂-H₂O system. Filled symbols represent experimental data measured in this work using electrometric technique and empty symbols represent the literature data measured using the electrometric technique.

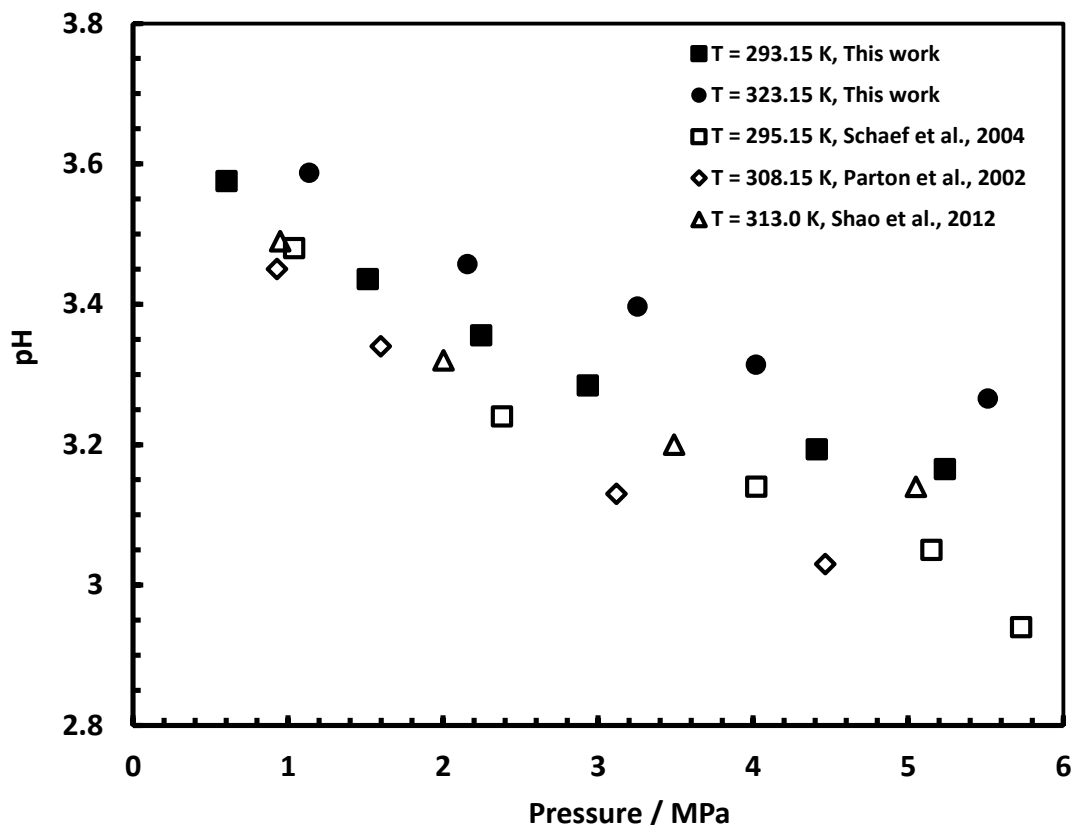


Figure 5.9. pH of CO₂ saturated solutions as a function of pressure in the CO₂-H₂O system. Filled symbols represent experimental data measured in this work using the spectroscopic technique and empty symbols represent the literature data measured using the spectroscopic technique.

Some limited data are available for pH in CO₂-brine systems at high pressures. Crolet *et al.* [143] reported the pH measurements for the CO₂-H₂O-0.5m NaCl system at temperatures from 289.15 to 347.15 K and pressures up to 6 MPa. Shao *et al.* [126] and Schaef *et al.* [119] measured the pH in CO₂-brine systems at temperatures up to 366.15 K and pressures up to 20 MPa using spectroscopic and electrometric methods respectively. In the current study, pH was measured for aqueous solutions with different ionic strengths (1, 2 and 3 mol.kg⁻¹) at temperatures up to 323.15 K and pressures up to 6 MPa. Measured pH values from this study and from those reported in the literature for solutions with different ionic strengths are illustrated in Figure 5.10 through Figure 5.11. As can be seen from Figure 5.10 and Figure 5.11, for CO₂-H₂O-1m NaCl and CO₂-H₂O-2 m NaCl systems, the measured pH values are lower by about 0.2 to 0.3 unit than those measured by Schaef *et al.* [119]. Furthermore, it is clear from aforementioned figures; the pH values increased with an increase in salinity. This opposite trend and also the large difference between the measured pH values from this study and those measured by Schaef

et al.[119] could be due to the occurrence of liquid junction potential between the liquid inside and outside glass electrode which produces some errors in pH measurement. Due to the presence of a high concentration of NaCl in the studied solutions, Na^+ ions can diffuse into the liquid junction and produce an undesirable potential difference between the filled solution inside the glass electrode and the liquid outside of the glass electrode, causing offset in the pH value.

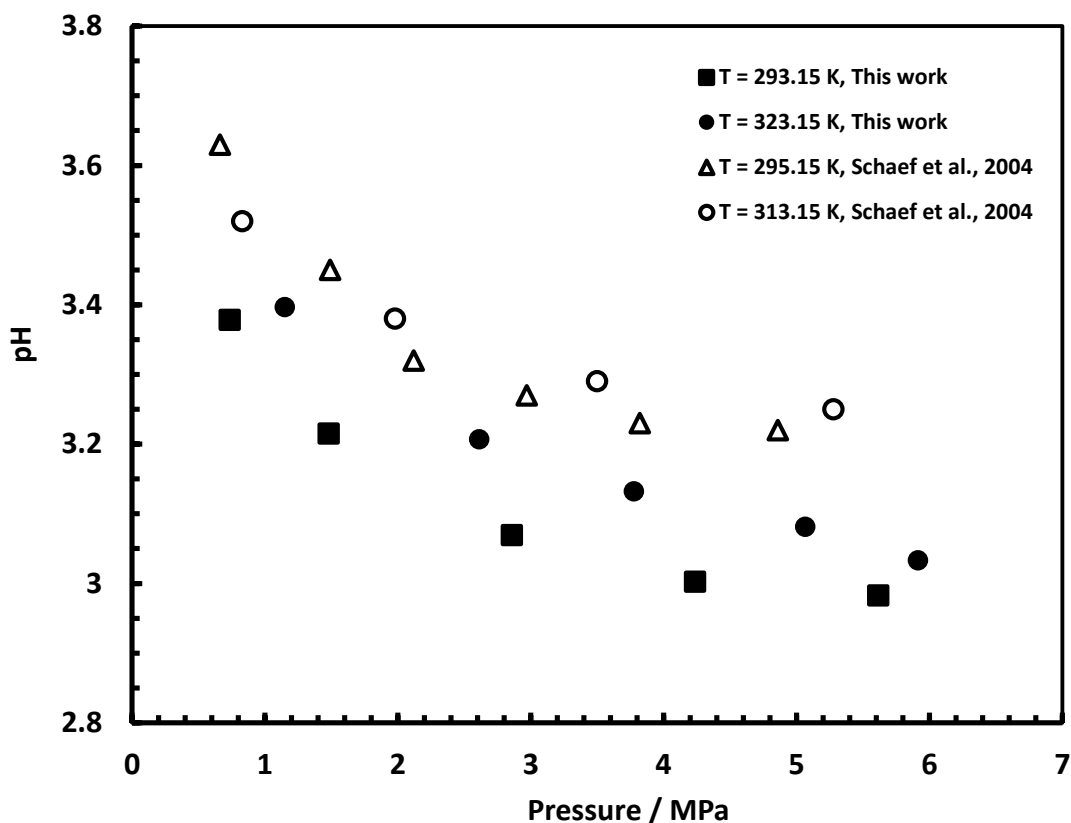


Figure 5.10. pH of CO_2 saturated solutions as a function of pressure in the CO_2 - H_2O -NaCl system. Filled symbols represent experimental data measured in this work using the spectroscopic technique ($m = 1 \text{ mol.kg}^{-1}$). Empty symbols represent the data measured using the electrometric technique by Schaef *et al.* [119], ($m = 1.01 \text{ mol.kg}^{-1}$).

As depicted in Figure 5.11, our measured pH values at $T = 323.15 \text{ K}$ in the CO_2 - H_2O -3 m NaCl system is close with data of Shao *et al.*[126] at a temperature of 313.15 K. It is worthy of note that the pK_a value that was measured at an ionic strength of 3 m in our study was about 0.2 units lower than the value that was reported by Shao *et al.* [126].

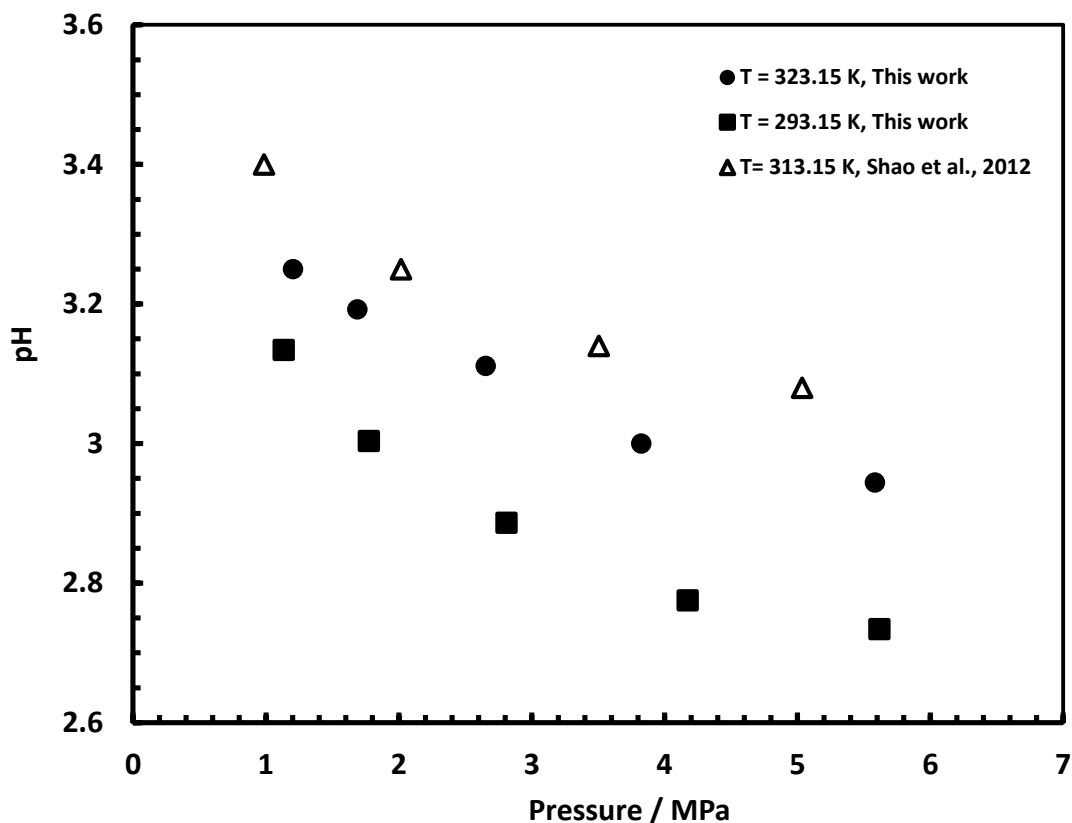


Figure 5.11. pH of CO₂ saturated solutions as a function of pressure in the CO₂-H₂O-NaCl system. Filled symbols represent experimental data measured in this work using the spectroscopic and empty symbols represent the data measured using the spectroscopic technique by Shao *et al.* [126]. ($m = 3 \text{ mol.kg}^{-1}$).

It is clear from Figure 5.12 that the salinity increase leads to a reduction of pH in acidified brine solutions over the entire pressure range at a constant temperature. This behaviour was more pronounced while the concentration of NaCl changed from 1 m to 3 m. For instance, as shown in Figure 5.12 and Table 5.4, the pH drops by 0.25 units at a pressure of about 5.5 MPa and temperature of 293.15 K. A similar trend was observed by Crolet *et al.* [143], they measured the pH in CO₂-brine systems (0 to 3.54 m) at 0.1 MPa and $T = 298.15 \text{ K}$, it was observed that the pH decreases from 3.76 to 3.57 when the ionic strength increases from 1.01 m to 3.54 m. Shao *et al.* [126] showed that the pH value increases in the CO₂-brine systems from 2.94 to 2.98 as the salt concentration increases from 1 m to 3 m at a pressure of 10 MPa and $T = 313.15 \text{ K}$. It is known that CO₂ solubility decreases with the increase of NaCl concentration in the solution but the activity coefficient increases significantly with the increase of NaCl concentration in the solution, causing a drop in the pH value. This opposite trend in the obtained experimental values by Shao *et al.* [126] could be due to error of their spectroscopy measurement at high pressures.

Table 5.4. Measured and predicted pH value (spectroscopic technique) for different CO₂ saturated brine systems.

T/K	P/MPa	m _{NaCl} (mol.kg ⁻¹)	pH (Experimental)	pH (Model)
T =293.15	0.73	1	3.37	3.39
	1.48	1	3.21	3.24
	2.86	1	3.07	3.11
	4.23	1	3.00	3.03
	5.61	1	2.98	2.99
T = 323.15	1.15	1	3.39	3.44
	2.61	1	3.20	3.26
	3.77	1	3.13	3.19
	5.06	1	3.08	3.13
	5.91	1	3.03	3.11
T = 293.15	0.84	2	3.33	3.28
	2.10	2	3.12	3.09
	3.50	2	3.05	2.99
	4.17	2	3.01	2.96
	5.07	2	2.98	2.92
	5.56	2	2.96	2.91
T = 323.15	0.82	2	3.49	3.45
	1.52	2	3.27	3.32
	2.96	2	3.14	3.19
	4.48	2	3.06	3.11
	5.61	2	3.02	3.07
T = 293.15	1.14	3	3.13	3.13
	1.78	3	3.00	3.04
	2.81	3	2.89	2.95
	4.18	3	2.78	2.88
	5.62	3	2.73	2.83
T = 323.15	1.20	3	3.25	3.32
	1.69	3	3.19	3.25
	2.65	3	3.11	3.16
	3.82	3	3.00	3.08
	5.58	3	2.94	3.02

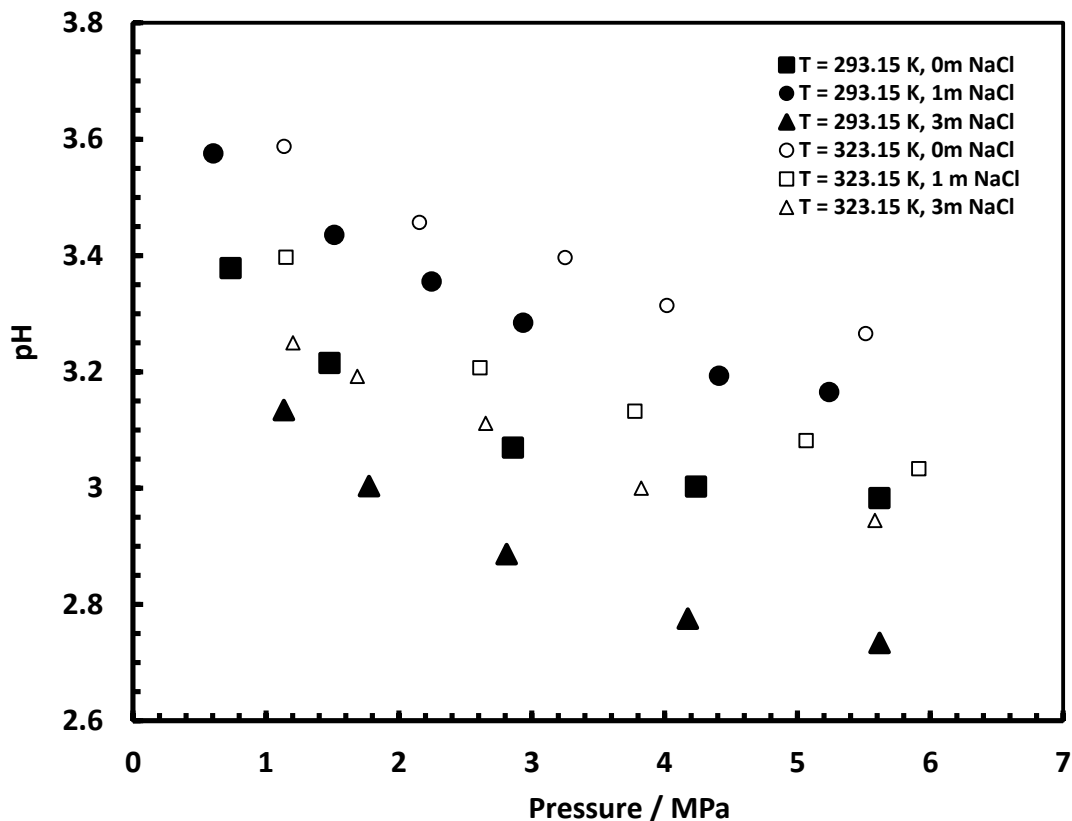


Figure 5.12. Effect of variation in ionic strength on the pH value of the CO₂ saturated solutions as a function of pressure.

5.6 Modelling Results

As depicted in Figure 5.13 through Figure 5.18, the pH predictions calculated with our model were evaluated against literature data and these new measurements. Summary of the calculated %AAD value between the predicted pH values by the model and the available experimental data in the open literature, as well as the experimental data obtained in this study, are listed in Table 5.5.

Table 5.5. Summary of the calculated %AAD value between the pH measured and predicted values in various fluid systems.

System	Data Source	T/K	P/MPa	NP ^a	%AAD ^b
CO ₂ -H ₂ O	Peng <i>et al.</i> [120]	308.3 to 423.2	0 to 15	37	1.11
	Shao <i>et al.</i> [126]	298.15 to 366.15	0 to 20	18	0.90
	Truche <i>et al.</i> [127]	423.15 to 553.15	0 to 15	14	1.46
	Schaef <i>et al.</i> [119]	295.15 to 343.15	0 to 11	12	6.58
	Meyssami <i>et al.</i> [117]	305.15 to 315.15	0 to 35	26	1.86
	Toews <i>et al.</i> [121]	298.15 to 343.15	7 to 20	20	8.49
	Parton <i>et al.</i> [122]	308.15	0 to 9	6	3.06
	Rosenqvist <i>et al.</i> [118]	294	0 to 1	3	1.95
	This work, ET ^c	293.15 to 353.15	0 to 6	18	0.76
	This work, ST ^d	293.15 to 323.15	0 to 5.5	11	1.82
CO ₂ -H ₂ O-1.01 m NaCl	Schaef <i>et al.</i> [119]	295.15 to 343.15	0 to 10	25	4.24
CO ₂ -H ₂ O-1 m NaCl	This work, ST	293.15 to 323.15	0 to 6	10	1.37
CO ₂ -H ₂ O-2.02 m NaCl	Schaef <i>et al.</i> [119]	295.15 to 343.15	0 to 11	9	9.76
CO ₂ -H ₂ O-2 m NaCl	This work, ST	293.15 to 323.15	0 to 6	11	1.57
CO ₂ -H ₂ O-3 m NaCl	Shao, Thompson [126]	298.15 to 366.15	0 to 20	18	1.78
	This work, ST	293.15 to 323.15	0 to 6	11	2.16

^a Number of points, ^b %AAD = $\frac{1}{NP} * \sum_1^{NP} \left| \frac{(pH_{Model} - pH_{Exp})}{(pH_{Exp})} \right|$, ^c Electrometric Technique and ^d Spectroscopic Technique.

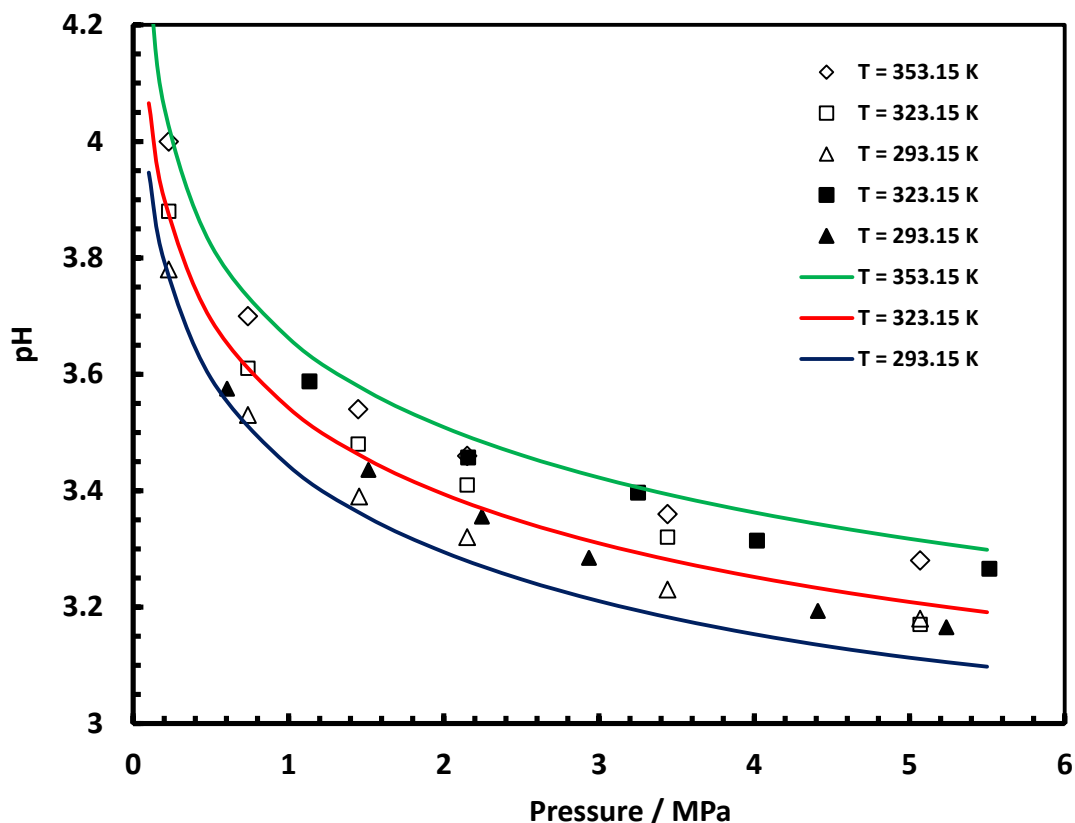


Figure 5.13. Experimental and predicted pH values in the CO₂-H₂O system. Empty symbols represent the experimental data obtained using the electrometric technique and filled symbol represent the experimental data obtained using the spectroscopic technique. Solid lines represents the prediction from the model.

As can be seen from Figure 5.14 and Figure 5.15, the pH appears to abruptly decrease with pressure increase while this reduction in pH value at pressures higher than 10 MPa is very small. The model is able to predict the pH value in CO₂ saturated water system with a %AAD of 1.11%, 0.90% and 1.46% to experimental points that were reported by Peng *et al.* [120], Truche *et al.* [127] and Shao *et al.* [126] respectively at pressures up to 20 MPa and temperatures up to 553 K. Toews *et al.* [121] reported the pH values for pressures between 7 MPa and 20 MPa in the CO₂-H₂O system. As can be seen in Figure 5.15, the changes in pH are very small at pressures higher than 7 MPa (about 0.03 units). Similar behaviour was observed for the model; the pH decreased by about 0.06 units while the pressure increases from 7 MPa to 20 MPa at a temperature of 298.15 K. This behaviour is closely linked to the amount of molecular CO₂ in the liquid phase (x_{CO_2}).

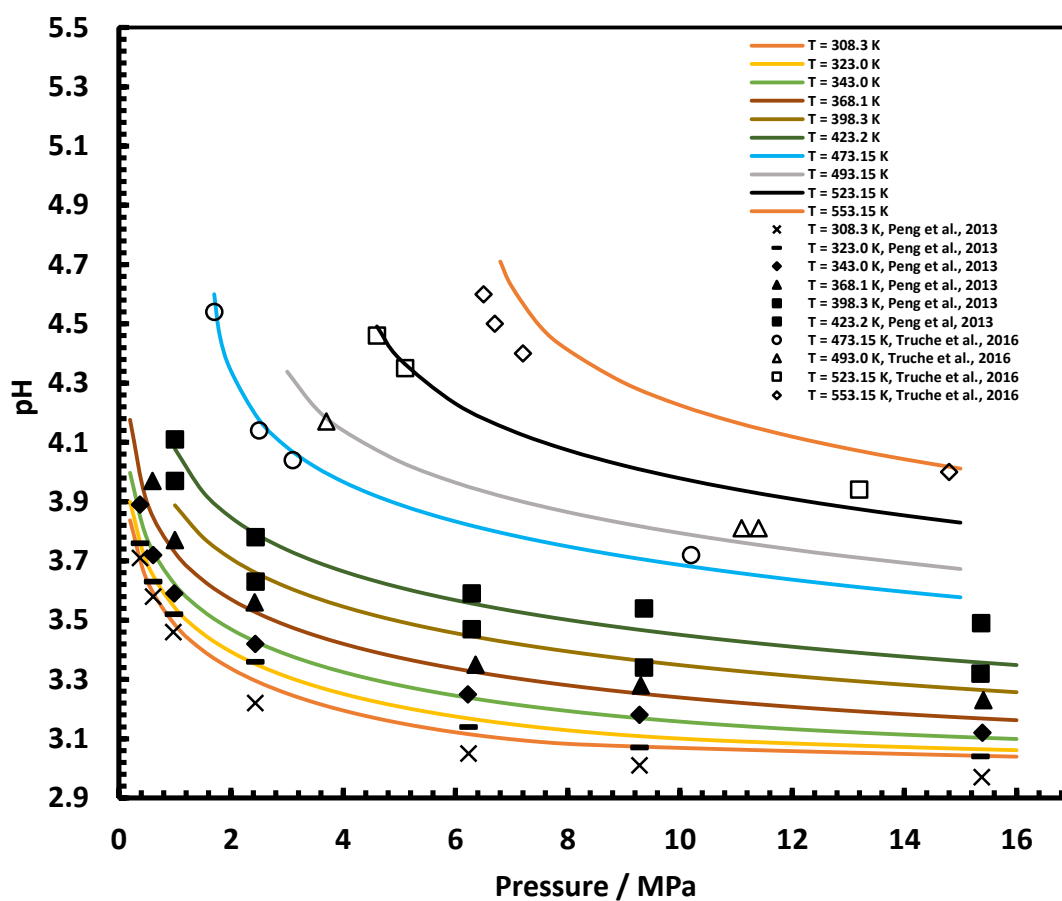


Figure 5.14. pH of CO₂ saturated solutions as a function of pressure in the CO₂-H₂O system. Symbols represent experimental data from the literature (electrometric technique).

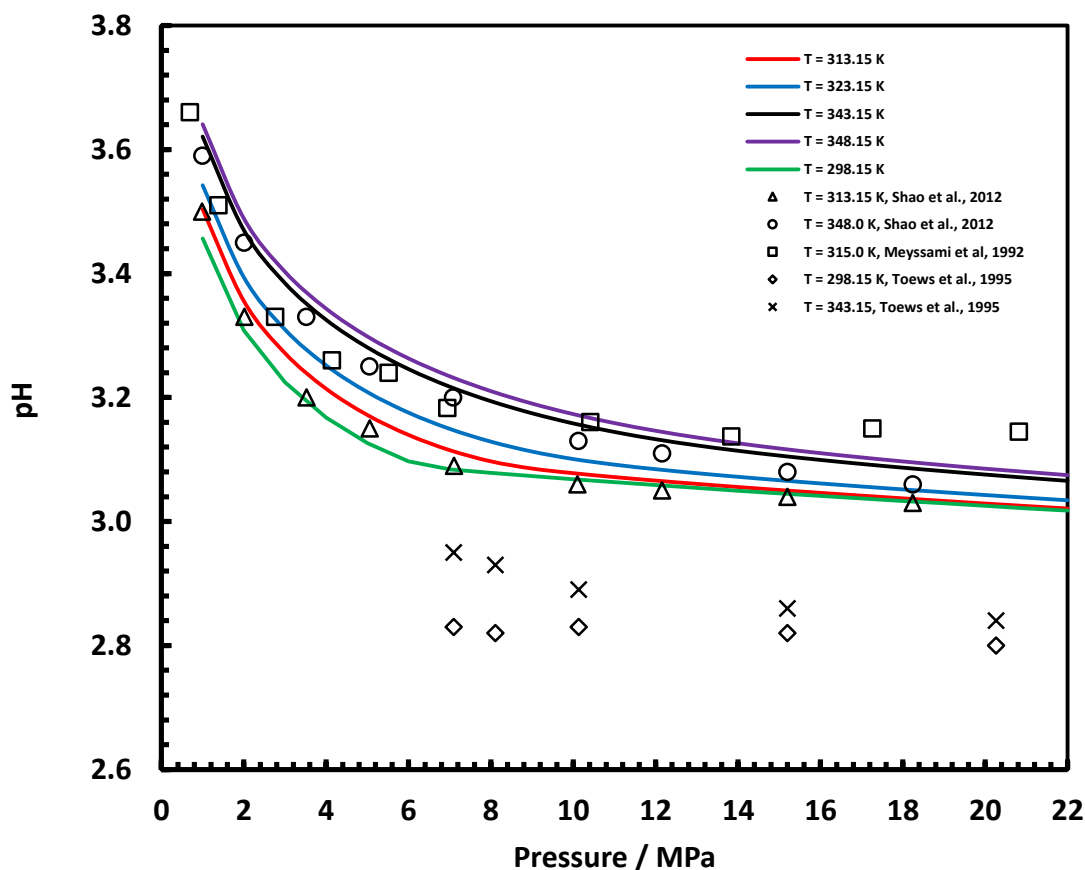


Figure 5.15. pH of CO₂ saturated solutions as a function of pressure in the CO₂-H₂O system. Empty symbols represent experimental data from the literature and solid lines represent the prediction from the model.

Figure 5.16, one can see a steep increase in the composition of CO₂ for pressures up to 10 MPa and a moderate rise of this quantity for higher pressures. Such singularity produces small changes in the concentration of the CO₂ in the aqueous phase. As depicted in Figure 5.16, the pH values seem to level off for higher pressures. We also plot the pH of the CO₂-H₂O system as a function of $-\log_{10}(x_{\text{CO}_2})$ (Figure 5.17). A linear relationship was observed between pH and $-\log(x_{\text{CO}_2})$ for the CO₂ saturated water system. It is worthy of note that, the measured pH values by Toews *et al.* [121] are about 0.2-0.3 units lower than pH values predicted by the model at same P-T conditions (see Figure 5.15, %AAD = 8.49). A possible reason for this large difference between the model and measured pH values is because the effect of pressure and ionic strength were not being considered in their calibration procedure.

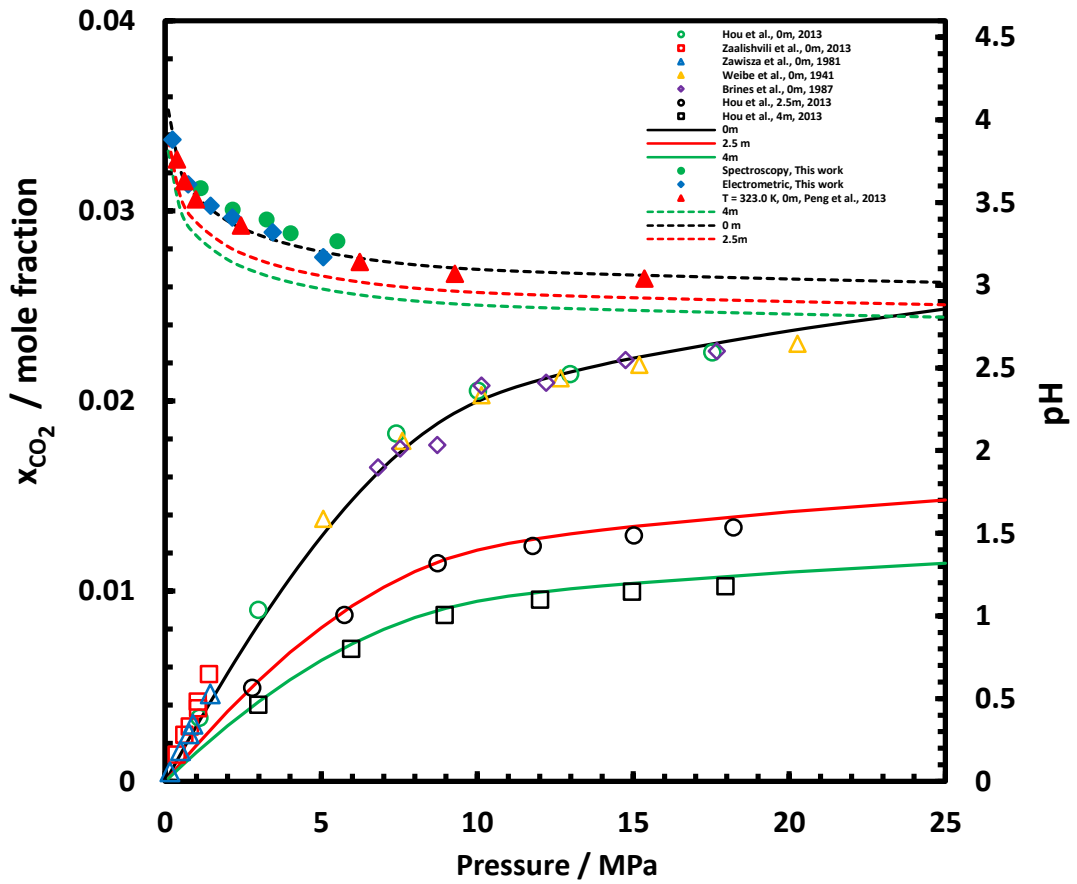


Figure 5.16. pH-pressure and x_{CO_2} -pressure diagrams of the CO₂-H₂O and CO₂-H₂O-NaCl systems at temperature of 323.15 K. Empty symbols represent experimental mole fraction data of CO₂ in aqueous phase and filled symbols represent experimental pH data. Dashed and solid lines represent the pH and x_{CO_2} predictions at various ionic strengths from the model respectively.

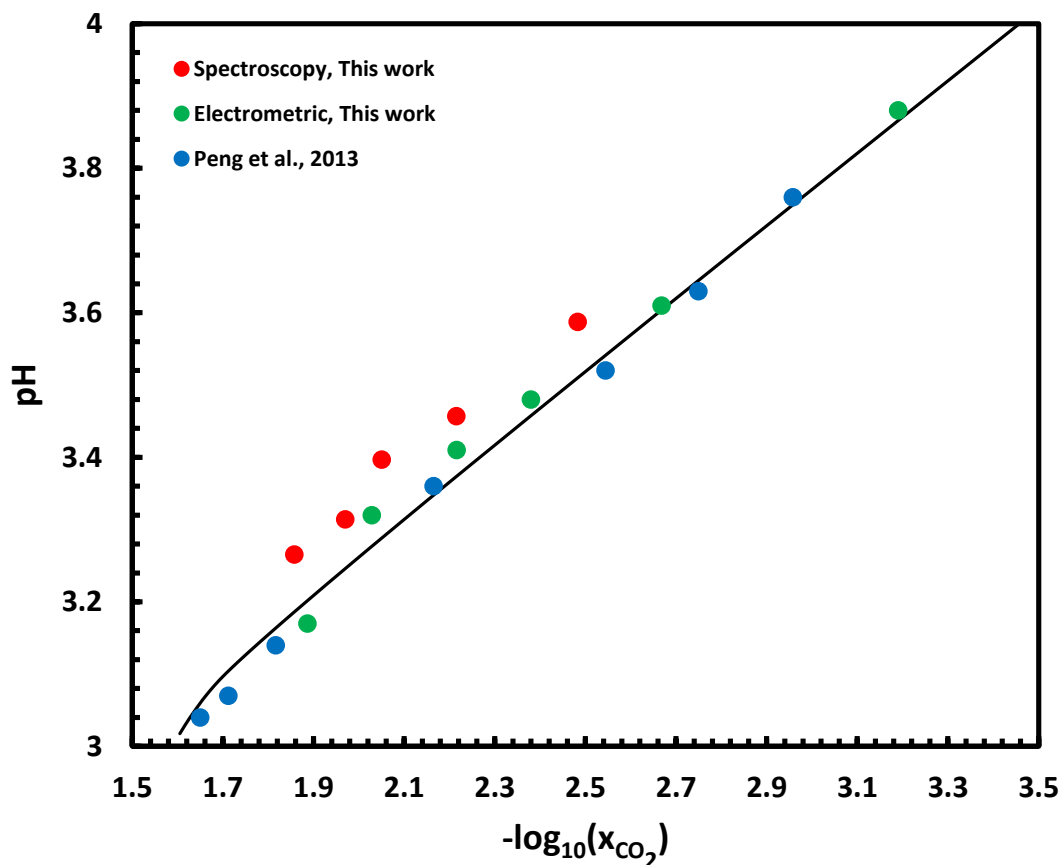


Figure 5.17. pH of the CO₂-H₂O system as a function of $-\log_{10}(x_{\text{CO}_2})$ at temperature of 323.15 K.

The capability of the model to predict the effect of salts was also tested and the results are plotted in Figure 5.18 and Figure 5.19. The deviation between the model and experimental data for various CO₂-brine systems are listed in Table 5.4. The measured pH values in this work for saline systems yield a good agreement with those obtained by the model. The model can reproduce the pH values in the CO₂-H₂O-1 m NaCl, CO₂-H₂O-2 m NaCl and CO₂-H₂O-3 m NaCl systems with AAD% of 1.37%, 1.57% and 2.16%, respectively. Similar to CO₂-H₂O system, there is a linear dependence among pH and $-\log_{10}(x_{\text{CO}_2})$ in the CO₂ saturated brine systems (Figure 5.19). Furthermore, low deviations were observed between the model and measured pH points by Shao *et al.* [126] in the CO₂-H₂O-3 m NaCl system with an AAD% of 1.78. Also indicating the adequacy of the model to predict the pH values at a variety of pressure and temperature conditions in highly concentrated NaCl brines. Overall, the model is performing well at various temperature and pressure ranges and various NaCl concentrations.

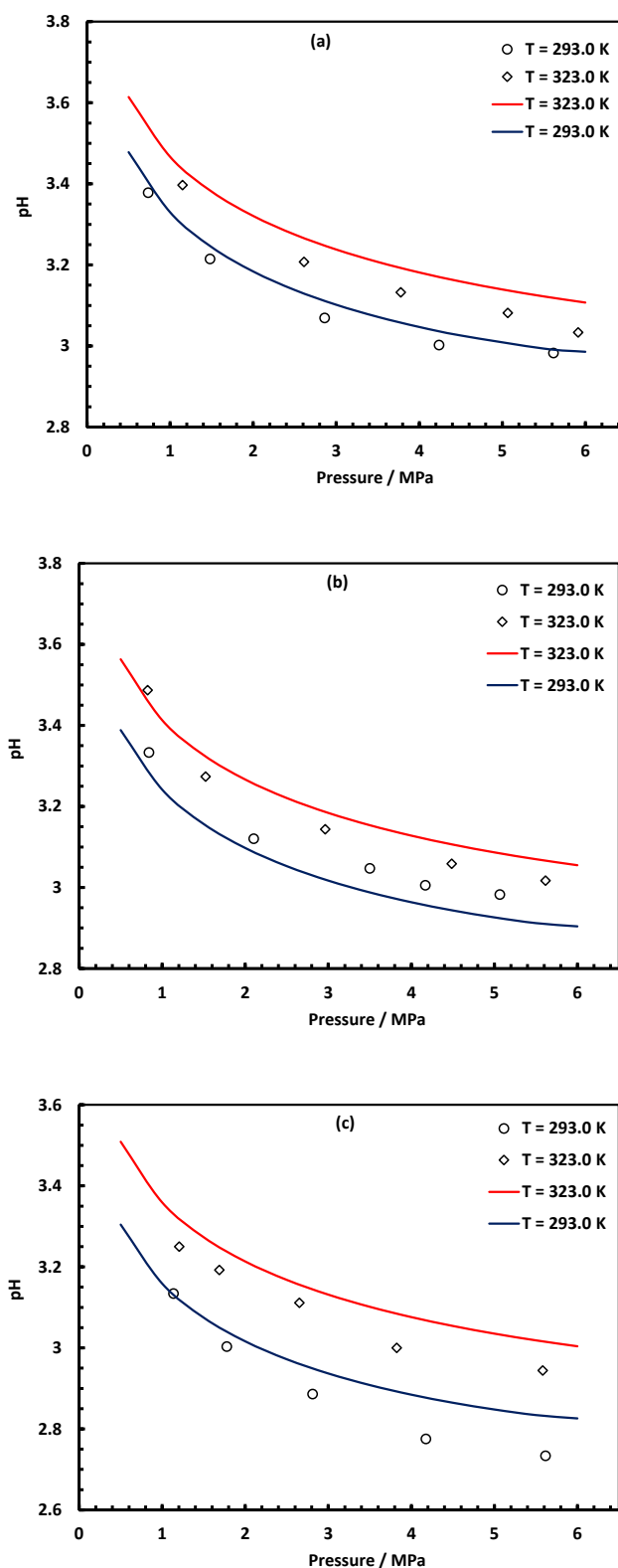


Figure 5.18. Experimental (Spectroscopic technique) and predicted pH values in the CO₂-H₂O-NaCl systems with various ionic strengths (1 m (a), 2 m (b) and 3 m (c) NaCl).

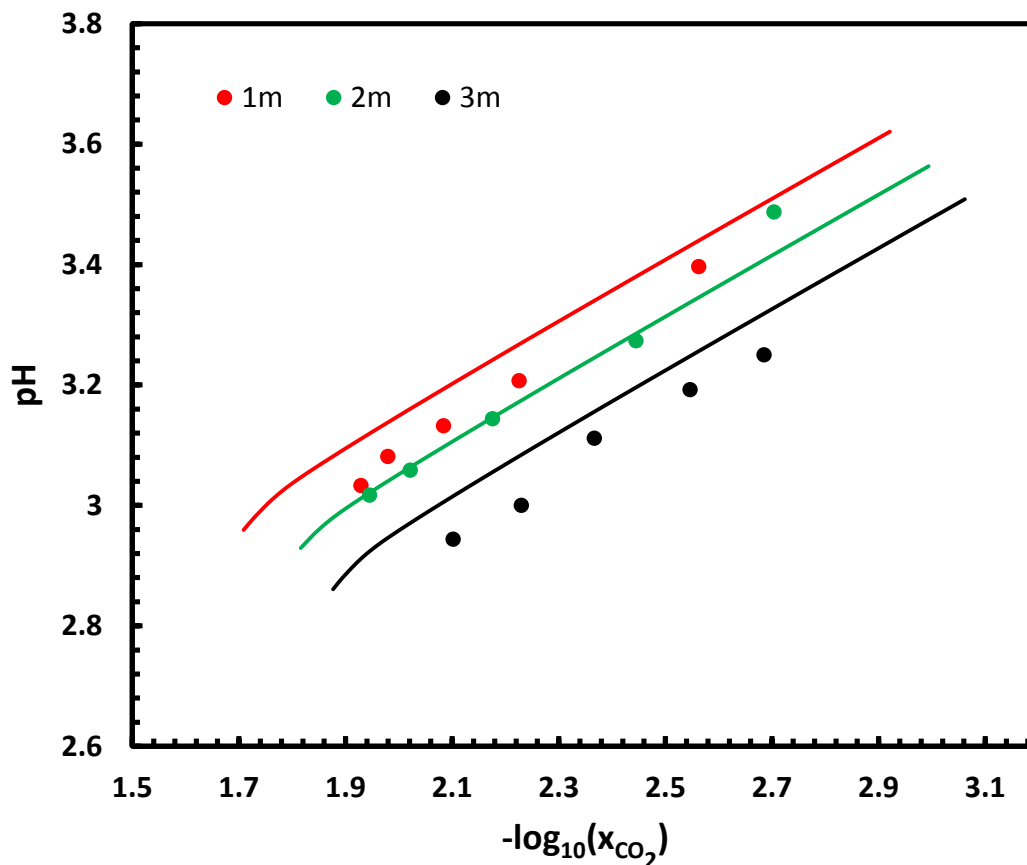


Figure 5.19. pH of the CO₂-H₂O-NaCl systems as a function of $-\log_{10}(x_{\text{CO}_2})$ at a temperature of 323.15 K (spectroscopic technique).

Overall, the model is performing well at various temperature and pressure ranges. For the first time, Truche *et al.* [127] measured pH of CO₂ in water at temperatures in the range (423.15 to 553.15 K) using an innovated technique by coupling Raman spectroscopy and electrometric techniques. Our model is able to reproduce the pH value with an AAD% of 1.46%, showing the ability of the model to predict the pH at elevated temperatures.

All these results confirm the capability of the UV-Visible spectrometer to measure the pH value in various fluid systems at high pressure and temperature conditions. By applying some modification on the experimental setup, this method can be employed as an online method to analyse the geological or experimental fluid at elevated pressures and temperatures. Moreover, this method can be useful for complex systems (i.e., gas mixtures) equilibrated with salty water for which reliable information about the solubility of gas mixtures in brine solutions is rare. It is known that CO₂ originating from capture processes is generally not pure and it can contain impurities such as N₂, H₂, O₂, H₂S, CH₄, SO₃, NO, NO₂, CO and water. Similarly, acid gases can vary greatly in composition. The nature of these fluids combined with compression and potentially long distance transportation could lead to challenging engineering and flow assurance issues, and the

presence of water may result in corrosion formation in the pipeline. There is no data for the pH of gas mixtures saturated in water or brine at high pressures. Hence, the pH of gas mixtures at HTHP conditions in different aqueous solutions was measured using UV-Vis spectrometer. The following section will detail the results.

5.6.1 Equilibrium pH of multicomponent mixtures in contact with water and brine

In this section, firstly, the capability of spectroscopy technique for measuring the pH of multicomponent mixtures in different solutions was investigated. Then, the accuracy of the model was investigated based on the results that were found experimentally. The same experimental procedure explained before was followed to measure the pH of the gas mixtures saturated in water and NaCl solutions. In the first step, one ternary gas mixture was tested for two fluid systems, one with zero salinity and the other with NaCl molality equal to 1 mol.kg⁻¹. First, spectroscopy measurements were carried out to measure the pH of one ternary mixture (CH₄-CO₂-N₂) and water at pressures up to 15 MPa and at temperatures up to 323.15 K. The composition of the ternary gas mixture and results are tabulated in Table 5.6 and Table 5.7.

Table 5.6. Ternary gas composition.

Components	mol%
CO ₂	Balance (38.65)
CH ₄	41.30 (± 2.06)
N ₂	20.05 (± 1.06)

Table 5.7. Measured and predicted pH values for ternary gas composition (Aqueous fraction = 0.921).

T / K	P / MPa	pH (Experimental)	pH (Model)
293.15	0.80	3.73	3.70
	1.48	3.63	3.57
	2.86	3.48	3.44
	4.24	3.42	3.37
	5.62	3.39	3.32
	7.00	3.35	3.28
	10.24	3.21	3.24
	13.96	3.20	3.21
323.15	0.79	3.75	3.80
	1.48	3.64	3.67
	2.86	3.53	3.53
	4.24	3.45	3.46
	5.62	3.40	3.40
	7.00	3.37	3.37
	8.75	3.34	3.33
	10.47	3.31	3.30
	15.27	3.24	3.25

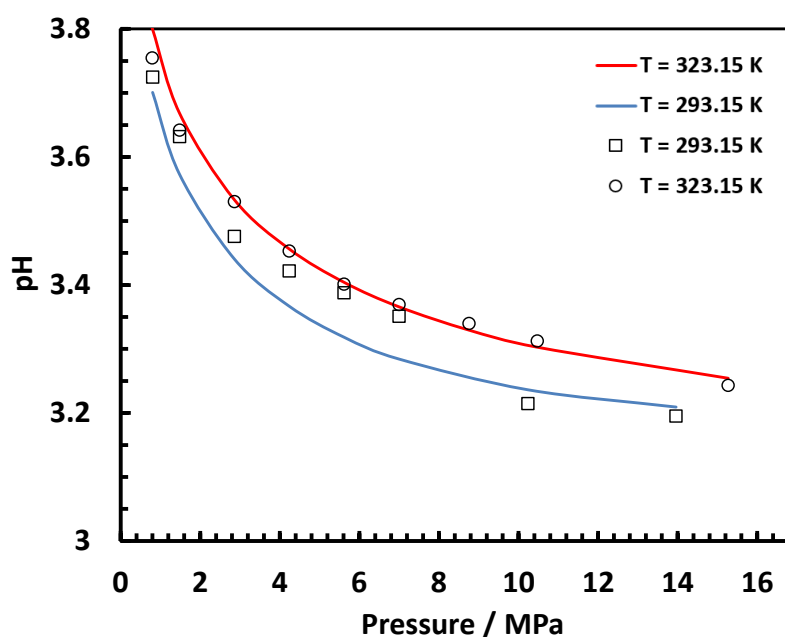


Figure 5.20. Experimental and predicted pH values in the $\text{CH}_4\text{-CO}_2\text{-N}_2\text{-H}_2\text{O}$ system. Filled symbol represent the experimental data that obtained using spectroscopic technique and Solid lines represent the prediction from the model using an aqueous fraction of 0.921.

The aqueous fraction is influencing the predicted pH values due to the presence of N_2 and CH_4 which are also soluble in water. Thereby, the aqueous fraction was calculated and used for pH prediction in the multicomponent gas mixtures. The %AAD to experimental

data was found to be (1.25% and 0.36%) for a CH₄-CO₂-N₂-H₂O system for pressures up to 15 MPa and at temperatures of 293.15 and 323.15 K respectively, endorsing the accuracy of the model to predict the pH value when water is in equilibrium with gas mixtures. As can be seen in Figure 5.20, the changes in pH value are very small while the pressure is changing from about 10 to 15 MPa because of the steep increase in the composition of CO₂ in the liquid phase.

By comparing the pH results that were obtained for pure CO₂ and ternary gas mixture, it is obvious that the pH value was increased about 0.1-0.2 units while the ternary gas mixture is in equilibrium with water at the same pressure and temperature conditions compare to CO₂ saturated water system. This is because the solubility of CO₂ decreased with the increasing simultaneous dissolution of other gases. Indeed, dissolution of CO₂ in water which is related to solubility trapping of CO₂ decreases with a drop in partial pressure of CO₂. Hence, as the higher concentration of impurities contains in the gas mixture, less CO₂ can dissolve in the aqueous solution, resulting in higher pH value.

Furthermore, the accuracy of the developed model was evaluated against the experimental data in the presence of NaCl in the aqueous solution. To achieve this, spectroscopic measurements were carried out to measure the pH at different P-T conditions while the ternary gas composition was in equilibrium with brine solution (1 m NaCl). Results are summarised and plotted in Table 5.8 and Figure 5.21. As mentioned earlier, the presence of salt in the solution causes a greater drop in pH value at same P-T conditions. By comparing the pH results in the presence and absence of salt at 10.24 MPa and temperature of 293.15 K, one can see the pH of ternary gas mixture saturated 1 m NaCl solution drops from 3.21 to 3.13, similar to what observed at different pressure conditions. Hence, this result again indicates that the pH of (CO₂ mixtures + NaCl) decrease with increase in salinity at constant temperature and pressure, causing an increase in solution acidity.

Table 5.8. Measured and predicted pH values for ternary gas mixture (Aqueous fraction = 0.942).

T / K	P / MPa	pH (Experimental)	pH (Model)
293.15	1.48	3.40	3.45
	2.79	3.31	3.33
	4.24	3.20	3.25
	5.58	3.17	3.20
	7.00	3.15	3.17
	10.24	3.13	3.12
	13.89	3.10	3.10
323.15	1.97	3.42	3.53
	4.18	3.32	3.38
	6.24	3.28	3.31
	6.93	3.25	3.30
	10.29	3.20	3.24
	15.20	3.15	3.19

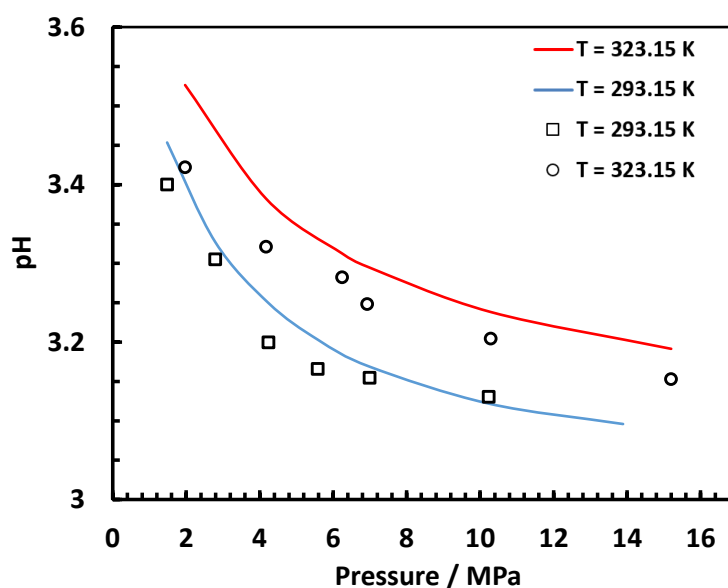


Figure 5.21. Experimental and predicted pH values in the $\text{CH}_4\text{-CO}_2\text{-N}_2\text{-H}_2\text{O-NaCl}$ system. Empty symbol represent the experimental data that obtained using spectroscopic technique. Solid lines represent the prediction from the model using an aqueous fraction of 0.921.

As can be seen from Table 5.8, there is no large difference between the measured pH values and the predicted pH values by the model, indicating the accuracy of the model to predict the pH value for $\text{CH}_4\text{-CO}_2\text{-N}_2\text{-H}_2\text{O-1 m NaCl}$ system. The measured pH values for both studied systems were found to be in excellent agreement with the model with an overall %AAD to experimental data of 0.76%.

Finally, the accuracy of the model was examined for one multicomponent gas mixture when it's in equilibrium with water. pH of multicomponent mixtures saturated water is nearly non-existent. The multicomponent system is a mixture of methane, ethane, propane, butanes, pentane, nitrogen and carbon-dioxide. The composition of gas mixture supplied by BOC is given in Table 5.9. This system was studied over two temperatures (293.15 and 323.15 K) and pressures up to 15 MPa.

Table 5.9. Multicomponent gas composition.

Components	mol%
CO ₂	Balance (69.30)
CH ₄	26.21 (± 0.018)
C ₂ H ₄	0.93(± 0.018)
C ₃ H ₈	0.29(± 0.006)
n-C ₄ H ₁₂	0.07(± 0.007)
i-C ₄ H ₁₂	0.07 (± 0.01)
n-C ₅ H ₁₆	0.02 (± 0.0004)
i-C ₅ H ₁₆	0.03 (± 0.0004)
N ₂	3.08 (± 0.06)

As one can see from Figure 5.22, the pH value starts to decrease with an increase in pressure, similar to what is observed for pure CO₂ and ternary gas mixture. It can be seen from the aforementioned figure, at a pressure higher than 10 MPa the pH was reached a plateau which is due to the very low solubility of CO₂ at elevated pressures.

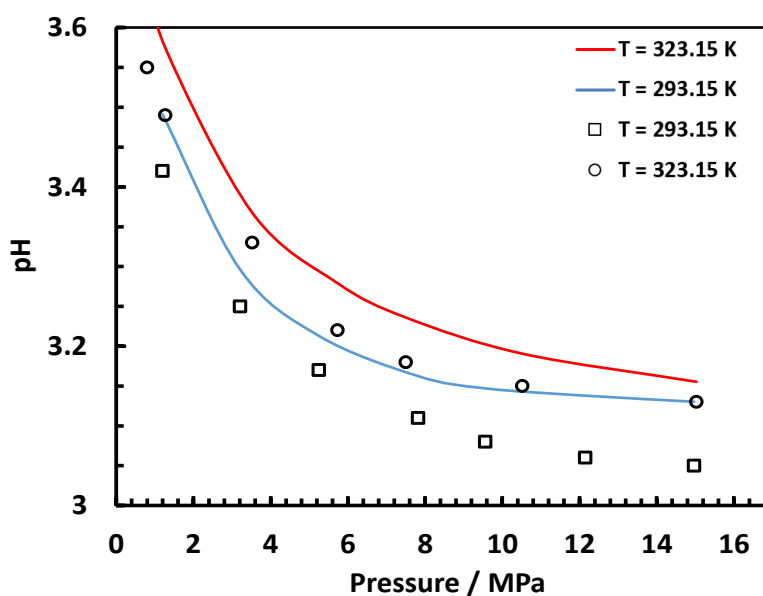


Figure 5.22. Experimental and predicted pH values in the multicomponent gas mixture system. Empty symbol represent the experimental data that obtained using spectroscopic technique. Solid lines represent the prediction from the model using an aqueous fraction of 0.921.

Table 5.10. Measured and predicted pH values for ternary gas composition for (Aqueous fraction = 0.912).

T / K	P / MPa	pH (Experimental)	pH (Model)
293.15	1.20	3.42	3.49
	3.21	3.25	3.30
	5.25	3.17	3.21
	7.82	3.11	3.16
	9.56	3.08	3.15
	12.15	3.06	3.14
	14.97	3.05	3.13
323.15	0.80	3.55	3.67
	1.27	3.49	3.57
	3.52	3.30	3.37
	5.73	3.20	3.28
	7.50	3.16	3.24
	10.52	3.11	3.19

Lastly, the result obtained for multicomponent mixtures was compared against values that predicted by the model. The model is able to represent the pH value well while the multicomponent gas mixture is in equilibrium with water with an over %AAD of 1.90 for all the studied pressures and temperatures.

5.7 Conclusions

Two experimental setups based on either electrical or spectroscopic methods were employed to measure the pH at various pressures and temperatures. The pH values were measured for the CO₂-H₂O, CO₂-H₂O-NaCl (NaCl: 1 to 3 m) systems at pressures up to 6 MPa and temperatures up to 353.15 K. Good agreement was obtained between literature data and measured values. It was shown that the pH of all the studied systems starts to decrease with increasing pressure. However, based on the spectroscopic, electrometric and modelling results this reduction is sharp while the pressure is less than 3 MPa because of the high solubility of CO₂ in the aqueous phase. This drop in pH value starts to reduce gradually at pressures higher than 3 MPa and at pressures higher than 6 MPa the reduction in pH value is very small due to the steep increase in the composition of CO₂ in the liquid phase. Moreover, the effect of variation in salinity on pH value was also investigated. It

was observed that the pH of CO₂-saturated solutions decreases with an increase in the concentration of NaCl in the solution while the pressure and temperature kept constant. Finally, the pH of two CO₂ rich gas mixtures water/brine saturated were measured using the UV-Vis spectrometer at pressures up to 15 MPa and temperature ranging from (293.15 to 323.15 K). No significant change was observed in the pH value at a pressure higher than 10 MPa. These results all confirmed the capability of the spectroscopic method to perform the pH measurements at HTHP conditions and high salinities. This method is applicable while the pH is varying from about 2.5 to 4.5. Geological CO₂ sequestration reservoirs contain highly soluble minerals like calcite (CaCO₃) and dolomite (CaMg(CO₃)₂) which are the most common minerals at or near the surface. The solubility of these minerals in water can increase significantly with an increase in temperature and pressure, results in higher pH values [144]. Thereby, it is required to use other dye indicators such as bromocresol green and bromocresol purple to extend the range of pH measurement in order to measure the pH under geological CO₂ sequestration conditions.

Furthermore, we described and evaluated a model that uses a robust thermodynamic basis for describing the solubility of gases in the liquid phase and Pitzer's theory for determining the activity coefficients of the ionic species involved. This approach proved to be capable of describing the chemical equilibria of the ionic species in the liquid phase under HTHP conditions and in systems of interest. The model was tested in concentrated NaCl solutions under CO₂ pressure at realistic industrial operating temperatures. The algorithm presented in this work and implemented in our in-house PVT software is prepared to account for the effect of dissolved acid gases such as carbon dioxide and hydrogen sulphide and the following ionic species: H⁺, Na⁺, OH⁻, Cl⁻, HCO₃⁻ and CO₃²⁻. All the experimental results for different fluid systems were compared with results that were reproduced by the model to investigate the capability of developed model for different fluid systems. A good agreement between predictions and experimental data is observed. It is noteworthy to mention very small deviations were observed at high NaCl concentration ($m = 3 \text{ mol.kg}^{-1}$), demonstrating the ability of the model to predict the pH at high salinities.

All the results confirm that spectroscopy is a viable method to measure the pH at elevated pressure and temperature conditions in various fluid systems. However, this method has some disadvantages. The presence of small suspended particles may produce some error in measurements due to light scattering. Moreover, there is a possibility of chemical reaction between the dye indicator and metal ions, causing some inconsistency in results.

Nonetheless, by selecting the appropriate dye indicator, the spectroscopic method can provide accurate results for in-situ pH measurement.

CHAPTER 6: CONCLUSIONS AND RECOMMENDATIONS OF FUTURE WORK

This thesis describes the development and uses of spectroscopy technology for measurements involving major flow assurance issues. A number of novel methods have been proposed and investigated for detecting early signs of hydrate formation, monitoring hydrate inhibition based on downstream sample analysis and online measurements. Another task of this work was to gain a better understanding of the interactions between CO₂ and CO₂-rich gas mixtures saturated with water/brines at downhole wellbore conditions (high pressure and temperature).

The conclusions that can be made from the work presented in this thesis are summarised below, following which suggestions for future work are given.

6.1 Conclusions

The conclusions from Chapters 2 and 3 which presented the work relating to the development and validation of an NIR spectroscopy setup to measure the composition of main hydrocarbon components (Methane through butanes) at high pressures and to detect early signs of hydrate formation in different fluid systems are as follows.

6.1.1 Initial Hydrate Formation Detection Techniques

- A method comprising of NIR spectroscopy and multivariate calibration model is developed for measuring the compositions of hydrocarbon components in gas samples in real-time. It was proved that multivariate regression methods such as the partial least squares could effectively remove non-selective part from the measurements and provide sufficiently accurate prediction models.
- The best results were obtained with the PLS (Partial Least Square) algorithm when considering the spectral region 1670-1800 nm with the first Savitzky-Golay derivative plus orthogonal signal correction (OSC) pre-treatment.
- The NIR prototype is able determine the major hydrocarbon components of natural gas at pressures from 3.44 to 13.78 MPa and temperatures from 278.15 to 313.15 K. The performance of the developed models was evaluated using analytical figures of merit such as root mean error of prediction (RMSEP), standard error of prediction (SEP) and limit of detection (LoD).

- A graphical user interface (GUI) was developed to control the FTNIR testing system using LabVIEW 2013. This GUI integrates the FTNIR setup into a prototype for online monitoring and real-time determination of the interested components.
- The developed PLS models were evaluated for different real natural gases and good agreement between the PLS model prediction and the gas chromatography (GC) analysis was gained at different pressures and temperatures.
- The sensitivity of the FTNIR spectroscopy technique to the system pressure and temperature was investigated. It was verified that changes in pressure and temperature within a certain range affect the accuracy of the PLS models. It was concluded that the developed PLS models could provide sufficient measurement accuracy if the shift in temperature and pressure is less than 2 K and 0.14 MPa, respectively.
- Results obtained by the developed NIR setup confirm that detection of the compositional change could provide information if gas hydrate is forming or formed and dissociated in a pipeline. Furthermore, the changes in the molecular ratios could maintain measurable for a certain period even if the hydrate is dissociated due to hydrate water memory phenomenon, which mainly depends on the thermodynamic conditions.
- Evaluations of the C_1/C_3 and C_1/C_2 ratios were monitored in the gas phase using the developed NIR setup. In all performed tests, it was seen the formation of gas hydrate results in a reduction in C_1/C_3 and C_1/C_2 ratios; this is because propane and ethane were consumed during hydrate formation, which is a sign of sII hydrate formation. During hydrate dissociation, it was noticed that the C_1/C_3 and C_1/C_2 ratios start to decrease while the system enters inside hydrate structure II and outside hydrate stability zone. It means that propane and ethane released from the aqueous phase and entered into the gas phase during hydrate dissociation. The results showed that gas phase compositional change technique could detect hydrate formation for more than 7 bbl/MMscf of water converted to hydrate.
- The results obtained in this study show that the NIR can operate accurately at pressures from 3.44 to 13.78 MPa. However, the commercial devices such as GasPT-based or GC-based compositional change technique can operate only at

atmospheric pressure. This does not always meet the need of flow assurance for some specific conditions, for example, for subsea application.

- The results show that the integration of the FTNIR spectroscopy technique with the V-V_{tc} technique forms the most applicable system for both hydrate monitoring and detection of initial hydrate formation.
- A trial of the compositional change technique was carried out at MEILLON gas condensate onshore field (France) by one of the sponsors to examine the feasibility of this method to detect initial signs of hydrate formation using an online GC (GC Micro GC SRA Instruments R3000) which was installed at the gas outlet of the separator. It was found that, as the hydrate formation progressed, preferentially propane and i-butane were consumed due to the higher affinity of sII hydrates to these hydrocarbons in the gas phase. However, at several points, some inconsistencies were observed that can be explained by the coexistence of both sI and sII hydrates due to consumption of heavy hydrocarbons in the gas phase which results in the enrichment of methane in the gas phase facilitating the formation of hydrate sI. The results demonstrate that composition changes in the gas phase can be used as a sign of hydrate formation.

6.1.2 Hydrate Inhibition Monitoring Techniques

One of the main objectives of this research study was to develop techniques for monitoring the hydrate safety margin and for detecting signs of early hydrate formation. Application of the early warning techniques along with the hydrate monitoring techniques can significantly improve the reliability of hydrate inhibition. The main findings from the work presented in Chapter 4 are listed in below:

- A new spectroscopy method was described for measuring the concentration of NaCl and hydrate inhibitors by combining the NIR and UV regions. The former was used to predict the concentration of NaCl and thermodynamic inhibitors (i.e., methanol, MEG), whereas the latter was employed to determine the concentration of kinetic inhibitor (i.e., PVCap) in water samples.
- Various PLS models were developed in different spectral regions. The best results for MEG, methanol and NaCl were obtained while the spectral range between 1400-1800 nm was selected for developing the PLS model. For PVCap, the optimal wavelength region was found to be between 300 and 350 nm in the UV region.

- The results show that the combination of NIR and UV spectroscopy technique can be successfully used for determining methanol, MEG and PVCap concentration in the presence of NaCl. All the developed PLS models show good linearity and low RMSEP and SEP values.
- Statistical tests exhibited that the created models have no sign of systematic errors or trends. Consequently, this method can be useful for fast, non-destructive, and low-cost monitoring of THIs and KHIs in water samples in the presence of salt.
- Moreover, the proposed method was evaluated for one typical inhibition system (MEG-salt systems) for the designed salt and inhibitor concentration ranges and pressure up to 20 MPa. The results showed that the developed PLS models could determine the concentration of NaCl and MEG with an acceptable accuracy.

6.1.3 pH of CO₂ saturated water and CO₂ saturated brines: Experimental measurements and modelling

Undoubtedly, thermodynamic properties of pure CO₂ and CO₂-rich mixtures play an important role in the design and modelling of CO₂ infrastructures. Chapter 5 concentrated on the pH measurement using two different techniques (i.e., spectroscopic, electrometric) and pH modelling. Both spectroscopic and electrometric methods were employed to measure the pH of water saturated with carbon dioxide at pressures up to 6 MPa, temperature ranges from 293.15 to 353.15 K and salinities up to 3 mol.kg⁻¹.

- Similar observations were found between the literature data and the measured pH values within the range of the P–T conditions studied. It was shown that the pH value decreases sharply with increasing pressure while the operating pressure is less than 3 MPa and this reduction in pH values are less for pressure higher than 3 MPa.
- The effect of variation in salinity on pH value was also investigated. It was observed that the pH of CO₂-saturated solutions decreases with an increase in the concentration of NaCl in the solution while the pressure and temperature kept constant.
- For the first time, spectroscopy measurements were carried out to measure the pH of one ternary mixture and one multicomponent mixture at pressures up to 15 MPa and at temperatures up to 323.15 K for different fluid systems. All the results

presented in Chapter 5 confirmed that spectroscopy is a viable method to measure the pH at elevated pressure and temperature conditions in various fluid systems.

- A fully predictive model was developed to predict the changes in the pH due to the solubility of CO₂ in the aqueous phase at high pressure and high temperature conditions as well as the effect of NaCl by coupling the Cubic-Plus-Association Equation of State (CPA EoS) and the Pitzer equations.
- The predictive capability of the pH model was evaluated against the data gathered from the literature and data measured in this work. The model allowed a prediction of the pH with an overall average absolute deviation (%AAD) to measured data of 0.76% and 1.82% in the CO₂-H₂O system using electrometric and spectroscopic techniques, respectively, and between 1.37% and 2.16% in the CO₂-H₂O-NaCl systems by employing the spectroscopic technique.

6.2 Recommendations of Future Work

This thesis shows the potential uses of spectroscopic methods for hydrate inhibition monitoring, initial hydrate formation detection and pH measurement at high pressure and temperature conditions and high salinities. Following recommendations are suggested for further research:

- Although the results of NIR spectroscopic technique showed that it is very viable technique, the main drawback of this method is that the measurements need to be performed at the pressures and temperatures close to the fixed calibrated points. It is suggested to extend this method to variable pressure and temperature systems. Strictly speaking, it is necessary to develop a global model that can work within the operating pressure and temperature ranges. Furthermore, the calibration models can be configured to cover a wider range of concentrations for all the components.
- The NIR prototype is able to determine the concentration of main hydrocarbon components in gas samples. It would be valuable to expand the applicability of this method for other species such as carbon dioxide (CO₂) and hydrogen sulphide (H₂S) as these components contribute to the formation of gas hydrates. However, such measurements are very challenging because of the toxic nature of these impurities and some modification need to be applied to experimental setups.

- For inhibition monitoring, it is suggested to extend this technology for other inhibition systems such as ethanol-NaCl system, Anti-Agglomerants (AAs)-NaCl system and make this method applicable in vast ranges of temperature as variation in temperature can affect the accuracy of the developed PLS models that calibrated at a single temperature.
- As mentioned in Chapter 4, the spectroscopic method was developed for NaCl solutions. Since in real conditions the aqueous solutions contain different types of salt such as KCl, MgCl₂, CaCl₂ and etc., it is necessary to investigate the applicability of the developed method for different types of salts.
- CO₂ originating from capture processes is generally not pure and can contain impurities such as H₂S, CH₄ and SO₂. The presence of some of these impurities can may change the thermophysical properties of CO₂-water/brine systems such as pH and CO₂ solubility. There are very few literature data concerning the impact of impurities on thermophysical properties of CCS mixtures. Thus, further research to find out their impact seems to be important.
- Some sour natural gas reservoirs contain high amount of H₂S and CO₂. Since H₂S and SO₂ are highly soluble in water, it is also very valuable to measure the pH of CO₂-H₂S and CO₂-SO₂ saturated water/brine systems at reservoir conditions. H₂S and SO₂ are both toxic, H₂S and SO₂ exposure under certain conditions can lead to serious health problems, and the subsequence of H₂S and SO₂ leakages from gas reservoirs to atmosphere could be disastrous. Thus, understandings of the chemical interaction between these components and reservoir fluids under reservoir conditions are vital.
- Field trials of the developed techniques in this study are highly recommended in order to provide a high level of confidence for their performance at real fields.

REFERENCES

1. Hammerschmidt, E., *Formation of gas hydrates in natural gas transmission lines*. Industrial & Engineering Chemistry, 1934. **26**(8): p. 851-855.
2. Harrison, S.E., *Natural Gas Hydrates*.
3. Sloan Jr, E.D. and C. Koh, *Clathrate hydrates of natural gases*. 2007: CRC press.
4. Rauh, F. and B. Mizaikoff, *Spectroscopic methods in gas hydrate research*. Analytical and bioanalytical chemistry, 2012. **402**(1): p. 163-173.
5. Ripmeester, J.A., S.T. John, C.I. Ratcliffe, and B.M. Powell, *A new clathrate hydrate structure*. Nature, 1987. **325**(6100): p. 135-136.
6. Makogon, I.U.r.F., *Hydrates of hydrocarbons*. 1997: Pennwell Books.
7. Haghighi, H., *Phase equilibria modelling of petroleum reservoir fluids containing water, hydrate inhibitors and electrolyte solutions*, 2009, Heriot-Watt University.
8. Sloan, E.D., *A changing hydrate paradigm—from apprehension to avoidance to risk management*. Fluid Phase Equilibria, 2005. **228**: p. 67-74.
9. Hoppe, R., R.L. Martin, M.K. Pakulski, and T.D. Schaffer. *Corrosion Mitigation With Gas Hydrate Inhibitors*. in *SPE Gas Technology Symposium*. 2006. Society of Petroleum Engineers.
10. Mokhatab, S. and W.A. Poe, *Handbook of natural gas transmission and processing*. 2012: Gulf Professional Publishing.
11. Lederhos, J., J. Long, A. Sum, R. Christiansen, and E. Sloan, *Effective kinetic inhibitors for natural gas hydrates*. Chemical Engineering Science, 1996. **51**(8): p. 1221-1229.
12. Argo, C., R. Blain, C. Osborne, and I. Priestley. *Commercial deployment of low dosage hydrate inhibitors in a southern North Sea 69 kilometer wet-gas subsea pipeline*. in *International Symposium on Oilfield Chemistry*. 1997. Society of Petroleum Engineers.
13. Cowie, L., P. Bollavaram, M. Erdogmus, T. Johnson, and W. Shero. *Optimal hydrate management and new challenges in GoM deepwater using "best in class" technologies*. in *Offshore Technology Conference*. 2005. Offshore Technology Conference.
14. Macpherson, C., P. Glenat, S. Mazloum, and I. Young. *Successful Deployment of a Novel Hydrate Inhibition Monitoring System in a North Sea Gas Field*. in *Proceedings of the 23rd International Oil Field Chemistry Symposium*. 2012.
15. Sloan, E.D., *Hydrate engineering*. 2000: Richardson, TX: Society of Petroleum Engineers.
16. Vajari, S.M., *Development of hydrate inhibition monitoring and initial formation detection techniques*, 2012, PhD thesis, Heriot-Watt University.
17. Kelland, M.A., *History of the development of low dosage hydrate inhibitors*. Energy & Fuels, 2006. **20**(3): p. 825-847.
18. Ford, K., T. Naehr, and G. Skilbeck. *The use of infrared thermal imaging to identify gas hydrate in sediment cores*. in *Proceedings of the Ocean Drilling*

- Program, Scientific results*. 2003. Ocean Drilling Program, Texas A&M University.
19. Sloan, E.D., C.A. Koh, and A. Sum, *Natural gas hydrates in flow assurance*. 2010: Gulf Professional Publishing.
 20. Tohidi, B., R. Anderson, A. Chapoy, J. Yang, and R.W. Burgass, *Do we have new solutions to the old problem of gas hydrates?* Energy & Fuels, 2012. **26**(7): p. 4053-4058.
 21. Tohidi, B., A. Chapoy, and J. Yang, *Developing a hydrate-monitoring system*. SPE Projects, Facilities & Construction, 2009. **4**(01): p. 1-6.
 22. Joshi, S.V., G.A. Grasso, P.G. Lafond, I. Rao, E. Webb, L.E. Zerpa, E.D. Sloan, C.A. Koh, and A.K. Sum, *Experimental flowloop investigations of gas hydrate formation in high water cut systems*. Chemical Engineering Science, 2013. **97**: p. 198-209.
 23. Gray, S.E.C., M.D. DeGrandpre, T.S. Moore, T.R. Martz, G.E. Friederich, and K.S. Johnson, *Applications of in situ pH measurements for inorganic carbon calculations*. Marine Chemistry, 2011. **125**(1): p. 82-90.
 24. Millero, F.J., B. DiTrollo, A.F. Suarez, and G. Lando, *Spectroscopic measurements of the pH in NaCl brines*. Geochimica et Cosmochimica Acta, 2009. **73**(11): p. 3109-3114.
 25. Babić, S., A.J. Horvat, D.M. Pavlović, and M. Kaštelan-Macan, *Determination of pK a values of active pharmaceutical ingredients*. TrAC Trends in Analytical Chemistry, 2007. **26**(11): p. 1043-1061.
 26. Gaus, I., *Role and impact of CO₂-rock interactions during CO₂ storage in sedimentary rocks*. International journal of greenhouse gas control, 2010. **4**(1): p. 73-89.
 27. Gray, L.G., B.G. Anderson, M.J. Danysh, and P. Tremaine, *Mechanism of carbon steel corrosion in brines containing dissolved carbon dioxide at pH 4*. Corrosion/89, paper, 1989(464).
 28. Crabtree, M., D. Eslinger, P. Fletcher, M. Miller, A. Johnson, and G. King, *Fighting scale—removal and prevention*. Oilfield Review, 1999. **11**(3): p. 30-45.
 29. Carroll, S.A., W.W. McNab, and S.C. Torres, *Experimental study of cement-sandstone/shale-brine-CO₂ interactions*. Geochemical transactions, 2011. **12**(1): p. 9.
 30. Kirk, J.L., A.L. Bristow, and A.M. Zanni, *Exploring the market for Compressed Natural Gas light commercial vehicles in the United Kingdom*. Transportation Research Part D: Transport and Environment, 2014. **29**: p. 22-31.
 31. Dai, Q. and C.M. Lastoskie, *Life cycle assessment of natural Gas-powered personal mobility options*. Energy & Fuels, 2014. **28**(9): p. 5988-5997.
 32. Burns, D.A. and E.W. Ciurczak, *Handbook of near-infrared analysis*. 2007: CRC press.
 33. Baker, R.W. and K. Lokhandwala, *Natural gas processing with membranes: an overview*. Industrial & Engineering Chemistry Research, 2008. **47**(7): p. 2109-2121.
 34. Glénat, P., J. Munoz, R. Haghi, B. Tohidi, S. Mazloun, and J. Yang, *Field Test results of monitoring Hydrates formation by gas composition changes during*

- gas/condensate production with AA-LDHI, in *Proceeding of the 8th International Conference on Gas Hydrates, Beijing, China* 2014.
35. Kondo, W., K. Ohtsuka, R. Ohmura, S. Takeya, and Y.H. Mori, *Clathrate-hydrate formation from a hydrocarbon gas mixture: Compositional evolution of formed hydrate during an isobaric semi-batch hydrate-forming operation*. Applied Energy, 2014. **113**: p. 864-871.
 36. Glénat, P., P. Saha, C. Macpherson, J. Yang, and B. Tohidi, *Field Tests Results of Production Inside Hydrate P&T Zone Using New Hydrate Monitoring Instruments*, in *Offshore Mediterranean Conference and Exhibition* 2015, Offshore Mediterranean Conference.
 37. Balabin, R.M., E.I. Lomakina, and R.Z. Safieva, *Neural network (ANN) approach to biodiesel analysis: analysis of biodiesel density, kinematic viscosity, methanol and water contents using near infrared (NIR) spectroscopy*. Fuel, 2011. **90**(5): p. 2007-2015.
 38. Mueller, J.J., S. Baum, L. Hilterhaus, M. Eckstein, O. Thum, and A. Liese, *Simultaneous determination of mono-, di-, and triglycerides in multiphase systems by online Fourier transform infrared spectroscopy*. Analytical chemistry, 2011. **83**(24): p. 9321-9327.
 39. Cervera-Padrell, A.E., J.P. Nielsen, M. Jøneh Pedersen, K. Müller Christensen, A.R. Mortensen, T. Skovby, K. Dam-Johansen, S. Kiil, and K.V. Gernaey, *Monitoring and control of a continuous Grignard reaction for the synthesis of an active pharmaceutical ingredient intermediate using inline NIR spectroscopy*. Organic Process Research & Development, 2012. **16**(5): p. 901-914.
 40. Balabin, R.M., R.Z. Syunyaev, and S.A. Karpov, *Quantitative measurement of ethanol distribution over fractions of ethanol-gasoline fuel*. Energy & fuels, 2007. **21**(4): p. 2460-2465.
 41. Ge, L.N., H.L. Zhan, W.X. Leng, K. Zhao, and L.Z. Xiao, *Optical characterization of the principal hydrocarbon components in natural gas using terahertz spectroscopy*. Energy & Fuels, 2015. **29**(3): p. 1622-1627.
 42. Alves, J.C.L. and R.J. Poppi, *Simultaneous determination of hydrocarbon renewable diesel, biodiesel and petroleum diesel contents in diesel fuel blends using near infrared (NIR) spectroscopy and chemometrics*. Analyst, 2013. **138**(21): p. 6477-6487.
 43. Eichmann, S., M. Weschta, J. Kiefer, T. Seeger, and A. Leipertz, *Characterization of a fast gas analyzer based on Raman scattering for the analysis of synthesis gas*. Review of Scientific Instruments, 2010. **81**(12): p. 125104.
 44. Eichmann, S.C., J. Kiefer, J. Benz, T. Kempf, A. Leipertz, and T. Seeger, *Determination of gas composition in a biogas plant using a Raman-based sensor system*. Measurement Science and Technology, 2014. **25**(7): p. 075503.
 45. Kiefer, J., *Recent Advances in the Characterization of Gaseous and Liquid Fuels by Vibrational Spectroscopy*. Energies, 2015. **8**(4): p. 3165-3197.
 46. Westbrook, S.R., *Army use of near-infrared spectroscopy to estimate selected properties of compression ignition fuels*, 1993, SAE Technical Paper.
 47. Dantas, H.V., M.F. Barbosa, E.C. Nascimento, P.N. Moreira, R.K. Galvão, and M.C. Araújo, *Screening analysis of natural gas with respect to methane content by near-infrared spectrometry*. Microchemical Journal, 2014. **114**: p. 210-215.

48. Makhoukhi, N., E. Péré, R. Creff, and C. Pouchan, *Determination of the composition of a mixture of gases by infrared analysis and chemometric methods*. Journal of molecular structure, 2005. **744**: p. 855-859.
49. Rohwedder, J., C. Pasquini, P. Fortes, I. Raimundo, A. Wilk, and B. Mizaikoff, *iHWG- μ NIR: a miniaturised near-infrared gas sensor based on substrate-integrated hollow waveguides coupled to a micro-NIR-spectrophotometer*. Analyst, 2014. **139**(14): p. 3572-3576.
50. Ribessi, R.L., T.d.A. Neves, J.J. Rohwedder, C. Pasquini, I.M. Raimundo, A. Wilk, V. Kokoric, and B. Mizaikoff, *iHEART: a miniaturized near-infrared in-line gas sensor using heart-shaped substrate-integrated hollow waveguides*. Analyst, 2016. **141**(18): p. 5298-5303.
51. Sharma, R., S. Poonacha, A. Bekal, S. Vartak, A. Weling, V. Tilak, and C. Mitra, *Raman analyzer for sensitive natural gas composition analysis*. Optical Engineering, 2016. **55**(10): p. 104103-104103.
52. Diller, D.E. and R.F. Chang, *Composition of mixtures of natural gas components determined by Raman spectrometry*. Applied Spectroscopy, 1980. **34**(4): p. 411-414.
53. Dong, C., M.D. O'Keefe, H. Elshahawi, M. Hashem, S.M. Williams, D. Stensland, P.S. Hegeman, R.R. Vasques, T. Terabayashi, and O.C. Mullins. *New downhole fluid analyzer tool for improved reservoir characterization*. in *Offshore Europe*. 2007. Society of Petroleum Engineers.
54. Manley, M., *Near-infrared spectroscopy and hyperspectral imaging: non-destructive analysis of biological materials*. Chemical Society Reviews, 2014. **43**(24): p. 8200-8214.
55. Fujisawa, G., M.A. Van Agthoven, F. Jenet, P.A. Rabbito, and O.C. Mullins, *Near-infrared compositional analysis of gas and condensate reservoir fluids at elevated pressures and temperatures*. Applied Spectroscopy, 2002. **56**(12): p. 1615-1620.
56. *A guide to near-infrared spectroscopic analysis of industrial manufacturing processes*, 2013, Metrohm Ltd.: Switzerland.
57. Robertson, J.R., C. Roux, and K. Wiggins, *Forensic examination of fibres*. 2002: CRC Press.
58. Jangale, V., *Real-time Characterization of Gaseous Fuels using NIR Spectroscopy and Multivariate Calibration*. 2013: North Carolina State University.
59. Bampi, M., A.d.P. Scheer, and F. de Castilhos, *Application of near infrared spectroscopy to predict the average droplet size and water content in biodiesel emulsions*. Fuel, 2013. **113**: p. 546-552.
60. Pasquini, C. and A.F. Bueno, *Characterization of petroleum using near-infrared spectroscopy: Quantitative modeling for the true boiling point curve and specific gravity*. Fuel, 2007. **86**(12): p. 1927-1934.
61. Camo Process, A., *Software Unscrambler*. Oslo, Norway, 2002.
62. Abdi, H., *Partial least square regression (PLS regression)*. Encyclopedia for research methods for the social sciences, 2003: p. 792-795.

63. Krishnan, A., L.J. Williams, A.R. McIntosh, and H. Abdi, *Partial Least Squares (PLS) methods for neuroimaging: a tutorial and review*. Neuroimage, 2011. **56**(2): p. 455-475.
64. Palermo, G., P. Piraino, and H.-D. Zucht, *Performance of PLS regression coefficients in selecting variables for each response of a multivariate PLS for omics-type data*. Advances and applications in bioinformatics and chemistry: AABC, 2009. **2**: p. 57.
65. Zeng, X.-Q., G.-Z. Li, G.-F. Wu, and H.-X. Zou. *On the number of partial least squares components in dimension reduction for tumor classification*. in *Pacific-Asia Conference on Knowledge Discovery and Data Mining*. 2007. Springer.
66. Balabin, R.M., R.Z. Safieva, and E.I. Lomakina, *Comparison of linear and nonlinear calibration models based on near infrared (NIR) spectroscopy data for gasoline properties prediction*. Chemometrics and intelligent laboratory systems, 2007. **88**(2): p. 183-188.
67. Vajari, S.M., *Development of hydrate inhibition monitoring and initial formation detection techniques*, 2012, Heriot-Watt University.
68. Tohidi, B., J. Yang, and A. Chapoy, *Hydrate monitoring system*, 2014, Google Patents.
69. Dorofki, M., A.H. Elshafie, O. Jaafar, O.A. Karim, and S. Mastura, *Comparison of artificial neural network transfer functions abilities to simulate extreme runoff data*. International Proceedings of Chemical, Biological and Environmental Engineering, 2012. **33**: p. 39-44.
70. Rinnan, Å., F. van den Berg, and S.B. Engelsen, *Review of the most common pre-processing techniques for near-infrared spectra*. TrAC Trends in Analytical Chemistry, 2009. **28**(10): p. 1201-1222.
71. Barnes, R., M. Dhanoa, and S.J. Lister, *Standard normal variate transformation and de-trending of near-infrared diffuse reflectance spectra*. Applied spectroscopy, 1989. **43**(5): p. 772-777.
72. Geladi, P., D. MacDougall, and H. Martens, *Linearization and scatter-correction for near-infrared reflectance spectra of meat*. Applied spectroscopy, 1985. **39**(3): p. 491-500.
73. Park, B. and R. Lu, *Hyperspectral imaging technology in food and agriculture*. 2015: Springer.
74. Wold, S., H. Antti, F. Lindgren, and J. Öhman, *Orthogonal signal correction of near-infrared spectra*. Chemometrics and Intelligent laboratory systems, 1998. **44**(1): p. 175-185.
75. Standard, A., *E1655 (2005) Standard practices for infrared multivariate quantitative analysis*, ASTM International, West Conshohocken, PA, 2005. doi: 10.1520/E1655-05R12.
76. Williams, P.C. and D. Sobering, *How do we do it: a brief summary of the methods we use in developing near infrared calibrations*. Near infrared spectroscopy: The future waves, 1996: p. 185-188.
77. Lutz, O.M., G.K. Bonn, B.M. Rode, and C.W. Huck, *Reproducible quantification of ethanol in gasoline via a customized mobile near-infrared spectrometer*. Analytica chimica acta, 2014. **826**: p. 61-68.

78. Adedipe, O.E., S.D. Johanningsmeier, V.-D. Truong, and G.C. Yencho, *Development and validation of a near-infrared spectroscopy method for the prediction of acrylamide content in French-fried potato*. Journal of agricultural and food chemistry, 2016. **64**(8): p. 1850-1860.
79. Ferreira, D.S., J.A.L. Pallone, and R.J. Poppi, *Fourier transform near-infrared spectroscopy (FT-NIRS) application to estimate Brazilian soybean [Glycine max (L.) Merrill] composition*. Food research international, 2013. **51**(1): p. 53-58.
80. Ni, W., L. Nørgaard, and M. Mørup, *Non-linear calibration models for near infrared spectroscopy*. Analytica chimica acta, 2014. **813**: p. 1-14.
81. Balabin, R.M. and S.V. Smirnov, *Variable selection in near-infrared spectroscopy: benchmarking of feature selection methods on biodiesel data*. Analytica chimica acta, 2011. **692**(1): p. 63-72.
82. Song, K., T. Tong, F. Wu, and Z. Zhang, *A novel partial least squares weighting Gaussian process algorithm and its application to near infrared spectroscopy data mining problems*. Analytical Methods, 2012. **4**(5): p. 1395-1400.
83. Siesler, H.W., Y. Ozaki, S. Kawata, and H.M. Heise, *Near-infrared spectroscopy: principles, instruments, applications*. 2008: John Wiley & Sons.
84. Mazloum, S., A. Chapoy, J. Yang, and B. Tohidi. *Developing a robust hydrate early warning system*. in *Proceedings of the 7th International Conference on Gas Hydrates (ICGH 2011)*. 2011.
85. Tohidi, B., J. Yang, A. Chapoy, and S. Mazloum, *Early warning system for hydrate or clathrate materials*, 2012, Google Patents.
86. Yang, J., S. Mazloum Vajari, A. Chapoy, and B. Tohidi. *Minimizing Hydrate Inhibitor Injection Rates*. in *International Petroleum Technology Conference*. 2014. International Petroleum Technology Conference.
87. Yang, J. and B. Tohidi, *Determination of hydrate inhibitor concentrations by measuring electrical conductivity and acoustic velocity*. Energy & Fuels, 2013. **27**(2): p. 736-742.
88. Vajari, S.M., *Development of hydrate inhibition monitoring and initial formation detection techniques*, 2012, Heriot-Watt University.
89. Giavarini, C., F. Maccioni, and M.L. Santarelli, *Formation kinetics of propane hydrates*. Industrial & Engineering Chemistry Research, 2003. **42**(7): p. 1517-1521.
90. KAWASAKI, T., I. YAMADA, and T. OKUI, ; *Composition of Guests in Hydrates from Gas Mixture*. Nihon Kikai Gakkai Nenji Taikai Koen Ronbunshu, 2003. **3**: p. 351-352.
91. Uchida, T., M. Moriwaki, S. Takeya, I.Y. Ikeda, R. Ohmura, J. Nagao, H. Minagawa, T. Ebinuma, H. Narita, and K. Gohara, *Two-step formation of methane-propane mixed gas hydrates in a batch-type reactor*. AIChE journal, 2004. **50**(2): p. 518-523.
92. Hester, K., R. Dunk, P. Walz, E. Peltzer, E. Sloan, and P. Brewer, *Direct measurements of multi-component hydrates on the seafloor: pathways to growth*. Fluid Phase Equilibria, 2007. **261**(1): p. 396-406.
93. Tohidi, B., J. Yang, A. Chapoy, and S. Mazloum, *Early warning system for hydrate or clathrate materials*, 2016, Google Patents.

94. Williams, T. and O.G. Solutions, *DEVELOPMENT OF REAL-TIME GAS QUALITY MEASUREMENT*.
95. ARCOptix FT-NIR Rocket 0.9-2.6 μ m Fibered near-infrared Fourier-transform spectrometer. Available from: <http://www.arcoptix.com/arcspectro-nir.htm>.
96. Wu, R., K.A. Kozielski, P.G. Hartley, E.F. May, J. Boxall, and N. Maeda, *Methane–propane mixed gas hydrate film growth on the surface of water and Luvicap EG solutions*. Energy & Fuels, 2013. **27**(5): p. 2548-2554.
97. Seo, Y., S.-P. Kang, and W. Jang, *Structure and composition analysis of natural gas hydrates: ^{13}C NMR spectroscopic and gas uptake measurements of mixed gas hydrates*. The Journal of Physical Chemistry A, 2009. **113**(35): p. 9641-9649.
98. Henning, B., P.-C. Daur, S. Prange, K. Dierks, and P. Hauptmann, *In-line concentration measurement in complex liquids using ultrasonic sensors*. Ultrasonics, 2000. **38**(1): p. 799-803.
99. Sandengen, K. and B. Kaasa, *Estimation of monoethylene glycol (MEG) content in water+ MEG+ NaCl+ NaHCO₃ solutions*. Journal of Chemical & Engineering Data, 2006. **51**(2): p. 443-447.
100. Lin, J. and C.W. Brown, *Near-IR spectroscopic measurement of seawater salinity*. Environmental science & technology, 1993. **27**(8): p. 1611-1615.
101. Grant, A., A.M. Davies, and T. Bilverstone, *Simultaneous determination of sodium hydroxide, sodium carbonate and sodium chloride concentrations in aqueous solutions by near-infrared spectrometry*. Analyst, 1989. **114**(7): p. 819-822.
102. Gowen, A., F. Marini, Y. Tsuchisaka, S. De Luca, M. Bevilacqua, C. O'Donnell, G. Downey, and R. Tsenkova, *On the feasibility of near infrared spectroscopy to detect contaminants in water using single salt solutions as model systems*. Talanta, 2015. **131**: p. 609-618.
103. Fernandes, H.L., I.M. Raimundo Jr, C. Pasquini, and J.J. Rohwedder, *Simultaneous determination of methanol and ethanol in gasoline using NIR spectroscopy: effect of gasoline composition*. Talanta, 2008. **75**(3): p. 804-810.
104. Guo, Q. and G.W. Small, *Quantitative determination of methanol and ethanol with synthetic calibration spectra in passive Fourier transform infrared remote sensing measurements*. Applied spectroscopy, 2013. **67**(8): p. 913-923.
105. Ouyang, A. and J. Liu, *Classification and determination of alcohol in gasoline using NIR spectroscopy and the successive projections algorithm for variable selection*. Measurement Science and Technology, 2013. **24**(2): p. 025502.
106. Anderson, R., F. Tohidi, H. Mozaffar, and B. Tohidi, *KINETIC HYDRATE INHIBITOR REMOVAL FROM PRODUCED WATERS BY SOLVENT EXTRACTION*. Journal of Petroleum Science and Engineering, 2016.
107. Gibbons, M.K. and B. Örmeci, *Quantification of polymer concentration in water using UV-Vis spectroscopy*. Journal of Water Supply: Research and Technology-Aqua, 2013. **62**(4): p. 205-213.
108. Panwar, N., S. Kaushik, and S. Kothari, *Role of renewable energy sources in environmental protection: a review*. Renewable and Sustainable Energy Reviews, 2011. **15**(3): p. 1513-1524.

109. Davison, J. and K. Thambimuthu, *Technologies for capture of carbon dioxide*. Proceedings of GHGT, 2004. **7**: p. 5-9.
110. Karadas, F., M. Atilhan, and S. Aparicio, *Review on the use of ionic liquids (ILs) as alternative fluids for CO₂ capture and natural gas sweetening*. Energy & Fuels, 2010. **24**(11): p. 5817-5828.
111. Gunter, W.D., S. Bachu, and S. Benson, *The role of hydrogeological and geochemical trapping in sedimentary basins for secure geological storage of carbon dioxide*. Geological Society, London, Special Publications, 2004. **233**(1): p. 129-145.
112. Seibel, B.A. and P.J. Walsh, *Potential impacts of CO₂ injection on deep-sea biota*. Science, 2001. **294**(5541): p. 319-320.
113. Brewer, P.G., *Ocean chemistry of the fossil fuel CO₂ signal: the haline signal of "business as usual"*. Geophysical Research Letters, 1997. **24**(11): p. 1367-1369.
114. Kakiuchi, T., *Salt bridge in electroanalytical chemistry: Past, present, and future*. Journal of Solid State Electrochemistry, 2011. **15**(7-8): p. 1661-1671.
115. Yamada, A., S. Mohri, M. Nakamura, and K. Naruse, *A Simple Method for Decreasing the Liquid Junction Potential in a Flow-through-Type Differential pH Sensor Probe Consisting of pH-FETs by Exerting Spatiotemporal Control of the Liquid Junction*. Sensors, 2015. **15**(4): p. 7898-7912.
116. Shibata, M., H. Sakaida, and T. Kakiuchi, *Determination of the activity of hydrogen ions in dilute sulfuric acids by use of an ionic liquid salt bridge sandwiched by two hydrogen electrodes*. Analytical chemistry, 2010. **83**(1): p. 164-168.
117. Meyssami, B., M.O. Balaban, and A.A. Teixeira, *Prediction of pH in model systems pressurized with carbon dioxide*. Biotechnology progress, 1992. **8**(2): p. 149-154.
118. Rosenqvist, J., A.D. Kilpatrick, and B.W. Yardley, *Solubility of carbon dioxide in aqueous fluids and mineral suspensions at 294K and subcritical pressures*. Applied geochemistry, 2012. **27**(8): p. 1610-1614.
119. Schaef, H.T. and B.P. McGrail, *Direct measurements of pH and dissolved CO₂ in H₂O–CO₂ brine mixtures to supercritical conditions*. in AAPG Annual Meeting, Dallas, Texas. 2004.
120. Peng, C., J.P. Crawshaw, G.C. Maitland, J.M. Trusler, and D. Vega-Maza, *The pH of CO₂-saturated water at temperatures between 308K and 423K at pressures up to 15MPa*. The Journal of Supercritical Fluids, 2013. **82**: p. 129-137.
121. Toews, K.L., R.M. Shroll, C.M. Wai, and N.G. Smart, *pH-defining equilibrium between water and supercritical CO₂. Influence on SFE of organics and metal chelates*. Analytical Chemistry, 1995. **67**(22): p. 4040-4043.
122. Parton, T., S. Spilimbergo, N. Elvassore, and A. Bertucco. *UV-vis spectroscopy for the determination of diffusion coefficient and pH in aqueous solutions/SC–CO₂ systems*. in High Pressure in Venice 4th International Symposium on High Pressure Process Technology and Chemical Engineering. 2002.
123. Raven, J., K. Caldeira, H. Elderfield, O. Hoegh-Guldberg, P. Liss, U. Riebesell, J. Shepherd, C. Turley, and A. Watson, *Ocean acidification due to increasing*

- atmospheric carbon dioxide*. 2005: The Royal Society, London (ISBN 0-85403-617-2)
124. Thomas, D.C. and S.M. Benson, *Carbon dioxide capture for storage in deep geologic formations-results from the CO₂ Capture Project: Vol 2-Geologic Storage of Carbon Dioxide with Monitoring and Verification*. 2015: Elsevier, Amsterdam (ISBN: 978-0-08-044570-0).
 125. Shao, H., C.J. Thompson, and K.J. Cantrell, *Evaluation of experimentally measured and model-calculated pH for rock-brine-CO₂ systems under geologic CO₂ sequestration conditions*. Chemical Geology, 2013. **359**: p. 116-124.
 126. Shao, H., C.J. Thompson, O. Qafoku, and K.J. Cantrell, *In situ spectrophotometric determination of pH under geologic CO₂ sequestration conditions: method development and application*. Environmental science & technology, 2012. **47**(1): p. 63-70.
 127. Truche, L., E.F. Bazarkina, G. Berger, M.-C. Caumon, G. Bessaque, and J. Dubessy, *Direct measurement of CO₂ solubility and pH in NaCl hydrothermal solutions by combining in-situ potentiometry and Raman spectroscopy up to 280° C and 150bar*. Geochimica et Cosmochimica Acta, 2016. **177**: p. 238-253.
 128. Usha, A. and G. Atkinson, *The effect of pressure on the dissociation constant of hydrofluoric acid and the association constant of the NaF ion pair at 25° C*. Journal of solution chemistry, 1992. **21**(5): p. 477-488.
 129. Bates, R.G., *Determination of pH: theory and practice*. Determination of pH: theory and practice., 1964.
 130. Kontogeorgis, G.M., M.L. Michelsen, G.K. Folas, S. Derawi, N. von Solms, and E.H. Stenby, *Ten years with the CPA (Cubic-Plus-Association) equation of state. Part 1. Pure compounds and self-associating systems*. Industrial & engineering chemistry research, 2006. **45**(14): p. 4855-4868.
 131. Kontogeorgis, G.M., M.L. Michelsen, G.K. Folas, S. Derawi, N. von Solms, and E.H. Stenby, *Ten years with the CPA (Cubic-Plus-Association) equation of state. Part 2. Cross-associating and multicomponent systems*. Industrial & engineering chemistry research, 2006. **45**(14): p. 4869-4878.
 132. Pitzer, K.S., J.C. Peiper, and R. Busey, *Thermodynamic properties of aqueous sodium chloride solutions*. Journal of Physical and Chemical Reference Data, 1984. **13**(1): p. 1-102.
 133. Pitzer, K.S., *Thermodynamics of electrolytes. I. Theoretical basis and general equations*. The Journal of Physical Chemistry, 1973. **77**(2): p. 268-277.
 134. Kontogeorgis, G.M., E.C. Voutsas, I.V. Yakoumis, and D.P. Tassios, *An equation of state for associating fluids*. Industrial & engineering chemistry research, 1996. **35**(11): p. 4310-4318.
 135. Huang, S.H. and M. Radosz, *Equation of state for small, large, polydisperse, and associating molecules*. Industrial & Engineering Chemistry Research, 1990. **29**(11): p. 2284-2294.
 136. Poling, B.E., J.M. Prausnitz, O.C. John Paul, and R.C. Reid, *The properties of gases and liquids*. Vol. 5. 2001: McGraw-Hill New York.

137. Chapoy, A., H. Haghighi, R. Burgass, and B. Tohidi, *On the phase behaviour of the (carbon dioxide+ water) systems at low temperatures: experimental and modelling*. The Journal of Chemical Thermodynamics, 2012. **47**: p. 6-12.
138. Chapoy, A., R. Burgass, B. Tohidi, and I. Alsiyabi, *Hydrate and phase behavior modeling in CO₂-rich pipelines*. Journal of Chemical & Engineering Data, 2014. **60**(2): p. 447-453.
139. Aasberg-Petersen, K., E. Stenby, and A. Fredenslund, *Prediction of high-pressure gas solubilities in aqueous mixtures of electrolytes*. Industrial & engineering chemistry research, 1991. **30**(9): p. 2180-2185.
140. Haghighi, H., A. Chapoy, and B. Tohidi, *Freezing point depression of electrolyte solutions: experimental measurements and modeling using the cubic-plus-association equation of state*. Industrial & Engineering Chemistry Research, 2008. **47**(11): p. 3983-3989.
141. Haghighi, H., A. Chapoy, and B. Tohidi, *Methane and water phase equilibria in the presence of single and mixed electrolyte solutions using the cubic-plus-association equation of state*. Oil & Gas Science and Technology-Revue de l'IFP, 2009. **64**(2): p. 141-154.
142. Pedersen, K.S., P.L. Christensen, and J.A. Shaikh, *Phase behavior of petroleum reservoir fluids*. 2014: CRC Press.
143. Crolet, J. and M. Bonis, *pH measurements in aqueous CO₂ solutions under high pressure and temperature*. Corrosion, 1983. **39**(2): p. 39-46.
144. Schaef, H.T., B.P. McGrail, and A.T. Owen, *Carbonate mineralization of volcanic province basalts*. International Journal of Greenhouse Gas Control, 2010. **4**(2): p. 249-261.